(4)

AD-A202 822

AFAL-TR-88-039 AD:

Final Report
for the period
August 1985 to
January 1988

RCS/Linear Discrete Actuator Study

August 1988

Authors:
T. Bailey
A. Gruzen
P. Madden

The Charles Stark Draper Laboratory, Inc.
555 Technology Square
Cambridge, MA 02139

CSDL-R-2075
F04611-85-K-0051

Approved for Public Release

Prepared for the: Air Force Astronautics Laboratory

Air Force Space Technology Center
Space Division, Air Force Systems Command
Edwards Air Force Base,
California 93523-5000

REPORT DOCUMENTATION PAGE

1a. REPORT SECURITY CLASSIFICATION UNCLASSIFIED	1b RESTRICTIVE MARKINGS
2a SECURITY CLASSIFICATION AUTHORITY	3 DISTRIBUTION / AVAILABILITY OF REPORT Approved for public release; distribution is unlimited
2b. DECLASSIFICATION / DOWNGRADING SCHEDULE	
4. PERFORMING ORGANIZATION REPORT NUMBER(S) CSDL-R-2075	5 MONITORING ORGANIZATION REPORT NUMBER(S) AFAL-TR-88-039
6a. NAME OF PERFORMING ORGANIZATION The Charles Stark Draper Laboratory, Inc.	6b. OFFICE SYMBOL (If applicable) 51993
7a. NAME OF MONITORING ORGANIZATION Air Force Astronautics Laboratory	
6c. ADDRESS (City, State, and ZIP Code) 555 Technology Square Cambridge, MA 02139	7b. ADDRESS (City, State, and ZIP Code) AFAL/VSSS Edwards AFB, CA 93523-5000
8a. NAME OF FUNDING / SPONSORING ORGANIZATION	8b. OFFICE SYMBOL (If applicable)
9. PROCUREMENT INSTRUMENT IDENTIFICATION NUMBER F04611-85-K-0051	
8c. ADDRESS (City, State, and ZIP Code)	10. SOURCE OF FUNDING NUMBERS

PROGRAM ELEMENT NO.	PROJECT NO.	TASK NO	WORK UNIT ACCESSION NO
62302F	2864	00	LG

11. TITLE (Include Security Classification)
RCS/Linear Discrete Actuator Study (U)

12. PERSONAL AUTHOR(S)
Thomas Bailey, Alexander Gruzen, Paul Madden

13a. TYPE OF REPORT	13b. TIME COVERED	14. DATE OF REPORT (Year, Month, Day)	15. PAGE COUNT
Final	FROM Aug 85 TO Jan 88	88/8	296

16. SUPPLEMENTARY NOTATION

17. COSATI CODES			18. SUBJECT TERMS (Continue on reverse if necessary and identify by block number)
FIELD	GROUP	SUB-GROUP	Linear discrete actuators, Flexible structure control, Proof-mass actuators
22	02		

19. ABSTRACT (Continue on reverse if necessary and identify by block number)

The objective of the program was to develop the technology and demonstrate the use of linear discrete actuators combined with a rocket control system (RCS) to control the large angle slew and fine pointing/tracking of a simulated large flexible space structure. The linear actuators included proof-mass actuators, and a hub torquer to simulate a control moment gyro or reaction wheel actuator. The demonstration used the CSDL/AFAL ground test facility located at CSDL, Inc. The facility comprises the flexible test structure and actuators which are mounted on a low-friction, air-bearing table, and associated test instrumentation.

The combined linear discrete and RCS actuators demonstrated significantly improved fine pointing/tracking and vibration suppression capability relative to the use of the RCS alone.

20 DISTRIBUTION / AVAILABILITY OF ABSTRACT	21 ABSTRACT SECURITY CLASSIFICATION
☒ UNCLASSIFIED/UNLIMITED ☐ SAME AS RPT ☐ DTIC USERS	UNCLASSIFIED

22a NAME OF RESPONSIBLE INDIVIDUAL	22b TELEPHONE (Include Area Code)	22c OFFICE SYMBOL
Timothy J. Strange, III, 1Lt, USAF	(805) 275-5147	VSSS

TABLE OF CONTENTS

LIST OF FIGURES

LIST OF TABLES

Section 1

Introduction

1.1 Background

This report presents the results of the Reaction Control System/Linear Discrete Actuator investigation sponsored by the Air Force Astronautics Laboratory. A predecessor program was initiated in June 1982 with the objective of demonstrating the use of on-off thrusters for the control of large space structures in a ground-based experiment. The major objectives of this program as originally proposed were achieved. The project validated an on-off control law developed by Professor W.E. Vander Velde of M.I.T. and, in addition, a second control law developed by Dr. Michael Floyd during the course of his Ph. D thesis research. An integral part of the project involved the development of an experimental test facility which could support the testing of such control laws and which could be further developed in an evolutionary manner to support future experimental projects in large space structure control.

Simulations developed by Floyd as part of his research demonstrated the benefit of the simultaneous use of nonlinear (on-off) thrusters and linear (proportional) actuators. Two types of conceptual actuator were simulated. One device was placed at each extremity of the flexible structure, while another simulated torque control of the central hub. In practice, the first device could be realized by a proof-mass actuator (PMA), and the second by a momentum exchange device such as a control moment gyro (CMG). The linear devices dramatically improved the character of the simulated slew response of the structure. The program reported herein derived directly from this observation. The objective of the present program was to verify experimentally the benefits of the simultaneous use of on-off thrusters and linear discrete actuators.

The high force capabilities of thrusters makes them ideal to effect rapid slewing maneuvers. However, for many missions the control system is required to accomplish fine pointing and target tracking. On-off thrusters are not suited to this task especially when flexible mode frequencies are close to or overlap the controller bandwidth. In this situation the use of linear actuators is essential.

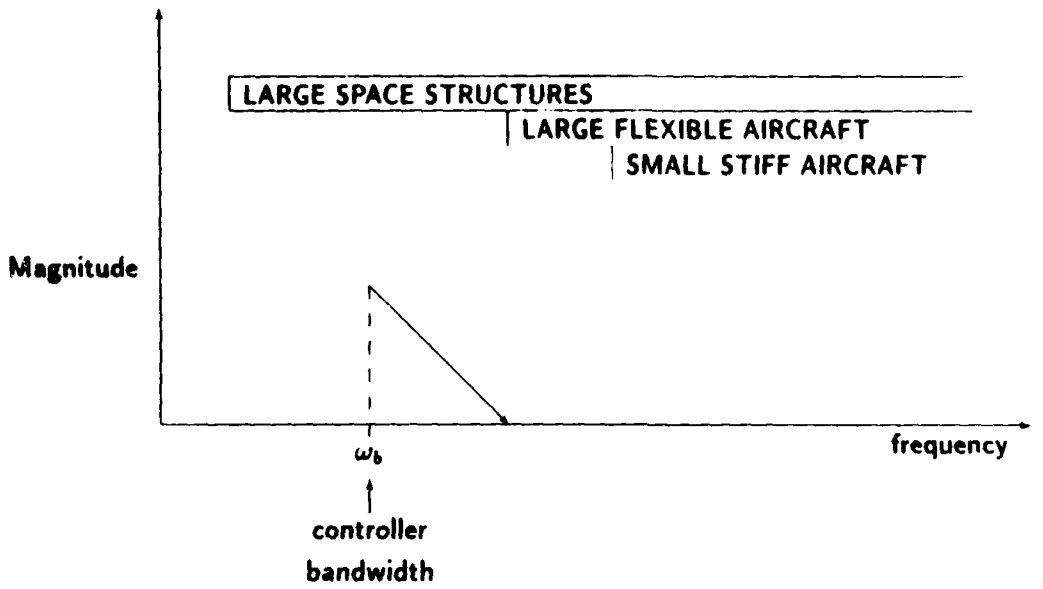

Figure 1-1. Modal frequency distribution of structural control problems vs. controller frequency response.

During the course of this investigation, a control system was conceptualized which uses both on-off thrusters and linear actuators. The intent was to use the thrusters primarily for slew maneuvers, for coarse vibration control, and for despinning momentum exchange devices. The linear devices would be used for fine pointing and tracking, and terminal vibration control. The use of thrusters to effect the rapid slew maneuvers must take account of the flexible modes so that residual vibrational energy is minimized. Therefore, the objective during the maneuver is satisfaction of the terminal error criterion while minimizing the vibration level at the end of the maneuver.

Until recently, the control system designer did not need to address the explicit control of a flexible structure. In aircraft flight control systems, for example, the control system bandwidth was usually well below the frequency of the first structural mode. It was possible to treat a small aircraft as a rigid body. For large flexible aircraft, one could implicitly control (through attenuation) the structural response using structural notch filters. These approaches were viable because of the frequency range of aircraft vibrational modes (see Figure 1-1). Because of the physical nature of large space structures (LSS), the frequencies associated with the first few vibrational modes are quite low. Given significant performance requirements for LSS slewing maneuvers, or fine pointing, these low frequency modes will necessarily fall within the control system bandwidth as is shown in Figure 1-1. One could, of course, reduce the control system bandwidth even further, or perhaps stiffen the structure thus permitting the classical methods of design. For example, this approach was chosen for the space shuttle remote manipulator system. However, a large penalty may result in overall system weight and

achievable performance levels. Consequently, active control of vibrational modes has become a new requirement, and has spawned new problems.

In order to control system vibrations, the flexible modes must be included in the model of the system dynamics, requiring accurate system identification. The task of predicting mode shapes and frequencies for LSS presents substantial problems. Ground based testing or simulation cannot truly determine the characteristics of a system when in the space environment. In some cases, the structure will be assembled in orbit, and computer modelling will be the only option for initial system identification. State-of-the-art modelling techniques still result in significant errors and this difficulty in properly characterizing a structure has led to a requirement for highly "robust" compensators. In this case, the compensator must maintain adequate system performance for a range of potential parameter variations.

Additionally, there is another form of modelling error that specifically relates to the LSS control problem— "spillover" from high-order unmodelled modes. The common approach for modelling flexible structures involves approximating the true modeshape as an infinite sum of sinusoidal modes. For computational reasons (i.e. numerical stability, accuracy, and cost), one generally truncates the model to a more manageable size. The eliminated higher order modes can destabilize the control system by contaminating the sensor measurements with high frequency signals. The "spillover" problem is only compounded by the need for lower order compensators.

To achieve high levels of performance, high sample rates are required for the compensators. To achieve these rates within the computational requirements of a particular processor, compensators of lower order than that of the plant model must be implemented. When these "reduced-order" compensators are designed, the most common methods use further model truncation to achieve the proper compensator order. With this additional truncation, the spillover problem becomes potentially more significant.

Consequently, major issues relevant to the control of flexible space structures are robustness with respect to both parameter modelling errors and truncation of higher order modes. These two issues form appropriate criteria for evaluating compensator design strategies.

1.2 The Ground-Based Structural Control Experiment

In order to evaluate the performance capabilities of various control strategies and generally to discover the practical difficulties of implementing slew controllers and vibration suppression devices, the Air Force Astronautics Laboratory (AFAL) funded the development of a ground-based experimental testbed. While the test apparatus is not a scaled model of any particular spacecraft, it was designed to mimic the following characteristics of a typical flexible space structure:

(1) First flexible mode frequency of 1 Hz. or less;

(2) Very low damping, with time constants on the order of 100 seconds; and

(3) Clearly visible deflections

The system consists of four cantilevered aluminum beams, mounted radially about a central hub. The structure is shown in Figure 1-2. This central hub is mounted on an air-bearing table, enabling the structure to rotate about its vertical axis. Consequently, there are minimal gravity effects in the single rigid body slewing mode. Various actuators can be mounted on the four arm tips, while the dynamic characteristics are maintained by varying the tip masses. Measurements are provided by accelerometers at each of the tips, and a central hub angle resolver.

1.3 The Predecessor Program

The initial research performed by Floyd on the AFAL experiment investigated the application of on-off thrusters to achieve rapid slew maneuvers of the structure [1]. In order to produce rapid slew rates, large control moments are needed. Thrusters located at the tips of the flexible arms provide these required torques. However, the use of discrete on-off, unthrottleable actuation devices introduces wide-band vibrational energy into the system. As the large angle slew requirement is associated with the requirement for precise fine-pointing, residual structural vibrations are quite detrimental to mission performance. Thus, the unthrottleable thrusters are not well suited to the fine-pointing task. There is a significant chance of limit cycling at the end of the maneuver and the required deadband puts a limit on the pointing capabilities of the system.

As a consequence of Floyd's research, the addition of linear actuators to the AFAL structure was proposed. Preliminary simulations using Floyd's control strategy to drive linear actuators as well as the thrusters showed a significant potential for performance improvement [1]. When employed primarily during the terminal phase of a slewing maneuver, the linear actuators greatly increased the rate at which vibrational energy was removed from the system.

A final and important observation from the first experimental program was that the friction of the air-bearing table used in that experiment prevented total verification of the controllers.

1.4 The Present Program

The objectives of the present program, reported herein, were as follows:

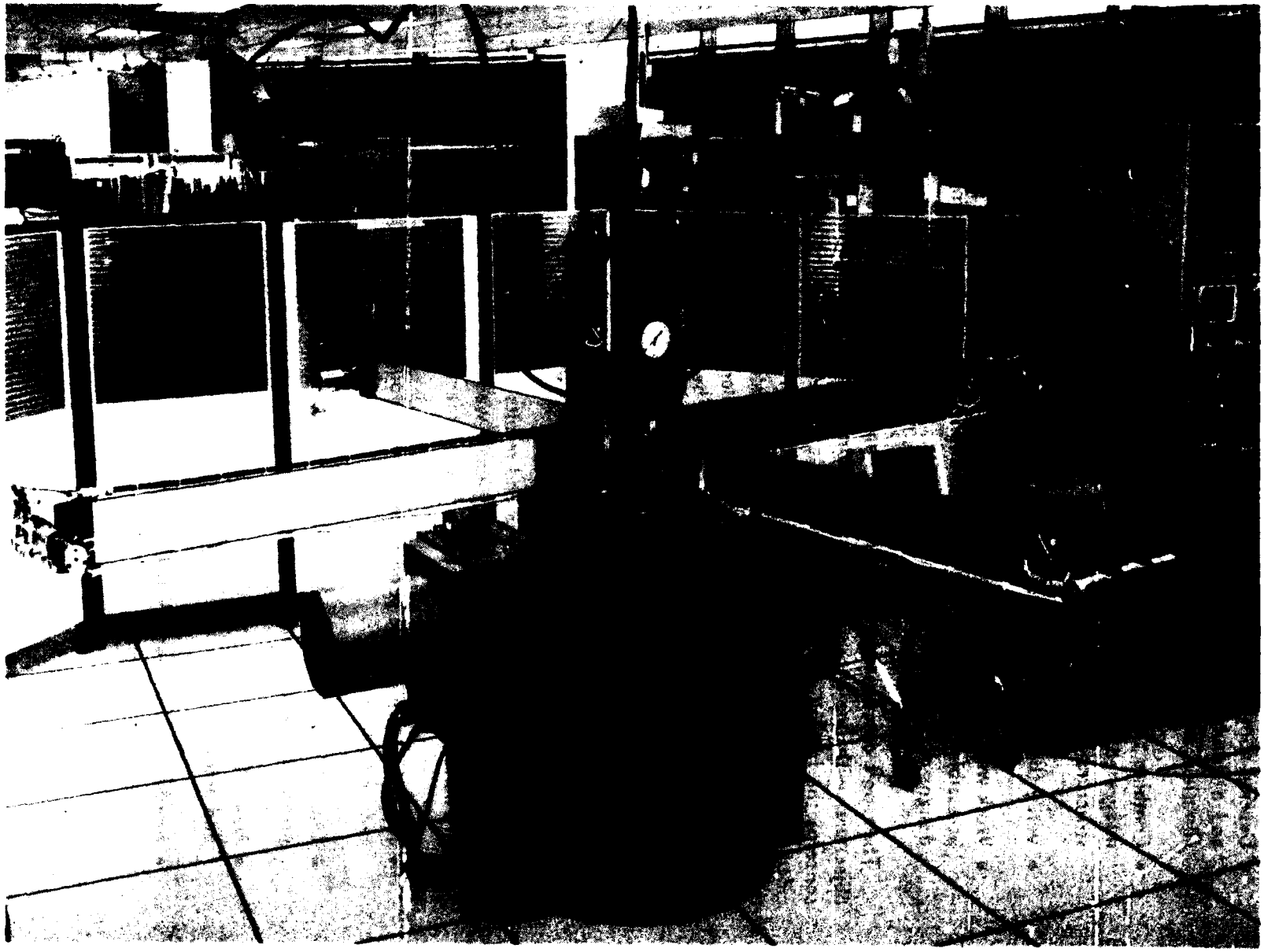

Figure 1-2. The CSDL/AFAL experimental structure.

- Develop control algorithms for using linear actuators (viz., proof-mass actuators and a simulated CMG hub torquer) for the simultaneous control of structural vibration, and fine pointing/tracking;
- Combine the linear discrete actuators with the on-off thrusters to achieve the integrated control of large-angle slewing maneuvers, fine pointing/tracking, and structural vibration;
- Verify the controller designs using a ground-based experimental facility; and
- Work with AFAL to make the CSDL/AFAL experimental facility both visible and accessible to the outside technical community for evaluating alternative controller designs in the future.

The report describes the approach taken and techniques developed to satisfy these objectives, with one exception, over the course of the investigation. The exception concerns the last objective noted above. At a late stage in the program AFAL decided to establish an experimental facility for space structures and controls research and development at Edwards AFB, California. This decision rendered the Draper facility superfluous. The Air Force has already developed plans and a conceptual design for the facility (to be called the ASTREX Laboratory). The intended use of the facility is to permit experimenters from the aerospace community and universities to demonstrate advanced control strategies on realistic spacecraft models.

1.4.1 Modifications to the Experimental Facility

As a consequence of the experience and results obtained from the predecessor program, and the objectives of the new program, it was decide to modify the experimental facility. The following changes were made to the facility:

- New Air-Bearing Table (Contraves/Goertz Model 51D) with specified changes to reduce table friction.
- Control Computer Upgrade (MicroVAX II) to increase computational capacity and provide a real-time operating system kernel (VAXELN).
- New I/O interface to the experiment to accommodate the larger number of sensors and actuators
- Relocation of the facility at CSDL, Inc. to facilitate access by outside researchers at the end of the program.

1.4.2 Modifications to the Experiment

In addition to facility modifications, changes were also made to the experiment structure and instrumentation. Briefly, these were as follows:

- New cold-gas supply hoses to reduce mass, damping and non-linear effects.
- Improved signal-to-noise ratio for the sensors by adjustment of the accelerometer dynamic range, and improved shielding of cables.
- Design and installation of proof-mass actuators for vibration control.
- Addition of the hub torquer to simulate, for example, a control moment gyro on a full-scale flexible spacecraft.

1.5 Organization of the Report

The reader is reminded that, generally, the nature of an experimental investigation of this type is evolutionary. Consequently, work performed in early phases may have a significant impact on the content and direction of later phases. The investigation reported herein was no exception to this general observation.

Approximately the first half of the report (Section 2 through Section 9) describes the work performed in the first fourteen months of the project. It was previously published as a Draper Laboratory interim report [2]. The work focused on the development of design tools for the implementation of linear control laws, and modifications to the experiment structure and computer to incorporate the linear actuators.

Section 5 through Section 8 describe the development of a proof-mass actuator control law based upon a theory for robust controller design called Optimal Projection/Maximum Entropy developed originally by Hyland and Bernstein [6]. This work was performed in the first half of the program concurrently with the design of new proof-mass actuators. The actual characteristics of the PMAs, as built, proved to be highly nonlinear. Consequently, an alternative strategy for control law development for these actuators was ultimately decided upon.

Section 9 presents the updated, more accurate dynamic model derived using NASTRAN. This model of the AFAL experiment structure was used for all subsequent control system analysis and design.

Section 10 discusses the computer hardware and software modifications required to replace the Labtech I/O interface and use the MicroVax II for all real-time control tasks.

The predecessor program developed a nonlinear controller for the on-off thrusters [1]. Section 11 discusses the modifications required to the control law to permit effective use

of the thrusters on the modified experiment structure which utilizes a very low friction air-bearing table.

The integration of the linear actuators into the overall experiment control strategy is discussed in Section 12. Potential interactions between the decentralized controllers are noted and addressed and the switching logic for transition from RCS to linear actuator control is described.

Section 13 provides an analysis of the dynamics of proof-mass actuators and develops an effective control law for vibration damping on the experiment structure. The new PMA control law was formulated to address the extensive nonlinearities which characterized the PMAs.

In Section 14, controller analysis and design for the hub torquer is described. An initial proportional-integral-derivative feedback design was developed which included a structural notch filter. However, the controller was found to be too sensitive to modelling errors. Subsequently, a more robust model-based compensator was developed using the Linear Quadratic Gaussian/Loop Transfer Recovery methodology. This controller phase stabilized the flexible structure modes.

Section 15 describes the major software applications and routines developed during the study to test and implement control laws for the thrusters and linear actuators.

Section 16 presents the experimental data from all test runs. Slew maneuver tests using the thrusters alone, and in conjunction with the PMAs and the hub torquer, are described.

Finally, Section 17 presents conclusions arising from the study.

1.6 Summary of Results and Conclusions

The experimental program verified the ability to perform fast, large angle slews on a simulated flexible space structure, and to successfully integrate additional discrete, nominally linear actuators with the reaction control system. The linear actuators improved significantly the fine pointing/tracking and vibration suppression capability of the controller.

The predecessor program was never able to fully demonstrate the suitability of the RCS single-step optimal control law for slewing and fine-pointing of the AFAL experiment structure [1]. Because of the high friction present in the first air-bearing table, the previous experiment was quite benign and did not accurately represent a lightly damped flexible space structure. While good slewing performance was demonstrated, the experiment limitations precluded an accurate indication of the performance capabilities or shortfalls of this type of thruster control.

The present program, utilizing a new low-friction air-bearing table, demonstrated

more convincingly the limited capability of an RCS to remove vibrational energy imparted to a structure during a high rate slew maneuver. More accurate system modelling and RCS thruster firing constraints improved performance significantly; however, the basic limitations of the unthrottleable nonlinear actuators remained and were readily demonstrated.

The addition of nominally linear actuators to the system improved remarkably the performance of the slew maneuver and terminal phase fine pointing/tracking. The proof-mass actuators mounted at each beam tip increased the system damping by a factor of fifteen over the uncontrolled damping. While the PMAs have essentially no capability to effect hub pointing, the high structural damping they provide prevented the large overshoot and limit cycling previously evidenced by the RCS thrusters. Because the PMAs are only effective for vibration damping, the system pointing performance is still limited by the deadband required for thruster control. The addition of the PMAs allowed reduction of the deadband from ± 0.5 degrees to ± 0.25 degrees, yet this limitation on absolute pointing still remained.

The hub torque actuator complements the other controls by eliminating the deadband during the terminal phase of the maneuver. By assuming the fine pointing control task, this actuator demonstrated a terminal pointing capability of ± 0.05 degrees, an accuracy that would have required an extremely narrow deadband and guaranteed limit cycling using the thruster controller alone.

The results show very emphatically how effective the linear actuators are in improving the fine-pointing/tracking and vibration suppression performance of the AFAL experiment. However, significant additional information gained in this investigation had less to do with pointing accuracies and more with the actual physical development of suitable actuator devices and the process of designing, constructing, and running a ground-based experiment of this type. Some of the more important conclusions concerning these aspects of the experimental program are noted in Section 17.

Finally, the implications of ground-based testing need to be better understood. While the AFAL experiment structure was probably well-suited to its early objectives as purely an RCS slewing maneuver testbed, the objectives of the present program might have been better addressed on a modified experimental facility. For example, the addition of the proof-mass actuators to the beam tips resulted in excessive torsional vibration and droop of the beams. This motion limited the frequency range over which the PMAs could be effectively utilized, thus limiting the scope of the vibration control experiment. The potential for higher bandwidth vibration suppression was consequently never realized.

Section 2

Modifications to the AFAL Test Facility

2.1 The Air-bearing Table

The AFAL structure mounts on an air bearing table and performs slewing maneuvers to emulate a flexible satellite in space. In the predecessor AFAL study, the air-bearing table used to support the structure displayed relatively high friction and "high spots", i.e., locations where the friction level jumps suddenly. In order to better approximate frictionless slewing maneuvers, a new air-bearing table was acquired.

The new table is a modified Contraves/Goertz model 51D two-axis table. The table axis has an air bearing while the tilt axis uses mechanical bearings. Table 2-1 shows the typical sources of friction and disturbance torques in an air-bearing table. With the help of Contraves representatives, a number of modifications designed to reduce table axis friction were explored. The possible modifications included a minimum number of slip rings, smaller DC torque motors (which would have less brush friction and cogging torque), brushless torque motors (AC and DC), servoed slip rings, and a special air bearing design.

A minimum of eight (8) slip rings are needed for the table axis position sensor, a 720 pole Inductosyn. As shown in Table 2-1, the minimum number of slip rings would contribute approximately 2.0 in-oz of friction torque, reduced from 30 in-oz of slip ring friction in a standard table. Servoing the slip rings is the only way to reduce the slip ring friction further, but this was rejected as too costly and complicated for the small additional reduction in slip ring friction which could be achieved.

An undersized torque motor with the same mounting requirements as the standard torque motor was available. The torque motor has two thirds less brush friction than the standard motor. Brushless torque motors which would further reduce the torque motor friction were not readily available for the table axis and would have required a major re-design of the air-bearing table. A special air bearing design was rejected as being too complicated and costly for the relatively small reduction in friction which could be achieved.

Table 2-1. Comparsion of table axis friction and disturbance torques for the CGC standard model 51D and model 51D-1.

Source of friction or disturbance torque	Model 51D (standard)	in-oz	Model 51D-1 (modified)	in-oz
a) DC Torquer				
- Brush friction, cogging torque, hysterisis drag	Inland model T-9910 20 ft-lbs peak	61.4	Inland model T-7202 11 ft-lbs peak	19.2
- Ripple torque, 4% average to peak of drive torque	2.5 ft-lbs of torque assumed	19.2	2.5 ft-lbs of torque assumed	19.2
b) DC tachometer 0.5%	Inland model TG-2936	2.7	Inland model TG-2936	2.7
c) Slip ring assembly with bearings	Airflyte model D-8031 139 rings	30.0	Airflyte model D-8031 8 rings	2.0
d) Resolver	Singer-Kearfott size 11	0.3	Singer-Kearfott size 11	0.3
Totals		113.6 in-oz		43.4 in-oz

Contraves supplied the new air-bearing table with a minimum number of slip rings (8) and an undersized DC torque motor (11 ft-lbs vs. 22 ft-lbs) for the table axis. The nominal friction torque for the table axis is 43.4 in-oz. These modifications, in addition to the fact the air-bearing is new, result in a significant decrease in friction compared to the air-bearing table used in the previous AFAL study. The reduced table axis friction makes terminal phase control of the AFAL structure more difficult. It is much harder to keep the structure positioned within a specified hub angle deadband, and there is a much greater tendency for the controller to enter limit cycles. The actual friction in the table axis will be determined as part of the overall task to characterize the entire AFAL structure with its new sensors and actuators.

2.2 Accelerometer Noise Problems

Severe signal-to-noise ratio problems were found in the digitized linear accelerometer signals used to monitor the vibrations of the tips of the arms. The noise was often 10-20% of the actual accelerometer readings. The accelerometer signals are digitized by the Labtech's 12 bit A/D converter. Most of the accelerometer noise was found to be due to the switching of the A/D converter multiplexer, and STD bus activity inside the Labtech. The A/D converter is sensitive to the switching noise because it has been configured with a gain of 100, which limits the full scale inputs to ± 0.1 volts. The gain is used to match the full scale A/D converter input range to the maximum range of accelerometer outputs encountered during a test maneuver. However, the gain also greatly increases the effect of small disturbance signals.

The switching noise consists mainly of high frequency components, but using low pass or anti-aliasing filters on the accelerometer signals as they enter the Labtech does not help because the major noise source is within the Labtech. Using anti-aliasing filters actually increases the effect of the noise within the Labtech system.

One solution is to increase the sensitivity of the linear accelerometers. This would decrease A/D converter gain needed to match the A/D input range to the maximum output of the accelerometers. The reduced gain will make the A/D converter much less sensitive to switching noise within the Labtech. Larger accelerometer signals will also reduce the effects of other disturbances. The reduced sensitivity to noise from within the Labtech may allow the use of anti-aliasing filters. However, increasing the sensitivity of the accelerometers also reduces their bandwidth.

2.3 Thruster Supply Hose Interactions

The "active" arms of the AFAL structure each have a pair of thrusters located at the tips of the arms. Originally, the hoses which supplied pressurized nitrogen from the

on-board storage tanks to the thrusters were caternaried from the hub to the tips of the arms, as shown in Figure 2-1. The supply hoses are made from 0.5 inch ID Aeroquip 2781-8 Hi Impulse two-wire braid hosing; they have a standard operating pressure of 1000 psi with a maximum operating pressure of 4250 psi. The hoses affected the vibrations of the active arms in several ways, namely:

(1) The caternaried hoses had their own modes of vibration which interacted with the vibrations of the active arms. For example, the second bending mode of an arm coupled very well with the first vibration mode of the hoses.

(2) The hoses are relatively massive and consequently mass-loaded the active arms. The massive hoses increased the effects of the hose vibrational modes.

(3) The hoses displayed a high internal damping due to friction between the layers of the hose. This added a large amount of damping to the active arms.

(4) The caternaried hoses introduced a force at the tips of the arms directed towards the hub. This force tended to buckle the arms as they vibrated, especially for large amplitude vibrations, and almost certainly caused the vibrations to be non-linear.

The high pressure hoses were replaced by 1/2" OD Nylo-Seal II brand plastic tubing. The tubing has a working pressure of 625 psi and a burst pressure of 2600 psi which easily satisfies the pressure and safety requirements for the AFAL experiments. The tubing is much lighter than the hoses (0.04 lbs/ft vs. 0.54 lbs/ft for the hoses) and has much less internal damping.

The new tubing is routed along the top edge of the active arms from the hub to the thrusters and is attached to the arms in several places. This prevents the tubing from having independent vibration modes, and eliminates the hub-directed force at the tip of the arms. The tubing is stiffer than the original hoses even though the tubing has a smaller diameter. The effect of the tube stiffness is to increase the bending stiffness of the arms because the tubing is directly attached to the top of the arms. The new thruster nitrogen supply configuration can be seen in Figure 1-2.

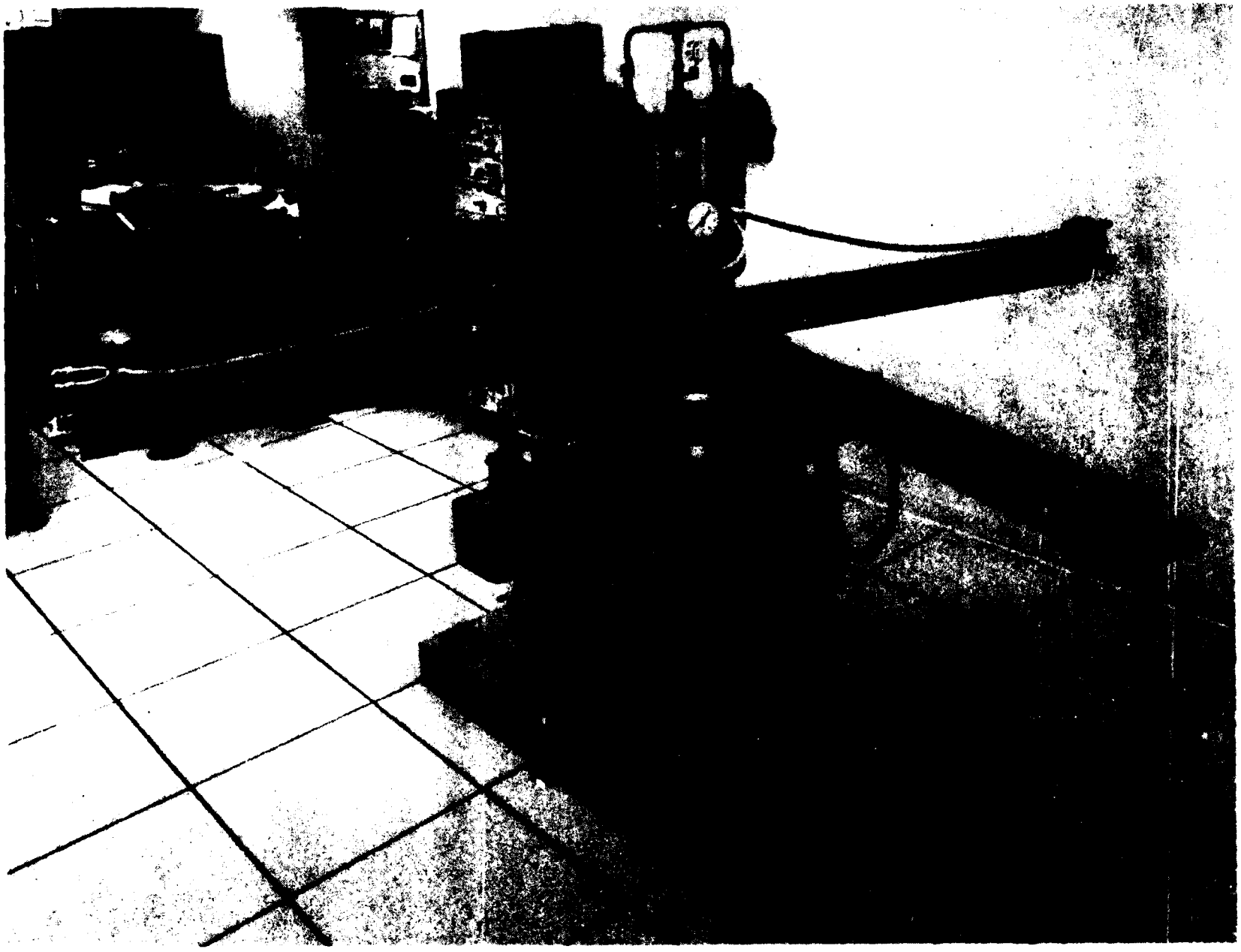

Figure 2-1. Original thruster nitrogen supply hose configuration.

Section 3

New Sensors and Linear Discrete Actuators

3.1 Proof-mass Actuators

Proof-mass actuators move a mass (the proof mass) and use the reaction force to perform the desired work. BEI KIMCO model LA16-19A electro-mechanical linear actuators were originally chosen to be used as the proof-mass actuators for the AFAL discrete actuator study. These linear actuators are moving magnet type actuators. A cylindrical permanent magnet is free to move along the axis of a cylindrical housing which contains a coil. The actuators have a stroke of $\pm$ 0.25" and the moving magnet weighs 0.22 lbs. Specifications for these actuators are given in Appendix A.

Computer simulations of PMA performance using the BEI KIMCO model LA16-19A linear actuators were performed. Section 8 discusses the results of these simulations. It was found that the LA16-19A based PMAs would be very ineffective for the first several modes of vibration of the AFAL structure. The reasons for poor performance include the relatively small proof mass and short stroke of these actuators. The maximum PMA reaction force available is limited, especially for low frequency vibrations, because the proof-mass must be prevented from hitting the physical end of its stroke (i.e., saturating).

To improve PMA performance on the low frequency modes of vibration, a larger proof-mass and longer stroke are needed. No standard linear actuators were found which could easily provide both a larger proof-mass and a longer stroke. BEI Kimco was able to modify an existing design to achieve a longer stroke ($\pm$.875"). The new actuators are KIMCO model LA23-43-001. This actuator is a "moving coil" type linear actuator. Moving coil actuators typically have a heavy base (which includes a permanent magnet) and a lightweight coil assembly. By mounting the coil assembly to the structure, the heavy magnetic base, which weighs 2.1 lbs, becomes the proof mass. Thus, the new actuators provide a significant increase in stroke and proof mass. Specifications of the new PMAs are included in Appendix A.

Two of the PMAs will be mounted "back-to-back" and located at the tip of each

arm of the structure. The PMAs will be mounted together as shown in Figure 3-1. The coil assemblies are mounted at each end of a linear bearing. The magnet assemblies are supported by a shaft which passes through the linear bearing and each of the coil assemblies. The shaft keeps the magnet assemblies aligned with the coils and constrains both of the magnets to move together. The shaft is designed to resist rotating about about its axis. The individual components of the PMA assembly are shown in Figure 3-3.

Mounting the two PMAs "back-to-back" with the proof masses coupled results in several advantages. Two PMAs operating together doubles the effective proof-mass and the peak force available. Also, having the PMAs operating in opposite directions reduces the non-linearities which are inherent in voice-coil type actuators.

3.2 Proof-Mass Actuator Position Sensors

The control laws which were developed for the PMAs require accurate knowledge of the proof-mass position along its stroke. To provide a position measurement, linear variable differential transformers (LVDTs) will be used. An LVDT consists of a ferrous metal core which moves inside a transformer. The position of the core can be determined from changes in the inductance of the transformer. These components are seen at the bottom of Figure 3-3.

The LVDTs will be mounted below the linear bearings which support the PMAs, as shown in Figure 3-2. The LVDT body will be attached to the linear bearing housing. The LVDT core will be connected to the PMA magnet assembly on each side. Configured in this manner, the LVDTs will measure the displacement of the PMA magnet assembly relative to the rest of the tip mass.

Schaevitz model 1000 DC-D LVDTs will be used. These transducers have a stroke of ± 1.0", require only DC excitation voltages, and provide DC output relative to the core position. All intermediate signal conditioning is performed by a conditioning module incorporated into the transducer. Specifications for the LVDTs are given in Appendix A . Teflon bore liners will be used inside the LVDT body to reduce friction as the core moves.

3.3 Table Axis Torque Motor

The table axis torque motor will be used as a torque actuator at the hub of the AFAL structure. The torque actuator will assist the thrusters in slewing the AFAL structure. The primary use of the actuator be to perform vibration control and fine pointing and tracking. The torque motor can emulate a reaction wheel or CMG type actuator by simulating the non-linearities of these devices in software, e.g., speed saturation of a

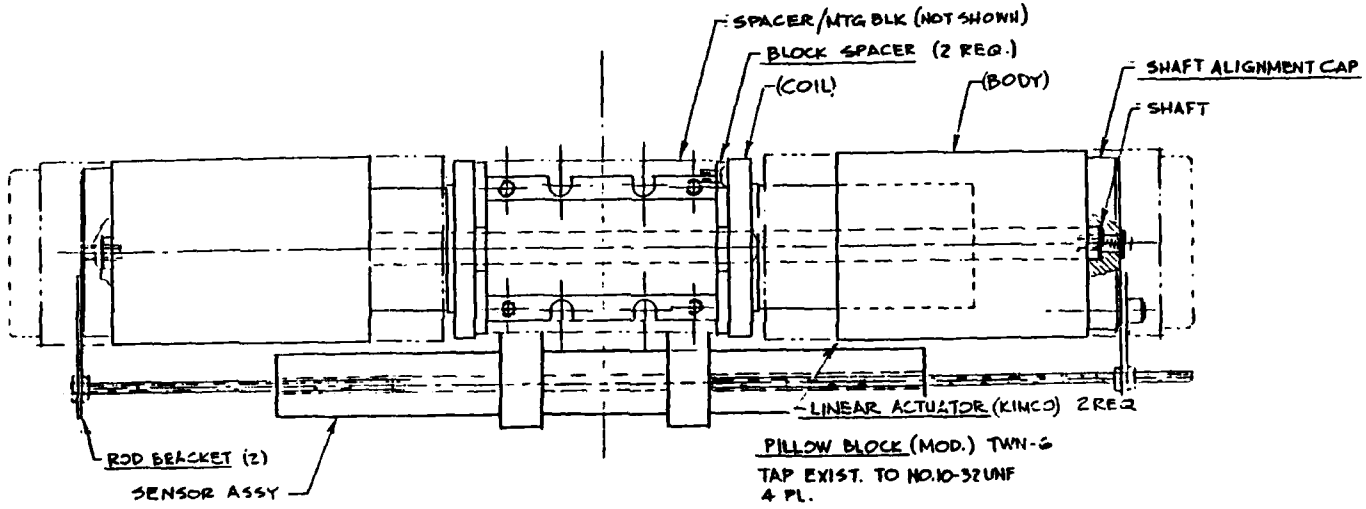

Figure 3-1. Proof-mass actuator mounting configuration (view from end of beam).

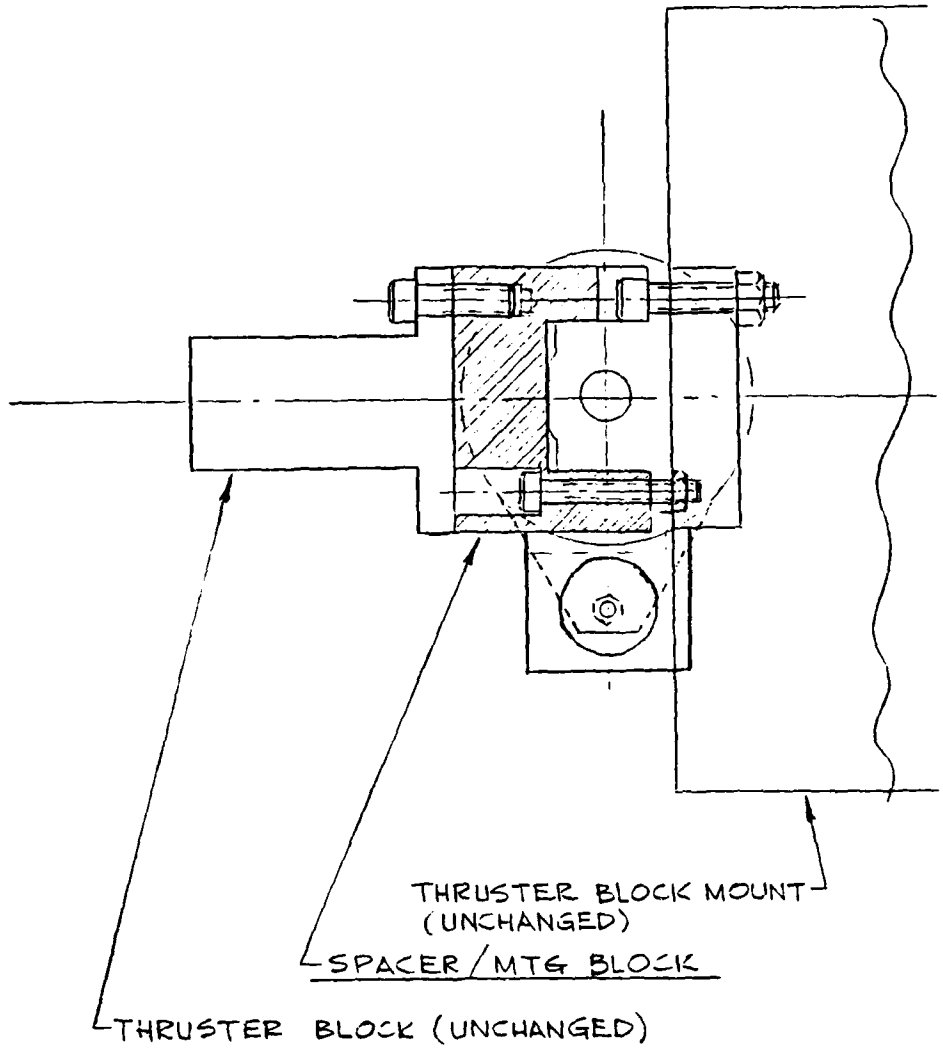

Figure 3-2. Proof-mass actuator mounting configuration (view from side of beam).

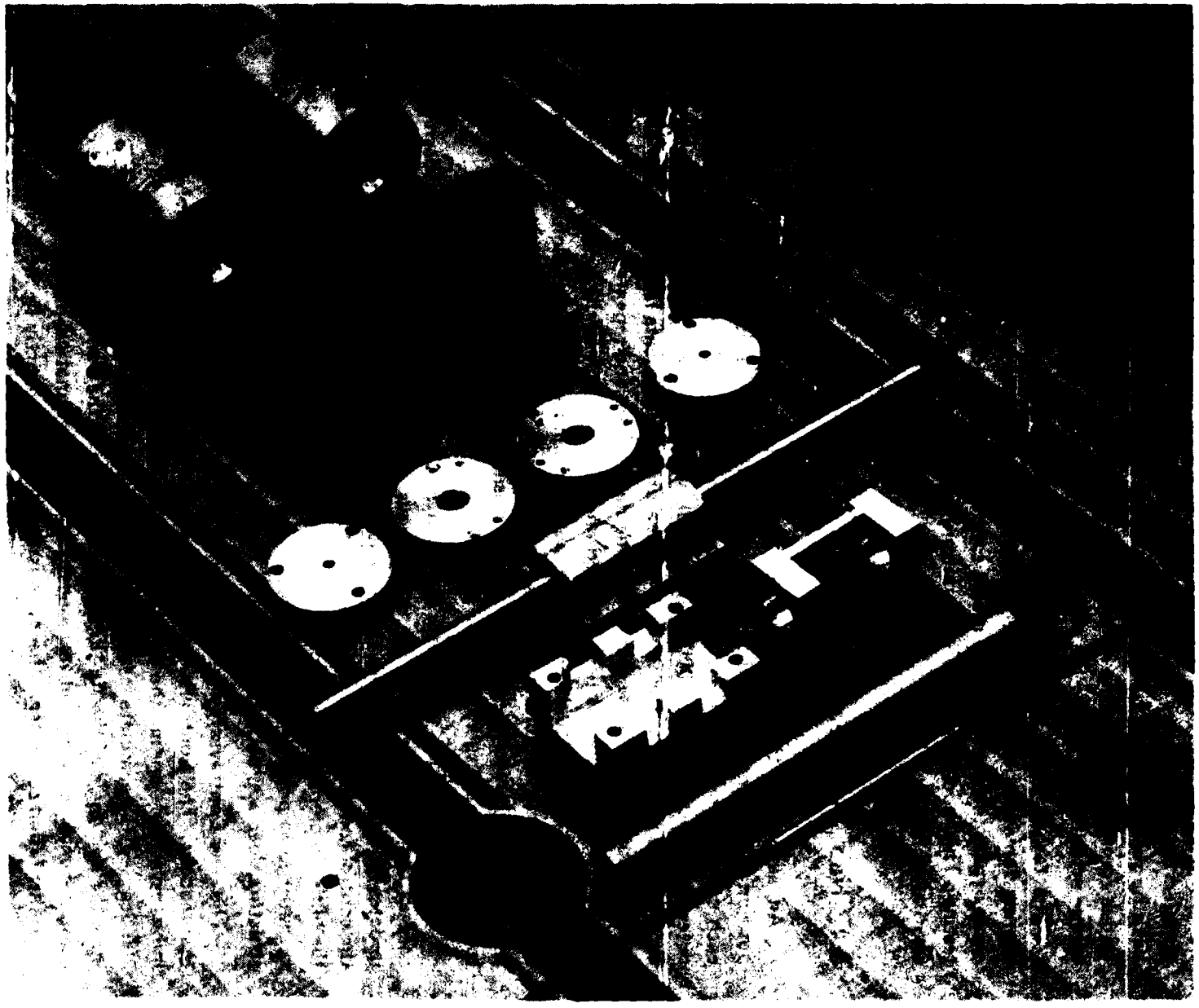

Figure 3-3. Proof-mass actuator components.

reaction wheel.

The table axis torque motor is an Inland model T-7202 DC torque motor and in powered by an Contraves/Goertz model 60CGM600 servo amplifier. The torque motor has a torque constant of 1.1 ft-lbs/amp and a maximum torque of ± 11 ft-lbs. The actual torque commanded from the motor will be limited to 5 ft-lbs or less. Consequently, the torque actuator can not be the primary slewing control actuator.

The torque motor and amplifier were provided by Contraves as part of the air-bearing table and associated electronics. Contraves has also provided a method to easily bypass the normal torque motor control circuits which are used during gyroscope testing. This modification permits arbitrary torque command voltages to be sent to the servo amplifier.

3.4 Hub Angle Readout

An air-bearing table typically uses an Inductosyn and a resolver as the angular position transducers. An Inductosyn has a high resolution but repeats its output for each degree of revolution. Hence position within a particular degree of motion can be determined accurately (± 0.0005 degree) but other information is needed to determine the absolute position of the table or to measure displacements larger than one degree. A resolver provides a coarse measure of angular position and repeats its output once per revolution. The resolver is used to determine table position to the nearest degree while the Inductosyn is used to determine the table position to higher resolution. Alternatively, one could count the number of times the Inductosyn output repeats to determine table position to the nearest degree. An angular position readout uses one of these methods to determine and display the table position.

A Farrand readout, which uses the latter method, and a table axis Inductosyn were used as the hub angle sensor for the previous AFAL study. The Farrand continuously updates its display and latches the current position into a buffer upon a command from the control computer. The control computer reads the data from the buffer and releases the buffer in preparation of the next latch request. A problem with the Farrand readout is that it loses position accuracy when the angular rate approaches 10 °/s. The AFAL structure does approach 10 °/s during 15 degree and larger slewing maneuvers.

The new Contraves/Goertz air-bearing table and electronics includes a table position readout. The Contraves readout uses information from both the resolver and the Inductosyn to determine the table position and maintains its accuracy for rates up to 200 deg/sec. To eliminate loss of accuracy, the Contraves readout will be used to determine the hub angle of the AFAL structure in place of the Farrand readout. The control computer must be modified to request hub angle information from the the Contraves instrumentation computer rather than issue commands directly to the position readout.

Section 4

Control Computer Upgrade

This section describes the upgrade of the AFAL controller to include a MicroVAX II computer. Section 4.1 presents the reasons for selecting a MicroVAX II to upgrade the control computer. Section 4.2 discusses the conversion of the control code from the Labtech 70 to run on the combined MicroVAX II/Labtech 70 computer system. Hardware and software problems which were encountered during the conversion process are also presented. Section 4.3 discusses the procedures used to verify the control code running on the new computer system. Section 4.4 describes the new control computer configuration which includes both the Labtech 70 and the MicroVAX II.

4.1 Selecting a New Control Computer

4.1.1 Background

The control computer used in the previous AFAL study was the Labtech 70: a STD bus and Intel 8088/8087 based microcomputer (see Figure 4-1). The Labtech interfaced to the AFAL structure through analog to digital converters (A/Ds) and digital I/O ports. The experiment used five sensors (four linear accelerometers and a hub position sensor) and four thrusters (controlled to act as a single actuator) with forward and reverse thrust capability. Timing is determined by a programmable counter which directly interrupts the cpu and initiates an interrupt service routine to perform the desired control action.

The control routines which were used consisted of a standard Kalman filter loop with a choice of two control calculation subroutines. These control routines were based on a model consisting of six states, five sensors, and one actuator. The highest frequency mode which was controlled had a frequency of 1.1 Hz. The control routine could run at a maximum update rate of 20 Hz which provided a "reasonable" margin between the highest controlled frequency and the update rate of the control routines. The latter were computation bound, not I/O bound.

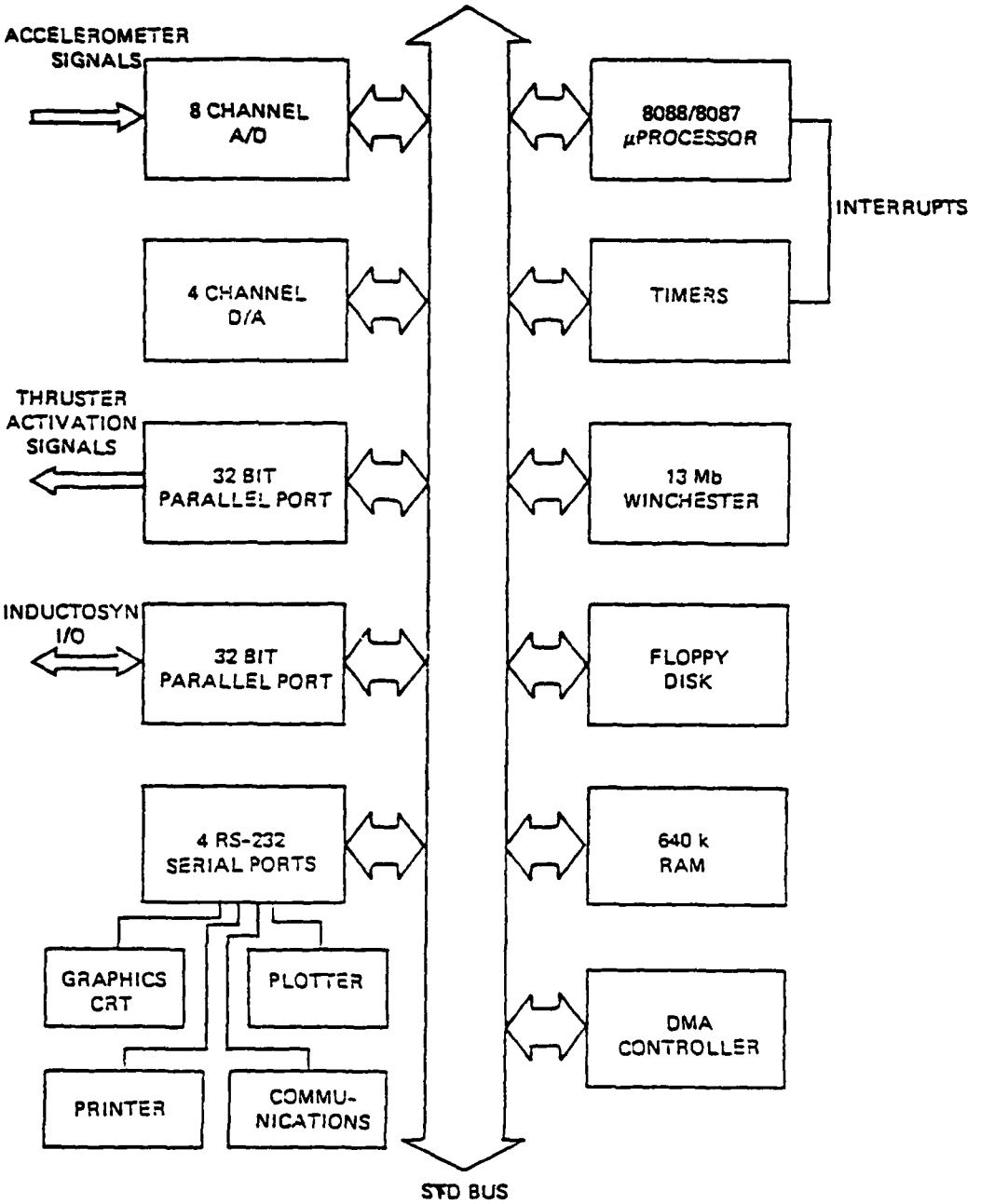

Figure 4-1. Labtech 70 computer configuration.

The work planned for the current AFAL studies will increase the number of sensors and actuators to at least ten of each and will possibly control higher frequency structural modes. Increasing the number of sensors and actuators will increase the computation required for state estimation and for control calculation. Likewise, controlling higher frequency modes increases the computation requirements in that the overall control routine must execute at a higher update rate to maintain an adequate frequency margin between the highest controlled frequency and the update rate of the control routine. These effects combine to greatly increase the computation requirements of the control computer. Because the Labtech control computer was computation bound, an upgrade of the existing computer was necessary.

One possible upgrade configuration retained the Labtech 70 as the hardware interface to the test structure while sending sensor data to (and receive new control commands from) a new computer over a parallel I/O interface. This would permit keeping the established hardware interface while taking advantage of the new computer's processing speed. Another configuration would replace the Labtech completely and use the new computer to provide both the hardware interface and the control computation.

4.1.2 Evaluating Candidate Computers

Two candidate computers were evaluated: a Masscomp and a MicroVAX II. A third computer, the MicroVAX I, was also evaluated to determine the performance improvement provided by the MicroVAX II. The main criteria in selecting these computers as candidates were their reported computational speed, which represented a significant increase in computing power over the Labtech 70, and their real-time control capabilities.

Masscomp computers are designed for high speed data acquisition. (The most powerful cpu available at the time was a 68010/68000 based computer. Masscomp currently has computers based on the 68020 microprocessor.) The computers have (i) a proprietary high-speed bus for the cpu, main memory, and floating point accelerators, (ii) a Multibus for peripherals, and (iii) dual STD buses for data acquisition. A wide range of products is available for both the Multibus and STD buses. The Masscomp supports a floating point processor, an array processor, and a dedicated data acquisition processor. The "real-time" Unix provided with the Masscomp is adequate for all data acquisition tasks and for process control (update rates $<$10 Hz) although the operating system may be modified to allow faster control. Another project at CSDL is using a Masscomp computer to control a magnetic suspension at an update rate of 5 kHz or greater.

The MicroVAX II is based upon a proprietary microprocessor from DEC and implements most of the instructions found on a larger VAX computer. The processor has a 32 bit cpu with a hardware floating point processor and is based on DEC's Q-bus. A MicroVAX II and the MicroVMS operating system have most of the features of larger

VAX systems which provides software transportability and ease of networking with other VAXes at CSDL. Real-time features are provided by VAX ELN, a tool kit which helps one to build real-time applications which may include multi-tasking and multi-programming. A wide range of products is available for the Q-bus.

A computational benchmark was created using typical control routines from the previous AFAL study. The benchmark program consisted of a standard Kalman filter loop with two different control calculation subroutines. The model used in the benchmark had six states, five sensors, and one actuator. The first control algorithm, EMCONTROL, uses Floyd's [1] single-step optimal control for energy minimization. This algorithm consists of a few vector multiplications and a branching search for a constrained optimum. The second control algorithm, VVCONTOL, uses Vander Velde's [1] optimal control approach which includes estimating the optimal cost-to-go. This algorithm consists of a few vector multiplications and the determination of the magnitude of the estimated cost. For the model used in this benchmark the control routine which uses VVCONTROL takes longer to execute. However, the computation required by the VVCONTROL algorithm increases linearly as the number of actuators increases while the computation required by the EMCONTROL algorithm increases quadratically.

To establish a reference point for comparing the microcomputers, the benchmark was also run an a VAX 11/780. The benchmark results for both the EMCONTROL and the VVCONTROL algorithms are summarized in Table 4-1. The configuration of the computers as tested is shown along with the time required to execute one update cycle of the control routine and the relative speed performance with respect to the VAX 11/780. Execution times are not shown for the Masscomp computer because the benchmark for the Masscomp was modified to better use the optimization of the Masscomp Fortran compiler. The relative performance values for the Masscomp were determined by running the modified benchmark programs on the VAX 11/780 and comparing the results. The results show that the Masscomp is nearly 10 times faster than the Labtech 70 and the MicroVAX is approximately twice as fast as the Masscomp.

Other areas in which the computers were compared include:

(1) Data acquisition: The Masscomp is a very good data acquisition system. It is fast, flexible, easy to use, and could easily be shared between projects. The MicroVAX II could be configured to perform the same functions, but would not be as easy to use or as flexible.

(2) Programming languages: The Masscomp supports C, Fortran, and Pascal. The MicroVAX II supports C and Pascal for real-time use with VAX ELN, although Fortran and other languages can be used for computation-only portions of the code.

(3) Ease of programming: Because its data acquisition capabilities are so good, the

Table 4-1. AFAL benchmark results.

Computer	EMCONTROL		VVCONTROL	
	sec/cycle (ms)	relative (780=1.0)	sec/cycle (ms)	relative (780=1.0)
VAX 11/780, w/FPA, G& H options, 4 MB core	0.970	1.0	1.16	1.0
MicroVAX II, w/FPU, 3 MB core	1.44	0.676	1.70	0.683
Masscomp w/FPP, 68010/68000 cpu 2 MB core	*	0.26-0.37	*	0.28-0.38
MicroVAX I, 2 MB core	5.31	0.18	6.42	0.18
Labtech 70, STD bus 8088/8087, 5 Mhz	27.3	0.035	29.8	0.039

* See text.

Masscomp would replace the Labtech as the hardware interface to the test structure. The MicroVAX II would (at least initially) send and receive data to and from the Labtech 70 over a parallel interface. This would require programming two different computers and developing an effective interface between them.

(4) Real-time control capabilities: The VAX ELN toolkit for the MicroVAX II allows one to write a real-time application program including interrupt handlers, multitasking, and multi-programming in high level languages. VAX ELN and the MicroVAX II support pre-emptive interrupts from other devices. Pre-emptive interrupting allows a high priority process to interrupt the execution of a lower priority process instead of waiting until the lower priority process is finished. One example would be a high priority vibration control process and a low priority pointing control process. The Masscomp does not support pre-emptive interrupts.

The standard Masscomp operating system has significant interrupt processing delays which limit the update rate to less than 10 Hz. The interrupt delay can be avoided by using polling to synchronize the processor with external devices. The MicroVAX with VAX ELN has an average delay of 33 μs from the time an interrupt occurs to the execution of the first instruction in an interrupt handler.

4.1.3 Recommendation

Based on the benchmark results and the other considerations listed above, the MicroVAX II was recommended to upgrade the processing capability of the AFAL experimental facility. Its speed advantage and real-time development capabilities were the most important factors in this choice. The data acquisition capabilities of the Masscomp were impressive, but since the computer is to be used primarily for the real-time control of the AFAL test structure the flexibility of use was given a relatively low priority. Choosing the MicroVAX II had the added advantage of being compatible with other VAXes at CSDL.

The initial configuration of the upgraded computer system would keep the Labtech 70 as the hardware interface to the test structure since this interface was already debugged. The Labtech would read the sensors and send the data to the MicroVAX, receive a new control command from the MicroVAX II, and issue the new control command to the actuators on the test structure. Event timing would be controlled by the timer board in the Labtech. The MicroVAX II would receive data from the Labtech 70, calculate a control command, and send the new control commands to the Labtech 70. The disadvantages of having to deal with two computers (the MicroVAX II and the Labtech 70) were thought to be outweighed by the ease of "real-time" program development on the MicroVAX.

4.2 Programming the Combined Computer System

The existing AFAL control software for the Labtech controller consists of (i) executive, (ii)control, and (iii) hardware interface routines written in FORTRAN. The executive routines handle initialization and user interface tasks. The control routines provide functions such as state and measurement estimation and control calculation. The hardware interface routines perform the detailed operations necessary to interact with devices such as the A/D converter and the digital I/O interface. The control and the hardware interface routines are the portions of the code which run in "real-time".

The software which has been developed for the combined MicroVAX/Labtech computer system duplicates the functionality of the existing AFAL control software for the Labtech controller. The Labtech still performs most of the hardware interface functions, but the executive and control routines were ported to the MicroVAX. New routines were needed for both the Labtech and the MicroVAX to allow the two computers to communicate and transfer data.

4.2.1 Programming Environments

Programming the combined MicroVAX/Labtech computer system required dealing with two computers and their respective program development tools and run time environments. Porting existing code from the Labtech to the MicroVAX also required translating from one run-time environment to the other.

The Labtech computer uses Intel's iRMX real-time operating system. iRMX provides a real-time environment which supports multi-tasking and multi-programming applications and can handle multiple external interrupts. iRMX also provides the program development environment. Programs can be edited, compiled, linked, and executed using the same operating system. FORTRAN and 8088 assembly are the languages available on the Labtech. The existing AFAL control code is written entirely in FORTRAN. A debugger is not available.

User devices such as the A/D converter are I/O mapped which means the device's control and data registers are associated with particular I/O port addresses. The hardware interface routines are implemented by reading or writing values in the appropriate device registers. The FORTRAN compiler has built-in functions which read from and write to a specified I/O port.

The MicroVAX uses separate operating systems for program development and execution. The MicroVMS operating system and the VAX ELN development toolkit are used to edit, compile, link, and build VAX ELN applications. The VAX ELN applications can then be booted and executed on the MicroVAX, without the presence of the MicroVMS operating system. The link step produces a relocatable image which has references to system routines that are usually resolved at run time. For VAX ELN applications, the build step combines multiple relocatable images, uses the VAX ELN kernel to resolve system routine references, and produces a bootable system image. A VAX ELN application can be booted on a target MicroVAX from disk, cartridge tape, PROM, or Ethernet.

The VAX ELN toolkit consists of a PASCAL compiler (EPASCAL), PASCAL, C, and FORTRAN run-time libraries, a system kernel, a debugger, and an application builder. Device drivers are included for many common peripherals (e.g., disk and tape drives, RS-232 interfaces, etc...). The VAX ELN kernel and run-time libraries provide support for multi-tasking, multi-programming, and interrupt handling with much less system overhead than the MicroVMS operating system. EPASCAL is a superset of ISO standard PASCAL with many extensions for real-time systems and is the recommended language for VAX ELN programming. Programs and subroutines for VAX ELN applications can be written in any VAX language which uses the VAX calling standard. However, no system services or run-time library functions may be called which are not supported by the VAX ELN kernel or run-time libraries. For instance, the version of VAX ELN originally received with the MicroVAX did not support any FORTRAN I/O routines.

The VAX ELN debugger consists of two parts: a local debugger which runs on the target computer and a remote debugger which runs on a host computer under VMS or MicroVMS. The local debugger can be used only from the console of the target computer and provides only assembly code level debugging. The remote debugger interacts with the local debugger via an Ethernet connection and provides full source code level debugging. The remote debugger can attach to a target computer which is already running a VAX ELN application or can downline load an application to boot a target system. A remote debugging session can also attach to and debug several target computers at the same time. This allows a single host VMS or MicroVMS system to perform VAX ELN application development and debugging for a number of different projects and target computers simultaneously.

4.2.2 Conversion of Existing Software

The executive and control routines from the existing control software were ported to the MicroVAX. These routines were approximately 90% of the control code for the Labtech computer. The conversion process included translating iRMX FORTRAN to VAX FORTRAN, using VAX ELN system services in place of iRMX system services, and translating portions of the software to EPASCAL. FORTRAN was used where possible to reduce the amount of code which needed to be translated to EPASCAL.

Several concerns when translating iRMX FORTRAN to VAX FORTRAN were to insure that variables used the same amount of storage on both computers, that COMMON blocks and EQUIVALENCE statements maintain their alignment, and that variables are are initialized and interpreted in the desired manner (e.g., a LOGICAL variable which would have a TRUE value on one computer would also have a TRUE value on the other). VAX ELN provides system services which are very similar to iRMX system services for creating and initializing interrupt service routines and waiting for a particular interrupt. The major difference is that some VAX ELN services are available only when called from EPASCAL.

Routines which performed I/O functions were translated to EPASCAL because FORTRAN I/O was not originally supported in VAX ELN. Also, it was decided that all VAX ELN system services would be called from EPASCAL. This decision led to a software structure where the FORTRAN routines are called as necessary from a main program loop written in EPASCAL. For instance, the code for the process which performs the control of the AFAL structure consists of a main program loop written in EPASCAL which determines the event timing and communicates with the Labtech. The main loop calls FORTRAN subroutines to perform the state estimation and control calculation.

The concerns when using both EPASCAL and FORTRAN in the same VAX ELN application include passing parameters between modules written in different languages (e.g., FORTRAN stores arrays in column major form while EPASCAL stores arrays in

row major form) and mapping EPASCAL data storage to FORTRAN COMMON blocks. The only method found for mapping EPASCAL data storage to FORTRAN COMMON blocks was to use assembly code to create a data storage area to which both languages could be linked. This is the only assembly code used in the control software for the combined MicroVAX/Labtech computer system.

4.2.3 New Software

New software was written for both the Labtech and the MicroVAX. Software for the Labtech was required to allow communication with the MicroVAX and to perform the functions which are requested by the MicroVAX. The new software for the MicroVAX included routines to communicate with and issue commands to the Labtech. Also, device driver routines were needed for three devices.

The Labtech communicates with the MicroVAX via three 16 bit parallel interfaces (on the Labtech side). The Labtech software implements a "handshaking" protocol which allows the MicroVAX and the Labtech to transfer data. The Labtech also responds to three interrupts from the MicroVAX which correspond to the three major functions the Labtech performs: read the sensors, issue the latest control command, and a general purpose routine. The general purpose routine implements three subfunctions which are get the sensor bias, receive a new control command from the MicroVAX, and reset which exits the control program. The particular subfunction is determined by reading a function selection command and (possibly) parameters from the parallel interface.

The new MicroVAX software generates the interrupts and commands to which the Labtech responds. The MicroVAX software also implements the protocol which allows communication with the Labtech. Device driver routines were written for three devices: a Codar M-Timer, a DEC DRV11-J, and a DEC DRV11-W. The M-Timer provides 15 counter/timers which are used for interrupts to the Labtech and the MicroVAX. The M-Timer is also used to provide handshaking signals to the Farrand angle readout when the MicroVAX is reading the hub angle. The M-Timer device driver routines initialize the M-Timer, assign an interrupt service routine to a counter/timer channel, program and start a particular counter/timer, and set the output value of a counter/timer channel. The DRV11-J has four 16 bit parallel interfaces. Three of the interfaces are used to read the Farrand hub angle readout. The DRV11-J device driver routines initialization the DRV11-J, transfer data to and from the parallel interfaces, and assign interrupt service routines as necessary. The DRV11-W is a 16 bit DMA parallel interface and is used to communicate with the Labtech. The DRV11-W routines provide initialization, assignment of the interrupt service routine, and mapping and unmapping of the data to be transferred. The routines also program and start the transfer. The actual transfer of data takes place using DMA under control of the DRV11-W.

4.2.4 Problems

The major problems encountered during the conversion of the Labtech control software to run on the combined MicroVAX/Labtech system were related to the behavior of the Labtech when interrupts occur. Other difficulties were the lack of remote debugging for much of the VAX ELN development and the lack of FORTRAN I/O support in VAX ELN.

The lack of VAX ELN FORTRAN I/O support required that a large portion of the existing control code be translated to EPASCAL. The translation was not difficult, but required much attention to the issues discussed in Section 4.2.2 which include transferring variables between modules of different languages. As a result, the translation was very time consuming.

An Ethernet connection was not available during most of the VAX ELN device driver development so only assembly code level debugging could be used. The development cycle when using local debugging consists of editting, compiling, linking and building the VAX ELN application. The VAX ELN application is booted and debugged at the assembly code level. If suspected errors are found, the MicroVMS operating system must be booted so the VAX ELN application can be changed. Since each boot cycle takes several minutes, program development is much more efficient if a host system is available to perform downline loading and remote debugging. The debugging is also much easier and faster at the source code level rather than the assembly code level.

The Labtech is sensitive to the timing of interrupts; if interrupts on different interrupt channels occur too close together, the Labtech computer crashes. The Labtech was first programmed to respond to single interrupts to debug the interrupt routines which perform the functions requested by the MicroVAX. The Labtech would crash occasionally, but the cause was unknown. When the Labtech was tested with multiple interrupts, the crashes occurred more often and could be produced when multiple interrupts were issued simultaneously. Care was taken to separate the three interrupts to the Labtech with nominal delays as necessary, but the crashed still occurred randomly.

The solution was found by turning off the system clock on the Labtech. The system clock normally interrupts the Labtech at a 100 Hz rate. When an external interrupt occurred to close to a system clock interrupt, the system would crash. With the system clock turned off, the Labtech runs reliably if the external interrupts do not occur too close together. The Labtech software was modified to turn off the system clock at the beginning of each test and to turn it on when the test is finished.

The Labtech will occasionally miss an interrupt if it occurs while the Labtech is executing the interrupt service routine for a previous interrupt. An interval of approximately 0.5 ms from the execution of the last instruction in an interrupt service routine to the occurrence of a new interrupt is required to insure that interrupts are not missed.

The Labtech now runs reliably, but only for 16306 sample intervals. The Labtech

stops consistently at this point for an unknown reason. Several possible reasons have been explored but without success. The stopping count is independent of the sample rate and does not depend on parameters such as the stack size of program. This stopping count will provide nearly three minutes of testing with a 100 Hz sample rate which will be ample time for the slewing tests which are planned. This problem will be addressed in the future as time permits.

The iRMX operating system on the Labtech does not clear interrupts which occur when a user written interrupt service routine is not attached to the interrupt channel. A default interrupt service routine is supposed to be available which handles such spurious interrupts. When such an interrupt occurs, the interrupt request waits for the user to assign an interrupt service routine to the interrupt channel and the user's interrupt service routine is immediately executed. This causes synchronization problems if the user's program does not expect and immediate interrupt.

This problem occurs when several experimental tests are run at a time. The Labtech resets device and interrupt service routines and exits the control program between tests. The MicroVAX saves data from the test and also performs reset functions. When the MicroVAX resets the M-Timer, the transitions on the counter/timer outputs cause the Labtech to be interrupted. At the start of the next test, the Labtech immediately responds to the spurious interrupts which makes the Labtech and the MicroVAX unsynchronized. A solution is to use dummy interrupt service routines which clear the spurious interrupts at the beginning of the Labtech control program. The control programs on the Labtech and the MicroVAX are synchronized by first allowing the MicroVAX to initialize its I/O and timing devices. The Labtech then clears any spurious interrupts which may have occurred since the last test and proceeds with its own initialization and program execution. Interrupts which now occur are handled correctly by both computers.

4.3 Verification

The basic procedure used to verify the combined MicroVAX/Labtech computer system was to compare the results of slewing maneuvers performed using the MicroVAX/Labtech controller with previous results from maneuvers performed using the Labtech controller. The comparison was based on the state estimates, sensor reading estimates, sensor readings, and control commands which were recorded for each sample interval during the slewing maneuvers. The tests were performed primarily using Floyd's single-step optimal control algorithm although Vander Velde's control algorithm was also used [1] . A sample interval of 35 ms and a control delay of 17 ms were used for all experimental tests.

4.3.1 Tests with the Existing Air-bearing Table

The initial verification tests were performed with the test structure on an existing air-bearing table instead of the new air-bearing table. Using an existing table permitted a comparison of the Labtech controller results with results from the previous AFAL study to insure the Labtech and test facility were functioning properly. Also, these tests provided baseline results to compare with tests to be performed using the new, low friction air-bearing table.

The initial verification tests confirmed that the Labtech controller and the test structure were working properly. The slewing maneuvers results were very similar to results from the previous AFAL study. The slewing maneuvers displayed distinct acceleration and deceleration phases, and a terminal phase which involved multiple thruster firings to control vibrations of the structure. The hub position at the end of the maneuver was within the specified deadband for most tests.

The tests performed using the combined MicroVAX/Labtech controller exhibited similar behavior during the acceleration and deceleration phases of the maneuvers but had many more thruster firings during the terminal phase. Also, the hub angle seemed to be driven to a set point several degrees from the desired set point.

The excessive thruster firings were the result of an incorrect modal weighting factor in the control algorithms. The weighting factor was given an incorrect default value when the control code was converted to run on the MicroVAX. When the same weighting factor was used for both the MicroVAX/Labtech controller and the Labtech controller, the terminal phase behavior for both controllers was very similar.

The set point error was due to differences in the Kalman filter gains used for each controller. The Kalman filter gains to be used for a series of tests are calculated before the tests are performed. The routines used to generate the Kalman filter gains were originally written for the Labtech and used single precision arithmetic. The routines were directly converted to run on the MicroVAX and used to generate the Kalman filter gains that the MicroVAX would use. The differences in the Kalman filter gains generated by Labtech (and used by the Labtech controller) and the gains generated by the MicroVAX (and used by the combined controller) are due to differences in the floating point arithmetic between the Labtech and the MicroVAX and the inaccuracies of single precision arithmetic. When the routines were re-written to use double precision arithmetic, the gains generated by the two computers agreed to at least seven significant digits. The double precision gains did not accurately agree with the single precision gains from either computer.

The single precision Kalman filter gains generated on the Labtech were used by both controllers for all subsequent verification tests. Using the Labtech generated gains allowed the Labtech controller results to continue be used as the baseline for comparisons when the combined MicroVAX/Labtech controller was used, and when the structure was

moved to the new air-bearing table. The double precision Kalman filter gains will be used in the control algorithms for future control work. The algorithms will continue to use single precision arithmetic for speed, but the Kalman filter gains which are implemented in the control algorithms will be generated using double precision arithmetic.

Using the new Kalman filter gains for the combined MicroVAX/Labtech controller eliminated the set point error. The slewing maneuvers performed using the combined MicroVAX/Labtech controller were now very similar to the results obtained using the Labtech controller, including behavior during the terminal phase. The differences between test results from the two controllers were of the same order as the differences between several tests using the same controller. The test result differences were caused by random disturbances in the test facility and not by either controller.

4.3.2 Tests with the new Air-bearing Table

The AFAL structure was moved to the new air-bearing table where the remaining experimental verification tests were performed. These tests were used to determine the effects of lower air-bearing table friction on the performance of the controllers. Test maneuvers were performed using both the Labtech and the combined MicroVAX/Labtech controllers. The test results from each controller were very similar. These results were also very similar to the results obtained with the test structure on the old air-bearing table with the exception that there was often a slow drift of the hub angle during the terminal phase of the maneuvers when using Floyd's single-step optimal control algorithm. The drift would result in set point errors of up to 20 degrees by the end of the test period. No thruster firings occurred while the hub angle was slowly drifting. The hub angle drift did not occur for every test maneuver and did not depend on which controller was being used.

The source of the hub angle drift was found by recording intermediate values in the control routine for each sample interval during several test maneuvers and manually checking the results. Floyd's control algorithm includes the option of constraining the thrusters to not fire if the estimated magnitude of the velocity at the tip of the arms is less than a chosen value. The purpose of this option is to reduce the tendency for limit cycling. When this option is used, the thrusters are constrained based only upon the estimated velocity at the tip of the arms; hub angle error and hub angle deadband are not included. When the test structure was mounted on an old air-bearing table, the table axis friction was high enough so the hub would soon come to rest if the tip velocity was below the chosen limit. The new air-bearing table has much less table axis friction which allows the hub to drift much longer (10-20 degrees) before coming to rest.

The thruster constraint control routine was modified to constrain the thrusters only if the hub angle is within the deadband specified for the maneuver. The modified con-

straint routine eliminated the hub angle drift. However, slewing maneuvers performed using the new thruster constraint routine had many more thruster firings during the terminal phase and had a much higher tendency to limit cycle, especially if a small hub angle deadband (less than 0.2 degrees) was specified.

4.3.3 Tests with "Captured" Inputs

The experimental test results obtained using the Labtech and the combined MicroVAX/Labtech controllers could not be compared exactly with each other because random disturbances were obviously different between test maneuvers (e.g., sensor readings are slightly different from test to test). Only the general performance of the controllers could be compared. A "captured simulation" was performed to compare the controllers more accurately. A captured simulation is defined as one in which the controller runs normally, except that sensor readings are obtained from data in memory or in file rather than actually from the sensors. The chosen sensor data can be used for multiple tests and can be transferred to different computers. This allows a consistent set of inputs to be used for each test so differences in the test results are guaranteed to be due only to differences in the control algorithms and the controllers used.

Recorded sensor readings from an slewing test using the combined MicroVAX/Labtech controller were chosen to be the input data used for the captured simulations. A captured simulation did not need to be performed for the combined controller because the results would be the same as the chosen experiment results because the same inputs would be used. The data acquisition routines for the Labtech controller were modified to obtain the sensor readings from a disk file instead of the A/D converter and the Farrand hub angle readout. The sensor readings were then transferred to the Labtech and a captured simulation performed.

The Labtech controller captured simulation results were compared to the combined MicroVAX/Labtech controller results on the basis of control command, state estimates, and sensor reading estimates for each sample interval. The control commands were exactly the same for each controller. The state and sensor reading estimates were the same to at least four significant digits. The small errors in the state and sensor estimates are the result of differences in the way single precision arithmetic is performed on the Labtech and the MicroVAX. The control commands match exactly because a thruster control command must correspond to one of three values: forward, off, and reverse. The state estimate errors were not large enough in this test case to cause the control commands from each controller to be different.

The combined MicroVAX/Labtech controller was compared with the existing Labtech controller using experimental slewing tests and captured simulations. The captured simulation results show that the combined controller produces essentially the same numerical results as the Labtech controller. Any differences in the experimental results

obtained using the two controllers are the result of implementation issues specific to each controller, or to random disturbances. One example of an implementation parameter is the delay for issuing a new control command. The Labtech controller issues the thruster command as soon as it is calculated while the combined MicroVAX/Labtech controller issues the command at a specified delay from the beginning of the sample interval. The uncertainty of the control delay is probably negligible for the low frequency modes which are currently being controlled, but could be significant for the control of higher order modes.

4.4 Combined MicroVAX/Labtech Computer System

4.4.1 Hardware

Figure 4-2 shows the configuration of the combined MicroVAX II/Labtech 70 computer system and how it interfaces with the AFAL test structure. The Labtech is used as a slave processor for the MicroVAX and provides most of the hardware interface to the AFAL structure. The Labtech digitizes the linear accelerometer signals from the AFAL structure and provides digital outputs for the thrusters. The MicroVAX and the Labtech communicate using a parallel interface. The MicroVAX reads the hub angle directly from the Farrand readout because there were not enough parallel ports available on the Labtech. Event timing is control by a counter/timer board in the MicroVAX.

The Labtech computer contains a variety of analog and digital I/O interfaces. The analog interfaces include an eight channel, differential input analog-to-digital (A/D) converter and a four channel digital-to-analog (D/A) converter. Four channels of the A/D converter are used to digitize the linear accelerometers from the AFAL structure. The four remaining channels will be used to digitize proof-mass actuator position or angular acceleration. The D/A converter is currently unused, but will used to control the proof-mass actuators or the table axis torque motor. The Labtech also contains eight 8 bit digital I/O ports. Six of the parallel I/O ports are used to communicate with the MicroVAX. One of the port is used to provide control signals to the thrusters on the AFAL structure.

The MicroVAX contains digital I/O interfaces and a counter/timer board. The digital I/O interfaces include a 16 bit parallel I/O interface with direct memory access (DMA) and four regular 16 bit parallel I/O ports. The parallel interface with DMA is used to communicate with the Labtech. DMA allows data transfers to occur without requiring attention from the MicroVAX cpu. Three of the regular parallel I/O ports are used to read the Farrand hub angle readout. The remaining parallel port is available for operator inputs and interrupts to the MicroVAX.

It was decided that any additional interfaces needed should be acquired for the

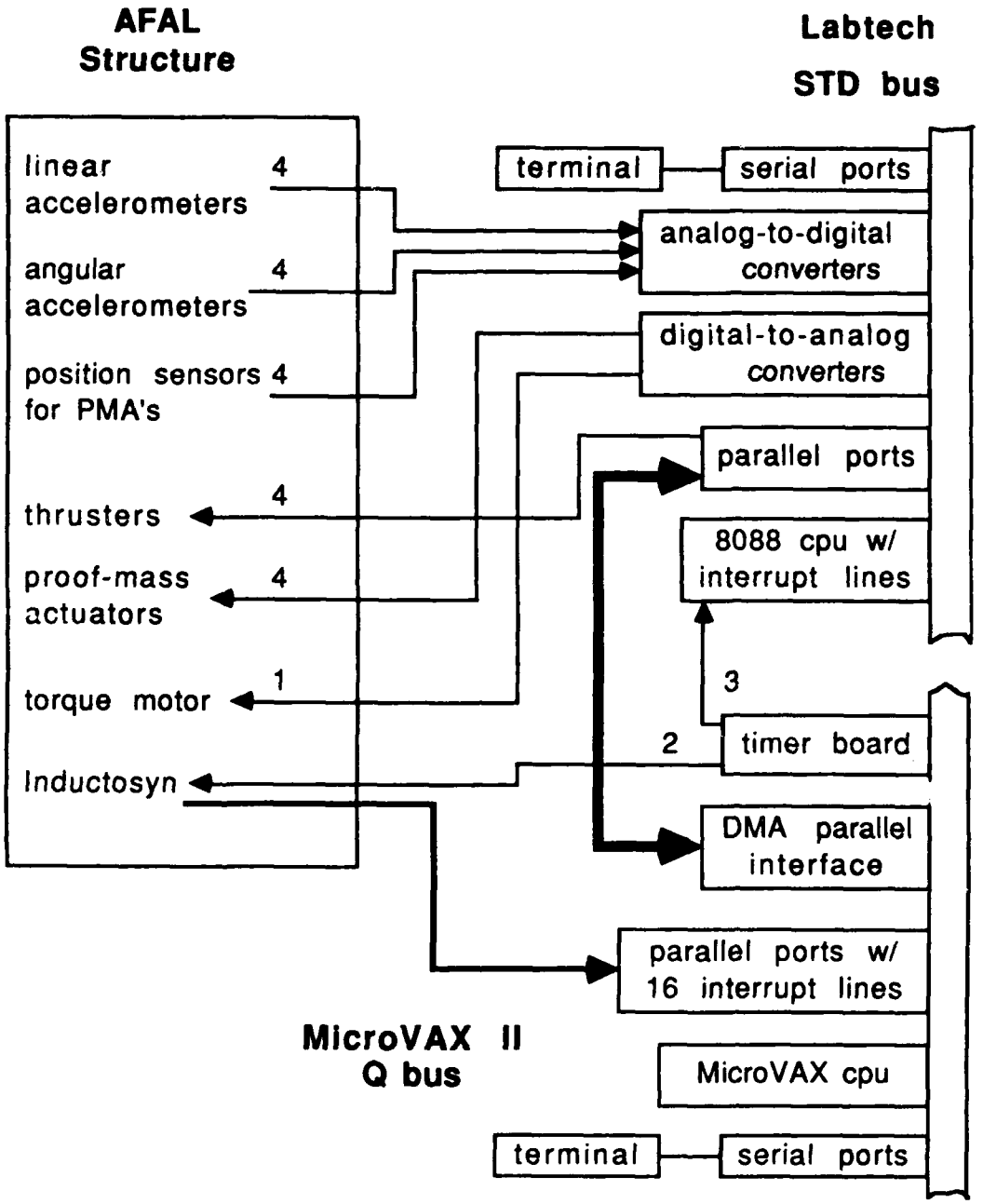

Figure 4-2. MicroVAX/Labtech computer system configuration.

MicroVAX rather than the Labtech because (i) interfaces available for the MicroVAX generally have better performance (faster speed, more channels per board) than interfaces for the Labtech, (ii) the MicroVAX is easier to program than the Labtech, and (iii) the MicroVAX can better handle the extra computation required to operate additional interfaces. There were not enough parallel ports available on the Labtech read the Farrand hub angle readout, so additional parallel ports for the MicroVAX. This is why the MicroVAX reads the hub angle instead of the Labtech.

The MicroVAX counter/timer board controls event timing and provides handshaking signals. Event timing was originally to be controlled by a counter/timer board in the Labtech. However, since the main control functions and event scheduling (waiting for interrupts) were being performed on the MicroVAX it was decided that the MicroVAX should control the event timing as well. The MicroVAX timer board has fifteen 16 bit programmable counter/timers. Three of the timers are used to issue interrupts to the Labtech. One of the three timers is the sample interval interrupt and interrupts the MicroVAX as well. Two timers are used to provide handshaking signals when the MicroVAX is reading the Farrand angle readout.

4.4.2 Software

In the combined MicroVAX/Labtech computer system, the MicroVAX provides the user interface to the computer system and performs the calculations needed to implement the chosen control algorithm. The Labtech is used an I/O processor for the MicroVAX. The Labtech provides most of the hardware interface to the AFAL test structure and only performs a limited set of functions upon command from the MicroVAX. The Labtech performs three major functions; (i) read sensors and transfer data to the MicroVAX, (ii) issue the latest control command, and (iii) execute a general purpose routine. The first two functions require accurate timing so these functions are initiated directly by interrupts from the MicroVAX timer board. The read sensor function executes at the beginning of every sample interval. The issue control function is performed at a fixed delay from the beginning of each sample interval.

The general purpose routine contains several subroutines. A particular general purpose subroutine is selected according to a command selection value transferred from the MicroVAX. The general purpose subroutines currently implemented are (i) get sensors biases, (ii) receive new control command, and (iii) reset and exit. The sensor bias subroutine samples each sensor 1000 times, averages each sensor reading, and sends the averaged sensor readings to the MicroVAX. The receive control subroutine receives a new control command vector from the MicroVAX. The reset subroutine sets all control outputs to zero and exits the control program.

The Labtech also has initialization routines which are used only when the control program is started. The initialization routines clear any spurious which occurred since

the previous test, read a configuration file to determine parameters such as how many sensors to read and how many actuator commands to issue, and initialize the hardware interfaces to the AFAL structure and to the MicroVAX.

The MicroVAX executes the executive and control routines needed to implement the desired control algorithm. The executive routines handle initialization, user interface, and reset tasks. The initialization tasks include loading pre-calculated Kalman filter gains and the state-space model from a disk file and initializing the timer board and parallel interfaces to known states. The user interface allows a user to determine parameters such as slew angle, modal weighting factors, and which control algorithm to use for a given test maneuver. The reset tasks include stopping the test in a controlled manner, writing time histories of stored variables (state and measurement estimates, sensor readings, etc.) to a disk file, and resetting the timer board.

The control routines schedule events and perform the calculations which implement the chosen control algorithm. The control routines consist of a program loop which is executed in "real-time" once every sample interval. The program loop waits for the sample interval interrupt and then starts the control delay counter. The digitized sensors readings are collected and incorporated into the state estimates. The control command is calculated based upon the state estimates and is transferred to the Labtech to be issued at the next control delay interrupt. State estimates for the next sample interval are calculated. The loop is repeated if the test time limit has not been reached.

4.4.3 Performance and Timing

The combined MicroVAX/Labtech computer system has improved the overall computational capability of the AFAL control computer. However, the increase was much less than the factor of 20 increase in raw cpu power provided by the MicroVAX. One reason for the limited improvement in computational capability is that the Labtech is performing more I/O than previously and is becoming I/O bound. Another reason is that the Labtech has a significant delay between the occurrence of an interrupt and the execution of the first instruction in the interrupt service routine. The Labtech now responds to three interrupts each sample interval instead of one. Also, because the interrupts to the Labtech cannot occur too close together, additional delays are introduced for each interrupt.

The data transfers between the MicroVAX and the Labtech are the extra I/O the Labtech must perform. Tests were performed to determine the maximum speed of the data transfers. The number of 16 bit words in each transfer was varied and the time for each transfer was determined. The average transfer rate (words per second) and the number of transfers per second were calculated. The results are shown in Figure 4-3. The average transfer rate increases as the number of words in each transfer increases because the overhead required to initiate a transfer is divided among more data words.

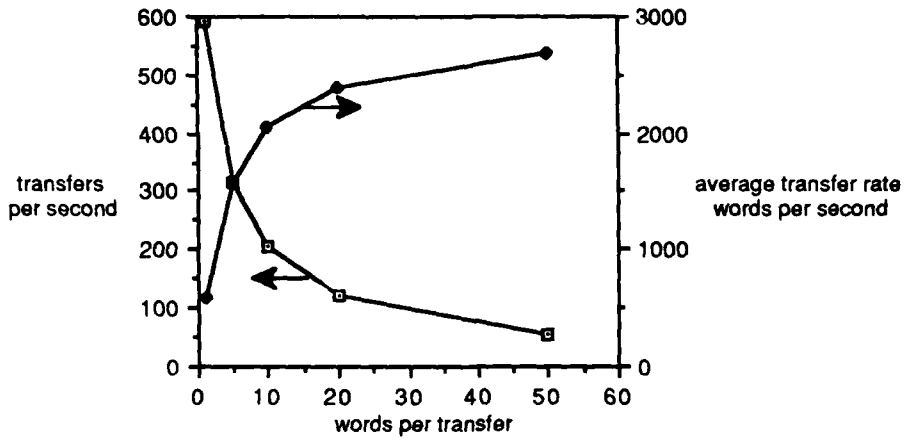

Figure 4-3. MicroVAX--Labtech transfer rates.

The transfer rate approaches 3000 16-bit words per second when more than 50 words are in each transfer. The parallel I/O interface on the MicroVAX side (a DEC DRV11-W uses DMA and can transfer data at rates up to 250,000 words per second so the transfer rate is limited by the Labtech. The transfer rates could easily become an I/O bottleneck if more sensor readings must be transferred and/or sample rates must be increased.

The Labtech has delay of approximately 1.5 ms from the time an interrupt occurs to the execution of the first instruction in the interrupt service routine. In comparison, the MicroVAX has an mean interrupt response time of 33 μs. The Labtech responds to three interrupts during each sample interval; the sample interrupt, general purpose interrupt to receive the new control command, and the issue control interrupt. The interrupt response delay adds 4.5 ms to the minimum achievable sample interval.

Additional delays are introduced to insure that the Labtech does not miss any interrupts. A delay approximately 0.5 ms from the end of an interrupt service routine to the occurrence of the next interrupt is required. This delay adds 1.5 ms to the minimum sample interval.

The verification tests were performed using a 35 ms sample interval ($\approx$ 28 Hz sample rate) and a control delay of 17 ms. Tests were also performed at higher sample rates. The combined computer system performs well using the same model and control algorithms with a 20 ms sample period and a 13 ms control delay. However, interrupt

cycles were missed when a 15 ms sample interval and 10 ms control delay were used. The control delay was too small to allow for the necessary interrupt delays to insure the Labtech did not miss interrupts.

The added computational power of the MicroVAX is not apparent in the relatively small increase in sampling rate achieved. However, the MicroVAX is idle for most of the sample interval. More complex control laws which do not require additional I/O or faster sampling rates could be readily implemented.

Section 5

Optimal Projection/Maximum Entropy Compensator Design

5.1 The Maximum Entropy Method for Robust Compensator Design

In compensator design, there is always a tradeoff between performance and robustness. When the highest performance is required, the robustness characteristics will be diminished. For example, the Linear Quadratic Gaussian *optimal* design approach was shown by Doyle to have arbitrarily small stability margins [22]. In order to increase compensator robustness, most of the recent control theory developments (such as the Model Based Compensator/Loop Transfer Recovery approach) require an *a posteriori* evaluation of the robustness of a particular design. This testing is then followed by an alteration of the design parameters and a redesign. The performance/robustness tradeoff is a consequence of the robustification, not a directly manipulated aspect of the design. While significant robustification is possible, achieving a desired performance level is not guaranteed.

The maximum entropy approach was developed as a means to design compensators with the performance/robustness tradeoff being explicitly determined by the quadratic cost-functional. In this case, robustness is with respect to parameter modelling uncertainties, as opposed to the effects of unmodelled dynamics. By explicitly including the parameter uncertainties in the plant, the performance/robustness tradeoff can be directly manipulated to suit the design requirements.

The optimal projection/maximum entropy synthesis methodology has been applied to the problem of designing a compensator for a structural vibration controller which uses effectors based upon the proof-mass actuator concept. The design process and simulated performance evaluation is described in Section 5 through Section 8.

The OP/ME design approach can be used to determine a robust reduced-order *dynamic compensator*. Given the linear system:

$$\begin{aligned} \dot{x} &= A\,x + B\,u + w_1 \\ y &= C\,x + D\,u + w_2 \end{aligned} \qquad (5-1)$$

where

$$x \in R^n \ , \ u \in R^m \ , \ y \in R^l$$
$$A \in R^{n \times n} \ , \ B \in R^{n \times m}$$
$$C \in R^{l \times n} \ , \ D \in R^{l \times m}$$
$$SD(w_1, w_2) = (V_1, V_2)$$

we wish to determine a dynamic compensator (output feedback) of order $n_c \leq n$:

$$\begin{aligned} \dot{q} &= A_c q + F y \\ u &= -K q \end{aligned} \qquad (5-2)$$

where

$$q \in R^{n_c} \ , \ n_c \leq n$$
$$A_c \in R^{n_c \times n_c}$$
$$F \in R^{n_c \times l}$$
$$K \in R^{m \times n_c}$$

that minimizes the Quadratic Cost function:

$$J = \int_{t=0}^{\infty} x^T R_1 x + u^T R_2 u \ dt \qquad (5-3)$$

The maximum entropy design approach is used to minimize J in the presence of parameter uncertainties. The Optimal Projection design approach minimizes J for a compensator of order $n_c \leq n$. When combined, the OP/ME design methodology provides a powerful tool for robust reduced-order compensator design.

5.1.1 Characterization of Model Errors

In most instances, the errors that are made in the modelling process will take on a particular structure. Usually, we can predict the form in which these errors manifest themselves. In an aircraft control problem, for example, we may want a compensator to be robust with respect to variations in fuel load. We then could predict how the parameters of our model will vary with the fuel mass. As fuel is used, some parameters may increase while others decrease. Thus, given the initial linear system matrices of Equation (5-1), we could determine a set of parameter error distribution matrices A_i, B_i, C_i, and D_i for the error "i", such that the "true" system dynamics would be represented by the following matrices:

$$\begin{aligned} A_{actual} &= A + A_i \\ B_{actual} &= B + B_i \\ C_{actual} &= C + C_i \\ D_{actual} &= D + D_i \end{aligned} \qquad (5-4)$$

The i subscript represents a set of correlated uncertainties within the Equations (5-1) resulting from one potential error source. In the aircraft example just used, $i = 1$ would represent the distribution of parameter error due to fuel usage, while $i = 2$ would be a different set of distributions, uncorrelated with the previous set, perhaps due to airspeed. There could be any number of uncorrelated uncertainties.

5.1.1.1 Stochastic Modelling of Errors

As shown in the Equation set (5-4), the *actual* system dynamics differ from the *nominal* model by an error distribution matrix. The basic premise of maximum entropy error modelling is that the magnitude of the error is a white-noise process. Thus the Equation set (5-4) is augmented with $\alpha_i(t)$, a zero-mean, unit-intensity multiplicative white-noise process [6]. Assuming there are p uncorrelated error sources, the system dynamics matrices become:

$$A_{actual} = A + \sum_{i=1}^{p} \alpha_i(t)\, A_i \qquad (5-5)$$

With the B_{actual}, C_{actual}, and D_{actual} matrices taking a similar form.

5.1.1.2 Justification for the Multiplicative White-Noise Model

The use of a multiplicative white-noise model for parameter variations is not a universally accepted approach. There are many skeptics who question the validity of the model. It is clear that the actual parameters do not behave in this manner. However, there is a very straightforward interpretation. Consider the context within which we are using the multiplicative white-noise— Quadratically Optimal control system synthesis. By including the parameter uncertainties in the system dynamics, we wish to determine their *effects upon the quadratic cost function*. Hyland has shown that the multiplicative white-noise process reproduces the second-moment effects of uncertainty in plant parameters upon the cost-functional [6]. No claims are made as to any other characteristics of this model— they are irrelevant to the optimization problem. The actual dynamics do not vary with time, despite the time dependence of the white-noise process in Equation (5-5). The white-noise solely represents a probability that the parameters will take on any particular values. Hyland invoked the Maximum Entropy Principle of Jaynes [23] to interpret the stochastic process in a probabilistic sense, not as an actual time varying process. By increasing the magnitude of the A_i, etc. terms, we are actually increasing the uncertainty associated with those specific parameters.

With the addition of multiplicative white noise, the ordinary differential equations

shown in Equations (5-1) become [6]:

$$\dot{x} = \left(A + \sum_{i=1}^{p} \alpha_i(t) A_i \right) x(t) \qquad (5-6)$$

Using the terminology of stochastic calculus, this ODE transforms to:

$$dx_t = \left(A_S dt + \sum_{i=1}^{p} d\alpha_{it} \right) x_t \qquad (5-7)$$

where A_S has two possible definitions:

for the Ito equation:

$$A_S = A \qquad (5-8)$$

for the Stratonovich differential equation:

$$A_S = A + \underbrace{\frac{1}{2} \sum_{i=1}^{p} A_i^2}_{\text{Stratonovich Correction}} \qquad (5-9)$$

The correction term present in the Stratonovich form results from a different interpretation of stochastic processes and the methods used to determine these equations. There are similar terms "correcting" the B and C matrices.

The "Stratonovich correction" is appropriate to flexible mechanical structures and important to the maximum entropy method for it dispels the myth of the "threshold uncertainty principle" promoted in the 1960's [24]. This theory was based upon the Ito interpretation of the stochastic differential equation above. The principle stated that for a sufficiently high level of uncertainty in the plant model, (i.e. $\|A_i\|$ large) there could be no guarantee of second moment stability for the closed-loop system. The threshold's existence does follow from the Ito equation, but is flawed for flexible mechanical systems. One could postulate a flexible structure with parameter uncertainty above the maximum uncertainty threshold— perhaps high uncertainties in the stiffness. The threshold uncertainty principle would indicate that there does not exist a stabilizing compensator in the presence of this uncertainty. However, in the limit the compensator gains could be reduced to zero, leaving the open-loop system, which obviously has no right half-plane poles (remember, this is a flexible structure).

The inclusion of the Stratonovich correction term into the stochastic form of the Lyapunov equation guarantees the existence of a steady-state solution for any level of

uncertainty [6]. The use of this alternative stochastic differential equation has enabled the maximum entropy method to introduce arbitrary levels of robustness into a compensator. Consequently, the robustness/performance tradeoff can be performed without restriction to suit the needs of a particular design.

5.1.2 Necessary Conditions for Optimality

Once the system dynamics are represented with stochastic differential equations, the necessary conditions for optimality can be easily derived. The resulting equations take the form of two Riccati equations and two Lyapunov equations, all coupled by the stochastic parameters. These equations are shown on the following page for *full-order compensators* [8]. Notice that these equations are valid only for the full-order case. Section 5.2 will examine the equations governing the optimal projection method for compensator order reduction. Finally, the complete OP/ME design equations will be presented in an integrated form.

Solve for nonnegative-definite P, Q, $\hat{P}$, and $\hat{Q}$
such that

$$\begin{aligned} 0 \;=\; & PA_S + A_S^T P + \sum_{i=1}^{p} A_i^T P A_i - \mathcal{P}_S^T R_{2S}^{-1} \mathcal{P}_S + R_1 \\ & + \sum_{i=1}^{p} \left(A_i - Q_S V_{2S}^{-1} C_i\right)^T \hat{P} \left(A_i - Q_S V_{2S}^{-1} C_i\right) \end{aligned} \qquad (5-10)$$

$$\begin{aligned} 0 \;=\; & A_S Q + Q A_S^T + \sum_{i=1}^{p} A_i Q A_i^T - Q_S V_{2S}^{-1} Q_S^T + V_1 \\ & + \sum_{i=1}^{p} \left(A_i - B_i R_{2S}^{-1} \mathcal{P}_S\right) \hat{Q} \left(A_i - B_i R_{2S}^{-1} \mathcal{P}_S\right)^T \end{aligned} \qquad (5-11)$$

$$0 \;=\; \hat{P} A_{QS} + A_{QS}^T \hat{P} + \mathcal{P}_S^T R_{2S}^{-1} \mathcal{P}_S \qquad (5-12)$$

$$0 \;=\; A_{PS} \hat{Q} + \hat{Q} A_{PS}^T + Q_S V_{2S}^{-1} Q_S^T \qquad (5-13)$$

where the following notation has been adopted:

$$A_S \triangleq A + \frac{1}{2}\sum_{i=1}^{p} A_i^2 \ , \ B_S \triangleq B + \frac{1}{2}\sum_{i=1}^{p} A_i B_i \ , \ C_S \triangleq C + \frac{1}{2}\sum_{i=1}^{p} C_i A_i$$

$$R_{2S} \triangleq R_2 + \sum_{i=1}^{p} B_i^T \left(P + \hat{P}\right) B_i$$

$$V_{2S} \triangleq V_2 + \sum_{i=1}^{p} C_i \left(Q + \hat{Q}\right) C_i^T$$

$$\mathcal{P}_S \triangleq B_S^T P + \sum_{i=1}^{p} B_i^T \left(P + \hat{P}\right) A_i$$

$$Q_S \triangleq Q C_S^T + \sum_{i=1}^{p} A_i \left(Q + \hat{Q}\right) C_i^T$$

$$A_{QS} \triangleq A_S - Q_S V_{2S}^{-1} C_S$$

$$A_{PS} \triangleq A_S - B_S R_{2S}^{-1} \mathcal{P}_S$$

The compensator matrices then take on the following form, corresponding to Equation (5-2):

$$A_c = A_S - Q_S V_{2S}^{-1} C_S - B_S R_{2S}^{-1} \mathcal{P}_S + Q_S V_{2S}^{-1} D R_{2S}^{-1} \mathcal{P}_S \qquad (5-14)$$

$$F = Q_S V_{2S}^{-1} \qquad (5-15)$$

$$K = R_{2S}^{-1} \mathcal{P}_S \qquad (5-16)$$

Notice that the "regulator" Riccati equation (5-10) and the "observer" Riccati equation (5-11) now have common elements which couple the two equations together and into the two Lyapunov equations (5-12) and (5-13). Thus the "separation principle", a foundation of LQG design, is *invalid* in the presence of parameter uncertainty. No longer can the feedback gains be determined independently of the observer gains and now an iterative approach is required.

5.1.3 Interpretations of Maximum Entropy Effects

An important observation to be made from the ME design equations is that the Linear Quadratic Gaussian solution is simply a special case of ME design. Suppose that we do not wish to model any uncertainty in our plant parameters. Thus we define A_i, B_i and C_i to be equal to zero. Consequently, the last term in both Equation (5-10) and Equation (5-11) drops out. The two Lyapunov equations, Eqn. (5-12) and Eqn. (5-13), are no longer required. The LQG solution is now determined by the newly "separated" Riccati equations. Therefore, the LQG optimal compensator is solely a special case of the more general maximum entropy design procedure, corresponding to the optimal extremum, where parameter uncertainty is nil. The opposing extreme would be a very low gain compensator, designed for systems of very high parameter uncertainty. With the elimination of the threshold uncertainty principle, as discussed in Section 5.1.1.2, maximum entropy design can be seen as spanning the spectrum of possible performance levels— from optimal to open-loop and from extremely sensitive to extremely robust.

In the cost function of Equation (5-3), the matrix R_2 puts a weighting on the control. An R_2 of small magnitude represents "cheap control", resulting in increased regulator gains. Similarly, a large R_2 results in lower gains. This relationship is clearly seen in Equation (5-16), where the regulator gain matrix K is proportional to the inverse of R_{2S}. Notice, however, that R_{2S}^{-1} is present in the maximum entropy design equations. If the notation for R_{2S} is examined, it is seen that $R_{2S} \geq R_2$ under all circumstances. Additionally, as the magnitude of B_i increases, the gap between R_{2S} and R_2 widens. Therefore, as uncertainty in the parameters of the B matrix increases, the regulator gains decrease. Similarly, from examination of Equation (5-15) one can see that parameter uncertainty in the C matrix reduces the compensator's gain matrix F. Consequently, increasing levels of uncertainty in the measurement matrix C reduce the dependence of the compensator upon the measurement signals, while uncertainty in the control distribution matrix B reduces the level of control commanded. This is a predictable and reassuring result.

A significant uncertainty in the modelling of flexible structures is the set of modal frequencies. The characterization of these potential errors will be discussed in detail in Section 7. However, the manifestation of modal frequency uncertainty in the maximum entropy design equations gives some significant insight into the effects of this method. Typically, a second order vibrational mode can be represented in modal coordinates as:

$$\frac{d}{dt}\begin{bmatrix} x \\ \dot{x} \end{bmatrix} = \begin{bmatrix} 0 & 1 \\ -\omega^2 & -2\zeta\omega \end{bmatrix}\begin{bmatrix} x \\ \dot{x} \end{bmatrix} + Bu \qquad (5-17)$$

If we scale the position coordinate by the modal frequency ω, Equation (5-17) is transformed into an equivalent representation:

$$\frac{d}{dt}\begin{bmatrix} x\omega \\ \dot{x} \end{bmatrix} = \begin{bmatrix} 0 & \omega \\ -\omega & -2\zeta\omega \end{bmatrix}\begin{bmatrix} x\omega \\ \dot{x} \end{bmatrix} + Bu \qquad (5-18)$$

Now consider the case of modelling uncertainty in modal frequency ω. Using the principles of maximum entropy design discussed in Section 5.1.1, and assuming that the modal damping is small (i.e. $\zeta \ll 1$), the uncertainty distribution matrix takes the following form.

$$A_i = \begin{bmatrix} 0 & 1 \\ -1 & 0 \end{bmatrix} \qquad (5-19)$$

Remember that the A_S matrix has replaced the A matrix in the design equations (5-10)-(5-13). The difference between A_S and A is the Stratonovich correction of Equation (5-9). For this uncertainty in modal frequency, the correction term is:

$$\frac{1}{2}\sum_{i=1}^{p} A_i^2 = \frac{1}{2}\begin{bmatrix} 0 & 1 \\ -1 & 0 \end{bmatrix}\begin{bmatrix} 0 & 1 \\ -1 & 0 \end{bmatrix} = \begin{bmatrix} -\frac{1}{2} & 0 \\ 0 & -\frac{1}{2} \end{bmatrix} \qquad (5-20)$$

These negative values along the diagonal serve to shift the eigenvalues of A_S further into the left half-plane than those of the nominal A. Furthermore, the degree to which this shift takes place is varied by the magnitude of A_i, a design variable. Thus the representation of the open-loop dynamics seen by the ME design equations has been altered by the Stratonovich correction which provides a variable left shift. The effects of this occurrence are significant. Model-based compensators (LQG and ME) operate by placing compensator poles close to the lightly damped plant poles near the imaginary axis. The interaction between these compensator and plant poles is important in achieving high performance levels. However, when there is high uncertainty as to the location of the plant poles (modal frequency errors), the potential for destabilizing interactions becomes significant. Either the compensator or the plant poles can migrate into the right half-plane, causing closed-loop instability. With the variable left shift, the compensator poles are forced further to the left. While this shift reduces the performance level, the robustness of the compensator is enhanced by decreasing the level of interaction between the compensator and plant poles. Alternatively, for a finite amount of control available, the compensator delegates less control authority to those modes which are already well-stabilized. As the variable left shift makes the modes with high uncertainty appear further to the left, less gain is apportioned to them. Of course, this lessening of the gains will reduce the performance of the closed loop system. As always, there is a performance/robustness tradeoff.

5.2 The Optimal Projection Method

The previous section examined robustness with respect to parameter uncertainties. This section, however, addresses the need for robustness with respect to unmodelled dynamics— the "spillover problem". For very practical and important reasons such as cost and ease of implementation, the order of a compensator is usually restricted

to some number $n_c \leq n$ (see page 44). As was discussed in Section 1.1, the contamination of sensor signals by high order unmodelled modes can destabilize a control system. Consequently, direct methods have evolved such as optimal projection (OP), the approach examined in this report, which take the compensator order constraint into account when determining gains *. Thus, when reduced order OP compensators are attached to their high order plants, stability and performance are guaranteed.

Optimality with respect to the cost function J of Equation (5-3) is still the objective of reduced-order compensator design. However, the introduction of the compensator order constraint severely complicates the design process. and the indirect design methods lose their guarantees of stability and performance when the order reduction step takes place.

The development of the LQG design methodology resulted from the study of necessary conditions for optimality. The algebraic Riccati equation represents the first-order necessary conditions of the problem. As a consequence of these developments, much insight was gained into the existence, uniqueness, and stability of solutions. However, no analytic solution procedure is known for the optimum reduced order compensator problem. The use of gradient search parameter optimization techniques could perhaps determine stable compensators with adequate performance. Nevertheless, this "brute force" technique would not be taking advantage of the structure of the problem, and convergence to the global minimum could not be guaranteed.

Reduced order compensator design approaches have typically used these parameter optimization techniques. While the necessary conditions for optimal reduced order compensators had been developed, their form was very complex [25]. As a result, the useful insights which had occurred for full order compensators, as described above, were not forthcoming. However, Hyland made a significant contribution to this area of research when he transformed these complex necessary conditions into a simpler form [14]. The simplified necessary conditions take the form of two Riccati and two Lyapunov equations, coupled by a projection from the full order state-space to the reduced order compensator-space **. These equations will be referred to as the optimal projection equations (OP). Notice that in the case of reduced order compensation, the classical separation principle once again is discarded due to coupling through this projection called τ.

Just as the algebraic Riccati equation solutions define the LQG compensator, the solution to these four matrix equations and the projection τ together define the reduced order compensator which is optimal with respect to the cost function J. Consequently, if a solution to these equations can be found, it defines the OP compensator which

*An alternative direct method using gradient search techniques will be used for comparison on an example in Section 6.2.2.

**For those not familiar with projections, see any modern linear algebra text, such as Strang, ref. [26].

is optimal among the set of all compensators of order n_c. Note that typically, this order reduction involves some sacrifice in system performance, analogous to the performance/robustness tradeoff. As lower and lower compensator orders are required, less performance will be possible. Remember, however, that by satisfying the necessary conditions, the compensator has the maximum achievable performance. No n_c order compensator designed through another method can better the performance of the OP compensator, thus the motivation for the OP methodology *.

5.2.1 The Projection τ

A projection from the order n state-space to the order n_c compensator space defines the observation and control subspaces of the design. In the context of the optimal projection method, τ has the following characteristics:

$$\tau \in R^{n \times n} \ , \ \text{rank}(\tau) = n_c \ , \ \tau^2 = \tau \qquad (5-21)$$

We define the control subspace of the reduced order compensator to be the span (τ) (i.e., the row-space of τ^T). Similarly, the observation subspace is defined as the span $\left(\tau^T\right)$ (i.e., the row-space of τ). Then we can factor the rank n_c projection into two $n_c \times n$ matrices G and Γ where the row-space of G is the control subspace, the row-space of Γ is the observation subspace, and where

$$G^T\Gamma = \tau \ , \ \Gamma G^T = I_{n_c} \qquad (5-22)$$

In this context, the closed loop system becomes [9]:

$$\dot{x} = Ax - B\hat{K}G^Tq + w_1 \qquad (5-23)$$

$$\dot{q} = \Gamma\left(A - \hat{F}C - B\hat{K} + \hat{F}D\hat{K}\right)G^Tq + \Gamma\hat{F}\underbrace{(Cx + Du + w_2)}_{y} \qquad (5-24)$$

with $\hat{K}$ and $\hat{F}$ given by

$$\hat{K} = R_2^{-1}B^TP \qquad (5-25)$$

$$\hat{F} = QC^TV_2^{-1} \qquad (5-26)$$

which are the gain expressions for a full order LQG design. Thus one can see from the above that there is a quasi-full order compensator imbedded within the reduced order design, with order reduction resulting from the projection's components G and Γ. Notice the effects of the control and observation subspaces:

*Of course, this assumes that the exact solution of the OP equations can be found. The issue of solution convergence will be discussed in a section to follow.

- The compensator state q generates feedback control u only if it lies within the row-space of G.
- Sensor inputs, $\hat{F}y$ are ignored unless they are in the row-space of Γ.

The use of a projection to reduce the order of a compensator is at least implicitly used in all compensator design methods. For example, in the case of compensator truncation where only the first n_c compensator states are included, the projection would be defined as:

$$\tau = \begin{bmatrix} I_{n_c} & 0 \\ 0 & 0 \end{bmatrix} \quad , \quad \Gamma = G = [I_{n_c}\, 0 \ldots 0] \qquad (5-27)$$

Introducing this projection into the closed loop dynamics shown above is equivalent to deletion of the last $n - n_c$ states from the full order design. Therefore, compensator truncation, and similarly modal truncation, are simply special "suboptimal" cases of the more general optimal projection equations. The difference lies in the determination of the projection τ. In the optimal projection method, the projection is chosen that spans the components of the n-state space which optimize the resulting compensator. Thus we are not just controlling the first n_c states, but rather an optimal linear combination of of the states in the system. It is this selection of the projection τ that guides the solution to the global minimum of the cost function J.

5.2.2 Necessary Conditions for Optimality

For a given compensator order n_c, the cost function J of Eqn. (5-3) is minimized by the compensator determined by the OP equations. These reduced order optimality conditions take the following form [9]:

Using the notation of Section 5.1.2, solve for
nonnegative-definite P, Q, $\hat{P}$, $\hat{Q}$
and the projection τ such that

$$0 = PA + A^TP - PBR_2^{-1}B^TP + R_1 + \tau_\perp^T PBR_2^{-1}B^TP\tau_\perp \qquad (5-28)$$

$$0 = AQ + QA^T - QC^TV_2^{-1}CQ + V_1 + \tau_\perp QC^TV_2^{-1}CQ\tau_\perp^T \qquad (5-29)$$

$$0 = \hat{P}A_Q + A_Q^T\hat{P} + \mathcal{P}_S^TR_{2S}^{-1}\mathcal{P}_S - \tau_\perp^T PBR_2^{-1}B^TP\tau_\perp \qquad (5-30)$$

$$0 = A_P\hat{Q} + \hat{Q}A_P^T + \mathcal{Q}_SV_{2S}^{-1}\mathcal{Q}_S^T - \tau_\perp QC^TV_2^{-1}CQ\tau_\perp^T \qquad (5-31)$$

where

$$A_Q = A - QC^T V_2^{-1} C \ , \ A_P = A - BR_2^{-1} B^T P$$

and the projection τ has the following properties:*

$$\tau = \sum_{k=1}^{n_c} \prod_k \left[\hat{Q}\hat{P}\right] \qquad (5-32)$$

$$\tau_\perp = I_n - \tau \ , \ \Gamma G^T = I_{n_c} \ , \ G^T \Gamma = \tau$$

The compensator matrices then take on the following form, corresponding to Equation (5-2):

$$A_c = \Gamma \left(A - QC^T V_2^{-1} C - BR_2^{-1} B^T P + QC^T V_2^{-1} D R_2^{-1} B^T P \right) G^T \qquad (5-33)$$

$$F = \Gamma Q C^T V_2^{-1} \qquad (5-34)$$

$$K = R_2^{-1} B^T P G^T \qquad (5-35)$$

5.2.3 Determination of the Projection τ

In Section 5.2.1 above, the importance of choosing the proper projection was emphasized. In this section, the means of determining τ will be discussed. Notice in Equation (5-32) that the projection is related to the product of $\hat{Q}$ and $\hat{P}$, two nonnegative-definite matrices that solve the Lyapunov equations (5-31) and (5-30) respectively. These matrix equations are similar to the control and observation grammians examined by Moore in his balancing approach to model reduction [3], the difference being the addition of projection terms and the rank of $\hat{Q}$ and $\hat{P}$ (see ref. [10]). Thus there is a relationship between the steady-state characteristics of the system and the formation of the projection. It is this consideration that is lacking in the truncation approach.

In order to determine the projection, we first find the $n \times n$ invertible transform ϕ that diagonalizes both $\phi Q \phi^T$ and $\phi^{-T} \hat{P} \phi^{-1}$, ** with the further restriction that

$$\phi \hat{Q} \phi^T = \phi^{-T} \hat{P} \phi^{-1} = \Sigma \qquad (5-36)$$

*Note that the $\prod_k$ operator represents the k^{th} eigenprojection which will be discussed later.

**We define $X^{-T} \triangleq \left(X^T\right)^{-1} = \left(X^{-1}\right)^T$

This latter restriction is the so-called "balancing condition". If this type of transformation were applied to a linear system, the observability and controllability grammians would be equivalent [3].

Our use of this transform is different, however. Notice that ϕ decomposes $\hat{Q}\hat{P}$ into a diagonal matrix containing its eigenvalues:

$$\hat{Q}\hat{P} = \phi^{-1}\Sigma^2\phi \qquad (5-37)$$

If Moore's balancing transformation is used (the transform is generated by singular value decomposition methods), the diagonal matrix becomes:

$$\Sigma \triangleq \text{diag}\,(\sigma_1, \cdots, \sigma_n) \quad , \quad \sigma_1 \geq \sigma_2 \geq \cdots \geq \sigma_n \qquad (5-38)$$

If we let u_k be the k^{th} column of ϕ^{-1} and let v_k^T be the k^{th} row of ϕ, then $\hat{Q}\hat{P}$ can be expressed as

$$\hat{Q}\hat{P} = \sum_{k=1}^{n} \sigma_k^2 u_k v_k^T \qquad (5-39)$$

where these vectors u_k and v_k are biorthonormal, i.e.:

$$v_k^T u_j = \begin{cases} 1 & \text{if } k = j \\ 0 & \text{if } k \neq j \end{cases} \qquad (5-40)$$

Thus we can now define the k^{th} **eigen-projection** of $\hat{Q}\hat{P}$ as:

$$\prod_k \left[\hat{Q}\hat{P}\right] = u_k v_k^T \qquad (5-41)$$

These eigen-projections are each unit-rank, $n \times n$, mutually disjoint projections where [9]

$$\left(\prod_k \left[\hat{Q}\hat{P}\right]\right)^2 = \prod_k \left[\hat{Q}\hat{P}\right] \quad , \quad \prod_k \left[\hat{Q}\hat{P}\right] \prod_j \left[\hat{Q}\hat{P}\right] = 0 \text{ if } k \neq j \qquad (5-42)$$

As can be seen in Equation (5-32), the projection τ consists of a summation of n_c eigen-projections. Consequently, in accordance with Equation (5-42), the rank$(\tau) = n_c$ and $\tau^2 = \tau$, satisfying part of the necessary conditions shown previously.

It is very important to notice that the LQG solution is simply a special case of the more general optimal projection equations. If a full order compensator is to be designed, then $n_c = n$. Thus, the projection τ becomes the identity matrix and $\tau_\perp = 0$. The two Lyapunov equations are then superfluous, with the LQG solution determined by the now *uncoupled* Riccati equations.

5.2.3.1 Selection of the Eigen-Projections

An alternative representation of the projection τ can be formed from Equations (5-39) and (5-41). Let E be a diagonal matrix with the diagonal elements being either 0's or 1's. Then τ can be shown to be:

$$\tau = \phi^{-1} E \phi \qquad (5-43)$$

where E has n_c nonzero (i.e. 1) elements along its diagonal, and rank$(E) = n_c$. In this simpler representation of τ, the placement of a 1 in the $(k,k)^{th}$ element of E corresponds to including the k^{th} eigen-projection in τ.

While the necessary conditions specify that τ is to be the sum of n_c eigen-projections, there is no requirement as to which n_c of the n should be chosen. As the selection of the proper projection is essential for convergence to the global minimum, the choice of the eigen-projections is a critical issue.

5.2.3.2 Eigenvalue Ranking

Moore used the similarity transform defined above to determine the dominant modes of the system— the modes associated with the largest eigenvalues of $\hat{Q}\hat{P}$ (the "principal components" in [3]). This particular transform arranges the eigenvalues in decreasing order down the diagonal of Σ^2; therefore, if n_c eigenprojections are to be selected, we choose the first n_c. This method of eigen-projection selection will be referred to as *eigenvalue ranking*. Using the notation of Equation (5-43), eigenvalue ranking corresponds to setting the first $n_c \times n_c$ block of E to the identity matrix, i.e.

$$\tau = \phi^{-1} \begin{bmatrix} I_{n_c} & 0 \\ 0 & 0 \end{bmatrix} \phi \qquad (5-44)$$

Additionally, the determination of Γ and G are both straightforward. Γ is formed from the first n_c rows of ϕ, while G is the first n_c rows of ϕ^{-T}. Eigenvalue ranking is usually appropriate for determining τ, and its simplicity makes it the preferred method.

5.2.3.3 Cost-Component Ranking

While eigenvalue ranking is the most straightforward method for selecting eigenprojections, there are certain cases where the dominant modes do not guide the equations to the global minimum. For these situations, the method of *cost-component ranking* was developed [10]. In this approach, the cost function is decomposed in terms of the projection τ and the current solutions to the OP equations. Through this decomposition, we can determine which projections will result in the least deviation of J from its LQG optimal value. Using these cost-component and eigenvalue rankings, we can

determine which modes give *both* the greatest reduction in J *and* create a dominant rank(n_c) projection.

The cost-component rankings lie along the diagonal of the matrix M [27], where

$$M \triangleq \phi^{-T} P B R_2^{-1} B^T P \phi^{-1} + \phi Q C^T V_2^{-1} C Q \phi^T \qquad (5-45)$$

To rank the projections, we use the eigenvalues σ_k of Equation (5-37), and the diagonal elements of M above to define:

$$\rho_k \triangleq \sigma_k M_{kk} \qquad (5-46)$$

Then the method of cost-component ranking consists of choosing the projections associated with the n_c largest values of ρ_k.

5.2.3.4 Summary of Eigen-Projection Selection Methods

Using the projection method of Equation (5-43), we use either of the following approaches to determine the matrix E:

Eigenvalue Ranking

Choose the diagonal elements e_{kk} of E such that:

$e_{kk} = 1$, if σ_k is one of the n_c largest members of the set $\{\sigma_k^2\}_{k=1}^n$

$e_{kk} = 0$, otherwise

Cost-Component Ranking

Choose the diagonal elements e_{kk} of E such that:

$e_{kk} = 1$, if ρ_k is one of the n_c largest members of the set $\{\rho_k\}_{k=1}^n$

$e_{kk} = 0$, otherwise

The effectiveness of these two approaches will be examined in the next later, where the optimal projection design methodology is applied to an example from the literature.

5.3 The Unified OP/ME Methodology

The previous two sections have presented the maximum entropy and optimal projection design methods separately. This was certainly valid, for they are each very useful design tools. However, there are alternative methods for robustifying compensators, and for reducing the order of compensators. It is the applicability of the optimal projection and maximum entropy design approaches to a combined methodology that makes them so powerful.

The maximum entropy design equations consisted of two Riccati equations and two Lyapunov equations, coupled by stochastic terms. The optimal projection design equations were similar, but were coupled by the projection τ. By combining both the stochastic modelling of errors and the restriction on the compensator order, we can determine the necessary conditions for an optimal reduced-order compensator in the presence of modelling uncertainties. These unified optimal projection/maximum entropy design equations have the same form as the OP and ME equations, but are coupled by *both* the projection *and* the stochastic terms.

5.3.1 Necessary Conditions for Optimality

The necessary conditions define the compensator which is both robustified with respect to modelling errors, and is of a reduced order. These conditions take the following form:

Solve for nonnegative-definite P, Q, $\hat{P}$, and $\hat{Q}$
such that

$$\begin{aligned} 0 \;=\; & PA_S + A_S^T P + \sum_{i=1}^{p} A_i^T P A_i - \mathcal{P}_S^T R_{2S}^{-1} \mathcal{P}_S + R_1 \\ & + \sum_{i=1}^{p} \left(A_i - Q_S V_{2S}^{-1} C_i\right)^T \hat{P} \left(A_i - Q_S V_{2S}^{-1} C_i\right) \\ & + \tau_\perp^T P B R_2^{-1} B^T P \tau_\perp \end{aligned} \qquad (5-47)$$

$$\begin{aligned} 0 \;=\; & A_S Q + Q A_S^T + \sum_{i=1}^{p} A_i Q A_i^T - Q_S V_{2S}^{-1} Q_S^T + V_1 \\ & + \sum_{i=1}^{p} \left(A_i - B_i R_{2S}^{-1} \mathcal{P}_S\right) \hat{Q} \left(A_i - B_i R_{2S}^{-1} \mathcal{P}_S\right)^T \\ & + \tau_\perp Q C^T V_2^{-1} C Q \tau_\perp^T \end{aligned} \qquad (5-48)$$

$$0 \;=\; \hat{P} A_{QS} + A_{QS}^T \hat{P} + \mathcal{P}_S^T R_{2S}^{-1} \mathcal{P}_S - \tau_\perp^T P B R_2^{-1} B^T P \tau_\perp \qquad (5-49)$$

$$0 \;=\; A_{PS} \hat{Q} + \hat{Q} A_{PS}^T + Q_S V_{2S}^{-1} Q_S^T - \tau_\perp Q C^T V_2^{-1} C Q \tau_\perp^T \qquad (5-50)$$

where the following notation has been adopted:

$$\tau = \sum_{k=1}^{n_c} \prod_{k} \left[\hat{Q}\hat{P}\right]$$

$$\tau_\perp = I_n - \tau \ , \ \Gamma G^T = I_{n_c} \ , \ G^T\Gamma = \tau$$

$$A_S \triangleq A + \frac{1}{2}\sum_{i=1}^{p} A_i^2 \ , \ B_S \triangleq B + \frac{1}{2}\sum_{i=1}^{p} A_i B_i \ , \ C_S \triangleq C + \frac{1}{2}\sum_{i=1}^{p} C_i A_i$$

$$R_{2S} \triangleq R_2 + \sum_{i=1}^{p} B_i^T \left(P + \hat{P}\right) B_i$$

$$V_{2S} \triangleq V_2 + \sum_{i=1}^{p} C_i \left(Q + \hat{Q}\right) C_i^T$$

$$\mathcal{P}_S \triangleq B_S^T P + \sum_{i=1}^{p} B_i^T \left(P + \hat{P}\right) A_i$$

$$\mathcal{Q}_S \triangleq Q C_S^T + \sum_{i=1}^{p} A_i \left(Q + \hat{Q}\right) C_i^T$$

$$A_{QS} \triangleq A_S - \mathcal{Q}_S V_{2S}^{-1} C_S$$

$$A_{PS} \triangleq A_S - B_S R_{2S}^{-1} \mathcal{P}_S$$

The compensator matrices then take on the following form, corresponding to Equation (5-2):

$$A_c = \Gamma \left(A_S - \mathcal{Q}_S V_{2S}^{-1} C_S - B_S R_{2S}^{-1} \mathcal{P}_S + \mathcal{Q}_S V_{2S}^{-1} D R_{2S}^{-1} \mathcal{P}_S\right) G^T \qquad (5-51)$$

$$F = \Gamma \mathcal{Q}_S V_{2S}^{-1} \qquad (5-52)$$

$$K = R_{2S}^{-1} \mathcal{P}_S G^T \qquad (5-53)$$

Notice that all of the previously discussed design situations are simply subsets of these very general design equations. Simply apply the following:

robustified reduced-order compensator design: Choose appropriate A_i, B_i, C_i, D_i, setting n_c to desired compensator order.

robustified compensator design: Choose appropriate A_i, B_i, C_i and D_i, setting $n_c = n$.

reduced-order compensator design: Set n_c to desired compensator order and A_i, B_i, C_i, $D_i = 0$.

LQG compensator design: Set $n_c = n$ and A_i, B_i, $C_i = 0$.

The next section examines the ways in which a solution to these design equations may be obtained.

Section 6

Implementation of the Optimal Projection/Maximum Entropy Design Methodology

The previous section described the design equations used to determine various compensators: maximum entropy, optimal projection, and the unified OP/ME approach. In all cases, the presentation of the necessary conditions began with "Solve for nonnegative-definite P, Q, $\hat{P}$, $\hat{Q}$, (and τ), such that ...". It was simply assumed that matrices could be found that would exactly solve the optimality conditions. However, this is not necessarily the case.

The very non-linear, highly coupled form of these equations defies the derivation of explicit independent equations for the solution matrices. The simplest alternative available is to perform an iterative algorithm and converge upon the optimal solution. This section examines the computer-aided design (CAD) software developed for this report and examines some of the design issues that are a consequence of the iterative algorithm. Finally, the CAD software's capabilities are verified on two examples from the literature, one for the maximum entropy algorithm, and one for the optimal projection algorithm.

6.1 The OP/ME Iterative Design Algorithm

The iterative algorithm is begun with a Linear Quadratic Gaussian solution to the design equations. Thus, we have an initial P and Q solution. The matrices $\hat{P}$ and $\hat{Q}$ are both set to zero, and the projection τ is set to the identity matrix. The design of a OP/ME compensator is converged upon by iterating through the four coupled Riccati and Lyapunov equations. The iteration strategy is illustrated in Figure 6-1.

If the Riccati equations (5-47) and (5-48) are examined, one can see that they do not exactly match the standard Algebraic Riccati Equation (ARE) form:

$$0 = PA + A^T P - PBR_2^{-1}B^T P + R_1 \qquad (6-1)$$

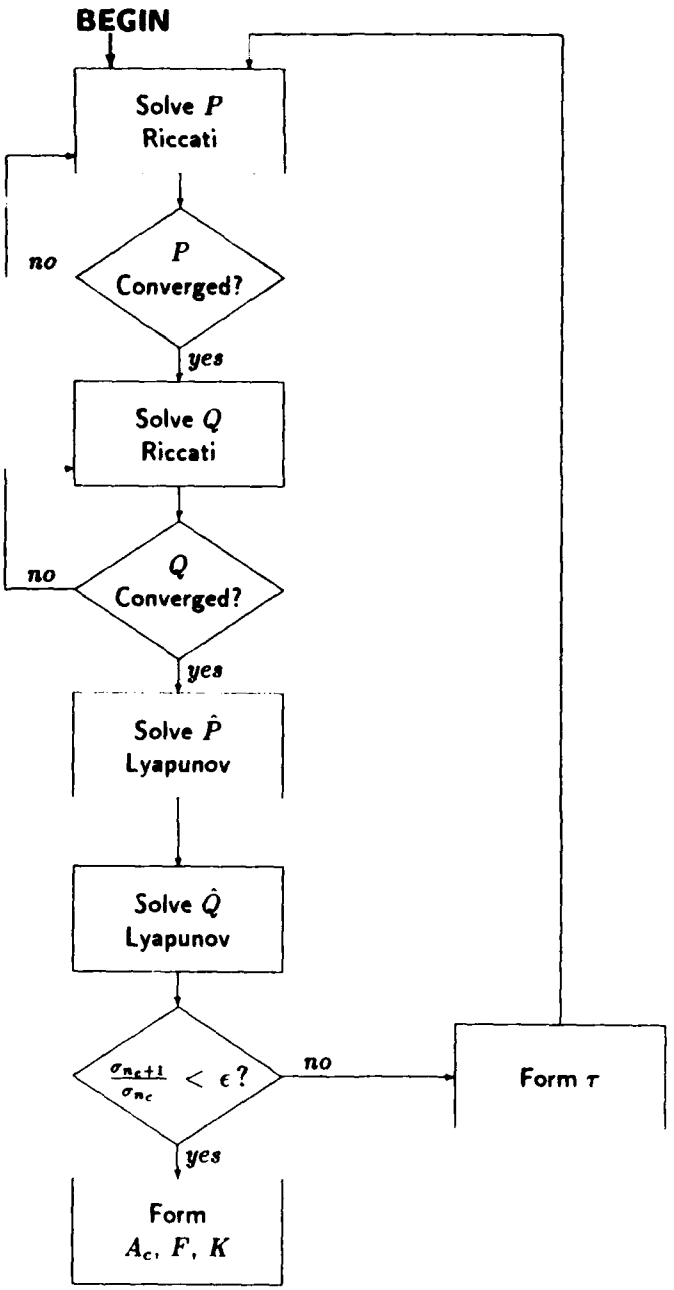

Figure 6-1. The OP/ME iteration strategy.

In order to use the ARE solving routines available, all of the nonstandard terms in the OP/ME equations must be lumped into the constant terms of the matrix equations. This requirement affects the iteration scheme significantly. The constant term of the P Riccati equation (5-47) now includes the P matrix. Consequently, the equation must be iterated through several times, updating the P solution in the constant term each time. Subsequently, the Q Riccati equation (5-48) must be iterated through using the new P solution; the Q in the constant term is updated in each iteration.

We now have P and Q solutions; however, notice that these are not a solution to both equations. The P equation was determined using the previous iterate for Q and therefore can only approximate the correct P. Nevertheless, this is a normal consequence of an iterative algorithm and the detrimental effects should be minimized as the equations converge to a solution.

These solutions for P and Q are now fed to the $\hat{P}$ and $\hat{Q}$ Lyapunov equations (5-48) and (5-48). The standard form for a Lyapunov equation is:

$$0 = PA + A^T P + V \qquad (6-2)$$

Once again there are nonstandard terms which must be added to the constant term V above. However, unlike the Riccati equations, $\hat{P}$ and $\hat{Q}$ will not appear in the constant term. Thus each of the Lyapunov equations do not have to be iterated through separately. The solutions for $\hat{P}$ and $\hat{Q}$ are then used to determine the projection τ, using either of the methods of Section 5.2.3.4. This projection is fed back up to the Riccati equations, and the iteration begins again.

The conditions for termination of the loop relate to dominance of the first n_c elements of Σ^2, the eigenvalues of $\hat{Q}\hat{P}$. When the ratio of σ_{n_c+1} over σ_{n_c} falls below a chosen tolerance, the algorithm is terminated— P, Q, $\hat{P}$ and $\hat{Q}$ are considered to be a solution to the OP/ME equations. Subsequently, the compensator gains can be determined by the Equations (5-51), (5-52) and (5-53).

6.1.1 The OP/ME Computer-Aided Design Software

The CTRL-C * software package provides a control system design and analysis environment. The primary use of this package was to simplify the tasks of matrix manipulation and matrix equation solution. While the CAD software for the OP/ME methodology could be implemented in a high-level language such as FORTRAN, ease of use makes the CTRL-C environment the preferred choice. Matrix multiplication and addition become trivial, and the Riccati and Lyapunov solvers are easy to use. Consequently, attention can be paid to the design algorithms, with less time required for programming. The ensuing simplification of the implementation task is significant—

*product of SCT, Inc., Palo Alto, CA

only 246 lines of CTRL-C macro code are required to create OP/ME designs, while a high level language implementation required *thousands* of lines [27].

6.1.2 Aids to Solution Convergence

Iterative algorithms often have difficulty finding the global minimum of the cost function when searching for a solution. Due to the many local extrema, this complication is particularly an issue for parameter optimization techniques. The issue of convergence was part of the motivation for developing the optimal projection method— proper selection of the projection τ guides the algorithm to the global minimum. However, there are design procedures which can be used to reduce the computational burden of finding this minimum of the cost functional.

Notice in Figure 6-1 that the iterations are initialized with the LQG solution. Alternatively, one could set the P and Q matrices to any values. However, we are assuming that the desired solution to the coupled equations is closer to this solution set than any other values that could be determined. This approach to initializing the solution before beginning the iterations is carried further into the design process. In the case of maximum entropy design, the LQG solution is used as a starting point for a first ME design. For the sake of argument, let the magnitude of the uncertainty distribution matrix A_i be $1 \times A_i$, with no other uncertainties modeled. Upon analysis of the robustness properties of this design, we may find that the system is still too sensitive to this potential modelling error and we wish to do another design with $A_i = 2 \times A_i$. Rather than begin with the LQG solution again, the latest ME solution is used. Following this approach helps the iterative algorithm to quickly converge on the solution. One can conceive of this step-by-step approach as another part of the iterative algorithm, used to converge upon the appropriate design.

It is also appropriate to use this initialization technique during optimal projection design. The solution for the $(n_c + 1)^{th}$ order compensator gives a better indication of the n_c^{th} order solution than does the LQG solution. A design approach similar to the above can be found in ref. [28], where Pearson applied this strategy to parameter optimization techniques.

The initialization methodology described above does reduce the computational burden during maximum entropy design, and is effective in the majority of optimal projection designs. However, when a significant order reduction is required, the approach is often insufficient to insure convergence. The root of the problem lies in the requirement that $\hat{Q}$ and $\hat{P}$ be nonnegative definite (i.e. that these matrices have nonnegative real eigenvalues). When the required compensator order is much less than the plant order ($n_c \ll n$), then the rank of the projection τ decreases. The constant terms in the $\hat{Q}$ and $\hat{P}$ Lyapunov equations (5-48) and (5-47) include the subtraction of a $\tau_\perp$ term. Thus, as τ decreases, the $\tau_\perp$ term can begin to alter the constant term of each Lyapunov equa-

tion significantly. Consequently, the eigenvalues of these constant terms can be shifted into the right half plane. As the Lyapunov equations are no longer being driven by a nonnegative-definite constant term, the resulting solutions will have negative eigenvalues and thus do not satisfy the necessary conditions. Furthermore, the algorithm used to determine the balancing transform ϕ cannot produce a suitable answer under these circumstances. As the projection cannot then be formed, the iterative algorithm no longer works.

6.1.2.1 The Augmented Rank Projection Method

In order to compensator is being designed, an alternative iterative strategy has been implemented. The rank deficiency of the projection is the source of the numerical difficulty in the original algorithm. Consequently, we can use a projection which approximates the rank n_c projection τ, yet is actually full rank. Form this augmented rank projection $\bar{\tau}$ by replacing each of the zero values of the E_i matrix (see Equation (5-43)) with a real number κ where $0 < \kappa \leq 1$. Now each of the eigen-projections are chosen by either eigenvalue ranking or the cost-component method as described in Section 5.2.3.4. However, the other eigen-projections are included with a weighting of κ. As the value of $\kappa \longrightarrow 0$, the projection $\tau \longrightarrow \tau$. Thus, in order to converge on the optimal projection solution, we begin with κ large, and progressively reduce it with each converged solution of the full design equations. The "augmented rank projection" iterative algorithm takes the following form:

(1) Begin algorithm with $\kappa = 1$. Notice that this value results in $\bar{\tau}$ being the identity matrix. The resulting solution to the design equations defaults to LQG. Thus we initiate the algorithm with the LQG P and Q matrices.

(2) Decrement κ and using the previous solution for P, Q, $\hat{P}$ and $\hat{Q}$ as initial iterates, converge on a new solution for these matrices.

(3) If κ is in the vicinity of zero, then $\tau \approx \bar{\tau}$. Stop the algorithm and form the approximately optimal compensator design from P, Q, $\hat{P}$, $\hat{Q}$ and τ.

(4) If $\kappa > 0$, return to step 2.

While this method requires many successive designs, many fewer iterations are required than with the previously discussed method. Rather than converge on a n_c order compensator by finding higher order designs, we converge by forcing $\bar{\tau}$ to τ. The full rank projection τ eases the solution of the P and Q Riccati equations, and convergence to a solution for a given κ occurs quite rapidly. Consequently, the *total* number of iterations for a particular low order compensator design is reduced. Thus, the new iterative algorithm has both reduced the computational burden and eliminated numerical difficulties, aiding convergence on a solution.

6.1.2.2 An Ordered Design Procedure

The previous discussion separately addressed the methods of optimal projection and maximum entropy design. This apparent disregard of the unified nature of the design approach is intentional. The most computationally efficient manner in which to design a robustified reduced-order compensator consists of specific steps. Initially, the cost function J is chosen to give adequate performance with the nominal plant. This procedure involves the selection of the appropriate R_1, R_2, V_1, and V_2 matrices. Notice here that V_1 and V_2, the process and measurement noise spectral density matrices, are chosen. The initial motivation for the inclusion of these matrices was for the design of a Kalman-Bucy filter. In that application, the resulting state-estimator was optimal with respect to state-estimate deviations in the presence of these noises. However, due to the steady-state nature of this evaluation, the resulting filter can have terrible transient properties. Because of this poor performance, the noise characteristics have been interpreted in a different manner. The main intent of V_1 and V_2 is to fix the relative weighting between sensor inputs and the internal system model when estimating the states. Higher sensor noises would induce more reliance upon the system model, and vice-versa. Thus the initial LQG design involves determination of the state weightings, the control weightings, and the noise intensities.

The second step in robustified reduced-order compensator design is the maximum entropy method. The appropriate A_i, B_i, and C_i are found which give sufficient robustness characteristics to the resulting compensator. In this instance, ME design equations are used, where $n_c = n$. In order to ease convergence to the proper solution, the LQG design is used to initiate the algorithm.

After the maximum entropy designs have been generated for the system, the compensator gains have usually been reduced somewhat. Consequently, the task of reducing the order of the system is eased [27]. Using the previous ME design to initiate the algorithm, the full OP/ME reduced order design is found using the full design equations. Notice, of course, that if solely a reduced-order compensator were desired (i.e. no additional robustness characteristics), the optimal projection design would proceed directly from the LQG solution.

6.2 Verification of CAD Software

In order to examine the capabilities of the design software package developed for this report, two examples were selected from the literature. The first example was chosen to verify the operation of the maximum entropy algorithm. Thus full order robustified compensators are generated. The second example forms a direct comparison between optimal projection and parameter optimization techniques for reduced order compensator design. The use of these examples aided in debugging the software and

gaining insight into the efficient use of the OP/ME iterative algorithm.

6.2.1 The Maximum Entropy Algorithm

Classical control design methods based their claims of system robustness in terms of gain and phase margins. Consequently, when the transition was made to state-space, modern control design approaches, attempts were made to translate these stability margins into the modern multivariable context. Safonov and Athans showed that LQ regulators maintained the familiar guarantee of 60 deg of phase and 6 dB of gain margin [29]. However, when the loop is closed with a Kalman-Bucy filter rather than the actual states, these guarantees no longer hold. In fact, Doyle showed in [22] that these margins are made arbitrarily small by one's selection of the cost functional and noise intensity matrices. Bernstein and Greeley used Doyle's example to illustrate the ability of the maximum entropy method to restore stability margins [8]. This section will verify the capabilities of this ME implementation by reproducing the results of Bernstein and Greeley's paper.

6.2.1.1 Doyle's Example

Doyle posed the following single-input single-output linear quadratic gaussian control problem: *

$$\begin{bmatrix} \dot{x}_1 \\ \dot{x}_2 \end{bmatrix} = \begin{bmatrix} 1 & 1 \\ 0 & 1 \end{bmatrix} \begin{bmatrix} x_1 \\ x_2 \end{bmatrix} + \begin{bmatrix} 0 \\ 1+\Delta b \end{bmatrix} u + \begin{bmatrix} 1 \\ 1 \end{bmatrix} w \qquad (6-3)$$

$$y = \begin{bmatrix} 1 & 0 \end{bmatrix} \begin{bmatrix} x_1 \\ x_2 \end{bmatrix} + v \qquad (6-4)$$

and the weighting and noise matrices take the following form:

$$R_1 = \theta \begin{bmatrix} 1 & 1 \\ 1 & 1 \end{bmatrix} \ , \ R_2 = 1 \qquad (6-5)$$

$$V_1 = \mu \begin{bmatrix} 1 & 1 \\ 1 & 1 \end{bmatrix} \ , \ V_2 = 1 \qquad (6-6)$$

For this example, Doyle showed that the gain margin is made arbitrarily small by the choice of parameters θ and μ. For sufficiently large values of θ and μ, the closed-loop system becomes extremely sensitive to variations in the B matrix. When Δb above deviates from its nominal value of zero, the closed-loop system becomes unstable. For example, if we choose $\theta = \mu = 60$, the system is stable only when $0.93 \leq 1+\Delta b \leq 1.01$.

*Some of Doyle's notation has been altered to avoid conflicts with previous definitions.

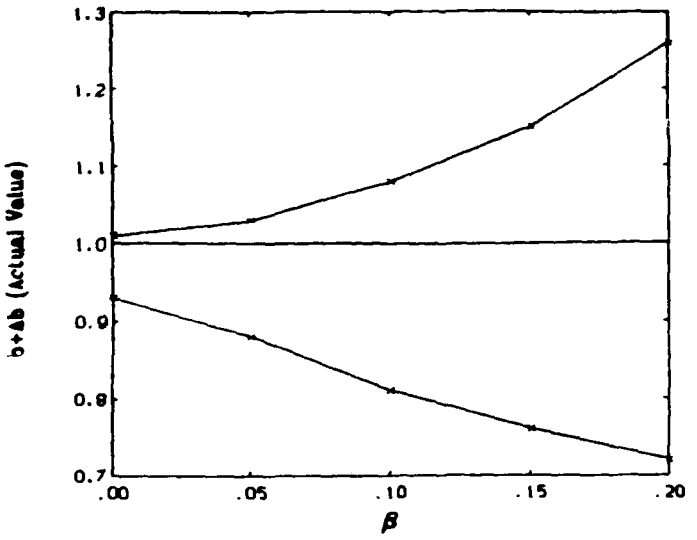

Figure 6-2. Stability bounds for maximum entropy designs.

In order to introduce robustness into the compensator design, we choose our parameter uncertainty distribution matrices as follows:

$$A_1 = \begin{bmatrix} 0 & 0 \\ 0 & 0 \end{bmatrix} \ , \ B_1 = \begin{bmatrix} 0 \\ \beta \end{bmatrix} \ , \ C_1 = \begin{bmatrix} 0 & 0 \end{bmatrix} \qquad (6-7)$$

where β is the maximum entropy design parameter which is varied to effect the performance/robustness tradeoff. Using the above definitions, five maximum entropy design were performed on Doyle's example, with β being varied from $0 \rightarrow 0.2$ in 0.05 increments. Thus the $\beta = 0$ is the default LQG design, while $\beta = 0.2$ will produce a substantially robustified compensator. These five compensators are shown in Table 6-1.

The improvements in robustness are significant using this approach, as can be seen in the rightmost column of Table 6-1. With each increase in the uncertainty magnitude parameter β, the range of tolerable perturbations increases. This improvement in stability bounds is illustrated in Figure 6-2. However, there is a price for this improved robustness characteristic— the performance decreases. The performance/robustness tradeoff is clearly illustrated in Figure 6-3 Notice that the cost function value evaluated on the nominal plant increases monotonically with increasing β. Nevertheless, the robustified compensators trade off these slight losses in nominal performance for large improvements in robustness. These results correspond to those presented in [8], thus the capabilities of the design software have been verified. Additionally, the basic premise of the maximum entropy method has been shown to be correct— the ability to directly effect the performance/robustness tradeoff to meet design requirements.

Table 6-1. Maximum entropy compensators for Doyle's example.

β	Compensator Gains A_c	F	K	Stable Range of $1 + \Delta b$
0 (LQG)	$\begin{bmatrix} -9 & 1 \\ -20 & -9 \end{bmatrix}$	$\begin{bmatrix} 10 \\ 10 \end{bmatrix}$	$\begin{bmatrix} 10 & 10 \end{bmatrix}$	$(0.93 \rightarrow 1.01)$
.05	$\begin{bmatrix} -9.255 & 1 \\ -20.69 & -7.356 \end{bmatrix}$	$\begin{bmatrix} 10.26 \\ 12.33 \end{bmatrix}$	$\begin{bmatrix} 8.356 & 8.356 \end{bmatrix}$	$(0.88 \rightarrow 1.03)$
.10	$\begin{bmatrix} -9.662 & 1 \\ -23.36 & -6.178 \end{bmatrix}$	$\begin{bmatrix} 10.66 \\ 16.18 \end{bmatrix}$	$\begin{bmatrix} 7.178 & 7.178 \end{bmatrix}$	$(0.81 \rightarrow 1.08)$
.15	$\begin{bmatrix} -10.18 & 1 \\ -27.73 & -5.368 \end{bmatrix}$	$\begin{bmatrix} 11.18 \\ 21.37 \end{bmatrix}$	$\begin{bmatrix} 6.368 & 6.368 \end{bmatrix}$	$(0.76 \rightarrow 1.15)$
.20	$\begin{bmatrix} -10.89 & 1 \\ -34.51 & -4.741 \end{bmatrix}$	$\begin{bmatrix} 11.89 \\ 28.77 \end{bmatrix}$	$\begin{bmatrix} 5.741 & 5.741 \end{bmatrix}$	$(0.72 \rightarrow 1.26)$

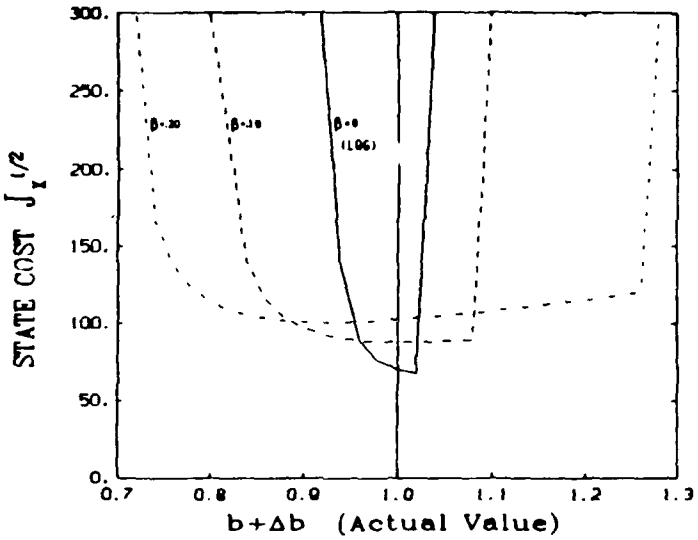

Figure 6-3. The performance/robustness tradeoff for Doyle's example.

This example of ME design also illustrates a major failing of the methodology. The design parameter β was incremented to generate increasingly robust compensators. However, there is no prior knowledge as to what improvements in robustness will be gained for any particular value of β, or in the more general case, A_i, B_i, and C_i. In any application of this methodology, the robustness will have to be evaluated after the design is created, as was shown for Doyle's problem above. While this *a posteriori* evaluation is definitely a drawback, the ease with which the robustness characteristics are altered minimizes the negative effects. Because the ME design step takes place before compensator reduction, the design equations converge more easily to a solution. Consequently, the need to iterate towards an appropriate uncertainty magnitude does not impact too severely upon the design process.

6.2.2 The Optimal Projection Algorithm

The most commonly used direct methods for reduced-order compensator design are parameter optimization techniques. The gradients of the cost-function are evaluated with respect to the compensator gains. These gains are then chosen to reduce the cost-function. Subsequently, the gradient is determined once again, and the gains readjusted. In this manner, the gradient is driven towards zero, while the cost-function converges upon a minimum. Some gradient search techniques converge quadratically to the minimum, while the optimal projection method will only converge linearly [11] until close to the minimum. However, the gradient search techniques often cannot find the global minimum, an issue which motivated the development of the optimal projection

method. OP designs may take longer to converge to a minimum, but Hyland and Bernstein claim that the global minimum will always be found— a guarantee that is not possible with the parameter optimization. Nevertheless, the validity of this claim is somewhat uncertain as will be demonstrated in the examples of OP design that follow.

Several computer programs have been written to perform the gradient search technique. An often-used routine at Stanford is known as "SANDY", developed by U.-L. Ly. Apparently, this code took several years to write and verify [30], a significant contrast with the easily implemented optimal projection method. Nevertheless, this parameter optimization method can be quite effective. Therefore, this design software can serve as a good reference point for evaluating the order-reduction capabilities of the optimal projection method.

6.2.2.1 Ly, Bryson, and Cannon's Example

Ly, Bryson, and Cannon examined the design of reduced order compensators for an aircraft glidepath control problem [20]. The relevant system dynamics and weighting matrices are as follows: *

$$A = \begin{bmatrix} -.045 & .036 & 0 & -.322 & 0 & .045 & -.036 \\ -.37 & -2.02 & 1.76 & 0 & 0 & .37 & 2.02 \\ .191 & -3.96 & -2.98 & 0 & 0 & -.191 & 3.96 \\ 0 & 0 & 1 & 0 & 0 & 0 & 0 \\ 0 & -1 & 0 & 1.76 & 0 & 0 & 0 \\ 0 & 0 & 1 & 0 & 0 & -.482 & 0 \\ 0 & 0 & 1 & 0 & 0 & 0 & -1.057 \end{bmatrix} \qquad (6-8)$$

$$B = \begin{bmatrix} 0 & 1 \\ -.282 & 0 \\ -11 & 0 \\ 0 & 0 \\ 0 & 0 \\ 0 & 0 \\ 0 & 0 \end{bmatrix}, \quad C = \begin{bmatrix} 1 & 0 & 0 & 0 & 0 & -1 & 0 \\ 0 & 0 & 0 & 1 & 0 & 0 & 0 \\ 0 & 0 & 0 & 0 & 1 & 0 & 0 \end{bmatrix} \qquad (6-9)$$

*The notation has been changed from [20] to be consistent with that used elsewhere in this report.

$$R_1 = \begin{bmatrix} 1 & 0 & 0 & 0 & 0 & -1 & 0 \\ 0 & 0 & 0 & 0 & 0 & 0 & 0 \\ 0 & 0 & 0 & 0 & 0 & 0 & 0 \\ 0 & 0 & 0 & 0 & 0 & 0 & 0 \\ 0 & 0 & 0 & 0 & .0625 & 0 & 0 \\ -1 & 0 & 0 & 0 & 0 & 1 & 0 \\ 0 & 0 & 0 & 0 & 0 & 0 & 0 \end{bmatrix}, \quad R_2 = \begin{bmatrix} 1 & 0 \\ 0 & 9 \end{bmatrix} \qquad (6-10)$$

$$V_1 = \begin{bmatrix} 0 & 0 & 0 & 0 & 0 & 0 & 0 \\ 0 & 0 & 0 & 0 & 0 & 0 & 0 \\ 0 & 0 & 0 & 0 & 0 & 0 & 0 \\ 0 & 0 & 0 & 0 & 0 & 0 & 0 \\ 0 & 0 & 0 & 0 & 0 & 0 & 0 \\ 0 & 0 & 0 & 0 & 0 & 5.0995 & 0 \\ 0 & 0 & 0 & 0 & 0 & 0 & 11.1825 \end{bmatrix}, \quad V_2 = \begin{bmatrix} .4 & 0 & 0 \\ 0 & .4 & 0 \\ 0 & 0 & 10 \end{bmatrix} \qquad (6-11)$$

Using these design parameters, reduced-order compensators were designed by Ly using parameter optimization techniques. For comparison, the optimal projection algorithm was used to generate compensators of equivalent orders. Evaluation of the effectiveness of the OP method was based upon the resulting cost function, and the RMS values of particular system states. The optimal projection compensators designed for this example can be found in Appendix B. The performance characteristics for the parameter optimization compensators are shown in Table 6-2 and those of the OP compensators can be seen in Table 6-3.

Notice that in either case there is very little degradation in performance when the compensator order is reduced. Virtually no performance is lost when the compensator is reduced to fourth order, while even lower order compensators show only a small increase in the cost function. Both of the compensator design methods seem to converge upon the same minimum of the cost function, as is clearly illustrated in Figure 6.2.2.1. Note, however, that the parameter optimization method has consistently lower values for J. This result is a consequence of the computer resources ($'s) available for this report. The optimal projection method is obviously converging to the same minimum of the cost-function. However, in order to achieve the small final reduction in J, many more iterations would be required. Suffice to say that each iteration was bringing the optimal projection cost functions closer to those presented in Ly, Bryson, and Cannon's paper. Ideally, the iterations will reduce J to values equivalent to those generated by parameter optimization. The general nature of parameter optimization techniques is such that these results probably required substantial computing time. The important conclusion to be drawn from this OP example is that in relatively few iterations, J was brought within a very close range of the supposed optimal value.

Table 6-2. Ly, Bryson, & Cannon Compensators

Order	RMS Values				Cost Function
n_c	$u - u_w$	d	δ_e	δ_t	J
7	2.024	3.453	.3668	.2741	5.652
4	2.023	3.455	.3663	.2749	5.653
3	2.087	3.540	.3480	.2677	5.904
2	2.182	3.708	.2727	.2496	6.255
1	2.301	5.269	.2488	.2930	7.862

Table 6-3. Optimal Projection Compensators

Order	RMS Values				Cost Function
n_c	$u - u_w$	d	δ_e	δ_t	J
7	2.023	3.452	.3670	.2746	5.652
4	2.023	3.453	.3666	.2747	5.653
3	2.334	2.630	.3711	.3673	5.976
2	2.171	3.738	.2971	.2624	6.275
1	2.924	2.444	.4776	.3543	8.841

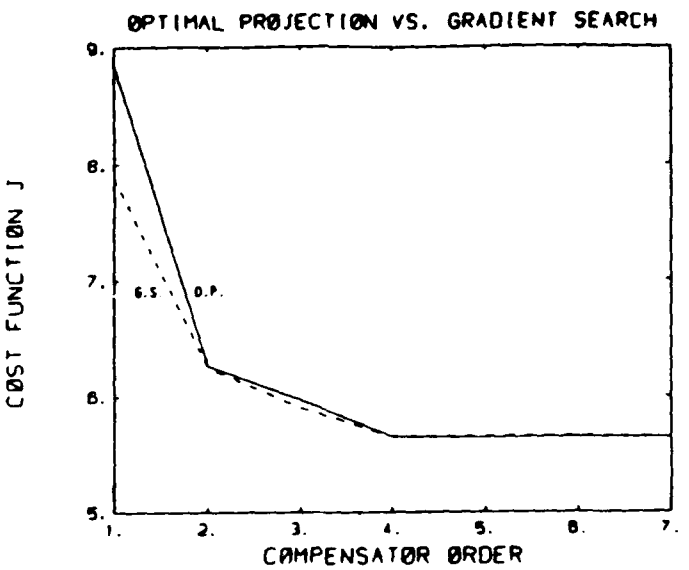

Figure 6-4. Cost function vs. compensator order.

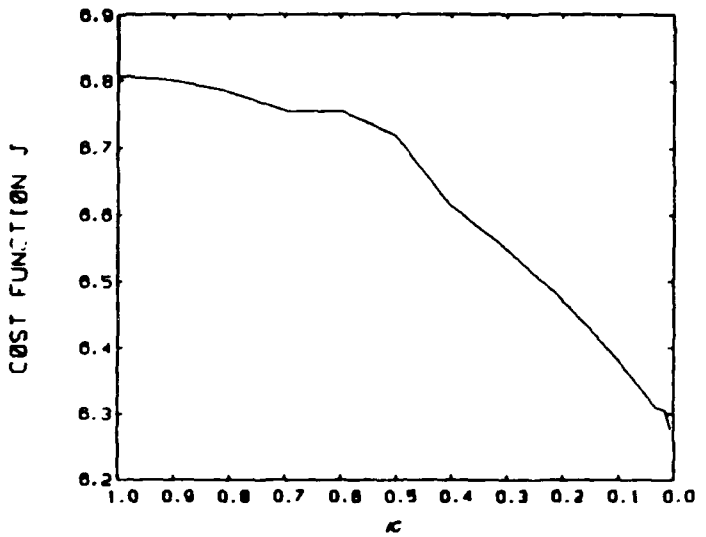

Figure 6-5. Convergence to the optimal projection.

This example also serves to demonstrate the effects of the "augmented rank projection" approach described in Section 6.1.2.1. This aid to convergence was used for the designs of order less than 4. Iterations through the design equations with lower and lower weights on the undesired eigen-projections forced convergence to the optimal projection. The associated reduction in the cost function J with decreasing weighting value κ is clearly shown in Figure 6-5 for the second order compensator design. Notice that as the optimal projection is approached (i.e. $\kappa \rightarrow 0$), the cost function decreases at faster and faster rate. This is consistent with the claims made about convergence rate in Section 6.2.2 above. However, as $\kappa \rightarrow 0$, the equations take many more iterations to converge upon a solution. Thus, finding the "exact" optimum becomes a tedious task.

In summation, the optimal projection methodology, as implemented for this report, has shown itself to be an efficient method for compensator order reduction. There are, however, numerical issues pertaining to extreme order reduction which should be addressed to ease the task of OP design.

Section 7

Modelling Considerations for the AFAL Experimental Structure

Whenever a distributed parameter system is reduced to a finite order model, some tradeoffs are being made. Ideally, one would like to include the infinite spectrum of modes in the design process, thus eliminating the potential for spillover destabilization. However, the practical requirements of the design process make this approach impossible. Reduction of the model to a finite order is required. Usually, this order is sufficiently large such that the dominant system dynamics are included; consequently, spillover is negligible. The optimal projection method is used to reduce the order of the compensator still further, to dimensions well below that of the plant model, while preventing the occurrence of high order mode spillover during closed loop control. Thus the selection of the plant dimension to be used during design is dependent upon the computing accuracy and capabilities available and is not restricted to the desired compensator order.

7.1 The AFAL Structure

As described in Section 1.2, the AFAL structure consists of four beams, cantilevered radially from a central hub. Two of the beams, the *primary arms*, have both thrusters and proof-mass actuators mounted at their tips. The two *secondary arms* have only the proof-mass actuators. Additionally, all of the arms have tip-mounted accelerometers, with a hub angle encoder providing rotation measurements.

Modelling software was previously developed for the AFAL structure in [1]. The modeshapes are based upon an assumed modes model whose parameters were determined by NASTRAN modelling and identification. The first 9 vibrational modes are shown in Figure 7-1, with their associated vibrational frequencies listed in Table 7-1. The damping associated with these modes was assumed to be $\zeta = 0.01$, the value proposed and identified in [1].

In order to control the fine-pointing of the hub, the actuators act in coordinated pairs;

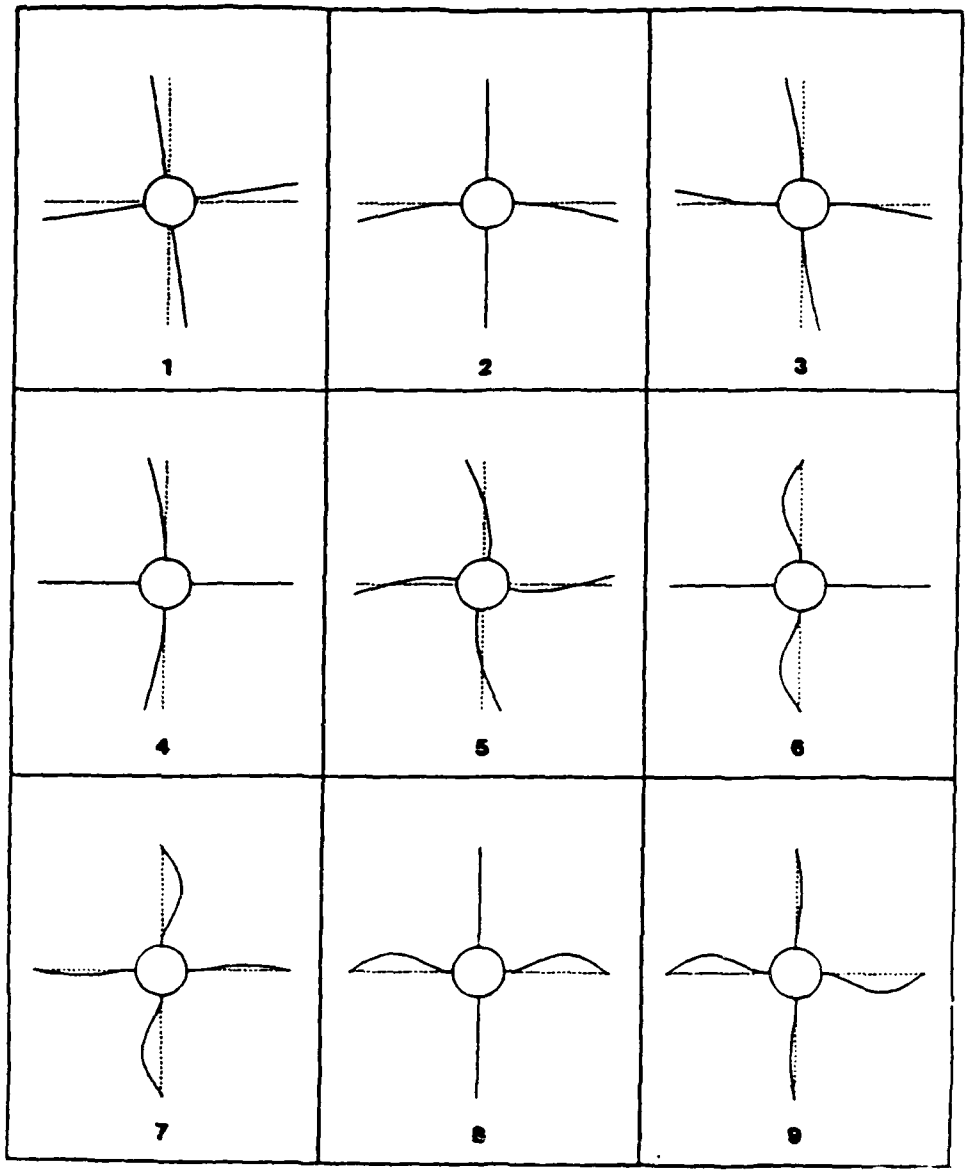

Figure 7-1. Finite element model mode shapes.

Table 7-1. Vibrational mode frequencies.

Mode #	Frequency (Hz)	Description
1	0.0	rigid body rotation
2	0.588	1^{st} bending, primary arms, symmetric
3	0.648	1^{st} bending, all arms, anti-symmetric
4	0.710	1^{st} bending, secondary arms, symmetric
5	1.110	1^{st} bending, all arms, anti-symmetric
6	8.190	2^{nd} bending, secondary arms, symmetric
7	8.244	2^{nd} bending, all arms, anti-symmetric
8	8.444	2^{nd} bending, primary arms, symmetric
9	8.544	2^{nd} bending, all arms, anti-symmetric

thus, only the anti-symmetric flex modes are excited by the control forces. Consequently, the symmetric flex modes need not be included in the model.

7.1.1 Selection of Structural Modes

In choosing the modes to be included in a plant model, consideration is often given to the controllability and observability of each mode. Modes that cannot be properly effected upon or sensed are then excluded from the model, assuming that these modes are stable. This procedure for model reduction was best illustrated by Moore in [3] where he refers to the method as "Principal Component Analysis". For a linear time-invariant system, a necessary and sufficient condition for controllability is that the solution to the following integral be nonsingular:

$$W_c(t) = \int_0^t \left\{ e^{At} B B^T e^{A^T t} \right\} dt \qquad (7-1)$$

This matrix W_c is commonly referred to as the controllability grammian. Similarly, the system is observable if the observability grammian W_o is nonsingular, where:

$$W_o(t) = \int_0^t \left\{ e^{A^T t} C^T C e^{At} \right\} dt \qquad (7-2)$$

If the eigenvalues of A are all left-half-plane and t is allowed to go to infinity, then these two grammians satisfy the following Lyapunov equations [31]:

$$AW_c + W_c A^T + BB^T = 0 \qquad (7-3)$$

$$A^T W_o + W_o A + C^T C = 0 \qquad (7-4)$$

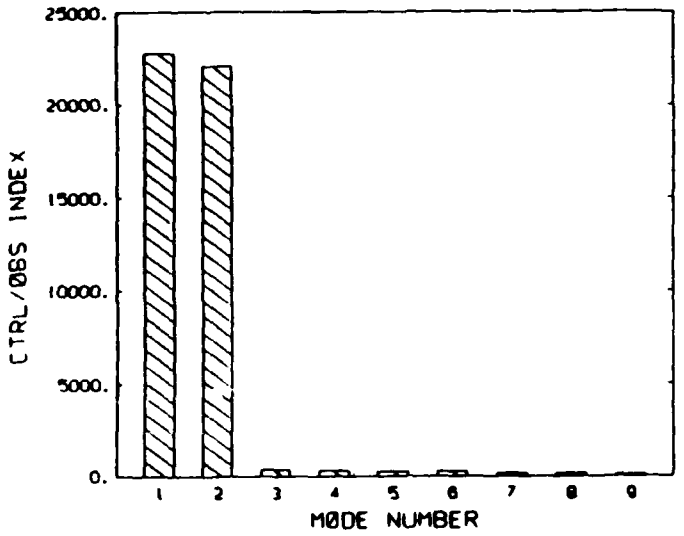

Figure 7-2. Controllability/observability indices for the displacement states.

Notice the requirement on the eigenvalues of A. The existence of a rigid-body mode in the AFAL structure model violates that condition. Additionally, for *vibration control* only, which is the problem addressed in this thesis, the two zero eigenvalues associated with the rigid-body mode remain at zero when the loop is closed. Thus for both this controllability/observability (C/O) analysis, and in future steady-state compensator evaluations, appropriate Lyapunov equation solutions will not be possible. To remedy this situation, an extremely light spring force and damping on the rigid-body mode has been assumed. The time constants of this altered rigid-body mode are on the order of thousands of seconds, thus satisfying our numerical needs while having little effect upon the dynamics of the model.

In Moore's study of principal components [3], he utilized balancing transformations to show the relative controllability and observability of each mode. These transformations result in the controllability and observability grammians being equivalent and diagonal. Thus the diagonal elements of these grammians indicate the utility of retaining any particular mode in the plant model. The C/O indices were calculated for the AFAL experimental structure with actuators and sensors colocated at the beam tips. Figure 7-2 illustrates the C/O indices for the displacement states of the first nine antisymmetric AFAL structural modes. Similarly, those for the velocity states are shown in Figure 7-3. Notice that for this particular structure, the rigid-body and the first flex mode dominate the dynamics of the model, particularly with regard to modal displacements. This characteristic of the AFAL structure is a significant drawback to the use of proof-mass actuators, as their control effectiveness is quite low at the frequencies associated with these first few modes.

In the experimental work of Floyd [1], only the rigid-body and the first two anti-

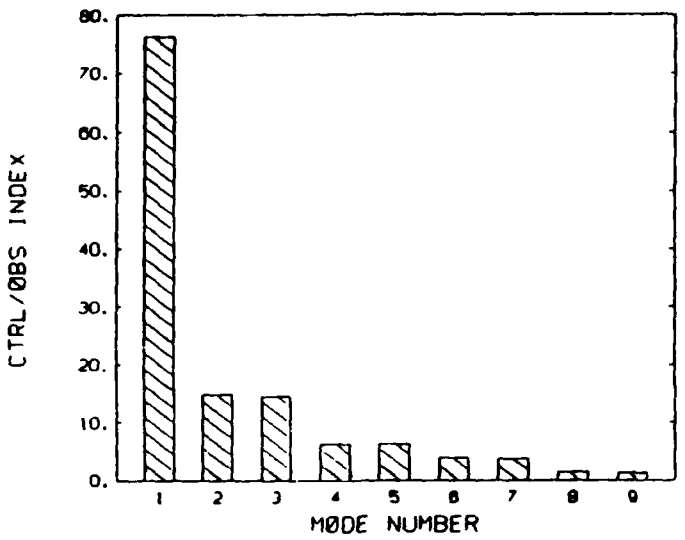

Figure 7-3. Controllability/observability indices for the velocity states.

symmetric flexible modes were included in the model for the purpose of controller design. The result was a 6^{th} order model. As Floyd's methods did not incorporate a capability for reduced order compensator design, his selection of modes was entirely consistent with the C/O indices shown in Figures 7-2 and 7-3. Due to this modal truncation, however, spillover from the high frequency modes into the sensor readings did occur. Nevertheless, Floyd showed that with modifications, a 6^{th} order Kalman filter was sufficient for the estimation task. This characteristic was demonstrated in simulations which incorporated higher order modes. Still, in order to guarantee spillover suppression, and to better demonstrate the capabilities of the optimal projection method, higher order modes have been included in the plant model for this study. The first eight anti-symmetric flex modes were chosen in addition to the rigid body mode. In selecting these modes, consideration was given to both the potential sampling rates of our compensator implementation, and the computational burden of working with a high order model in the design process. The modeshapes and frequencies for these modes can be seen in Appendix C.

7.2 Modelling of Proof-Mass Actuators

Modelling of a proof-mass actuator is a simple task if the PMA is constrained to remain within its linear operating range. We begin by defining the following variables, consistent with Figure 7-4.

x: The modal state vector of the structure.

q: The cantilevered beam tips' deflection.

x_m: The movement of the proof-mass in inertial space.

d: The displacement of the proof-mass, *relative* to its track center. This represents the PMA motion in beam tip fixed coordinates as opposed to inertial space.

u_F: The commanded electromagnetic force applied to the proof-mass.

F: The reaction force acting upon the structure.

m: The mobile mass of the PMA.

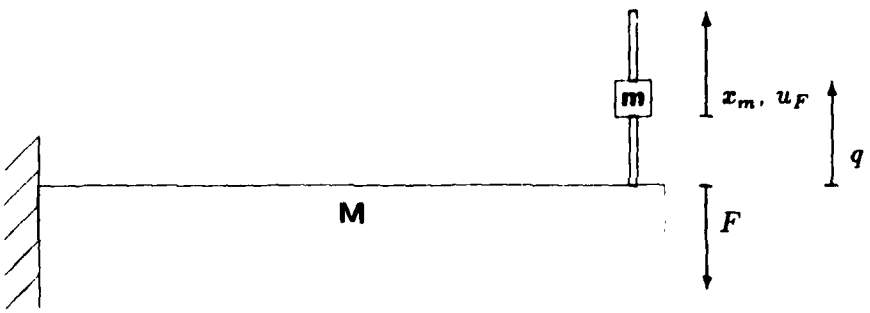

Figure 7-4. Proof-mass actuator variables and coordinates.

The displacement variable is defined by:

$$d = x_m - q \tag{7-5}$$

thus,

$$\ddot{d} = \ddot{x}_m - \ddot{q} \tag{7-6}$$

By neglecting the very fast electrodynamics of the actuator, the acceleration of the proof-mass is given by:

$$\ddot{x}_m = \frac{1}{m} u_F \tag{7-7}$$

In this application of PMAs, we have colocated sensors and actuators. Thus, there exists a row of the C and D matrices which represents the accelerometer located at the same position as the PMA. Denote this accelerometer row as C_a and D_a. If we assume that the reaction force F equals the electromagnetic force u_F (we will soon discard this assumption), we then have a simple expression for the acceleration of the beam tip, $\ddot{q}$:

$$\ddot{q} = C_a x - D_a u_F \tag{7-8}$$

Substituting Equations (7-7) and (7-8) into Equation (7-6), we get:

$$\ddot{d} = -C_a x + \left(\frac{1}{m} + D_a\right) u_F \qquad (7-9)$$

However, if these dynamic equations are added to those of the AFAL structure, the combined system will be neither controllable nor observable, because of the undamped rigid-body modes of the proof-masses. In order to present a well-posed problem, and to better represent the actual characteristics of the PMAs, damping and a return-to-center spring force were postulated, as well as a sensor to measure proof-mass displacement. Equation (7-7) now becomes:

$$\ddot{x}_m = \frac{1}{m} u_F - 2\zeta_m \omega_m \dot{d} - \omega_m^2 d \qquad (7-10)$$

transforming the displacement dynamics to:

$$\ddot{d} = -C_a x + \left(\frac{1}{m} + D_a\right) u_F - 2\zeta_m \omega_m \dot{d} - \omega_m^2 d \qquad (7-11)$$

F is thus no longer equal to u_F, but rather:

$$F = -u_F + 2m\zeta_m \omega_m \dot{d} + m\omega_m^2 d \qquad (7-12)$$

Notice that due to the PMA spring and damping forces, there are now open-loop interactions between the PMAs and the structure, therefore the equations for the structural modal states become:

$$\dot{x} = Ax - B\left(u_F - 2m\zeta_m \omega_m \dot{d} - m\omega_m^2 d\right) \qquad (7-13)$$

If the states d and $\dot{d}$ are made part of an augmented state vector, the two vectors $[B2m\zeta_m\omega_m]$ and $[Bm\omega_m^2]$ enter the system dynamics as columns in the A matrix. The state dynamic equations thus take on the following form:

$$\frac{d}{dt}\begin{bmatrix} x \\ d \\ \dot{d} \end{bmatrix} = \begin{bmatrix} A & Bm\omega_m^2 & B2m\zeta_m\omega_m \\ 0 \cdots 0 & 0 & 1 \\ \cdots -C_a \cdots & -\omega_m^2 & -2\zeta_m\omega_m \end{bmatrix} \begin{bmatrix} x \\ d \\ \dot{d} \end{bmatrix} + \begin{bmatrix} -B \\ 0 \\ \frac{1}{m} + D_a \end{bmatrix} u_F \qquad (7-14)$$

As can be seen from this derivation, there are two additional states added to the system dynamics for each PMA. In the case of the AFAL experimental structure, where the actuators act in coordinated pairs, four states were added, two for each PMA pair. As the previously selected structural model contained eight flex modes plus the rigid body mode, the full dynamics of the system now contain 22 states. The A, B, C, and D

matrices representing these linear system dynamics can be found in Appendix D. A 22^{nd} order dynamic compensator would require substantial computing resources to be effective in real-time control and lower order systems will have to be implemented. Thus the potential utility of the optimal projection method to reduce compensator order will be clearly illustrated.

7.3 Characterization of Potential Model Errors

For the purpose of evaluating the robustness characteristics of a particular compensator design, one must characterize the potential model errors. In this thesis, no consideration is being given to effects of nonlinearities or unmodelled dynamics such as the torsional modes of each beam. Rather, the primary modelling error under study is uncertainty in the plant parameters themselves. In the modelling of flexible structures, errors primarily manifest themselves in the modal frequency and the predicted modeshape.

Having postulated a certain degree of uncertainty in the plant parameters, a set of ten perturbed plants were generated. These altered systems contained perturbations in both modal frequencies and modeshapes. Plant parameters associated with these characteristics were given a Gaussian distribution about their nominal values*. In this manner, the frequency uncertainties were reflected in the A matrix. Additionally, modeshape errors for each mode were added to the rows and columns of the B and C matrices respectively.

This random variable approach is somewhat similar to a Monte Carlo analysis, although a set of ten plants is by no means an exhaustive verification of a particular compensator's robustness. Nevertheless, analysis of the closed-loop performance of a compensator over this set of plants will give some indication of the system's sensitivity to modelling errors. The perturbations found in each of the ten plants are shown in Appendix F. The generation of these altered plants leads to a convenient robustness criterion wherein a compensator is sufficiently robust if it can form stable closed-loop systems with each perturbed plant in the set. These perturbed plants will be used to illustrate robustness characteristics in a later section.

7.4 Selection of an Initial Condition

The motivation for installing the proof-mass actuators on the AFAL structure was to provide vibration damping in the terminal phase of a rapid slewing maneuver. The proposed control strategy consists of a thruster-based slew initiation and termination,

*Selection of the standard deviation for this distribution is discussed in a later section.

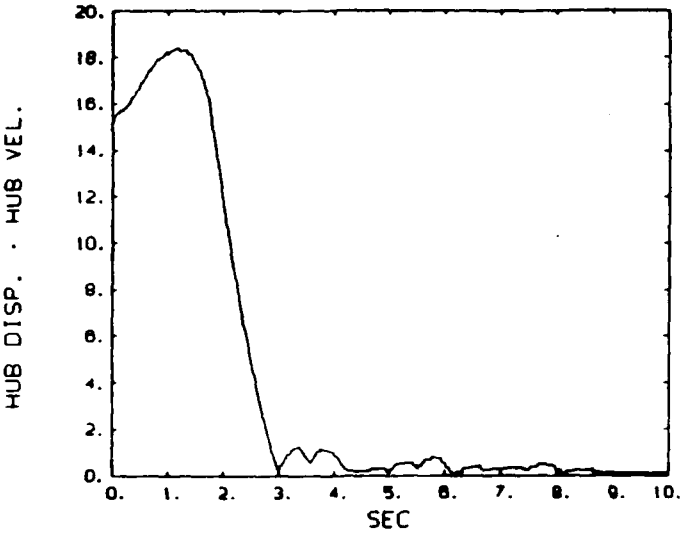

Figure 7-5. Controller switching criterion.

after which the thruster controller is disabled. Subsequently, the control switching logic activates the proof-mass actuator controller for final vibration damping. Thus the primary goal of this design procedure is to find compensators which have excellent transient characteristics.

In order to evaluate the transient response of a given compensator, a state-vector has been chosen from a typical thruster control simulation, the results of which are summarized in Appendix E. This state vector will represent an appropriate moment to switch control authority to the PMA controller, near the end of a slew maneuver. The selection criterion used here was to switch when the summed absolute values of hub velocity and displacement fell within a chosen tolerance. The time history of this quantity is shown in Figure 7-5 for the simulation cited above. As can be seen in the figure, the quantity reaches its first minimum at 2.98 seconds. The state vector corresponding to this moment was chosen as the initial condition for transient evaluations of the PMA-based compensators.

7.5 Open-Loop Response to Initial Conditions

Figures 7-6 through 7-10 show the time responses of the first five flex modes as they affect the displacement of the hub. The true hub angle response is the superposition of these modes plus those that have not been shown (rigid body, and flex modes 6, 7 & 8).

Notice that the dynamics are dominated by the first two flex modes, agreeing with the controllability/observability discussion of Section 7.1.1. The largest hub displace-

ment component is due to the second flex mode. This fact is unfortunate as the tip-mounted actuators are near to a node of that mode and thus have decreased control effectiveness. Additionally, the mode for which a tip-mounted actuator is best suited— the first flex mode— is of such a low frequency that the proof-mass actuators are barely effective. As the potential effectiveness of the vibration damper has thus been limited by the actuator selection and our configuration constraint, any gains in performance over the previously developed thruster-based compensators will be even more significant.

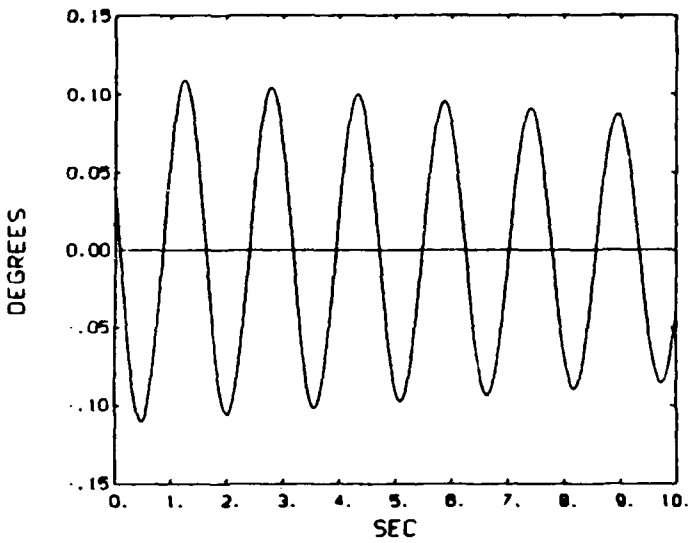

Figure 7-6. First flex mode response to I.C.

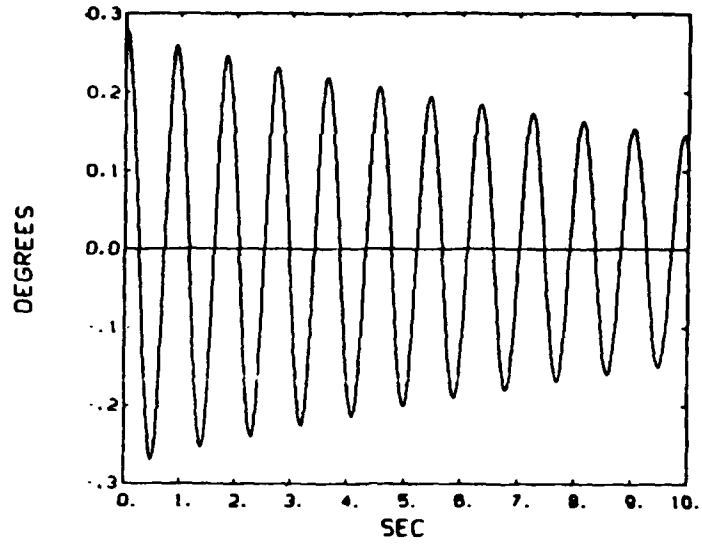

Figure 7-7. Second flex mode response to I.C.

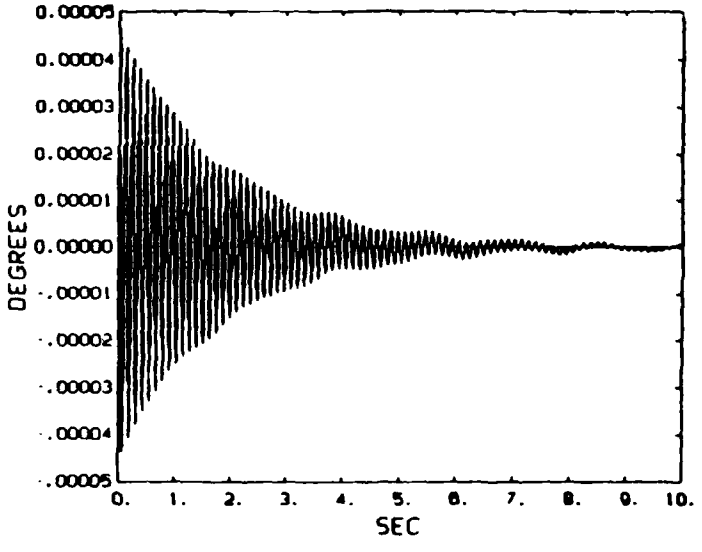

Figure 7-8. Third flex mode response to I.C.

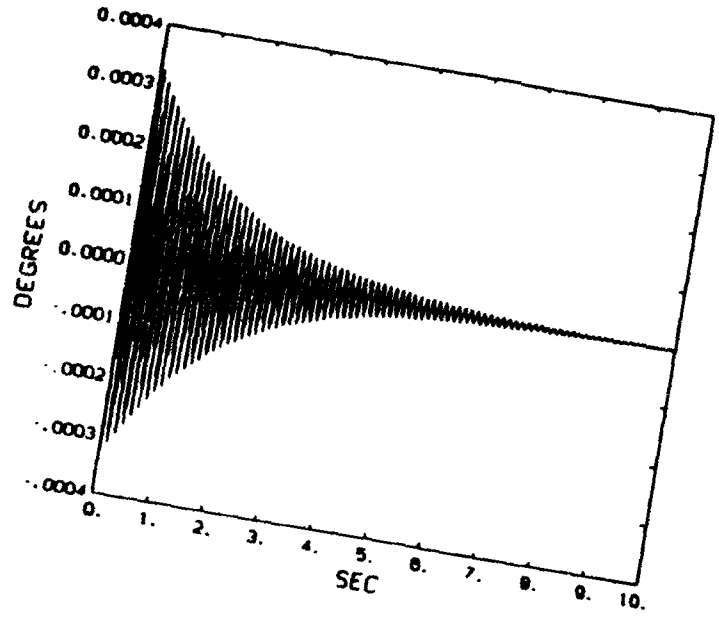

Figure 7-9. Fourth flex mode response to I.C.

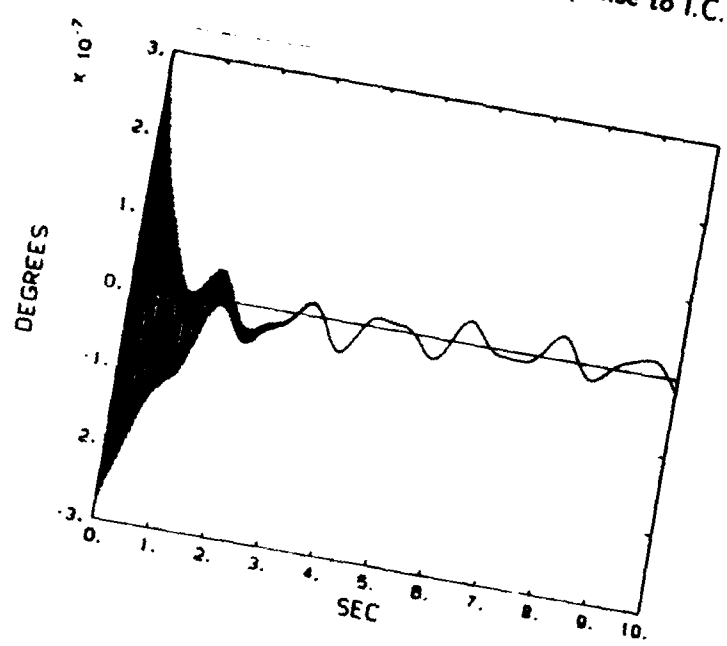

Figure 7-10. Fifth flex mode response to I.C.

Section 8

Application of the OP/ME Design Methodology to the AFAL Experiment

As was discussed in Section 6, the task which must precede any OP/ME design is the development of a full-order, Linear Quadratic Gaussian model-based compensator. From this baseline design, reduced-order and robustified compensators can then be derived.

8.1 Evaluation of Compensator Performance

There has been much discussion in this thesis about effecting the performance/robustness or performance/compensator-order tradeoff. In order to make these comparisons, appropriate evaluation criteria must be established. The primary characteristic used for comparisons in optimal control is the cost function J, a measure of the steady-state regulation performance of the closed-loop system. As minimizing this quantity is the objective of our design algorithm, it forms a convenient measure of a compensator's performance level. For this reason, cost functional analysis will be used for design comparisons. Nevertheless, a goal of this research is to find active vibration dampers which are effective in damping structural modes after a rapid slew maneuver. A steady-state performance measure does not necessarily reflect the compensator's transient capabilities. However, using the initial condition chosen previously, the compensator's ability to remove vibrational energy from the system can be directly measured. With the state-space representation of the structure in modal coordinates, the calculation of vibrational energy becomes a simple task, where

$$E_i(t) = \omega_i^2 x_i^2(t) + \dot{x}_i^2(t) \quad \text{for each mode } i \qquad (8-1)$$

By calculating the time history of total vibrational energy in the system, direct compensator effectiveness comparisons can be made. One particular initial condition cannot form a totally general evaluation of a compensator's transient capabilities. However, we

can get some indication of relative performance. Thus our criteria for compensator evaluation take on two very different forms— evaluation of a steady-state cost functional, and direct simulation of the transient energy dissipation characteristics.

8.2 Generation of an LQG Compensator

The design procedure for an LQG compensator is simple in relation to that of the OP/ME approach. The separation principle remains valid for the full order compensator, and the regulator and observer gains are found separately. However, in the design of a LQG compensator for the AFAL experiment, there is a complication due to the proof-mass actuators. As the proof-mass is constrained to remain within its linear operating range, the design process becomes an iterative procedure. Simulations are used to evaluate whether the displacement constraints have been violated, and the design parameters are appropriately adjusted if necessary. The parameters used to alter the transient characteristics of the compensator are the state weightings (matrix R_1), the control weightings (R_2), the process noise (V_1) and the sensor noise (V_2).

8.2.1 Selection of the Cost Function and Noise Parameters

In the context of control system design for the AFAL experiment, the use of optimal control theories must be somewhat altered. The utility of a cost function which considers solely the steady-state characteristics of the closed loop system is somewhat lacking for this experimental evaluation of transient performance. We are not particularly concerned with the system's response to observation and process noise. Rather, we wish to achieve the best possible response to initial conditions generated by an on-off thruster slew maneuver. Consequently, the tools of optimal control are used simply because they are very convenient, and with proper selection of the design parameters, can deliver the required transient performance.

8.2.1.1 Defining Regulator Gains by Choice of Cost Function

The proof-mass actuators have been added to the AFAL experiment in order to dissipate vibrational energy from the system at a higher rate than was possible with the on-off thrusters. Additionally, we are primarily interested in damping those vibrations which have an effect upon the fine pointing capabilities of the central hub. Thus an appropriate cost function could be based upon the steady-state hub pointing, weighting vibrational modes only as they affect hub motion. This approach was also used by

Martin and Bryson in [32]. The cost function takes the following form:

$$J = \int_0^\infty \left\{ y_h^T y_h + \dot{y}_h^T \dot{y}_h + u^T R_2 u \right\} dt \qquad (8-2)$$

where y_h is the measure of hub angular displacement and $\dot{y}_h$ is the hub's angular velocity. The first component of our sensor output vector is the hub displacement measurement. While we do not have a corresponding measurement of hub velocity for use in the cost function above, we can simply apply the coefficients of the displacement measurement to the modal velocity components of the state vector. Thus we form the following equation for hub displacement and velocity:

$$\begin{bmatrix} y_h \\ \dot{y}_h \end{bmatrix} = \begin{bmatrix} C_h & 0 \\ 0 & C_h \end{bmatrix} \begin{bmatrix} x \\ \dot{x} \end{bmatrix} \qquad (8-3)$$

For simplicity, we refer to the measurement matrix above as C_h and refer to the full state vector as x. Then, the cost function of Equation (8-2) reduces to:

$$J = \int_0^\infty \left\{ x^T C_h^T C_h x + u^T R_2 u \right\} dt \qquad (8-4)$$

Thus by selecting $R_1 = C_h^T C_h$, we have weighted each vibrational mode in direct proportion to its contribution to hub angle displacement and velocity. However, the mode with the greatest contribution to the hub motion is the rigid-body mode, for which we have essentially no control authority with the proof-mass actuators. Consequently, the rows and columns associated with both the rigid-body displacement and velocity are set to zero. The resulting compensator is then a pure vibration damper, with no rigid-body control. Additionally, in order to maintain the proof-masses within their displacement constraints, weightings are placed in the elements of the R_1 matrix corresponding to the PMA displacement states of each actuator pair.

8.2.1.2 Defining Observer Gains by Choice of Noise Parameters

As discussed above, we wish to choose the design parameters which give an appropriate transient response. This change in design philosophy from the original LQG practice allows us some flexibility. No longer is the designer required to establish the system noise characteristics for the design of a Kalman-Bucy filter. Rather, the filter is simply considered model-based, with a reduced emphasis on the system's *optimality*. In this design context, the traditional Riccati equations are still used; however, the noise parameters are now manipulated in order to achieve the desired performance. This approach also forms the basis of the LQG/Loop Transfer Recovery methodology which has recently received much attention, although the respective performance criteria are quite different.

While we have just stated that the true noise parameters are not required for the compensator design, our estimates of these characteristics were used as a starting point. The form of the LQG design equations requires characterization of the process noise and that the sensor noise intensity matrix be nonsingular (i.e. V_2^{-1} exists).

Previous system identification work by Floyd determined the noise characteristics of the AFAL experiment sensors [1]. The addition of PMA displacement sensors to the system required an estimate of their noise properties. An assumption was that the 3-σ value was on the order of 0.1% of full scale. The process noise was assumed to result from a digital to analog quantization error in the control command. The electrodynamic force field of the PMAs would thus fluctuate very slightly, resulting in a very minute excitation of the beams. While this noise parameter was included in the design of the observer, the values were so small that the noise process was not included in simulations of the various compensators. It is important to remember that these noise parameters need not be accurate because they will be altered as part of the design process.

8.2.2 Characteristics of the LQG Compensator

Using the LQG design approach outlined above, an appropriate compensator was designed. The displacement constraint for the PMAs was initially restricted to ± 0.25 inches, characteristic of the proof-mass actuators available for this research. However, this very small stroke length restricted the compensator's effectiveness significantly. The majority of the control force was directed towards maintaining the proof-mass within it's operating range. Only a small component of the commanded force was used for vibration damping. Consequently, an alternative PMA was postulated with four times the original stroke. For the long-stroke actuator, an LQG compensator was generated using the state weightings and noise characteristics listed in Appendix G. These parameters were chosen to utilize the maximum amount of control force on the structure while still remaining within the actuator displacement constraints. The resulting LQG compensator design proved to be significantly more effective in removing vibrational energy from the system than was previously the case. The gain matrices for this long-stroke LQG compensator can be found in Appendix H. A comparison of these two compensators' energy dissipation capabilities is shown in Figure 8-1. The dotted line represents the open-loop dissipation due to damping in the structure. It is obvious that a significant performance improvement occurs when the stroke limit is increased from ± 0.25 inches (solid line) to ± 1.0 inch (dashed line). Thus, to better illustrate the capabilities of both the OP/ME design methodology and of PMAs as active vibration dampers, the long-stroke PMA will be used for the remainder of this study.

There is an additional motivation for increasing the stroke length of the PMA which is a consequence of the goals of this thesis. A primary consideration in the choice of model for this experimental work was the desire to evaluate the OP/ME design method-

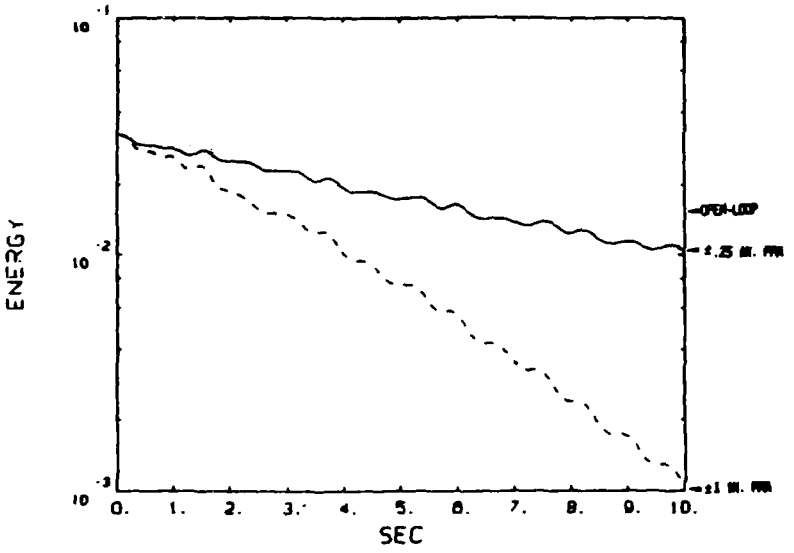

Figure 8-1. Effect of stroke length on PMA effectiveness.

ology. To better exercise the order reduction capabilities of the methodology, a 22^{nd} order plant was selected. Similarly, to better evaluate the robustification capabilities of the maximum entropy method, we wish to have a full order compensator which is somewhat sensitive to parameter errors (i.e. a candidate for robustification). However, the compensator design for the short-stroke PMA was necessarily a very low-gain system and thus extremely robust. Very little performance degradation occurred over any reasonable variation in system parameters. Rather than postulate some unlikely level of uncertainty in the model, the gains, and thus sensitivity of the system, were increased by postulating the alternative actuator.

8.2.3 Evaluation of LQG Compensator Robustness

As discussed previously, the robustness characteristics of a compensator will be evaluated by closing the loop about a set of perturbed plants. As the state-space system has been formed in modal coordinates, it is quite simple to introduce uncertainty into specific plant parameters. For this evaluation, it was postulated that there were uncorrelated $33\frac{1}{3}\%$ (2-σ) uncertainties on the modal frequencies and mode shape parameters. It is interesting to note that for the short-stroke actuator system, these uncertainties would have had little noticeable effect. However, for the long-stroke system, around which all further discussion will center, these were significant perturbations. Figure 8-2 shows the cost function evaluated for each of the perturbed plants, with the value for the nominal plant represented by the horizontal line. Of particular importance is the fact that the closed loop systems are unstable for plants 1, 7, and 10. Notice that per-

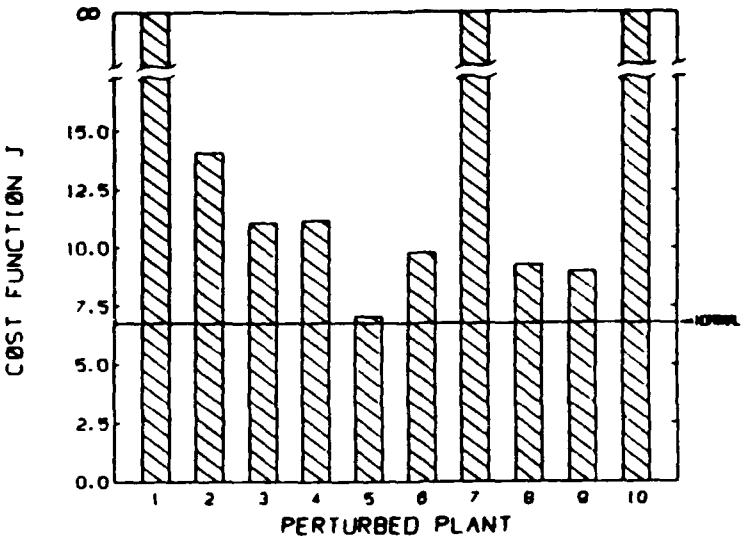

Figure 8-2. LQG compensator: cost functions over set of perturbed plants.

formance, as measured by the cost function, has been severely degraded in every case. The extent of the performance loss is clearly seen in Figure 8-3, where the percentage degradation from the nominal system is shown.

The effects of these uncertainties upon the closed loop system has been illustrated solely in terms of cost functional evaluation. Of equal importance are the transient characteristics of the LQG compensator on the ten perturbed plants. Energy dissipation trajectories for the ten plants are illustrated by the dotted lines of Figure 8-4. As a reference, the time histories for the nominal plant (solid line) and for the open-loop response (dashed line) are also shown. Notice that the unstable closed-loop systems are clearly driving the structure, causing the total vibrational energy to increase with time. This figure also gives the first indication that the cost function alone can not adequately represent the desired performance characteristics. Figures 8-2 and 8-3 show the cost function to be worse for all perturbed plants, as compared to evaluation on the nominal plant. However, the transient performance of one of the perturbed plants is in fact better than that of the nominal plant, confirming that the cost function alone cannot characterize each compensator and simulations will be required for final performance assessment.

If the expected uncertainties are truly of this nature and magnitude, then the LQG compensator is obviously unsuited to the task. Additionally, the LQG design may be of too high an order to be effectively implemented. However, this design can now serve as a reference point for subsequent robustified and reduced order compensators generated using the OP/ME methodology.

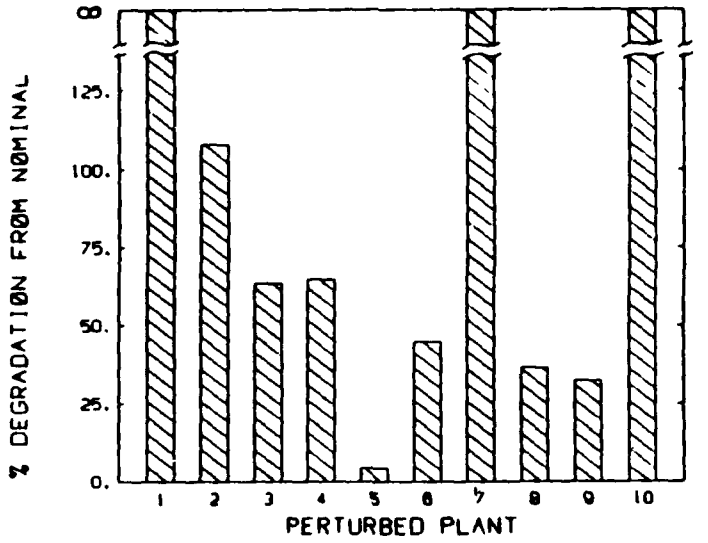

Figure 8-3. LQG compensator: performance degradation over set of perturbed plants

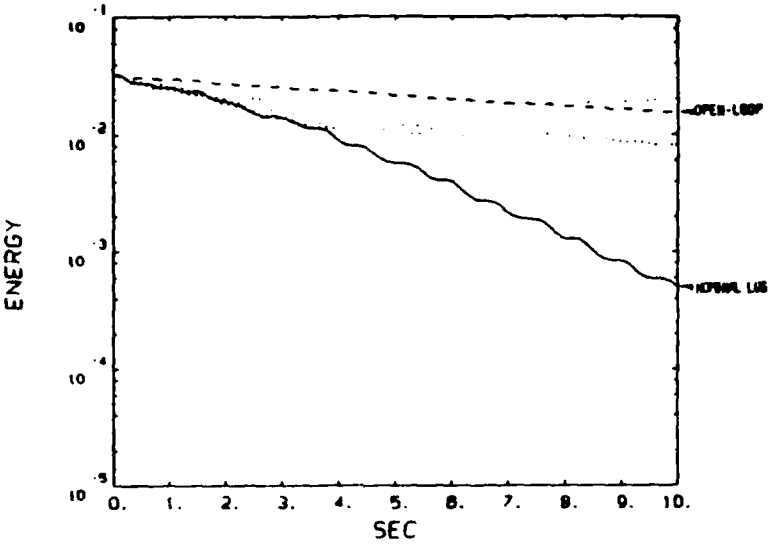

Figure 8-4. LQG compensator: vibrational energy trajectories for set of perturbed plants.

8.3 Reduced Order Compensator Design

Having defined the appropriate cost function and noise properties during the LQG design process, reduced order compensators were developed using the optimal projection methodology. For the 22^{nd} order plant, the OP/ME design equations converged upon solutions for compensators of order n_c = 18, 14, 10, 8, 6 and 4.

In all cases, cost component ranking was used to select the proper eigenprojections. For comparison, some test designs were generated using eigenvalue ranking. These projection selection methods were described in Section 5.2.3.4. When the order reduction was less significant (i.e. n_c = 18 & 14), eigenvalue ranking selected essentially the same eigenprojections as the cost component approach. However, as the desired compensator order decreased, the effects of the two selection methods diverged. Using cost component ranking, the design equations converged to a solution faster and the resulting compensators had lower cost functions than those found with eigenvalue ranking. In fact, for very low order compensators (n_c = 6 & 4), the eigenvalue ranking regularly generated projections with which the design equations would not converge, a situation that did not occur with cost component ranking.

In addition to the need for cost component ranking, a specific difficulty arose in the design of the 4^{th} and 6^{th} order compensators. While the proper choice of eigenprojections served to speed up convergence, the large magnitude of the Riccati equations' $\tau_\perp$ terms slowed the process significantly. This common situation motivated development of the augmented rank projection method as described in Section 6. With a careful progressive reduction in the weighting (κ) on unchosen eigenprojections, the low order designs were generated.

Consequently, by using the optimal projection methodology we created a full range of compensators, illustrating the tradeoff to be made between compensator performance and order. Figure 8-5 shows the cost function evaluated for each of the different compensators. Notice that there is barely any degradation in performance from the full order LQG design down through to the 8^{th} order compensator. Only the 4^{th} and 6^{th} order compensators show evidence of performance loss, perhaps consistent with the difficulty with which the design equations converged. It is also important to realize that there is a monotonic increase in the cost function with decreasing compensator order. This characteristic agrees with the results of Section 6.2.2 and with claims made by Hyland and Bernstein regarding the ability to directly effect the compensator order/performance tradeoff [6].

Once again the performance measure must be qualified— the optimal projection algorithm optimizes only with regard to the cost function, and these design results reflect that fact. The discrepancy between steady-state performance and transient performance is once again illustrated in Figure 8-6. For the 18^{th}, 14^{th}, and 10^{th} order compensators, there is little noticeable degradation in transient performance. However,

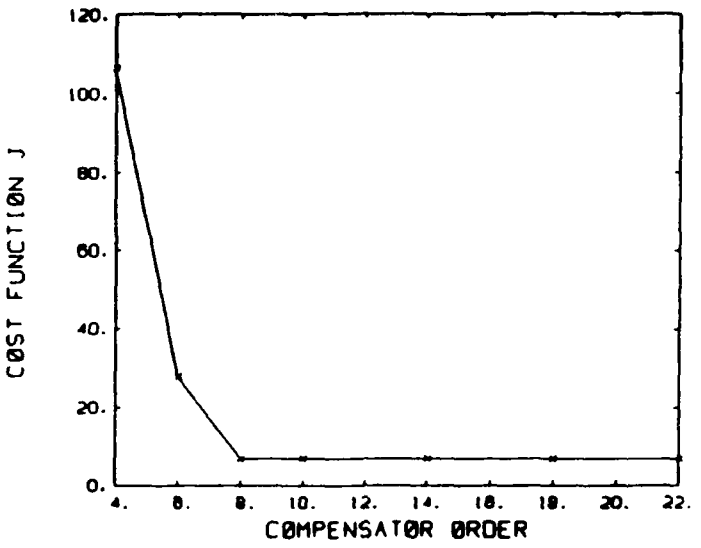

Figure 8-5. Compensator order/performance tradeoff.

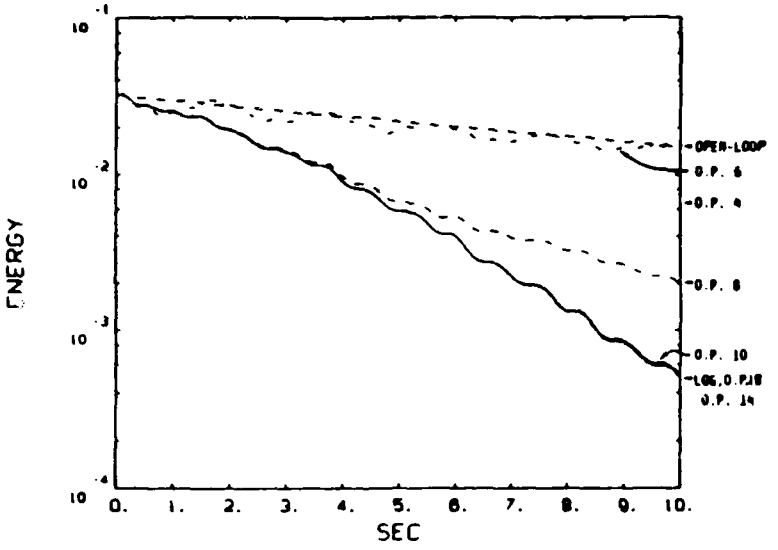

Figure 8-6. Vibrational energy trajectories for reduced order compensators.

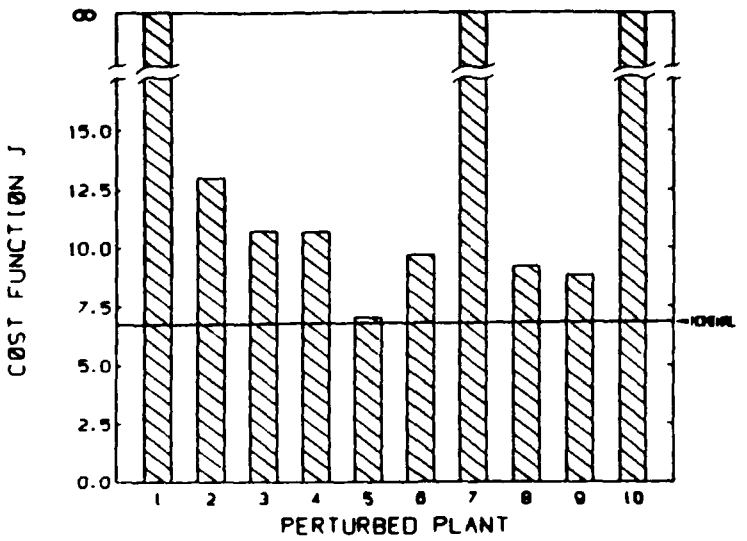

Figure 8-7. 10^{th} order compensator: cost functions over set of perturbed plants.

the 8^{th} order design shows the first signs of a reduced energy dissipation capability, this despite only a minimal increase in cost function. The inadequacy of the cost function for predicting transient response is best shown by the 4^{th} and 6^{th} order systems. Notice that despite the former's significantly higher cost function, the compensator has much better transient performance than is achieved with the 6^{th} order system.

The 10^{th} order compensator represents the highest order reduction before performance, both steady-state and transient, begins to degrade. Additionally, this compensator is of an implementable size, given the computing resources of the AFAL experimental facility. Considering these characteristics, the 10^{th} order system was chosen as the baseline reduced order system. The robustness of the compensator was evaluated for comparison with the LQG design and the results are illustrated in Figures 8-7 and 8-8. In comparing these results with those of the LQG design shown in Figures 8-2 and 8-3, it is apparent that the process of order reduction has robustified the compensator somewhat. The three unstable closed-loop plants remain unstable. However, those with a finite cost function exhibit less performance degradation when the 10^{th} order compensator closes the loop. This robustification effect is consistent with the observations regarding reduced order compensators made by Martin and Bryson in [32]. A possible mechanism for the effect is that the direct interactions between plant and compensator poles, a primary characteristic of LQG designs for flexible structures, are diminished for reduced order compensators. As there are fewer compensator poles, they must be located so as to have an effect on multiple plant poles. Consequently, the effects of shifting any particular plant pole is less significant than in the LQG case. Nevertheless, the robustification that results from the order reduction is still not significant enough to stabilize the full set of perturbed plants. Consequently, the next step in the design

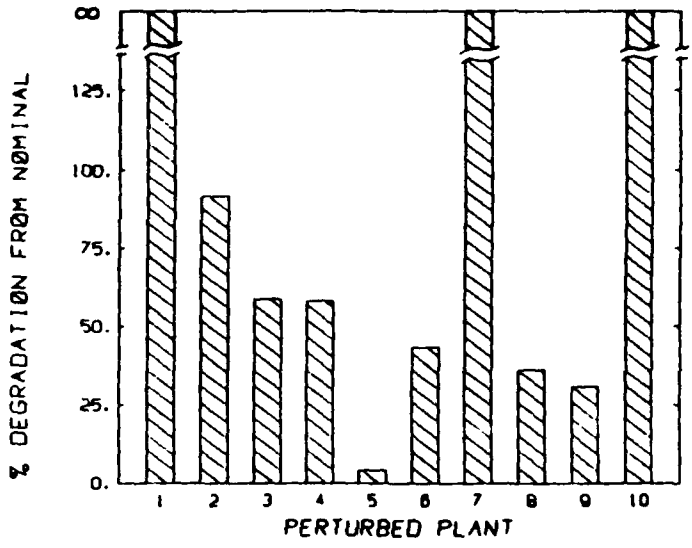

Figure 8-8. 10^{th} order compensator: performance degradation over set of perturbed plants.

process is the generation of robustified maximum entropy designs.

8.4 Robustified Compensator Design

In order to robustify the LQG compensator, the maximum entropy methodology is invoked. As described in Section 5.1.1, the errors in the system must first be reduced to a set of A_i, B_i, and C_i matrices. As the uncertainty in modal frequency manifests itself in a very straightforward manner, the form of the A_i, B_i and C_i patterns are also quite simple. However, there is no criterion for selecting the magnitude of these matrices. In order to reduce the computational burden of varying each mode's characteristics, an initial examination of the LQG system's sensitivity was performed. The stability ranges of the closed-loop system for independent variations in the modal frequencies were evaluated. The ranges associated with the first three flex modes are shown in Table 8-1. Notice that the system is most sensitive to variations in the first flex mode, the only mode whose stability range lies well within the predicted range of modelling errors. While the use of a gaussian distribution in forming our perturbed plants could certainly result in a 2^{nd} mode perturbation of more than 40%, it is more likely that the 1^{st} mode perturbations are causing the LQG instability problems. Additionally, while the perturbed plants also have errors in the predicted modeshapes, the sensitivity to these parameters was found to be minute. Therefore, in order to robustify the compensator, the uncertainty distribution matrices will only reflect a frequency error in the first flex mode. While robustification can be achieved for as many modes as desired,

Table 8-1. Stability bounds for multiplicative frequency perturbations.

Flex Mode	Stability Bound
1	$0.83 \Longleftrightarrow >20$
2	$0.60 \Longleftrightarrow >10$
3	$0.10 \Longleftrightarrow >10$

the computational burden is reduced if we only act upon those parameters which cause the sensitivity problem.

Introducing one frequency uncertainty into the design equations requires the definition of the A_1, B_1, and C_1 uncertainty distribution matrices. Having represented our plant according to the coordinate transformation discussed in Section 5.1.3, A_i is a 22×22 matrix with three nonzero elements modelling the frequency uncertainty in the first flex mode. The nonzero elements are in positions corresponding to the frequency ω in the dynamics of a 2^{nd} order mode, as follows:

$$\frac{d}{dt}\begin{bmatrix} x\omega \\ \dot{x} \end{bmatrix} = \begin{bmatrix} 0 & \omega \\ -\omega & -2\zeta\omega \end{bmatrix}\begin{bmatrix} x\omega \\ \dot{x} \end{bmatrix} + Bu \qquad (8-5)$$

$$y = \begin{bmatrix} \frac{1}{\omega}c_x & c_{\dot{x}} \end{bmatrix}\begin{bmatrix} x\omega \\ \dot{x} \end{bmatrix} \qquad (8-6)$$

where c_x and $c_{\dot{x}}$ are the original coefficients of the C matrix. Therefore, having identified the structural damping as $\zeta = 0.01$, the A_1 matrix for the AFAL model takes the following form:

$$A_1 = \begin{bmatrix} 0 & \rho \\ -\rho & -.02\rho \end{bmatrix} \qquad (8-7)$$

The scaling factor ρ determines the extent of the robustification by varying the intensity of the multiplicative white noise process, as described in Section 5.1.1.1. Notice that the coordinate transformation shown above has introduced the frequency ω into the C matrix. Consequently, there is now a ρ factor in the C_1 matrix. As the frequency manifests itself as a $\frac{1}{\omega}$ multiplicative term, an increase in frequency will be seen as a decrease in the C matrix coefficients. Thus using simple linear approximation, the components of C_1 become:

$$C_1 = \begin{bmatrix} -\rho & 0 \end{bmatrix} \qquad (8-8)$$

Our general lack of experience in using the maximum entropy algorithm made the selection of the scaling factor ρ very difficult. There is no *a priori* knowledge as to the effects of using any particular white-noise intensity in the maximum entropy error

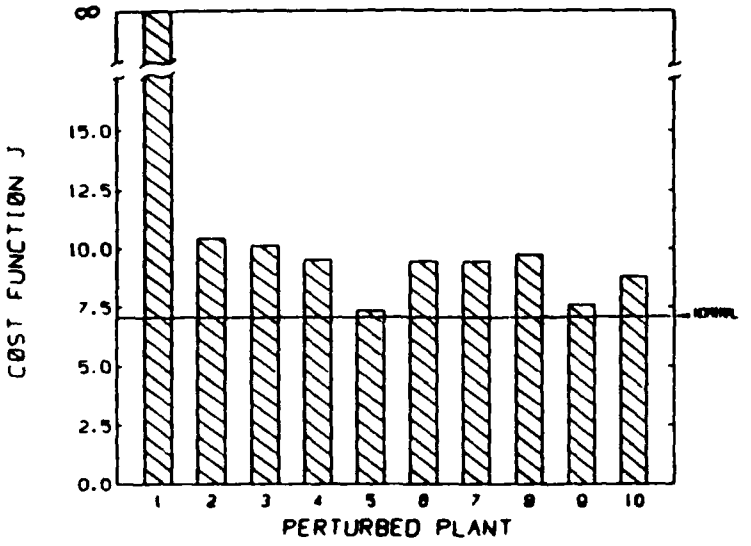

Figure 8-9. Initial robustified compensator: cost functions over set of perturbed plants.

modelling. The robustification becomes an iterative process, forming a balance between the requirements of cost function performance and robustness.

8.4.1 The Initial Robustified Design

The initial guess for the scaling factor was $\rho = 0.25$. There was no particular basis for choosing this value, it was just a "shot in the dark". Solving the four OP/ME design equations for a full order robustified compensator was simple in comparison to the reduced order design process. The four equations converged rapidly to a solution, although the procedure would certainly be more time consuming if more than one uncertainty was being modelled. Nevertheless, the ME design required substantially fewer iterations than required for adequate convergence during the optimal projection design process.

The resulting compensator was in fact quite robust in comparison to the LQG design. The new maximum entropy design formed stable closed loop systems with all but one of the perturbed plants. The gain matrices for this new robustified compensator can be found in Appendix H. To best illustrate the effects of the robustification, the cost functions were evaluated with the new compensator and each of the perturbed plants and are shown in Figure 8-9. The nominal cost function (horizontal line) for this compensator can be seen to be slightly higher than that of the LQG design (see Figure 8-2); However, that result is to be expected in the context of a robustness/performance tradeoff. The improvement in compensator robustness is worth the slight loss in nominal performance. Figure 8-10 shows the performance degradation from the nominal for

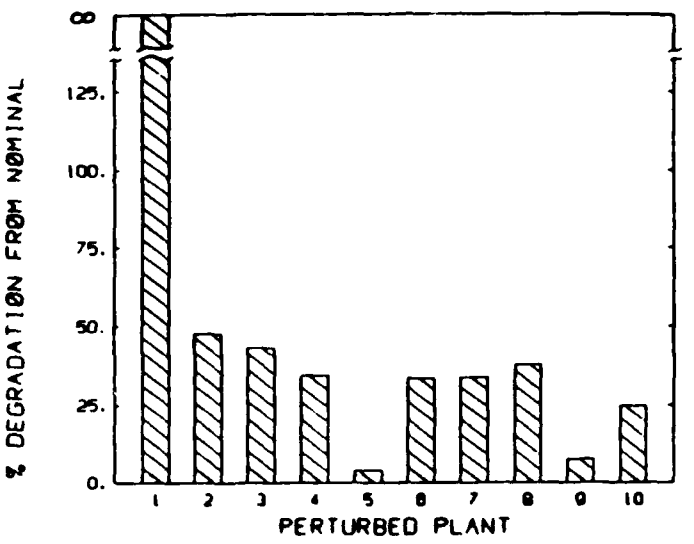

Figure 8-10. Initial robustified compensator: performance degradation over set of perturbed plants.

each of the perturbed plants. Not only have plants 7 and 10 been stabilized, but the performance losses due to perturbations are significantly less for all plants except the unstable case of plant 1. In the extreme limit of robustification, the degradation plot would have all the values reduced to nearly zero (i.e. uniform performance despite any plant perturbations). However, achieving that level of robustness would most certainly require too high a performance penalty.

Nevertheless, this compensator does not satisfy our robustness goal. While two of the three unstable LQG closed-loop systems have been stabilized, we must trade off additional nominal performance in order to fully robustify the compensator with respect to the predicted uncertainties.

8.4.2 A Final Robustified Design

One of the greatest benefits of using the maximum entropy design methodology is the ease with which the degree of robustness can be manipulated. The previous design demonstrated that the modelling of errors in just the first mode could in fact result in a less sensitive compensator. Thus in order to improve the robustness characteristics of the compensator, the white noise process intensity was increased by setting $\rho = 0.5$.

The resulting compensator did in fact satisfy the robustness criterion delineated in Section 7.3 as it formed stable closed loop systems with each of the perturbed plants. The cost functions associated with each of these plant are now all finite and are shown in Figure 8-11. While there is an increase once again in the nominal cost function,

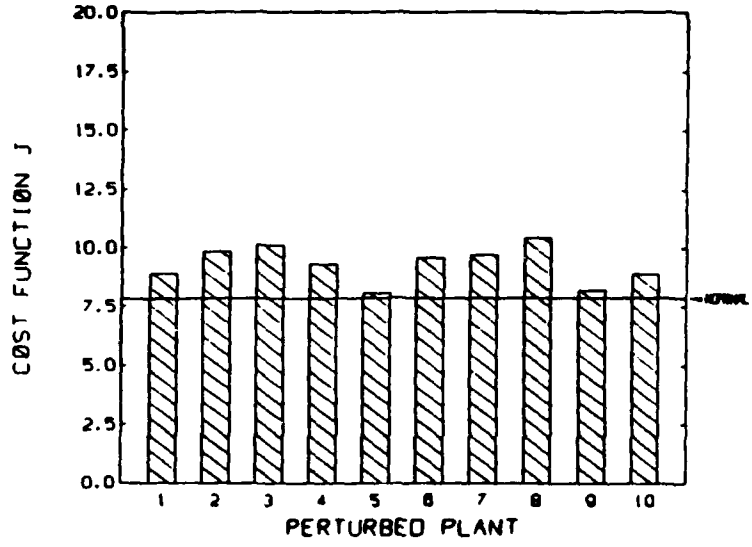

Figure 8-11. Final robustified compensator: cost functions over set of perturbed plants.

it is a minimal effect considering the improvement in robustness. Not only is the full set of perturbed plants stabilized, but the performance degradation of each plant has been decreased, as seen in Figure 8-12. Thus for what appears to be a minimal loss in nominal performance, the performance over the complete set of plants is significantly improved. Performance in this case refers to the cost function evaluation. However, the robustification effects also show up in the system responses to the chosen initial condition. As can be seen in Figure 8-13, all the trajectories are now stable, with the energy dissipating at rates substantially faster than the open loop case. It is interesting to note that the transient performance for the majority of the plants is better than that achieved with the LQG compensator, this is in addition to the fact that all the plants were stabilized. While there is no guaranteed correlation between good steady-state characteristics and the transient performance, in this case the overall improvement in cost functions was essentially reflected in the energy dissipation capabilities.

8.4.2.1 Variable Left-Shift Effects

One of the postulated mechanisms for ME robustification was the effect of a variable left-shift (see Section 5.1.3 for an explanation). In these designs for the AFAL experimental structure, the uncertainty model used in the design equations only incorporated errors in the first flex mode. Thus the left shift characteristics should apply solely to that mode. This hypothesis does in fact hold true, as can be seen in Figure 8-14. The plot shows the first six compensator poles for the LQG, the initial robustified, and the final robustified designs. The magnitude of the left shift is thus directly affected by the scaling

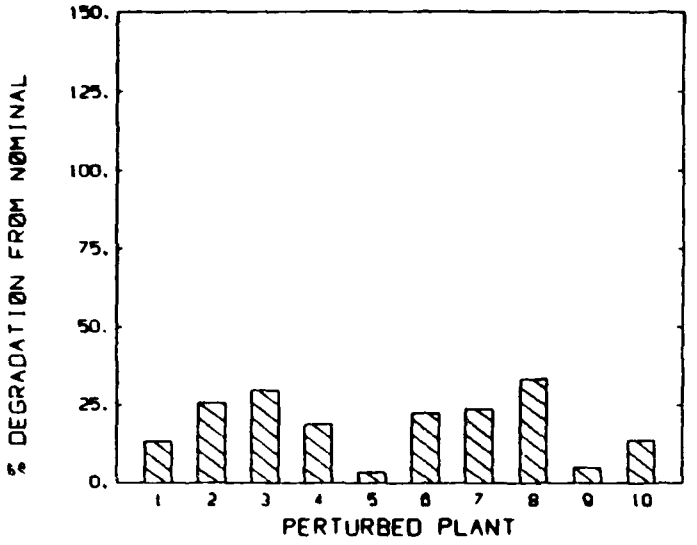

Figure 8-12. Final robustified compensator: performance degradation over set of perturbed plants.

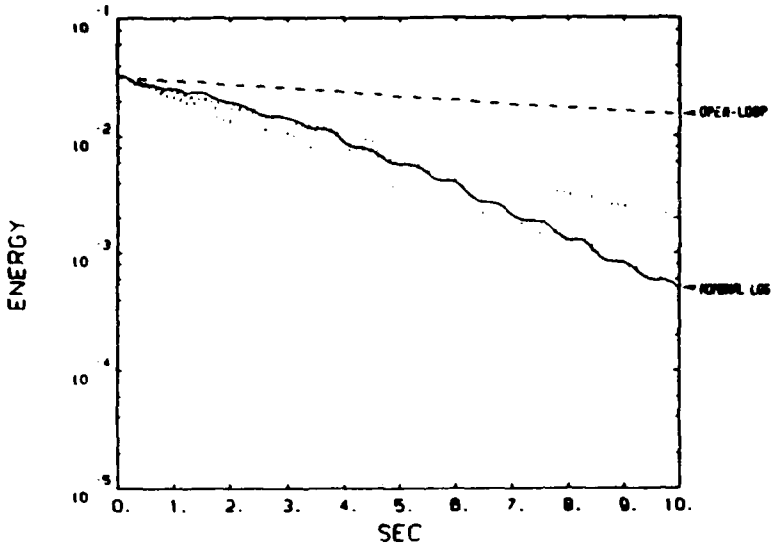

Figure 8-13. Final robustified compensator: vibrational energy trajectories for set of perturbed plants.

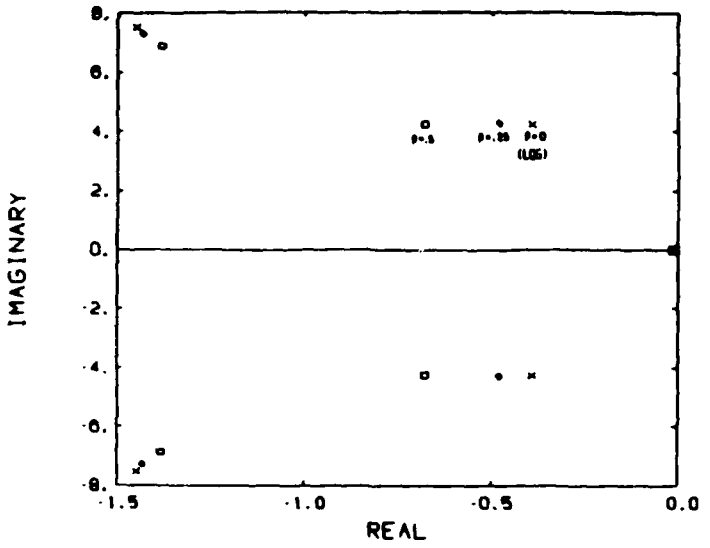

Figure 8-14. Left shift characteristics of LQG and maximum entropy designs.

factor ρ, resulting in the varying degrees of robustification. It is interesting to note that the other compensator poles remain relatively unaltered. Consequently, by including only the first mode uncertainty in the ME design process, the sensitivity to other parameter variations should remain relatively unchanged. The benefit of this characteristic is reflected in the performance loss that occurs in robustification. As only the necessary parameters are altered to reduce sensitivity, the minimum amount of performance loss is incurred in designing a robust compensator. This minimal penalty contrasts with the LQG/Loop Transfer Recovery methodology where the particular structure of the errors is not taken into account. Thus equipped with greater knowledge of the system and its errors (i.e. structured uncertainties), we can design robust compensators which have potentially better performance than those developed with the LQG/LTR approach.

8.5 Robustified Reduced Order Compensator Design

The previous sections have illustrated the potential for independent order reduction and robustification. However, with the OP/ME design methodology the designer is able to integrate these two design characteristics into a particular compensator. In the development of active vibration dampers for the AFAL experimental structure, a reduced order, robustified compensator was required. Thus the OP/ME methodology was an attractive alternative to other design approaches.

As discussed in Section 8.3, the 10^{th} order compensator was chosen as the baseline reduced order design. While this is an appropriate size for implementation ($n_c = 10$), the compensator was overly sensitive to the modelling errors expected for this structure.

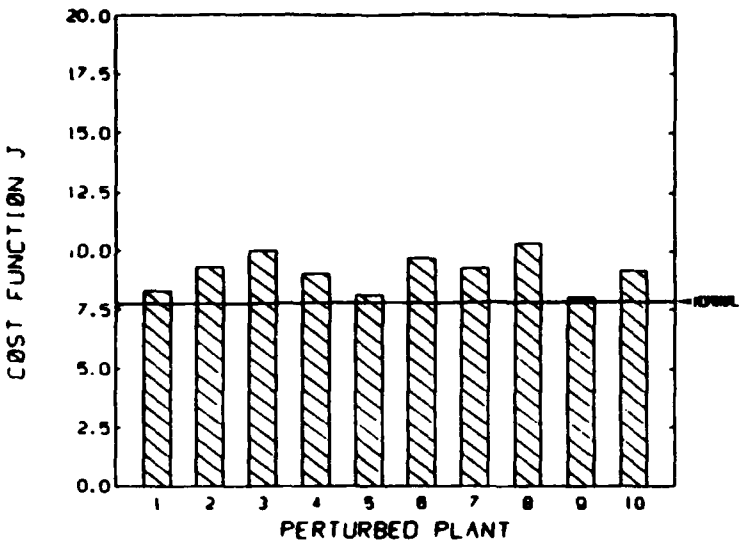

Figure 8-15. Robustified reduced order compensator: cost functions over set of perturbed plants.

Conversely, the final robustified compensator (uncertainty scaling factor $\rho = .5$) had the appropriate robustness characteristics, yet was still full order and thus might not be implemented effectively. However, by setting $n_c = 10$ and $\rho = .5$ in the full OP/ME design equations, the resulting compensator combined the appropriate characteristics. See Appendix H for the gains associated with this design.

The cost functional performance of this compensator was the best of those developed in this study. The robustness characteristics of the full order system are maintained, while the compensator order has been reduced by 12 states. There is even some additional robustification due to the order reduction process, as was first described in Section 8.3. In this case, however, the secondary robustification does seem to be somewhat dependent upon the perturbation's direction in the parameter space. This robustification occurred for all of the "stable" perturbed plants during optimal projection order reduction from LQG, as can be seen by comparing Figures 8-3 and 8-8. In contrast, the performance of plants 5, 6 and 10 is degraded somewhat as the order of the robustified compensator is reduced. Nevertheless, the overall trend in the set was toward better performance after the order reduction.

Once again, the improvements in cost functional behavior did translate to better transient performance, as illustrated in Figure 8-17. The set of simulations for this compensator shows transient performance superior to that of the LQG or the robustified full order compensator. The majority of the perturbed systems display energy dissipation rates even better than the baseline LQG system, as represented by the solid line.

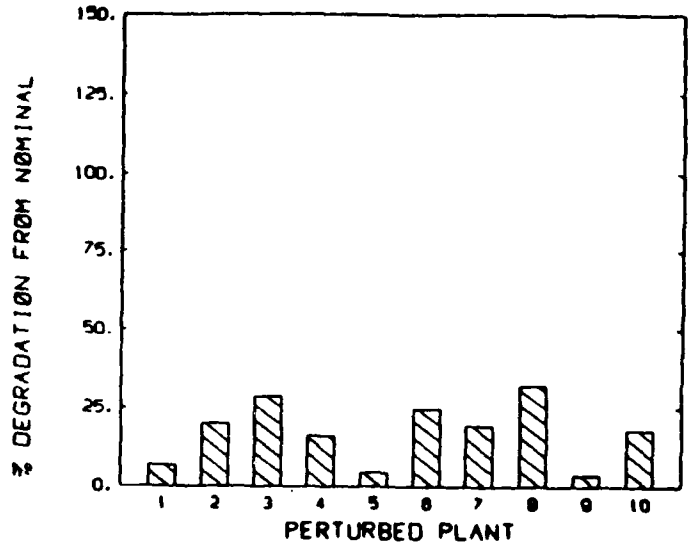

Figure 8-16. Robustified reduced order compensator: performance degradation over set of perturbed plants.

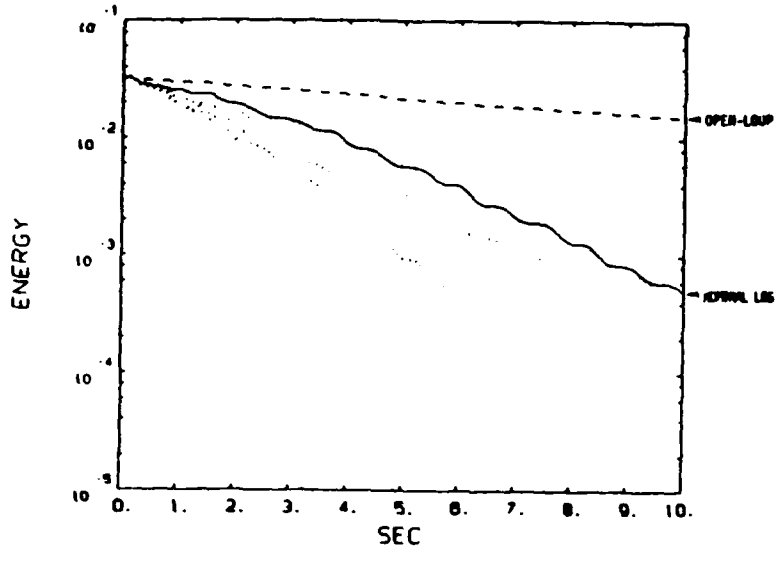

Figure 8-17. Robustified reduced order compensator: vibrational energy trajectories for set of perturbed plants.

Table 8-2. Nominal performance of each compensator.

Compensator Type	Cost Function	Relative Degradation
LQG	6.775	0.0%
10^{th} Order	6.780	0.08%
Initial Robust	7.065	4.28%
Final Robust	7.822	15.45%
10^{th} Order Robust	7.782	14.95%

8.6 Tradeoffs in the Design of Robust, Reduced OrderCompensators

The design process illustrated here has raised some of the performance issues which are encountered in control system development. The effects upon the nominal performance of the various design steps are shown in Table 8-2 in terms of cost functional evaluations. Apparently, the majority of the performance loss occurs from robustifying with respect to parameter uncertainties. Reducing the compensator order had very little negative effect upon the nominal performance, while it improved compensator robustness and simplicity. Consequently, if only a small degree of robustification is required in any given design, perhaps some consideration should be given to solely reducing the compensator order. However, as was shown in Figure 8-5 there will exist some limit of reduction before the cost starts to rise significantly. At this point, the use of the maximum entropy algorithm would surely be more effective for robustification. Interestingly enough, the 10^{th} order robustified compensator had better nominal performance than its full order counterpart. The apparent cause is that the full order design equations had not yet fully converged to the appropriate solution. In any case, the difference is minimal.

8.7 Performance Gains Due to PMAs

The original purpose of this research was to evaluate the use of proof mass actuators as active vibration dampers. The hypothesis was that a linear actuator could help dissipate vibrational energy in the terminal phase of a rapid slew maneuver. The reduced order robustified compensator of Section 8.5 shows the substantial capabilities of a PMA vibration damper, even in the presence of parameter uncertainties. Nevertheless, the usefulness of the compensator should be judged in comparison with the existing thruster-based system. In order to evaluate the overall performance of a thruster/PMA

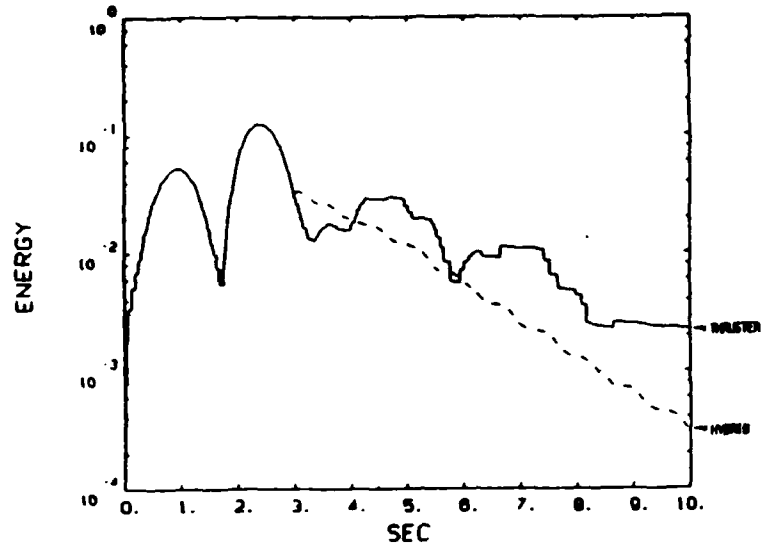

Figure 8-18. Vibrational energy trajectories: on-off thruster vs. hybrid thruster and PMA system.

combination, the switching logic of Section 7.4 was used to transfer control to the PMA-based compensator. In Figure 8-18, the solid line represents the vibrational energy introduced into and dissipated from the system by the thruster-based control system. Notice, however, that if the PMA vibration damper is activated at 2.98 seconds as commanded by the switching logic, the overall energy level at the end of the maneuver is reduced. An additional benefit of using the linear actuator is that the energy level will continue to decrease with time. As the thruster controller operates with a deadband, there will be no further control firings, and the energy is left to dissipate at the open loop rate. Consequently, the addition of proof mass actuators to the AFAL experimental structure will improve the overall system performance in a rapid slew maneuver.

Section 9

Revision of the Structural Dynamic Model

9.1 Motivation for Model Update

Sections 5 through 8 introduced the use of proof-mass actuators to control structural vibrations. The modelled PMAs were relatively small, yet still could provide significant vibration damping during the terminal phase of a large angle slew maneuver. In the course of this preliminary examination, the inclusion of these small PMAs was not considered to have a significant affect upon the structure open-loop dynamics. However, in the course of this study the mass of the proposed actuators was increased to provide higher control effectiveness. The new PMAs and their mounting configuration were described in Section 3. Due to the increase in tip mass, the development of a new dynamic model was required.

The previous dynamic model of the AFAL experimental structure was generated using the assumed modes method. Because the thrusters were constrained to operate in opposing pairs, the symmetric structural modes were discarded during the modelling process. This simplification of the model was reasonable, given the constraints placed upon the thrusters and their location on only two of the four arms. However, with the placement of PMAs on all four arms, the capability to both excite and control symmetric vibrational modes has increased. Consequently, any revised model must include both the symmetric and anti-symmetric vibrational modes.

In order to best predict the dynamic characteristics of the AFAL experimental structure, a complete finite-element modelling procedure was undertaken.

Table 9-1. Vibrational mode frequencies with PMAs locked.

Mode #	Frequency (Hz)	Description
1	0.0	rigid body rotation
2	0.382	1^{st} bending, primary arms, symmetric
3	0.396	1^{st} bending, all arms, anti-symmetric
4	0.411	1^{st} bending, secondary arms, symmetric
5	0.981	1^{st} bending, all arms, anti-symmetric
6	5.827	2^{nd} bending, primary arms, symmetric
7	5.875	2^{nd} bending, all arms, anti-symmetric
8	5.984	2^{nd} bending, secondary arms, symmetric
9	6.110	2^{nd} bending, all arms, anti-symmetric

9.2 Dynamic Effects of New Proof-Mass Actuators

9.2.1 Modal Frequencies

The inclusion of the new PMAs has had two significant effects upon the dynamics of the AFAL experimental structure. As predicted, the increase in tip mass has lowered the modal frequencies of the structure when compared to those presented in Ref. [1], especially when the proof-masses are locked in position. The frequency values with the PMAs locked are displayed in Table 9-1. When the PMAs are constrained to maintain a zero relative displacement, the reduction in modal frequencies are greatest as can be seen by comparing Table 9-1 and Table 7-1.

However, when the PMAs are free to slide within their displacement range, four new rigid body modes are added to the system. Additionally, the reductions in modal frequencies are not as great, as can be seen in by examining Table 9-2.

The PMAs can be locked through the use of a position feedback loop during the slew maneuver, then released for terminal phase vibration control. Even when activated for vibration suppression, this position loop will remain in place. Consequently, the NASTRAN model of the PMAs fixed was selected for controller design and analysis purposes. The state-space model derived with this NASTRAN analysis is given in Appendix I

Table 9-2. Vibrational mode frequencies with PMAs free.

Mode #	Frequency (Hz)	Description
1-5	0.0	rigid body rotation & PMA displacements
6	0.453	1^{st} bending, primary arms, symmetric
7	0.478	1^{st} bending, all arms, anti-symmetric
8	0.504	1^{st} bending, secondary arms, symmetric
9	1.023	1^{st} bending, all arms, anti-symmetric
10	5.838	2^{nd} bending, primary arms, symmetric
11	5.890	2^{nd} bending, all arms, anti-symmetric
12	6.023	2^{nd} bending, secondary arms, symmetric
13	6.143	2^{nd} bending, all arms, anti-symmetric

9.2.2 Increased Torsional Mode Effects

Due to the increase in tip mass, the torsional modes have become more a significant problem. In the previous configuration, the effect of the torsional modes was to introduce noise into the accelerometer signals. Angular deflections at the tip caused the accelerometers to pick up a component of gravity. As the frequency of the torsional vibration was above the bandwidth of the control system, these unmodelled dynamics were not too detrimental to the system's performance.

However, with the addition of mass at the tip, the frequencies of the torsional modes have decreased significantly. These frequencies are within the bandwidth of the control system and could very well present a control system stability problem. As the proof-mass moves off center, gravity will serve to twist the beam. Thus, the potential for destabilizing effects is compounded by the fact that the motion of the PMAs induces some torsional bending.

Notice, however, that the detrimental effects of torsion in the AFAL experimental structure are largely due to the ground based nature of this research. In applying these control techniques to a true space-based application, the torsional characteristics would have much less significance. Thus a potential solution to this problem may be the torsional stiffening of the beams, while maintaining the flexible nature desired for the in-plane vibrations.

Section 10

Control Computer I/O System Upgrade

10.1 Introduction

This section describes the addition of analog interfaces to the MicroVAX II computer and the conversion of the control code to use the new interfaces in place of the Labtech computer. Use of the Labtech computer was discontinued due to I/O limitations and interrupt response delays. The evolutionary and experimental aspects of the research program precluded clairvoyance with respect to the actual I/O requirements in the beginning and early phases of the study. Upgrading the analog interfaces resulted in a factor of six increase in maximum sample rate attainable using the baseline control program. The upgrade also allowed unlimited time tests to be performed.

10.2 I/O Limitations of the Combined MicroVAX II/Labtech Controller

Section 4.4.3 discussed some issues concerning the limitations of the combined MicroVAX/Labtech control computer. The limitations generally concerned the I/O performance and interrupt response time of the Labtech computer. The combined MicroVAX/Labtech control computer could reliably run Floyd's single-step optimal thruster control algorithm with a minimum sample period of 15 ms (67 Hz). This baseline algorithm required four analog linear accelerometer inputs and one digital output (for the thruster commands). The Labtech had a maximum transfer rate to the MicroVAX of approximately three thousand 16-bit words/second, a relatively long interrupt response time (1.5 ms), and was very sensitive to spacing of interrupts. If interrupts occurred too close together (< 0.5 ms), the Labtech would either miss the interrupt or crash.

The delays associated with the above limitations became a concern as the additional sensors and actuators for this study were incorporated into the thruster control logic. The additional actuators required processor time to calculate their control command, while both sensors and actuators required more I/O time. It was estimated that the

delays would consume 10-12 ms of a desired 20 ms (50 Hz) sample period.

Another limitation of the Labtech processor was that it always halted after precisely 16306 sample cycles. The cause for this behavior was never found. For transient slewing tests, this limit was acceptable because the tests were over before the limit was reached. However, some of the tests contemplated for this study included an extended 'tracking' phase which required longer duration tests and which would have exceeded the cycle limit.

The tests for the study required five digital-to-analog (D/A) outputs for the PMAs and the hub torquer commands. The Labtech had only four D/As available, so at least one additional channel of D/A output was needed. Given the above I/O limitations of the Labtech, and the existence of readily available higher performance analog interfaces for the MicroVAX, it was decided that any additional analog I/O channels needed should be located in the MicroVAX rather than the Labtech. Furthermore, because at least a portion of the analog interface to the experiment was to be based on the MicroVAX, it was decided that the entire analog interface should be moved to the MicroVAX to avoid the limitations imposed by the Labtech. An additional factor was the concurrent activity of another project at CSDL which used Q-bus (the MicroVAX I/O bus) analog interface boards and the VAX ELN real-time operating system. Device driver software routines written for those boards could also be used in the AFAL experimental project.

The Q-bus analog interface boards chosen were those manufactured by Data Translation. The analog-to-digital (A/D) board, model # DT3382, provided 32 channels with differential inputs. The DT3382 used DMA and programmable channel lists to provide a maximum sample rate of 250 kHz. The D/A board, model # DT3366, provided 8 (expandable to 32) analog output channels. The DT3366 also used DMA and programmable channel lists to provide a throughput up to 100 kHz/channel with an overall maximum throughput of 500 kHz. Both boards shared a similar architecture which simplified the development of device driver software routines.

10.3 Conversion of Existing I/O Routines

The conversion of the MicroVAX control code to use Q-bus analog interface boards instead of the Labtech I/O for data acquisition was straightforward. The hardware details of the analog interface had been confined to several main I/O procedures. Device driver routines for the analog boards were obtained from another project at CSDL and the main I/O procedures were re-written to use the new driver routines. The conversion process consisted primarily of replacing the main I/O routines with the new versions and insuring proper initialization and resetting of the analog interface boards.

The conversion was verified by comparing slewing test results between the combined MicroVAX/Labtech and the MicroVAX-only controller, and tests which exercised

the new analog interface boards and routines. Slewing tests performed with the two controllers produced nearly the same results, provided that the tests ran to completion without I/O problems. Because the only MicroVAX control code which was changed during the conversion was related to the I/O routines, the verification process focused on reliable input and output of the correct values. Two I/O problems which arose and were corrected during the verification are described below.

One problem occurred initially due to incorrectly resetting the D/A board between sample cycles. When using several output channels, the commanded outputs would appear to switch sequentially from one channel to the next at random time intervals. After closely examining the program code and several discussions with Data Translation (the board manufacturer), Data Translation revealed an undocumented step which was required when resetting the board. Incorporating the additional step into the control code solved the problem.

Another problem which arose was the interaction of other Q-bus devices with the activity of the analog interface boards. When the control computer used the Ethernet, either for remote debugging or file access, the Ethernet interface board occasionally interrupted the processor and caused a delay resetting the analog boards. The delay sometimes resulted in a loss of synchronization with the real-time clock which generated the sample interval and control delta interrupts.

The interrupts occurred at times when the MicroVAX was not explicitly using the Ethernet device. The interrupts were possibly caused by broadcast messages on the main Ethernet network or were required by Ethernet protocols. The solution was to not use the Ethernet network for actual test runs. Initialization and data files were kept on the control MicroVAX rather than on the host node. Debugging runs were performed using the network and the remote debugger, but the remote debugger and network support were removed from the control application for the actual test runs.

The analog I/O interface conversion was considered complete when analog I/O operations could be performed reliably and repeatably for hours at-a-time. With the new I/O system, the MicroVAX-only controller produced essentially identical slewing test results when compared to the combined MicroVAX/Labtech controller but with the limitations of the latter configuration removed.

10.4 MicroVAX Controller Configuration

Figure 10-1 shows the configuration of the updated MicroVAX controller and the details of the interface to the AFAL test structure. The major differences between the MicroVAX controller and the combined MicroVAX/Labtech controller (shown in Figure 4-2) were the removal of the Labtech processor and the associated interprocessor communication hardware, the addition of analog interface boards to the MicroVAX, and

the technique for reading the hub angle. In the MicroVAX controller, the timer board directly interrupted the A/D and D/A boards to initiate a sample or output cycle. The hub angle reading was obtained by communicating over a parallel interface to the Contraves air-bearing table control processor. The Contraves table electronics provided more accurate hub angle readings at higher angular rates than was previously possible using the Farrand inductosyn readout.

10.5 Performance of the MicroVAX I/O Interface

The MicroVAX II with the new analog I/O system greatly increased the maximum throughput of the AFAL experiment control computer. The MicroVAX controller could run Floyd's single-step optimal thruster control algorithm with a minimum sample period of 2.5 ms (400 Hz), a factor of six improvement over the combined MicroVAX/Labtech controller. Only approximately 0.5 ms of the sample cycle was used to perform I/O related tasks. The computational power increase of the MicroVAX II over the Labtech was finally evident.

The MicroVAX controller could also run infinite time (or continuous) tests (i.e., no sample cycle limit). Preliminary testing of the PMAs used an infinite control loop to permit excitation of the structure and observation of the behavior of the PMAs during vibration damping. Continuous testing was also used to obtain transfer function measurements with the PVF_2 film actuators used in the related AFAL/CSDL program, the RCS/Piezoelectric Distributed Actuator Study.

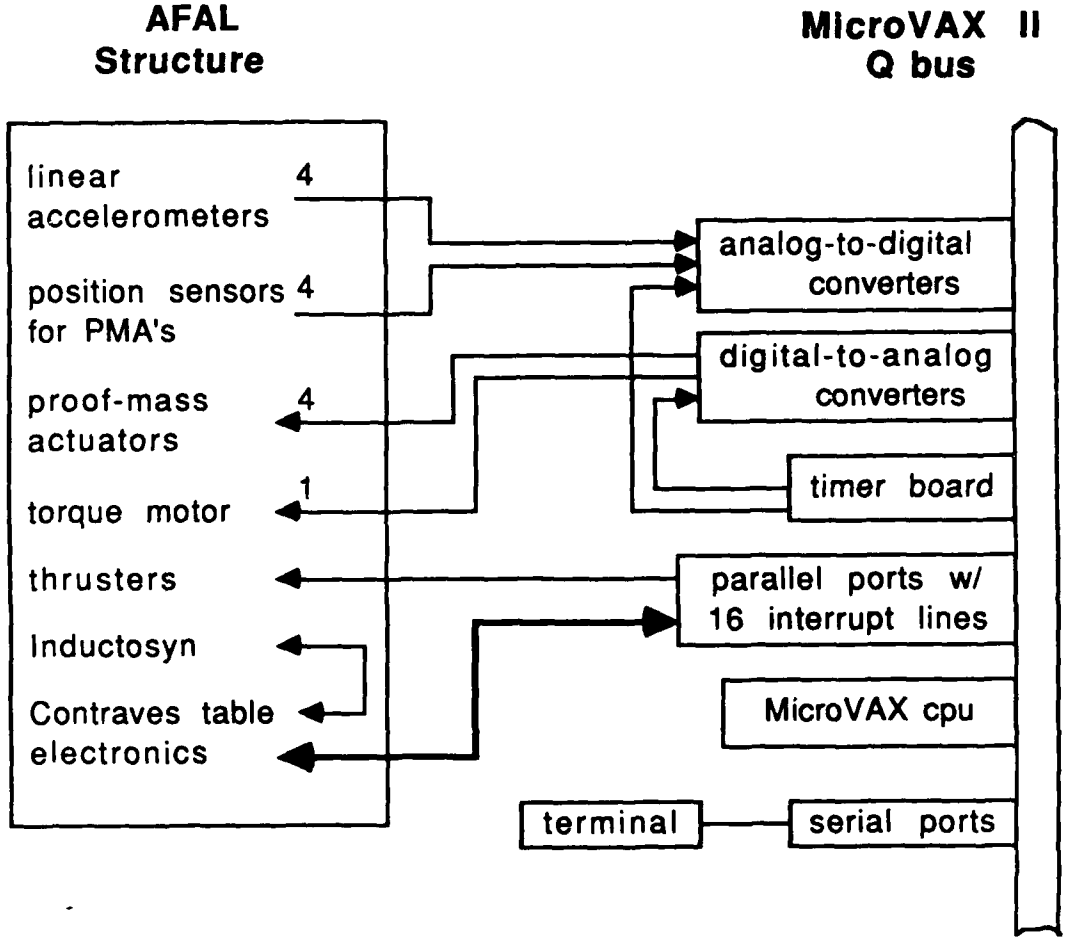

Figure 10-1. MicroVAX II computer system configuration.

Section 11

Implementation of Single-Step Optimal Thruster Control for the Modified Structure

11.1 Overview

This section describes the implementation of Floyd's single-step-optimal control algorithm [1] for the modified AFAL structure and provides an overview of the thruster control routines. Several of the modifications made to the experimental facility significantly altered its dynamic characteristics. The effects of these modifications are discussed and the procedures used to generate an updated model from NASTRAN data are presented. Testing of the single-step-optimal control algorithm with the new model is discussed.

Severe limit cycles occurred initially when using the new model as the basis for calculating RCS commands for slewing maneuvers. An undocumented gain of '814' was discovered in the thruster calibration initialization which caused major scaling errors for the control routines. With the gain removed, the slewing maneuvers produced by the new model compared well with maneuvers produced by the old model.

The slewing maneuvers exhibited a large-amplitude limit cycle during the terminal phase. Several approaches were explored to reduce or eliminate the limit cycle. The nominal thruster control parameters used did not weight the flexible mode states (i.e., the control only depended on the rigid body states). Adding non-zero flexible mode weights would increase control over the flexible modes. However, the flexible mode weights also resulted in very frequent thruster firings which excited higher frequency modes of the structure, and significantly reduced the slewing performance of the controller.

Thruster constraints were added to increase damping of the flexible modes and to reduce the limit cycle during the terminal phase. A deadzone was placed around the set point so the thrusters would not fire if the desired pointing accuracy was within the deadband. The thrusters were constrained to not fire in the direction of the estimated

local tip velocity to insure that energy was not added to the system. Nevertheless, this constraint alone still allowed relatively large-amplitude limit cycles. A tip displacement constraint was added to prevent the thrusters from firing in the direction of the local tip displacement. This constraint allowed a flexible mode to approach zero displacement and maximum velocity before the thrusters were permitted to fire, which resulted in increased damping of the flexible modes.

11.2 The Thruster Control Routines

This subsection reviews the thruster control routines as implemented originally by Floyd in the predecessor study [1] and transferred to the MicroVAX control computer during the first part of this investigation (see Section 4). The objective of the study was to combine new linear actuators with the existing RCS, not to necessarily improve upon the thruster control algorithms demonstrated in the predecessor study. Therefore, the control routines were considered to be debugged and trusted and only minor modifications to the control routines were expected to be necessary when they were transferred to the MicroVAX. The changes corrected minor programming logic errors which were discovered when the structure was moved to the low friction air-bearing table.

The thruster control routines implemented the single-step-optimal control algorithm developed by Floyd. The control strategy assumes that every time step is the final time step of a discrete-time optimal control problem. The functional optimization problem over a complete trajectory is reduced to a parameter optimization problem for each time step. The method is inherently capable of handling known actuator nonlinearities and failures as constraints in the parameter optimization problem.

A slewing maneuver was divided into two parts: an acceleration and coasting phase, and a deceleration phase. Feedback gains were selected for each phase so the single-step-optimal switching lines were similar to the switching curves for a weighted minimum-time, minimum-fuel control problem. This required maneuver-specific information such as slew angle and thruster supply pressure, in addition to the system model. The feedback gains for the acceleration phase were chosen with a low weighting on velocity so the structure was accelerated towards the desired set point. The feedback gains for the deceleration phase weighted both position and velocity so the structure was brought to rest at (or near) the set point. The relative weighting between modes could be adjusted. The transition between phases was chosen to be the point at which the rigid body states would cross the minimum-time switching curve.

Additional thruster control logic was introduced as the structure approached the set point to reduce limit cycling and provide better vibration control. These constraints essentially adding a third phase to the maneuver which was referred to as the terminal phase. The thrusters were constrained to fire against the estimated tip velocity so that,

ideally, energy would always be removed from the system. In practice, errors in the estimated tip velocity resulted in energy occasionally being added to the system. In addition, a deadzone was placed around the set point in such a way that the thrusters would not fire if the tip velocity was less than a specified (absolute) value, and the hub angle was within a specified deadzone about the set point. The absolute velocity limit chosen was 0.05 ft/sec, and the rigid body deadzone was usually 0.5 degrees.

A classic Kalman filter state estimator was used to provide state estimates for the single-step-optimal control routines. The filter routines used a modal system model (which results in a block diagonal system dynamics matrix) to reduce computation. The filter gains were precalculated based on process and sensor noise variances measured during identification tests.

The thruster control routines were written to be independent of model-specific information. The routines assumed only that the system matrices were in a block diagonal modal model format. This allowed the routines to be used with any set of system matrices. In addition, the routines were written using a vector formulation, where possible, to allow the number of states, actuators, and sensors included in the system model to be changed easily.

11.2.1 Test Procedure

A typical run started with the model matrices, Kalman filter gains, and computer hardware initialization data (e.g., A/D and D/A channel parameters) being loaded from disk. Default maneuver specific parameters (such as slew angle and deadzone) were also loaded from disk. The computer hardware was then initialized; interface boards were reset and loaded with channel configuration information, and the selected timer channels were initialized.

The operator was allowed to modify selected maneuver-specific parameters such as slew angle, deadzone, thruster supply pressure, and cost-of-control. The control routines then calculated the feedback gains for each phase of the selected maneuver using the model information and the maneuver-specific information.

Sensor biases were obtained by sampling the sensor outputs 100 to 1000 times and averaging the results. The Kalman filter states were initialized based on the desired slew angle and the model information.

The timers were started and the control algorithm was allowed to run for 20 seconds to perform the selected slewing maneuver. The structure slewed to near the set point in approximately three seconds. During the remainder of the run, the thrusters attempted to damp flexible mode vibrations while keeping the rigid body angle within the selected deadzone. State estimates, measurement estimates, actual sensor readings, and control commands were logged in a data file for each time step. The data file was transferred

via Ethernet from the MicroVAX control computer to a VAX 8650, where the data was loaded in to CTRL-C (a matrix manipulation and control design and analysis application) to be plotted and analyzed.

11.3 Changes Requiring an Updated Model

Modifications to the AFAL experiment structure were made as described in Section 2 and Section 3. The major changes to the structure were the addition of the PMA assemblies (at the tip of each arm), and the mounting of the structure on a new, low-friction air-bearing table. Several modifications were made to the facility which did not directly affect the basic modal structural model but changed the resulting discretized model and the parameters used by the control computer to implement the control law. These modifications involved re-wiring the sensors and actuators to reduce electrical noise, and increasing the sample rate from 28.5 to 50 Hz.

The PMA assemblies nearly doubled the tip mass of each arm, significantly reducing the first bending mode frequency of an active arm from 0.59 hz to 0.38 hz. Also, because the PMA assemblies were mounted at the large tip radius (5 ft.) from the hub, the rigid body inertia of the structure was greatly increased. The new air-bearing table resulted in a change in the hub inertia. These mass property changes (and numerous additional smaller changes) were incorporated into a NASTRAN model of the AFAL structure to establish updated modal parameters of the structure. These results were presented in Section 9. The updated mode shapes were nearly the same as before the modifications, but the modal frequencies were significantly reduced.

The effects of the reduced table friction were apparent only during the terminal phase of slewing maneuvers. Additional thruster control logic was needed to prevent the structure from slowly drifting away from the set point (see Section 4.3), and there was a much greater tendency for the thruster control to limit cycle.

Re-wiring the sensors and actuators reduced the electrical noise levels on the accelerometer signals from 20-40 mV rms to approximately 5 mV rms. The improved signal-to-ratio achieved by re-wiring the structure did not directly affect the structural model, but the reduced sensor noise variances affected the Kalman filter feedback gains generated for the state estimator.

The higher sample rate was originally chosen to allow control of the second group of structural modes which all had frequencies near 6 Hz. However, these modes were highly coupled with the first torsional mode of the arms, which was uncontrollable. It was beyond the resources of the study to modify the structure to reduce the torsional mode coupling or design an actuator which could control the torsional modes.

The new sample rate required that the continuous-time system matrices be discretized again. All other parameters which depended on the discretized system matrices

(such as the Kalman filter feedback gains) were recalculated as well.

11.4 Generation of a Modal Model and Control Parameters

The updated NASTRAN model (described in Section 9) provided mode shapes and frequencies for the modified structure. A general purpose utility program was written to produce continuous-time modal system matrices from the NASTRAN output data file. The utility program requires sensor and actuator placement and type as input, as well as the selected modes to include in the model. Sensors and actuators can be placed at any node of the NASTRAN model. Displacement, velocity, and acceleration sensors and force (or torque) actuators can be oriented in any direction. The units of the system matrices produced are consistent with the units used for the NASTRAN model (i.e., if displacements in the model were given in feet then displacement sensor output will be in feet). The units for displacement and mass used in the NASTRAN model of the AFAL structure were feet and slugs, respectively.

The rigid-body mode and the first two anti-symmetric modes of the structure were included in the model. The first two symmetric modes were not included in the model because the thrusters could not control the symmetric modes. Because the thrusters were constrained to act as a single thruster, only one actuator was used in the model. The thruster actuator effectiveness was later multiplied by two to account for the thrusters on both arms. Models of the tip accelerometers and hub angle inductosyn and resolver were included. The continuous-time system matrices generated from the NASTRAN output are listed in Appendix J.

The output matrices were scaled so that the state estimator output was in the same units as the output of the data acquisition routines in the control computer. The accelerometer outputs were scaled from ft/sec^2 to g's, and the hub angle sensor was scaled from radians to degrees. The input matrix was already scaled to expect pounds-force as input, but the matrix elements were multiplied by two to account for the second pair of thrusters. Also, the input and output matrices were transformed to obey the sign convention that positive modal displacements resulted in positive (counter-clockwise) hub angle displacements. These scalings and transformations resulted in a system model that used the same sign convention as the old model, but the accelerometer sensor outputs were now in units of g's instead of volts.

The continuous-time system matrices were then combined with process and sensor noise variances to generate discrete-time system matrices and Kalman filter gains using a program originally developed by Floyd [1]. The input routines were modified to accept the continuous-time model as the basic model input. The sample interval and noise variances were input from another data file. The original computer code was used instead of a general matrix manipulation utility (such as CTRL-C or Matrix-X) to insure

that any undocumented scaling performed on the system matrices in preparation for the single-step-optimal control algorithm would be applied to the new system matrices as well.

The sensor noise variances used to generate the Kalman filter gains were the same as those determined by Floyd during the predecessor study. Although the quiescent electrical noise levels were significantly reduced as a consequence of sensor re-wiring, the disturbances due to thruster force variations (the variance was approximately 5% at a force level of 0.5 lbs.) and spillover from unmodelled modes (the symmetric modes) were the largest noise sources during any test maneuver. The noise variances used by Floyd were identified during test maneuvers and hence included the thruster noise and spillover effects. These noise variances were chosen as the most appropriate to use in slewing maneuvers.

The discretized system matrices, Kalman filter gains, and miscellaneous parameters needed to initialize the single-step-optimal control algorithm were written to a floppy disk file to be loaded into the MicroVAX II control computer.

11.5 Testing of the Updated Model with the Modified Structure

Initial testing of the updated system model was accomplished by comparing 15 degree slewing maneuvers performed with the old model and control parameters with maneuvers performed using the new model. In both cases the maneuvers were performed with the modified structure. The old model produced a typical response: an initial thruster pulse to accelerate the structure towards the set point, a coasting period, another thruster pulse to decelerate the structure, and a few short thruster firings during the terminal phase to damp flexible mode vibrations and keep the structure within the rigid body deadzone. Occasionally, there was some small-amplitude limit cycling of the first anti-symmetric flexible mode (the scissors mode) during the terminal phase.

By contrast, the initial tests with the new model produced very atypical responses. There was no coasting phase between the acceleration and deceleration pulses which resulted in large flexible mode vibrations, primarily the scissors mode. Also, there were very large amplitude, growing limit cycles of the scissors mode during the terminal phase. Some tests were halted because the motion of the structure became dangerously large.

Several possible sources of the atypical behaviour were (i) incorrect model information (frequencies and/or mode shapes), (ii) control parameters (such as cost-of-control) in the wrong range for the system units chosen, and (iii) inconsistent units used to develop the system matrices (i.e., a routine was expecting radians while the model used degrees). A new system model was generated using the mode shape information from the NASTRAN analysis but with experimentally identified resonant frequencies. Table 11.5 compares the NASTRAN determined frequencies with the experimentally iden-

Table 11-1. Experimentally identified modal frequencies vs. NASTRAN model frequencies with PMA's locked.

Mode	Modal frequencies (Hz)	
	Experimental	NASTRAN
first anti-symmetric (scissors mode)	0.346	0.396
second anti-symmetric (twist mode)	0.768	0.981

tified frequencies. Tests with the new model showed no improvement in performance.

The cost-of-control was varied over a large range to determine if any change in units had unexpectedly affected the appropriate range of this parameter. It was found that a small normalized control cost ($b_m = 0.1$ vs. 1.0) resulted in a more typical run (an acceleration pulse, a coast period, and a deceleration pulse) but a large, growing limit cycle was still present during the terminal phase. Other control parameters (such as the size of the rigid-body deadzone) were also varied, but only extreme values had any significant effect on the limit cycle.

The model generation routines were next examined closely to determine if any programming errors had introduced an unexpected scaling of model parameters. Open-loop simulations of the system were performed using CTRL-C with both the old and new models. Thruster control commands recorded from a test maneuver performed using the old model were used to drive each of the systems. The simulated response of the structure was very similar for each model. This indicated that the new model matrices were generated using consistent units and did not contain any major scaling errors. The thruster control routines were also examined in search of any unexpected scaling of model parameters. None were found.

Finally, an examination of the initialization data revealed an undocumented gain of approximately 814 in the thruster calibration. The same initialization data was used for both the old and new model. Apparently Floyd had scaled the old system matrices to use 814'ths of a pound-force as the input unit instead of unity pound-force. This scaling error (when using the new model) had several direct effects on the control routines: the control value calculated and used in the optimization process was incorrect, the state estimator received incorrect input which caused incorrect state estimates, and the process noise variance used the wrong units so that the Kalman filter gains were also incorrect.

The new model was re-calculated using the correct process noise variance, and the thruster calibration data was changed to units of pounds-force. Test maneuvers were performed using with nominal control parameter values (i.e., control cost, deadzone,

etc.). The updated model resulted in very typical maneuvers. The terminal-phase limit cycle was still present but with a slightly reduced amplitude, and the limit cycle did not grow. The old and new models now produced similar slewing maneuver results (except for the terminal phase limit cycle). Therefore, the new model and its associated control parameters were judged to be consistent (in terms of units) and acceptable for use in subsequent slewing experiments.

State estimator performance was significantly improved using the new model and Kalman filter gains. With this model, accelerometer measurement estimates tracked the actual measurements very well from the beginning of the maneuver. This was an indication that the state estimator was accurately estimating the flexible mode states. In contrast, the old model produced accelerometer measurement estimates which usually needed five to six seconds to settle. One possible reason for the improved performance is that the old model may not have accurately modelled the flexible modes. The identification process in the previous study only used data from relatively short tests (5 second, or 3-5 cycles of the flexible mode vibrations) which could lead to errors in the flexible mode parameters estimated.

11.6 Attempts to Further Reduce Limit Cycle Vibration

One possible cause of the limit cycle was the spillover of the flexible modes into the rigid-body-mode state estimates. The arms of the structure displayed a significant lateral droop at their tips during flexible mode vibrations which introduced a gravity component into the accelerometer signals, thereby contaminating the state estimates. The larger the vibration amplitude, the greater the gravity component added. One indication that some disturbance was affecting the rigid-body state estimates was the following: the velocity estimate often was not constant when the thrusters were not firing. The apparent accelerations were not friction related because the amplitude of the velocity estimate was observed to both increase and decrease. The gravity component is one example of the difficulty in conducting ground-based verification experiments for space applications.

The terminal phase limit cycle vibration consisted primarily of the first anti-symmetric mode (the scissors mode) of the structure. Two contributors to the large amplitude vibration were (i) the amplitude of the scissors mode vibration excited during the slewing maneuver, and (ii) the lack of effectiveness of the thrusters in damping the scissors mode vibration because of the limit cycle. The methods used to reduce the terminal phase vibrations thus focused on decreasing the amplitude of the scissors mode excited during the maneuver and changing the nature of the limit cycle to increase the damping of the flexible modes.

The nominal 15 degree slew maneuvers presented a difficult vibration control task

to the thruster control routines because the timing of the acceleration and deceleration thruster pulses nearly coincided with the half-cycle period of the first anti-symmetric mode (scissors mode) of the structure. As a result, a large amplitude of scissors mode vibration was present as the structure approached the set point and entered the terminal phase of the maneuver. By comparison, when a 45 degree maneuver was performed, the scissors mode amplitude as the structure entered the terminal phase was less that half of the amplitude which was obtained for a 15 degree maneuver.

The terminal phase limit cycle was not intrinsically related to the scissors mode of the structure. However, for the nominal choices of control parameters, the frequencies of the limit cycle and the scissors mode were very close, resulting in essentially undamped vibrations of the scissors mode. If the limit cycle frequency was changed (for example, by varying a control parameter such as cost-of-control), the scissors mode vibration exhibited a 'beating' effect as the mode moved in-phase and then out-of-phase with the limit cycle.

11.6.1 Non-zero Flexible Mode Weights

One method which both reduced the amplitude of the scissors mode vibration and changed the limit cycle involved the use of non-zero weights on the flexible mode states. During debugging tests for the new model, it was discovered that the default relative weighting values were unity for the rigid body mode, and zero for the flexible modes. The thruster control routines essentially ignored the flexible mode states to calculate the thruster command. The control algorithm only depended upon the rigid body state estimates. The initialization data was modified to permit the operator to specify flexible mode weights prior to a test maneuver.

Performing a slewing maneuver with non-zero mode weights drastically altered the behavior of a run. There were no longer distinct acceleration and deceleration thruster pulses. The non-zero mode weights resulted in feedback gains which required many thruster firings to keep the amplitude of the flexible modes small throughout the maneuver. Depending upon the relative weighting of the first and second anti-symmetric modes, the limit cycle could be adjusted to be near the second (or twist) mode instead of the scissors mode, or could be moved to much higher frequencies.

The two major problems associated with using non-zero flexible mode weights were (i) the poor slewing performance and (ii) the many thruster firings. A slewing maneuver took longer to perform because the controller emphasized reduced excitation of the flexible modes. The frequent thruster firings excited higher frequency modes of the structure, including the torsional modes of the arms, which contaminated the state estimates and were not controllable using the thrusters. Even for small flexible mode weights (1.0, 0.05, and 0.01 for the rigid body, scissors, and twist modes, respectively), these problems obscured any benefit from the use of non-zero mode weights.

A modified approach involved using the non-zero flexible mode weights only during the deceleration and terminal phases of the maneuver. This permitted the structure to be accelerated towards the set point normally but would control the flexible mode vibrations as the entire structure was brought to the set point. The control routines did not allow mode weights to be varied within a maneuver, so the VAX ELN debugger utility was used to insert the desired feedback gains directly into the memory of the controller during the initialization procedures. The control routines calculated two sets of feedback gains: one for the acceleration phase and one for the deceleration phase. Modifying either set of gains with the debugger effectively allowed the flexible mode weights to be varied between the acceleration and deceleration phases of a maneuver.

A breakpoint was set in the control program immediately after the feedback gains were calculated, and the gains determined for various selections of flexible mode weights were recorded using the debugger. When the program reached the breakpoint in the initialization during an actual test maneuver, the desired feedback gains were then inserted into memory and the program was allowed to continue.

Several slewing maneuvers were performed using zero flexible mode weights for the acceleration phase, and non-zero mode weights for the deceleration and terminal phases. The acceleration phase was typical, consisting of a long thruster pulse and a coasting period. However, the deceleration phase had frequent thruster firings and a large overshoot.

Using non-zero flexible mode weights provided greatly increased control of the flexible modes. However, the non-zero mode weights also resulted in poorer slewing performance and significant excitation of higher frequency modes because of frequent thruster firings. No combination of flexible mode weights was found that significantly increased the damping of the flexible modes without adversely affecting the slewing performance. Consequently, non-zero mode weights were not ultimately used to help control the flexible mode vibrations.

One alternative which was not explored because of programming constraints involves the use of non-zero flexible mode weights only after the thrusters bring the rigid body mode of the structure to within the deadzone, near the set point. At this stage the acceleration and deceleration phases of the maneuver would be completed, resulting in good slewing performance. The non-zero mode weights would then be used primarily to allow the thrusters to control the flexible modes. Implementing this option would have required major modifications to the control routines to calculate a third set of feedback gains for the terminal phase. This was judged to be beyond the resources available to the study.

11.6.2 Additional Terminal-Phase Thruster Constraints

Section 4.3 discusses the existing terminal-phase thruster constraints. The constraints were implemented to insure that the thrusters did not add energy the structure during the terminal phase of a maneuver and, thereby, reduce or eliminate the tendency to limit cycle. The constraints consisted of a deadzone around the set point inside of which the thrusters do not fire, and a local velocity constraint which prevented the thruster from firing in the same direction as the estimated local tip velocity. However, these constraints still allowed large amplitude limit cycles, so additional thruster constraints were implemented to further reduce the tendency to limit cycle.

The additional constraints included provisions to permit independent adjustment of the thruster deadzone about the set point, and the conditions which determine entry into the terminal phase. In this manner, the transition to the terminal phase could be delayed until the rigid body states were very near the set point, while a larger thruster deadzone could be used to keep the controller from limit cycling.

The local tip velocity constraint was modified to add a condition on the local tip displacement. The original local velocity constraint required that the thrusters did not fire in the direction of the local velocity (which would add energy to the system). It was found during slewing tests that the local velocity constraint alone often produced a limit cycle wherein the thrusters would immediately fire a small pulse when the tip velocity passed through zero and became opposite the desired thrust direction. This occurred at the peak amplitude of a vibration. Although the pulse was initially fired opposite the local tip velocity, the pulse contained enough energy to change the direction of the tip velocity, adding as much energy to the structure as it had removed.

The added tip displacement constraint precluded the thrusters firing in the same direction as the tip was displaced. The intent of this constraint was to cause the vibrations to achieve maximum velocity (which occurs at zero displacement) before the thrusters were allowed to fire. The thrusters would then remove more energy from the structure at the higher velocity, and any limit cycle due to a minimum thruster pulse would occur nearer to zero displacement.

These additional constraints were added to the thruster control routines and resulted in improved flexible mode damping during the terminal phase. The results from selected slewing maneuver tests are presented in Section 16. The effectiveness of the terminal phase constraints can be seen by comparing the results of thruster maneuvers performed both with and without the constraints enabled.

Although the constraints significantly increased the damping of the flexible modes and reduced the tendency to limit cycle, they did not add as much damping to the flexible modes as expected. One possible reason for the reduced effectiveness was the contamination of the state estimates because of the gravity components in the accelerometer signals. The tip velocity and displacement were derived from the state

estimates. Any errors in the state estimates would also cause errors in the velocity and displacement estimates, and hence would reduce the effectiveness of the constraints.

Section 12

Implementation of On-Off Thruster Slew Control in Combination with the Linear Actuators

12.1 Introduction

This section discusses the control strategies used to combine the linear actuators (PMAs and hub torquer) with the single-step-optimal control of the on-off thrusters. The linear actuators could be added to the single-step-optimal control algorithm or controlled independently. A decentralized control approach was chosen in part because of lack of design tools for the single-step-optimal control methodology. The linear actuator control algorithms were designed to minimize the possibility of one actuator control loop destabilizing another, or contaminating the state estimator (Kalman filter) used for the thruster control algorithm. Preliminary tests showed that the linear actuator control laws actually increased the stability of the thruster control algorithm.

12.2 Possible Control Strategies

Several strategies were considered to combine the linear actuators with the single-step-optimal control for the thrusters. The linear actuators used in this study were proof-mass actuators (PMAs) and the air-bearing table torque motor described in Section 3. The linear actuators can be integrated into the single-step-optimal control algorithm. Alternatively, a decentralized control approach can be taken in which the linear actuators are controlled by independent control laws.

The single-step-optimal control algorithm is inherently capable of handling multiple actuators and known actuator failures. Floyd [1] performed simulations which combined linear actuators with on-off thrusters using a single-step-optimal control methodology. The control routines in the main control application which implement the single-step-optimal control strategy for the thrusters were written in a vector formulation to allow changes in the number of sensors, actuators, and states of the system.

However, a close inspection of the control routines revealed discrepancies between the actual program code and the description of the algorithm given in the final report of the predecessor AFAL study [1]. Assumptions about the dimensions of various matrices were hard-coded into the control routines. Also, there were errors in the code associated with the use of multiple actuators. The single-step-optimal control routines would have had to be re-written and debugged to allow inclusion of the linear actuators.

Another drawback of the single-step-optimal control algorithm was the unavailability of design tools. The single-step-optimal algorithm results in a non-linear control law for non-linear actuators such as the on-off thrusters. When multiple actuators are used with the single-step-optimal algorithm, an actuator lumping criteria is used to combine the effects of all the actuators. There is no guarantee that parameters chosen using linear control design techniques will be satisfactory when implemented. As was demonstrated in Section 11, tuning the thruster control parameters for the flexible modes was largely a matter of trial and error, even when only one actuator was used.

Independent control laws for the linear actuators can readily be designed and simulated using standard linear control design techniques. However, decentralized control laws introduce the possibility of one controller destabilizing another. Also, the Kalman filter estimates used in the thruster control routines can be contaminated by the linear actuators if they are not explicitly included in the Kalman filter model.

It was decided to combine the linear actuators and the thrusters using independent (decentralized) control laws. The alternative approach which involved re-writing and debugging the single-step-optimal control routines was judged to be a major task. Even after the single-step-optimal control routines were corrected, the selection of appropriate control parameters would be tedious and error prone, at best, because of the lack of design tools. Colocated sensor/actuator control laws were developed for the linear actuators to minimize the possibility of destabilizing the integrated system.

12.3 Effects of Independent Linear Actuator Control

Independent control laws for the linear actuators introduce the possibility of interaction between the controllers. The actuator dynamics might also contaminate the state estimates for the single-step-optimal thruster control routines. These undesirable effects were minimized in two ways: the PMA control law was chosen to insure stability and the slewing tests were designed so that the hub torquer and thrusters would not be active at the same time.

Section 13 presents the development of the PMA control law. A PMA and a linear accelerometer were located at the tip of each arm, forming a colocated sensor/actuator pair. A local velocity feedback control law was chosen to insure maximum stability robustness. Using local velocity feedback, the PMAs introduced additional damping to

the flexible modes of the structure. The PMAs still affected the Kalman state estimator for the thruster control algorithm, but they primarily appeared as modelling errors in the damping terms.

Section 14 describes the development of the hub torquer control law. The hub torquer appears as a disturbance or bias torque to the state estimator for the thruster control algorithm. Simultaneous operation of the hub torquer and thruster control algorithms could possibly destabilize the thruster control. Therefore, it was decided to use the hub torquer and thrusters during different phases of the slewing maneuver. The thrusters were used to accelerated and decelerate the structure while the hub torquer was used for fine pointing and vibration control during the terminal phase of the maneuver. Because the thrusters were not used after the hub torquer was activated, the thruster control loop could not be destabilized.

The state estimator continued to run during the terminal phase of the maneuvers (for data collection purposes). However, the thrusters slewed the structure to very near the set point so the torque applied by the hub torquer during the terminal phase was relatively small and, consequently, did not significantly contaminate the state estimates.

12.4 Combining the Independent Control Algorithms

The main experimental control application implemented the single-step-optimal thruster control algorithm. Combining the control algorithms for the linear actuators with the thruster control algorithm consisted primarily of including the control routines from the PMA and hub torquer development applications into the main control application. Also, control logic was added to permit actuators (e.g., all of the PMAs) to be activated or deactivated at various points throughout a maneuver. Modifications were made to the initialization and data logging routines to include specific PMA and hub torquer requirements.

Baseline slewing tests were run using the thrusters only to verify that the additional control logic worked correctly. Additional tests were performed with various combinations of actuators to verify the initialization and data logging routines. Only minor programming mistakes were discovered during these preliminary tests. The decentralized control strategy performed as intended with no indication of control loop interaction or destabilization. In fact, the added damping from the PMAs eliminated limit cycling of the structure when the thrusters were used during the terminal phase of a slewing maneuver. The state estimates required for the thruster control algorithm were not significantly affected by either the PMAs or the hub torquer.

Section 16 describes and discusses the results from a series of slewing tests performed using various combinations of the actuators.

Section 13

Proof-Mass Actuator Development

13.1 Characterization of the Proof-Mass Actuators

The proof-mass actuators are mounted in pairs at the tip of each beam. Initially, it was anticipated that there could be non-linearities in the force constant (lbs/amp) of each proof-mass/voice coil pair, wherein the force generated would vary with the stroke of the actuator. In order to minimize this particular non-linearity, the PMAs were mounted back-to-back so that a lower control force in one unit would be compensated for by a greater force exerted by its partner. Figure 13-1 illustrates the design of this back-to-back mounting.

However, BEI Kimco had difficulty in predicting the performance of their linear actuators because they had not previously produced a voice-coil linear actuator with the required extended stroke. The extended stroke was needed for the PMA to be effective in damping low-frequency structural vibrations. Nevertheless, BEI Kimco assured CSDL that the non-linearities would not be excessive and would be dependent solely upon position.

However, upon receipt of the actuators, the accompanying calibration test results showed that the PMAs were extremely non-linear, with variations in the force constant dependent upon position, current level, and the direction of the applied force. A graphical representation of these varying parameters can be seen in Figure 13-2. The force constant varies over the stroke of the device, varies with the amperage (here shown at three discrete levels), and depends upon whether a pulling or pushing force is being commanded.

The back-to-back mounting of the PMAs, at first thought to be a solution to the non-linearities, did prove to correct for some of the force dependency upon position. This helpful effect is illustrated in Figure 13-3. Notice that the curves flattened somewhat, showing less variation with stroke. Still, the force constant was dominated by the remaining non-linearities, and these effects remained to be addressed in the development of control laws for the proof-mass actuators.

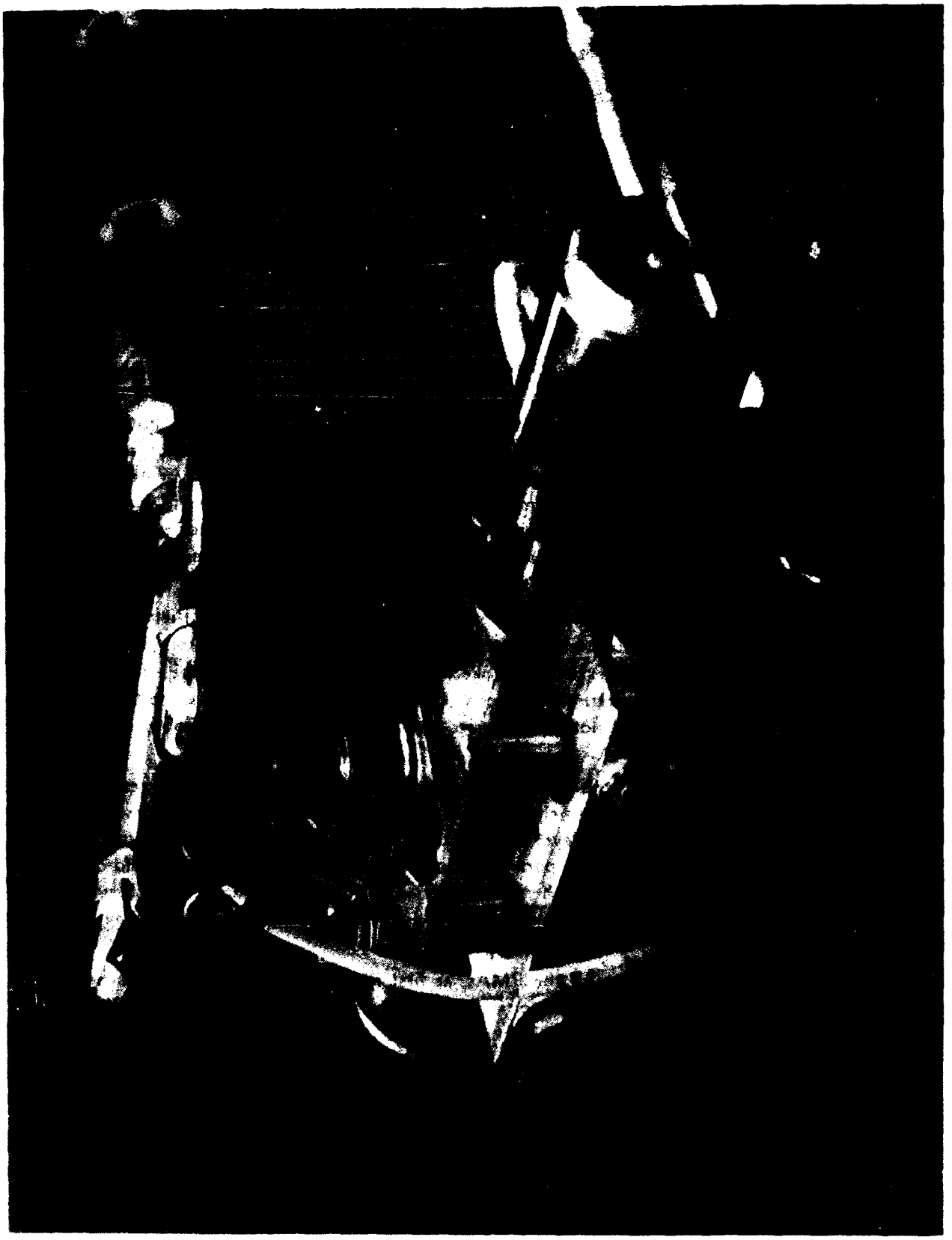

Figure 13-1. Back-to-back mounting of linear actuators at tip of beam.

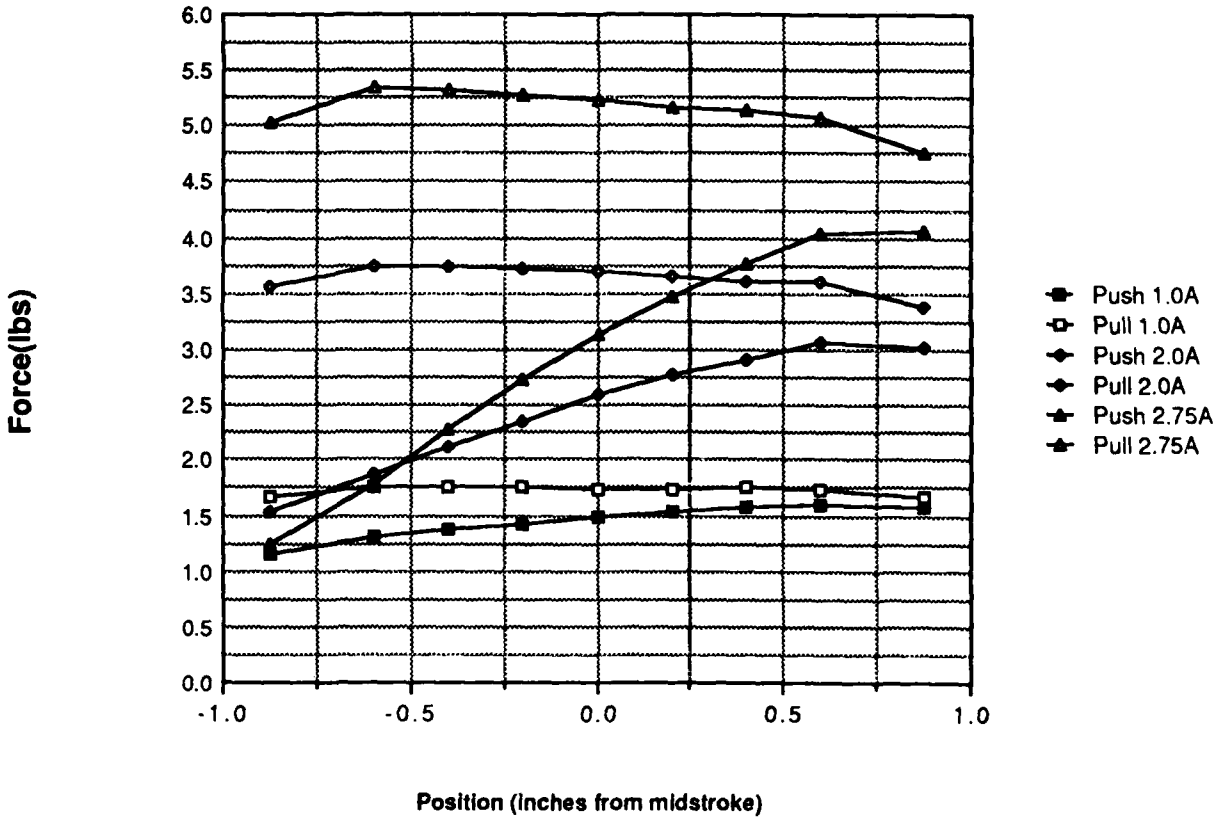

Figure 13-2. Force non-linearity of voice coil/magnet proof-mass actuator

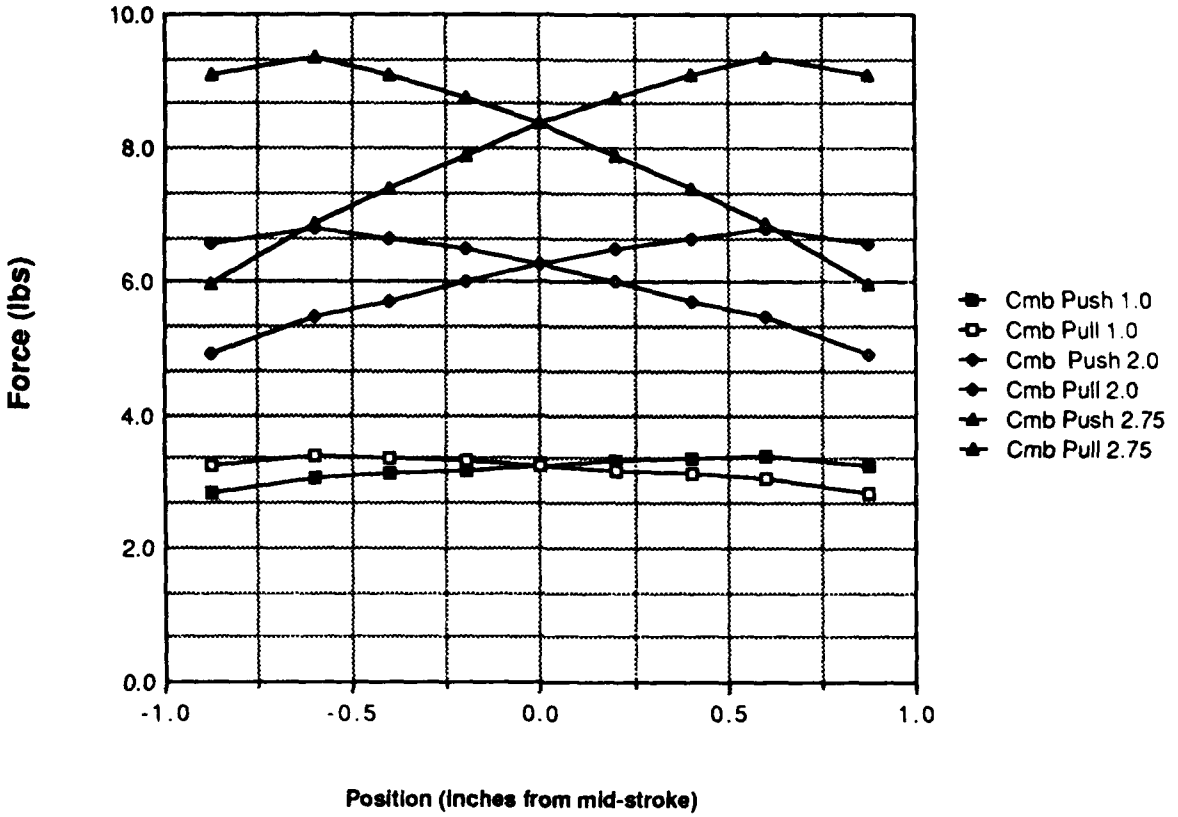

Figure 13-3. Force non-linearity of back-to-back PMA configuration

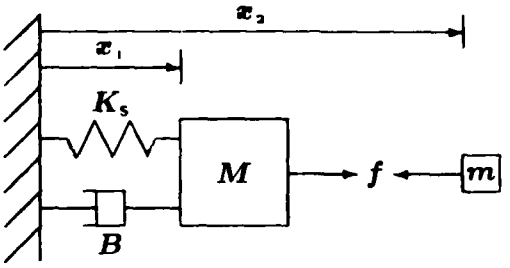

Figure 13-4. Dynamics of proof-mass coupled to a second-order oscillator.

13.2 Development of Decentralized Control Laws for the PMAs

The prior development of PMA control laws, described in Section 5 through Section 8, required accurate knowledge of the force being applied by the actuators. This requirement is characteristic of all linear control law development. In order to apply these control laws, it would be necessary to use extensive gain-scheduling to guarantee the expected force, or to design an extremely robust dynamic compensator, thus sacrificing performance.

However, an alternative decentralized control approach was possible due the fact that that the sensors and actuators were colocated. Control laws were formulated which are dependent solely upon velocity and displacement at the actuator location. By generating control forces which oppose local velocity, additional damping is provided, and the nonlinearity disappears as an issue. Specifically, while the amplitude of the force varies with the stroke, it still opposes the velocity and thus still adds some amount of damping. Consequently, the complexity and computational requirements of gain-scheduling were avoided, while an adequate level of damping performance was maintained.

13.2.1 Local Variable Control Laws for the PMAs

For a single beam, the dynamics of the structure appear as a simple second-order oscillator. The proof-mass is then coupled to the oscillator by the commanded force, f. This model is illustrated in Figure 13-4. As the PMA exerts reaction forces, note that a positive commanded force results in a positive acceleration of the beam M, but a negative acceleration of the proof-mass m. An examination of the dynamics of this system shows the significance of the sign difference.

The system shown in Figure 13-4 can be modelled by the following two second-order equations:

$$M\ddot{x}_1 + B\dot{x}_1 + K_s x_1 = f \qquad (13-1)$$

and

$$m\ddot{x}_2 = f \qquad (13-2)$$

Note that the two systems are coupled only by the force f. When the feedback loop is closed, the simple oscillator has become part of a more complex fourth-order system. Thus the manner in which these two systems interact is determined by the details of the feedback law.

The system described by Eqs. (13-1) and (13-2) can be put into a state-space format that allows a straightforward examination of the dynamics of the closed-loop system. The state vector is defined as:

$$x = [x_1\ \dot{x}_1\ x_2\ \dot{x}_2]^T \qquad (13-3)$$

and there is one input, f. There are three measurements in the output vector y, as follows:

(1) the velocity of the large mass M ($\dot{x}_1$);

(2) the relative position of the proof-mass m to the large mass ($x_2 - x_1$); and

(3) the relative velocity of the proof-mass m to the large mass ($\dot{x}_2 - \dot{x}_1$).

Using this notation, the standard state-space representation follows:

$$\begin{aligned} \dot{x} &= Ax + Bf \\ y &= Cx \end{aligned} \qquad (13-4)$$

with

$$A = \begin{bmatrix} 0 & 1 & 0 & 0 \\ -K_s/M & -B/M & 0 & 0 \\ 0 & 0 & 0 & 1 \\ 0 & 0 & 0 & 0 \end{bmatrix} \qquad (13-5)$$

$$B = \begin{bmatrix} 0 & 1/M & 0 & 1/m \end{bmatrix}^T \qquad (13-6)$$

$$C = \begin{bmatrix} 0 & 1 & 0 & 0 \\ -1 & 0 & 1 & 0 \\ 0 & -1 & 0 & 1 \end{bmatrix} \qquad (13-7)$$

The model parameters derive from the NASTRAN modelling described in Section 9 and are reproduced in Table 13-1. By including frequency, modeshape, damping, and mass property information, the dynamic model of Eq. (13-4) characterizes the physical system which consists of a single cantilevered beam with a proof-mass actuator attached to its tip. This representative model was the basis for stability analyses and the evaluation of various control laws.

Table 13-1. PMA model parameters from NASTRAN analysis

M (slugs)	m (slugs)	K_s (lb./ft.)	B (lb./ft/sec)
0.971	0.136	5.598	0.0396

13.2.1.1 Feedback Laws

Using the dynamic model of Eq. (13-4) the control feedback matrix $\bar{K}$ is defined as follows:

$$f = \bar{K}\, y \qquad (13-8)$$

with

$$\bar{K} = \begin{bmatrix} K_{\text{vel}} & K_{\text{pmadisp}} & K_{\text{pmavel}} \end{bmatrix}$$

where

K_{vel} is the feedback gain for the velocity of the large mass M;

K_{pmadisp} is the feedback gain on the position of the proof-mass m relative to the large mass M (it is this gain which produces a restoring force between the proof-mass and the beam to keep the PMA centered); and

K_{pmavel} is the feedback gain on the velocity of the proof-mass m relative to the large mass M. This gain provides extra damping to prevent the PMA from oscillating about its nominal position.

The closed-loop system dynamics then take the following form, permitting both stability analysis and system simulation:

$$\begin{aligned} \dot{x} &= \left(A + B\bar{K}C\right) x \;+\; B f \\ y &= \qquad C x \end{aligned} \qquad (13-9)$$

13.2.1.2 Local Velocity Feedback for Vibration Damping

As shown by Balas in Reference [33], the use of negative velocity feedback guarantees stability for systems with colocated sensors and actuators.* The effective damping of the closed-loop system will vary directly with the feedback gain. In the case of the feedback law represented by Eq. (13-8), if the motion of the proof-mass m (setting K_{pmadisp} and K_{pmavel} to zero) is disregarded, K_{vel} can be set to any negative value and thereby

*In a practical control system finite actuator and sensor time constants limit the bandwidth for which stability robustness is guaranteed; however, this frequency can be made arbitrarily large.

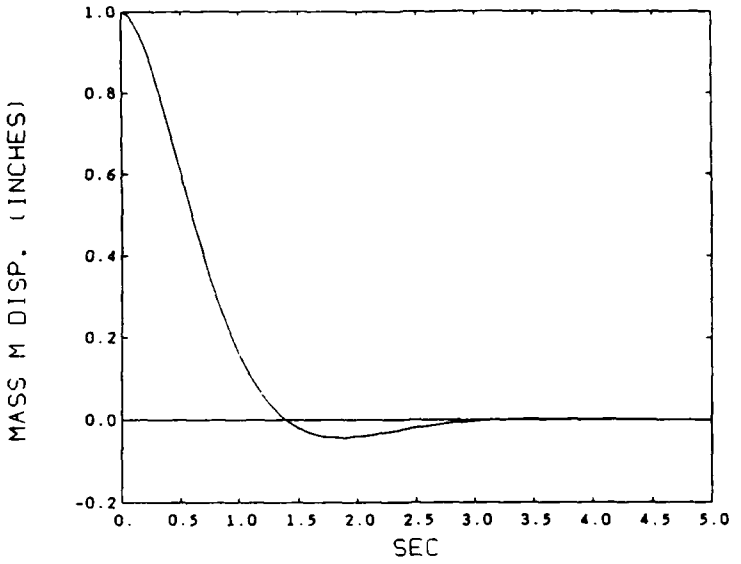

Figure 13-5. Large mass M response to initial conditions, with negative velocity feedback and no proof-mass position constraints.

guarantee additional damping in the oscillation of the mass M. The response of this negative velocity feedback closed-loop system to a 1 inch initial displacement of both masses is shown in Figures 13-5 and 13-6. Note that the oscillation of the mass M is almost immediately eliminated.

This very effective negative velocity feedback relationship is clearly illustrated in Figure 13-7 where the solid line represents the mass M velocity and the dotted line represents the commanded force. However, Figure 13-6 shows that this force command results in excessive displacement of the proof-mass.

For implementation of a realizable PMA system, some constraints had to be placed upon the displacement of the proof-mass. The first attempt to resolve this problem led to the addition of the K_{pmadisp} and K_{pmavel} gains. However, when the loop is closed with sufficient gain to prevent the PMA from violating the displacement constraint, the resulting fourth-order system is **unstable**.

Figures 13-8 and 13-9 show the initial condition response of this unstable system. As the proof-mass is accelerated to produce a force opposing the velocity of mass M, the PMA position restoring gain commands a force which acts to oppose the velocity feedback. Consequently, the **net force** acting upon the beam does not increase the system's damping but actually acts as a destabilizing positive velocity feedback. This effect is most clearly seen in Figure 13-10 where both the velocity of the mass M and the total commanded force $\left(f = \bar{K}y\right)$ are shown.

However, root-locus analysis of this system pointed toward an interesting solution. When there were no constraints on proof-mass displacement, negative velocity feedback

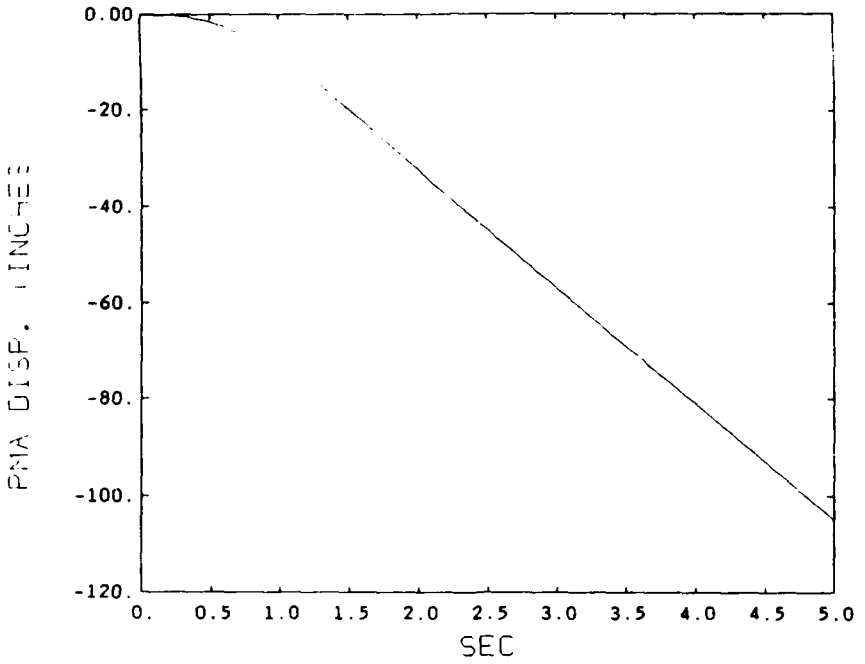

Figure 13-6. Proof-mass displacement response to initial conditions, with negative velocity feedback and no proof-mass position constraints.

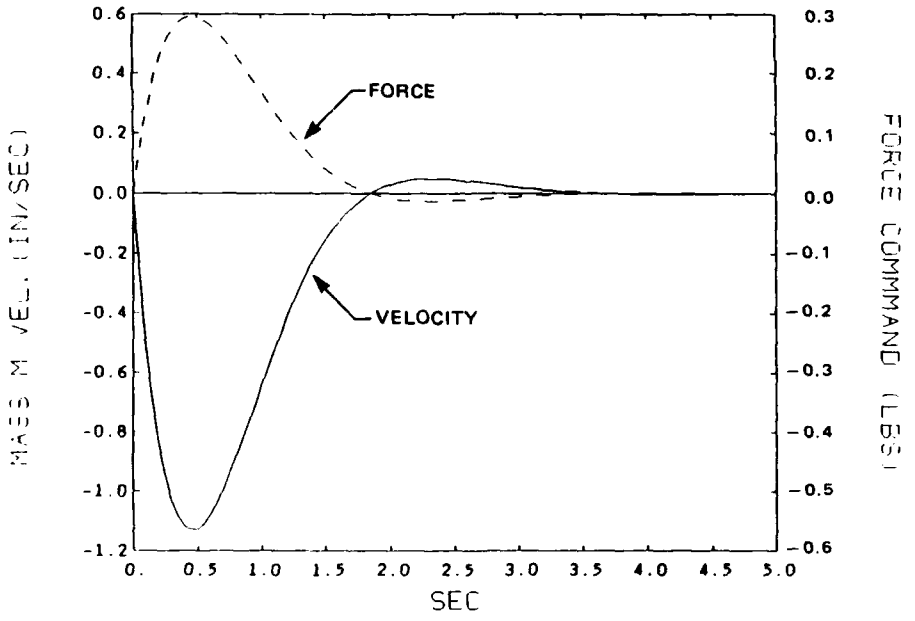

Figure 13-7. Phase relationship between large mass M velocity and commanded force for negative velocity feedback with proof-mass position constraints.

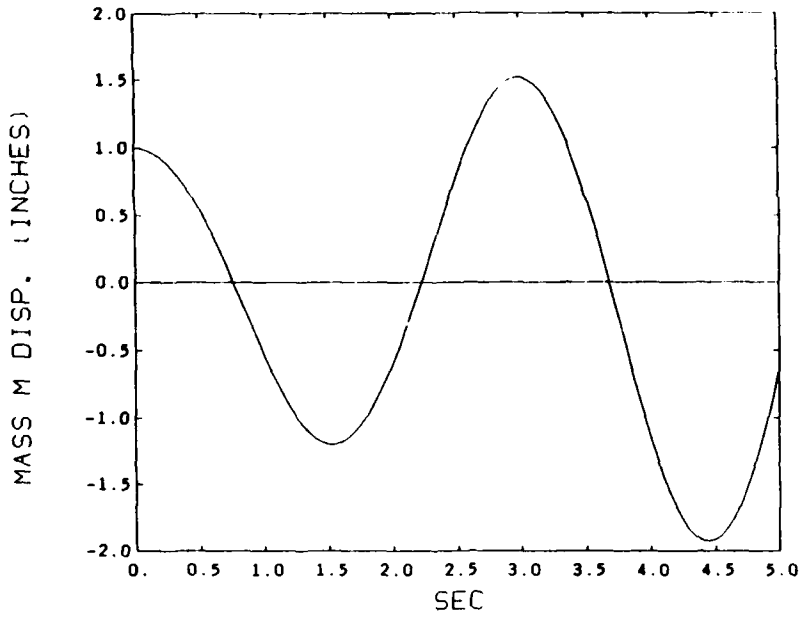

Figure 13-8. Large mass M response to initial displacement, with negative velocity feedback and proof-mass position constraints.

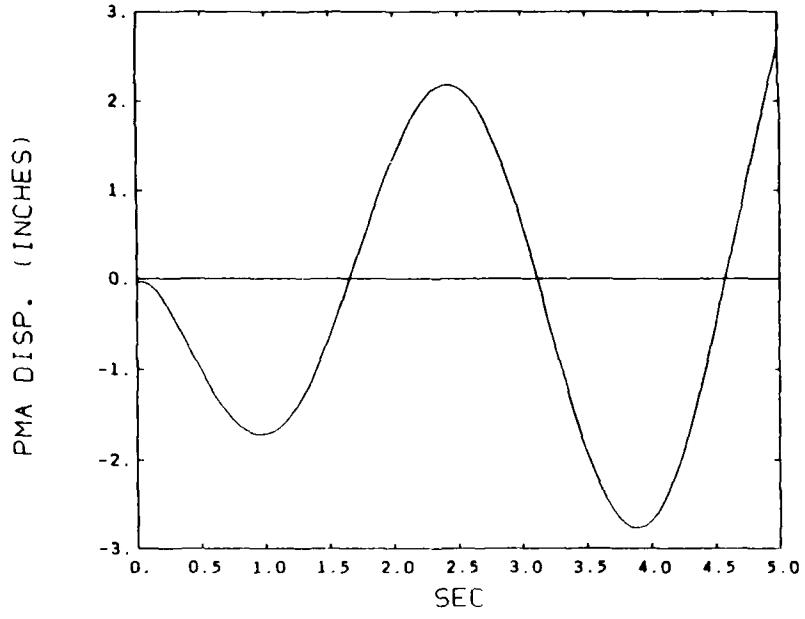

Figure 13-9. Proof-mass response to initial displacement, with negative velocity feedback and proof-mass position constraints.

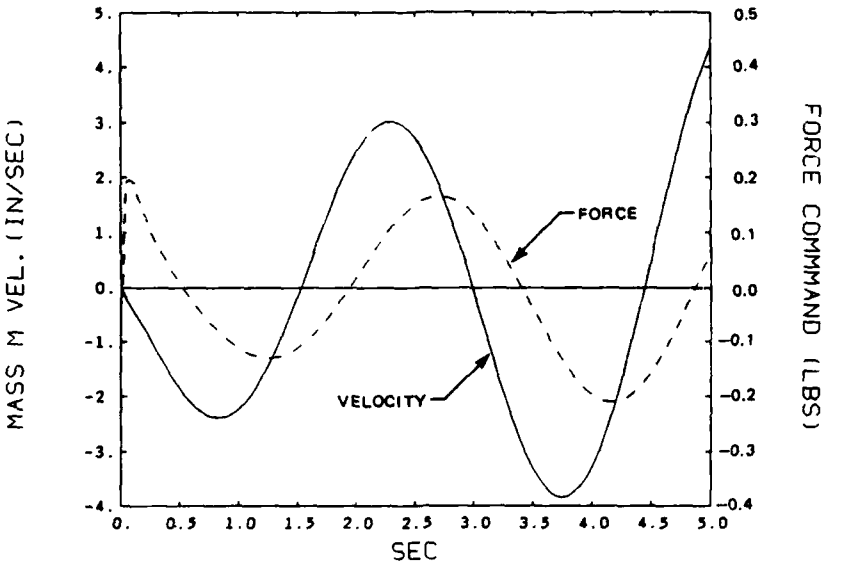

Figure 13-10. Phase relationship between large mass M velocity and commanded force for negative velocity feedback with proof-mass position constraints.

increased the damping of the system, while positive velocity feedback would null the small amount of natural damping and result in an unstable system. However, examination of the root-locus of Figure 13-11 (and the more detailed view in Figure 13-12) shows that the opposite effect occurs when there are proof-mass displacement constraints. The lightly damped poles near to the origin are associated with the dynamics of the mass M. The faster poles are those of the proof-mass and its restoring force loop. Notice that even a small negative feedback gain sends the poles of the mass M into the right half-plane where previously this same gain had a stabilizing effect. When a positive velocity feedback gain is applied, the system shows greatly improved damping. This trend continues until the PMA poles go unstable with higher gain. Thus, we have a system which is unstable for negative feedback gains and stable for positive feedback (up to a limiting value).

However, this reversal of the required feedback sign does not reflect a change in the force applied to the oscillator by the PMA. Applying force in phase with the velocity is counter-intuitive, and simulations show that the net force applied does, in fact, oppose the local velocity. Figure 13-15 shows how the composite force command computed from the gain vector $\bar{K}$ does imply negative velocity feedback despite the positive gain on mass M velocity. Damping has been increased significantly, as seen in Figure 13-13, while still satisfying the displacement constraints on the proof-mass. This analysis verified the PMA control concept; implementation of the control law is described next.

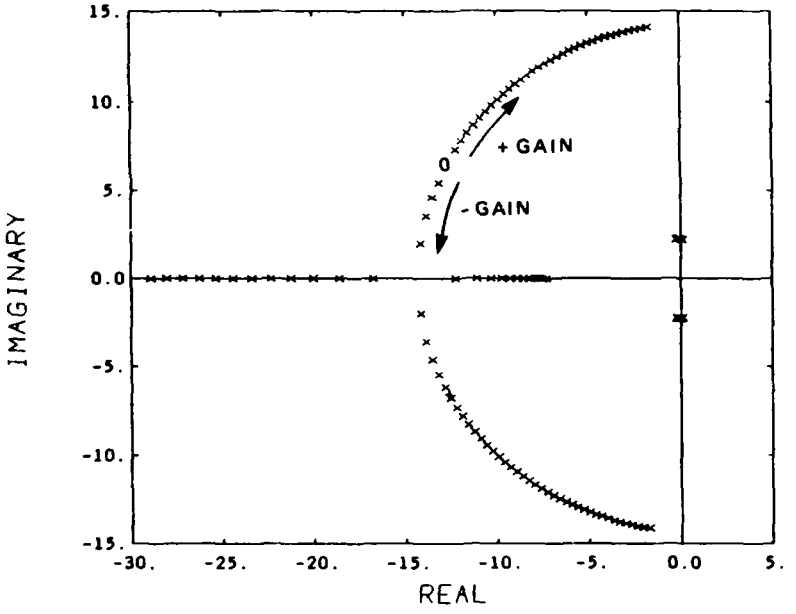

Figure 13-11. Root locus as K_{vel} varies from negative to positive values, proof-mass position loop closed.

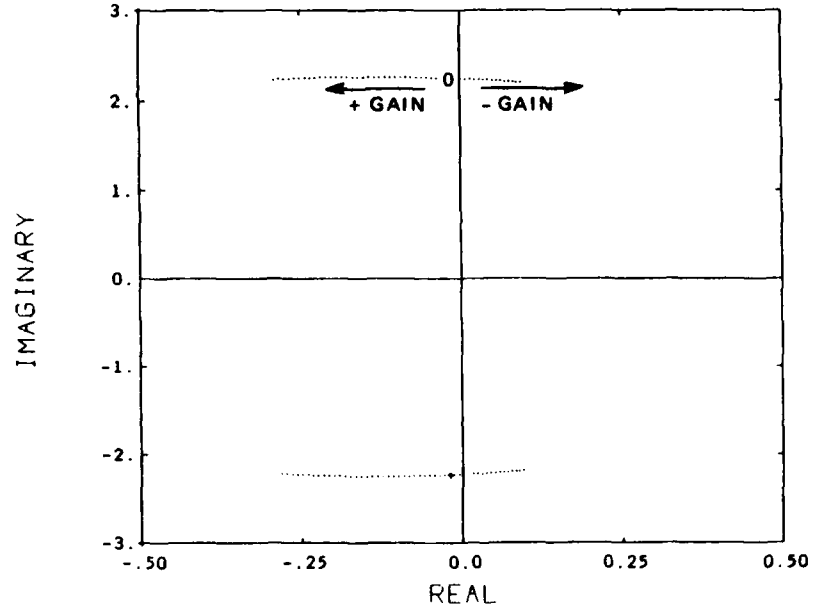

Figure 13-12. Root locus detail: poles of large mass M.

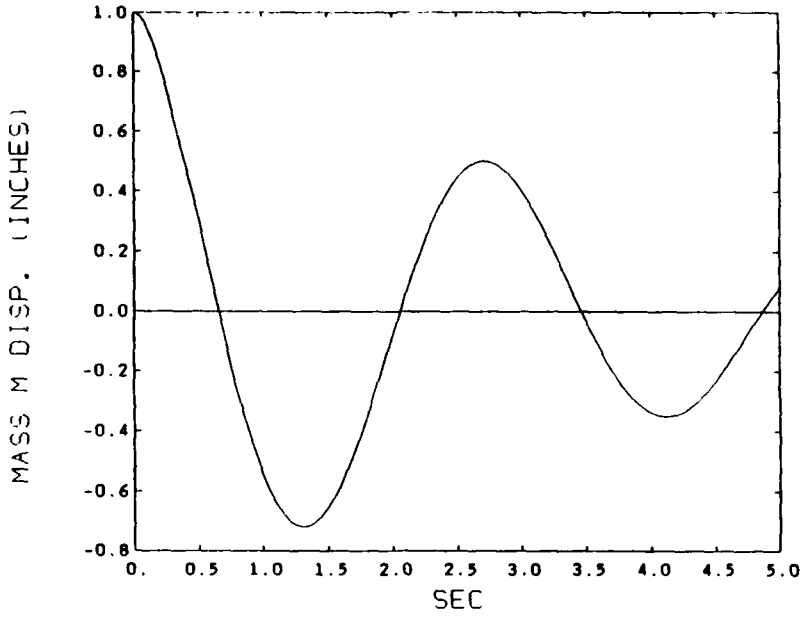

Figure 13-13. Large mass M response to initial displacement, with positive velocity feedback and proof-mass position constraints.

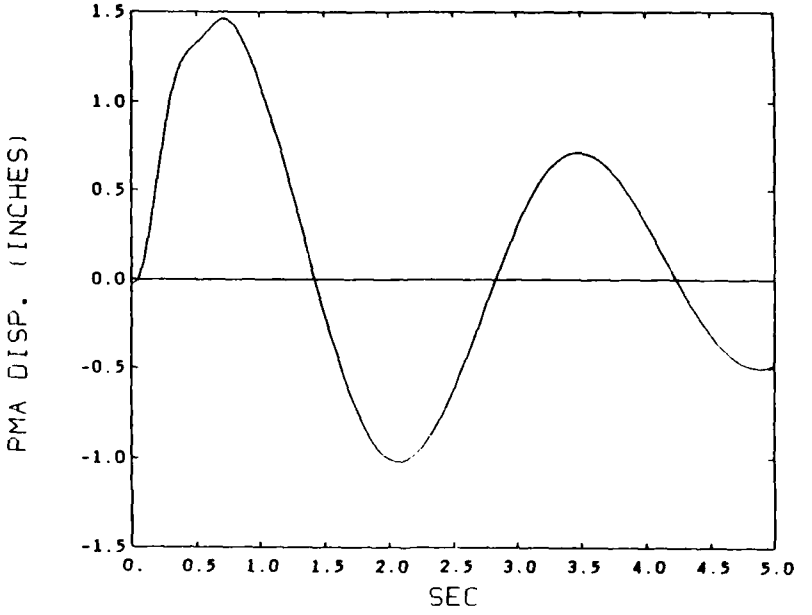

Figure 13-14. Proof-mass displacement response to initial conditions, with positive velocity feedback and proof-mass position constraints.

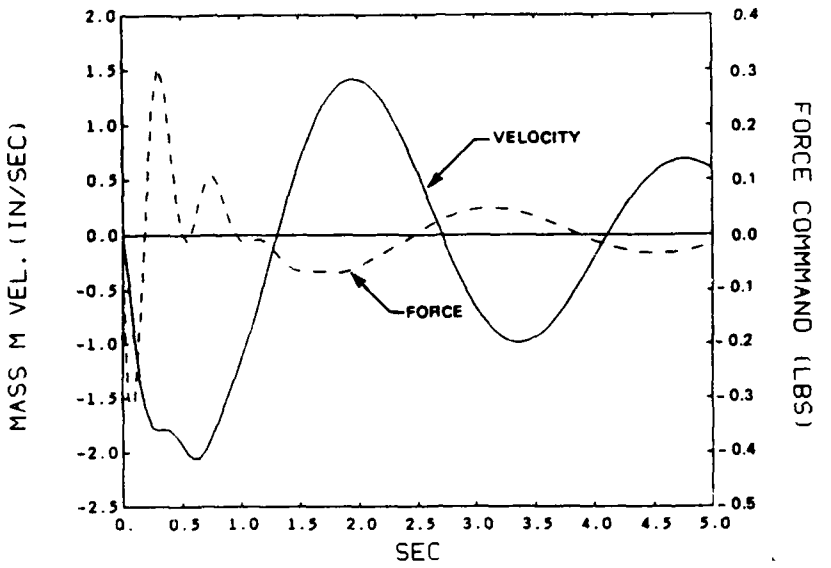

Figure 13-15. Phase relationship between large mass M velocity and commanded force for positive velocity feedback with proof-mass position constraints.

13.3 Single-beam Verification of PMA Control Concept

As an initial step in verifying the capabilities of the proof-mass actuator, a single cantilevered beam was mounted to a test-bed as illustrated in Figure 13-16. In this way the control parameters could be tuned before the actuators were installed on the full-scale experiment. The previous section described a control strategy based on the feedback of three variables which are either directly measured or derived from the sensor complement. The variables are as follows:

Tip velocity: accelerometers are colocated with the PMAs at the tip of each beam. This signal can be integrated to determine the tip velocity.

PMA displacement relative to the beam: there are LVDTs affixed to the PMAs which directly measure this parameter.

PMA velocity relative to the beam: the LVDT signal can be differentiated to form this parameter.

These signals were combined with their respective gains via the gain vector $\bar{K}$ and fed back into the servo-amplifiers which drive the PMAs.

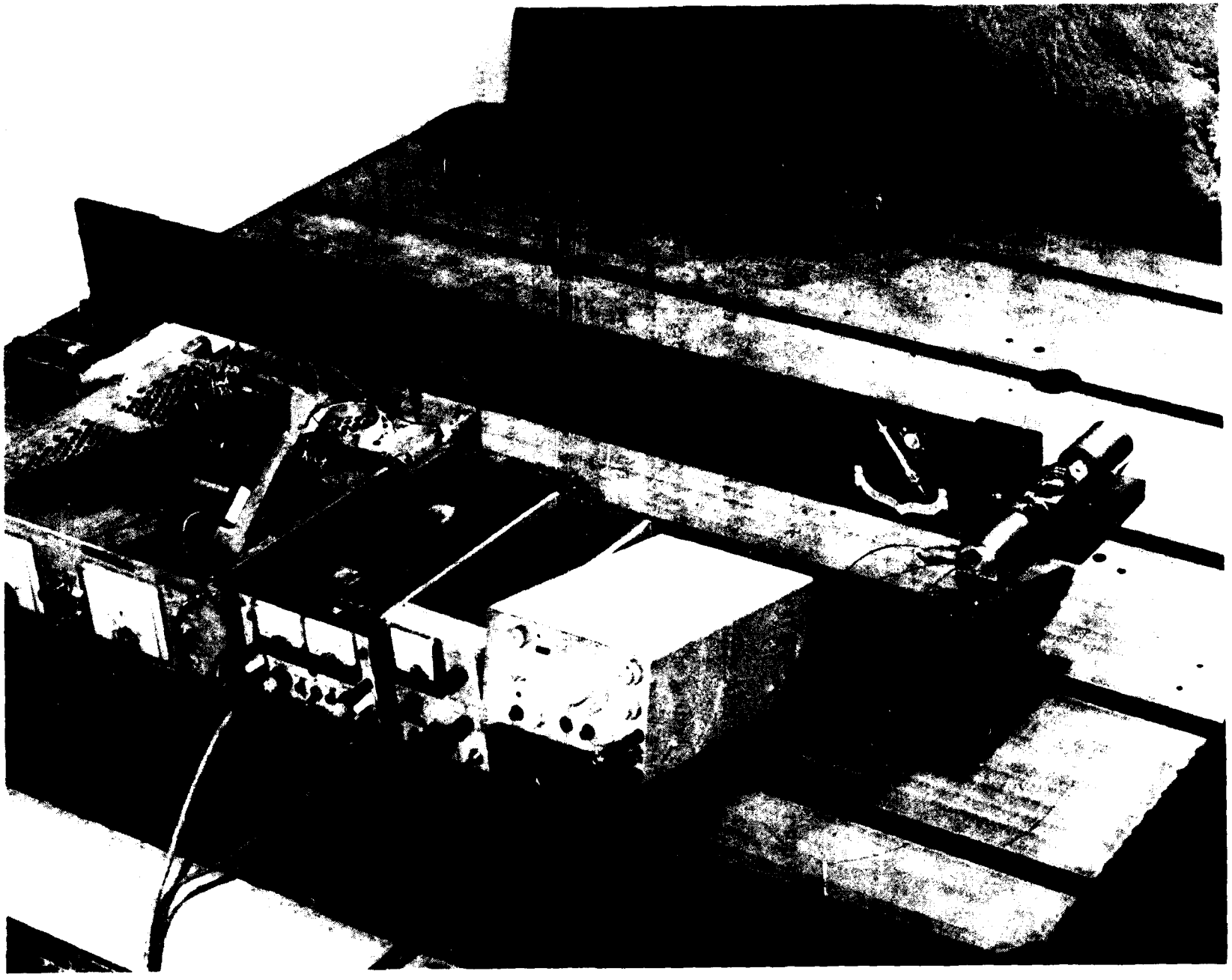

Figure 13-16. Test-bed experiment with single cantilevered beam and PMA.

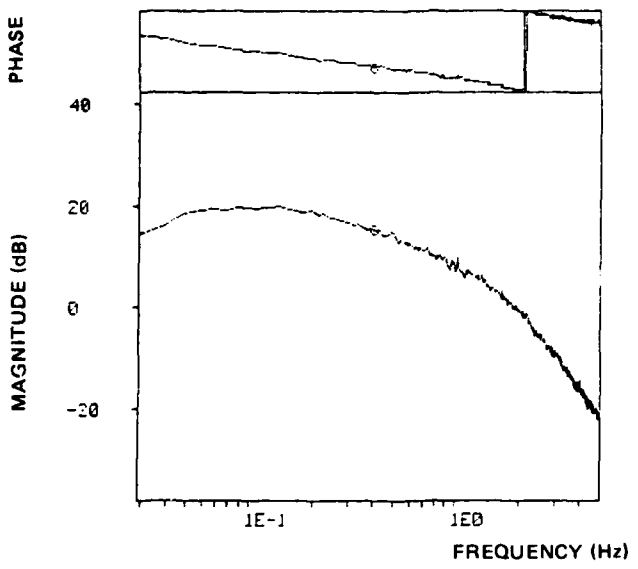

Figure 13-17. Frequency response function for PMA analog band-pass integrator.

13.3.1 Implementation of the Analog PMA Control Law

Preliminary testing of the control strategy was accomplished using an analog compensator. There were two major design considerations concerning the integration of the accelerometer signal to generate the tip velocity. The first concern arose from the PMAs ability to excite the torsional modes of the beam. It was necessary to low-pass the accelerometer signal to minimize the control force commanded at frequencies higher than the first bending mode of the beam (0.39 Hz). Secondly, when the PMAs are mounted on the full-scale CSDL/AFAL experiment, they are subjected to large angle slews of the whole structure. Because the actuators are constrained with respect to available stroke, it was not desirable to permit the actuators to respond to the near DC velocities that occur during a large-angle slew. Consequently, a high-pass filter with a cutoff frequency placed below the first bending mode frequency was used to reject DC and slowly varying velocities. The resulting composite accelerometer filter consisted of a band-pass integrator with 90° of phase shift at the first bending mode frequency, and signal attenuation both below and above this frequency. The frequency response function of this analog filter, implemented with op-amps and passive components, was determined using the Zonic modal analyzer. This plot is shown in Figure 13-17.

The remaining feedback variables, namely PMA position and velocity, required more straightforward implementations. The LVDT included built-in signal conditioning, and the position signal required only a gain stage for inclusion in this experiment. Similarly, the LVDT signal was differentiated to derive the PMA relative velocity signal which was then fed back with an appropriate gain. The overall PMA controller implementation is shown in Figure 13-18.

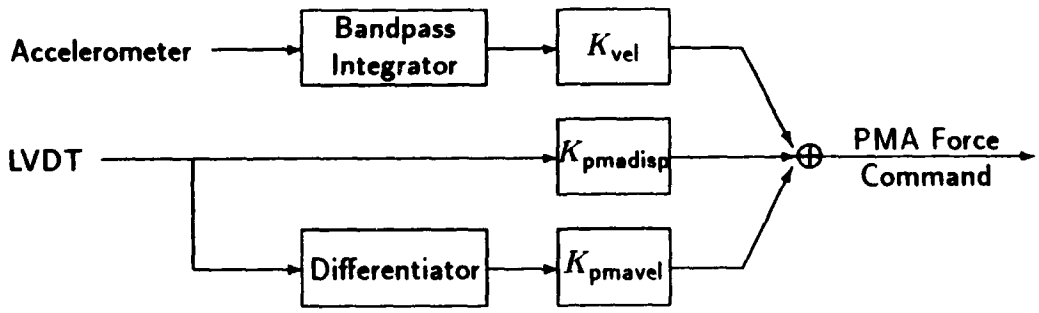

Figure 13-18. Control law implementation for proof-mass actuators.

13.3.2 PMA Performance on the Single-Beam Test Bed Installation

For preliminary PMA effectiveness evaluation, a single cantilevered beam with proof-mass actuator attached was mounted to a test-bed as shown in Figure 13-19. The PMA proved to be quite effective at attenuating vibration of the single-beam in this configuration. Transient response was used to determine the performance of the closed-loop system relative to free decay. An initial displacement was given to the beam with only the PMA centering loop active. The baseline damping ratio of $\zeta = 0.0085$ was established for the beam by fitting an exponential envelope to the response. A plot of this free decay is shown in Figure 13-20.

In order to determine the effectiveness of the PMA, a similar initial displacement was given to the beam, the system was allowed to settle into free oscillation, then the PMA vibration control was activated. A plot of the ensuing response is shown in Figure 13-21.

Note that the vibration is effectively removed within approximately 3 cycles. A fit of the exponential envelope indicated that $\zeta = 0.018$, or 18% damping. **This damping ratio represents an increase by more than a factor of twenty over the natural damping of the system**. These results sufficiently proved the suitability of the PMA control strategy. Consequently, application of the PMAs to the full-scale CSDL/AFAL experiment was initiated.

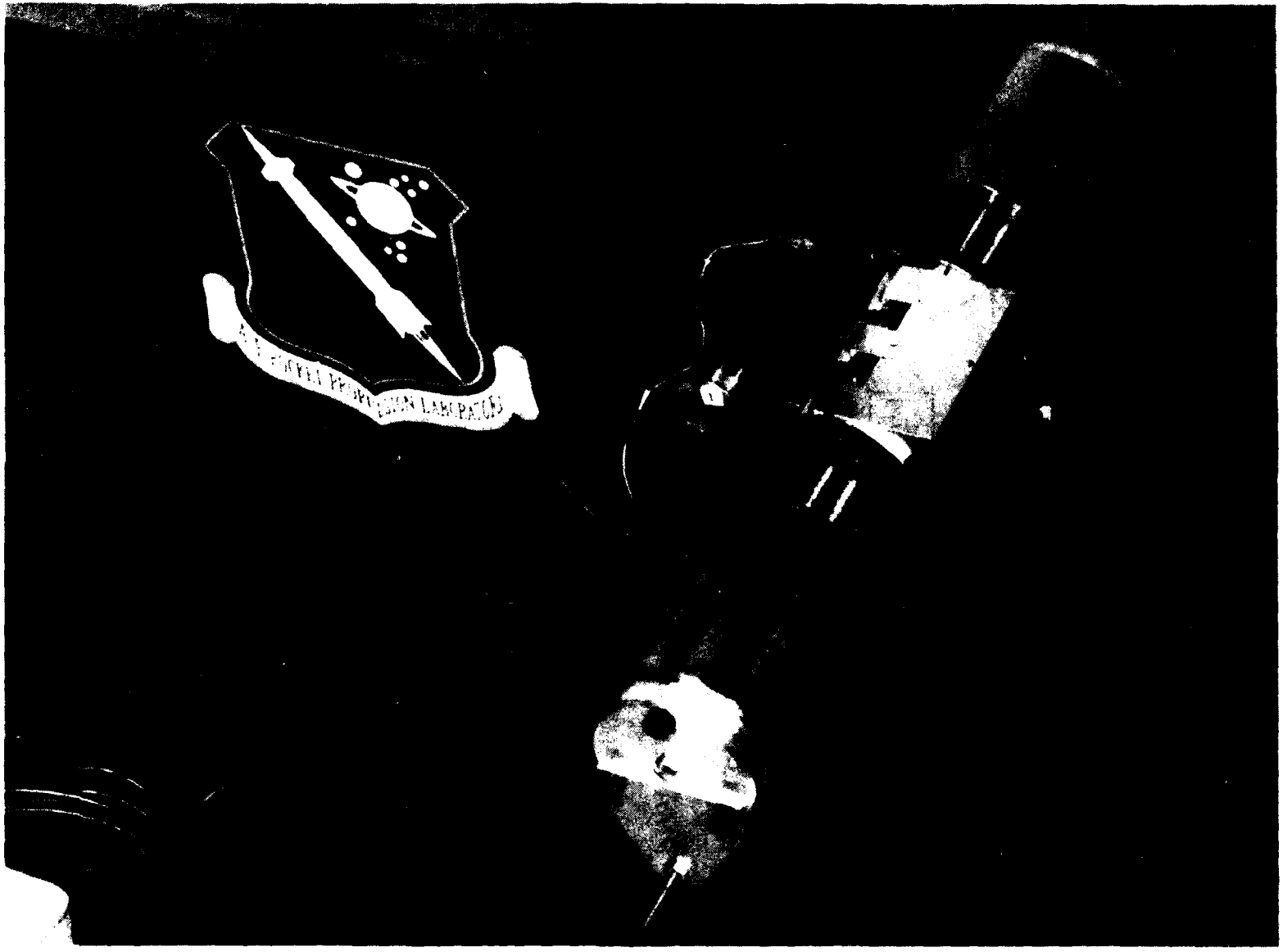

Figure 13-19. Detail of proof-mass actuator mounted on the cantilever beam.

13.4 Development of Real-Time Software for PMA Control

The analog implementation of the PMA control laws, described in the previous section, proved that the appropriate control parameters were established. However, for better integration with the overall CSDL/AFAL experiment, a conversion to digital control was desirable.

In order to implement a digital controller, discrete-time representations of the analog filters must be generated. For a linear time-invariant system, the discrete-time representation of the continuous-time differential equations takes the form of the following difference equation evaluated at each time step:

$$x[n+1] = \Phi x[n] + \Gamma u[n] \qquad (13-10)$$

$$y[n] = Cx[n] + Du[n] \qquad (13-11)$$

where Φ is the state transition matrix, Γ is the discrete-time control influence matrix, and the C and D matrices are unchanged from the continuous-time case. The discrete-time matrices were derived using the zero-order hold (ZOH) transformation, which results in a very satisfactory match of frequency response characteristics with the equivalent continuous-time filter (see Reference [34]).

The ZOH transformation was applied to the continuous-time system using the Ctrl-C control system design package. Within Ctrl-C, the frequency response characteristics of the bandpass integrating filter were adjusted to match those of the analog filter previously determined with the Zonic modal analyzer. The resulting compensator matrices are given in Appendix K. Note that the Bode plot of this discrete-time filter shown in Figure 13-22 is equivalent to that of the corresponding analog filter shown in Figure 13-17.

The discrete-time representation of the filters was subsequently coded using VAX-ELN Pascal which incorporates real-time programming features. A general filter routine, *GENFILTER*, was developed which could be called at each time step during the experiment run to propagate the filter states and determine the outputs. The initial parameters of this routine were read from a disk file, thus providing a simple means of altering the control parameters without having to change and recompile the real-time software.

The discrete-time control loops were first verified on the single-beam test bed experiment. Running at a 50 Hz sample rate, the performance of the digitally controlled PMA was found to be equivalent to that of the analog benchmark. In addition, there was much more flexibility in the use of the PMAs because of the software implementation. Active control could easily be turned on or off, leaving the position loop intact. These were activated by the software, eliminating the need to flip switches or disconnect wires as was the case with the analog controls.

13.5 Application of PMAs to the Full-Scale CSDL/AFAL Experiment

The addition of the proof-mass actuators to the full-scale experiment structure was made much easier by the decision to implement the controls in software. No new analog filter hardware was required. Only four identical filter routines had to be run (in parallel) in the software.

An initial concern was whether the four independent control loops associated with the PMAs could destabilize the system through their interaction. While this possibility is usually a major concern in decentralized control applications, the decision to implement a velocity feedback control law at each tip diminished the potential for instability because of the colocated sensor/actuator configuration. As was discussed previously, when the net control force opposes the local velocity with negligible time delay due to phase lag effects, energy will be removed from the system. It was this characteristic of the PMA damper which permitted the use of decentralized control. Consequently, the addition of the PMAs to the full experiment derived directly from the single beam experiments—global control was not required to insure robust stability and performance.

Previous tests on the single beam were primarily concerned with damping the first bending mode of the beam. However, there are multiple structural modes associated with each bending mode of a single beam. These structural modes involve symmetric and antisymmetric motion of the opposing pairs of beams. Consequently, the frequencies of the modes which the PMAs were required to damp were spread over a small range, and no longer exactly matched the frequency of the band-pass integrating filter. During slewing maneuvers, the two antisymmetric structural modes dominated the response of the structure in this frequency range. These are referred to as the 'scissors' and 'twist' modes; they are illustrated in Figures 13-23 and 13-24.

In order to evaluate the PMA effectiveness, the structural modes were excited by injecting white noise into the hub torquer. Frequency response functions (FRFs) were generated between the input to the hub torquer and the output of the accelerometers at each tip. These responses were analyzed using the "Zonic Modal" software package to determine the frequency and damping of each structural mode. The open-loop (no active PMA control) FRF is shown in Figure 13-25; it displays the two resonant peaks of the scissors and twist modes.

The closed-loop system response was quite different. The damping provided by the proof-mass actuators resulted in lower resonant peaks, as evidenced in Figure 13-26. Note how the scissors mode peak is nearly eliminated, while the twist mode peak is reduced and somewhat smoothed. Analysis with the Zonic software resulted in the damping information presented in Table 13-2. These values highlight some differences between the test-bed and full-scale experiments. The baseline open-loop damping of the twist mode was significantly greater than that of the single beam or of the scissors mode. This was because of the friction in the air-bearing table and the large amount of

Table 13-2. Open and closed loop PMA damping data for full scale experiment.

Mode	Open Loop		Closed Loop	
	Freq.(Hz)	Damping (%)	Freq.(Hz)	Damping (%)
scissors	0.35	0.86%	0.36	12.29%
twist	0.78	3.70%	0.81	5.33%

hub motion present in the twist mode (see Figure 13-24). However, the most notable change was a small decrease in the additional damping provided by the PMAs. These discrepancies may be described as follows.

First of all, the damping was previously calculated by fitting an exponential envelope to a single transient response. The values calculated with the modal analyzer are certainly more accurate and reliable.

Secondly, the twist mode presents a very different boundary condition in comparison with the cantilevered beam. Hub motion permits a pinned-free mode in which there is less tip motion and more rotation and displacement at the base of the beams. Consequently, the control effectiveness of a tip mounted linear actuator is reduced. In this case, examination of the NASTRAN-generated modeshapes (see Appendix C) shows that the PMA would be 50% less effective on the twist mode than it would be on either the scissors mode, or the first bending mode associated with the test-bed experiment.

Finally, the bandpass integrator which filters the accelerometer signal begins to attenuate at the frequency of the scissors mode. Consequently, the gain of this filter is reduced by approximately 50% at the twist mode frequency. A combination of all these factors resulted in less additional damping of the twist mode due to the PMAs.

Nevertheless, the PMAs proved to be quite effective in this application. A significant amount of damping is introduced into the system, although the greatest effect is restricted to the scissors mode. Later, this mode will be shown to be the primary source of residual vibrational energy in a slew maneuver. Consequently, the bias of PMA effectiveness towards the scissors mode was appropriate. Additionally, the implementation of a hub torquer control system is an effective supplement to the PMAs. The torquer will be shown to be quite effective on the twist mode because this mode exhibits significant hub motion which can be directly controlled by the hub torque actuator. The development of this hub control strategy and its implementation is described in the next section.

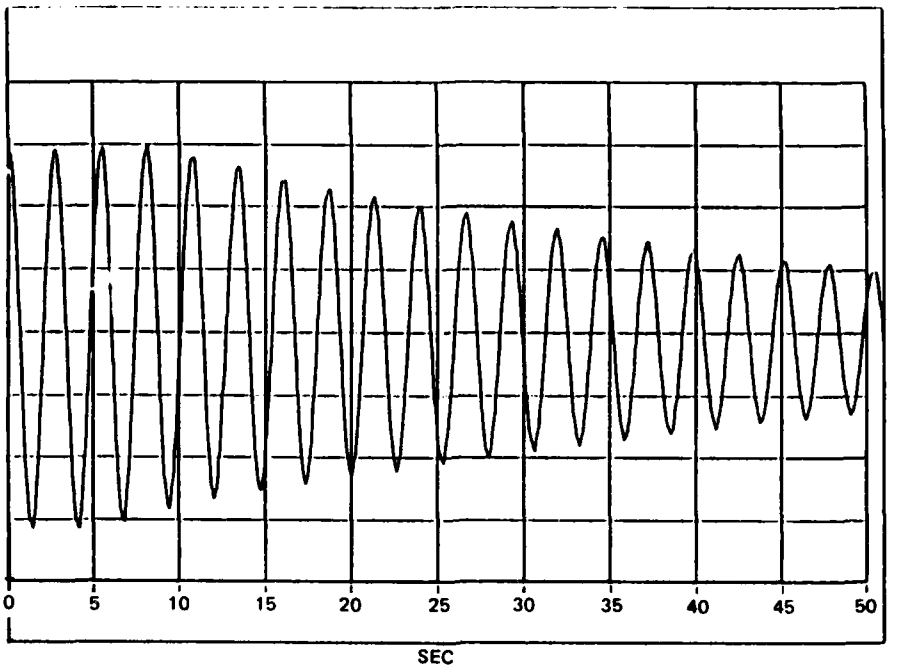

Figure 13-20. Free decay of single-beam.

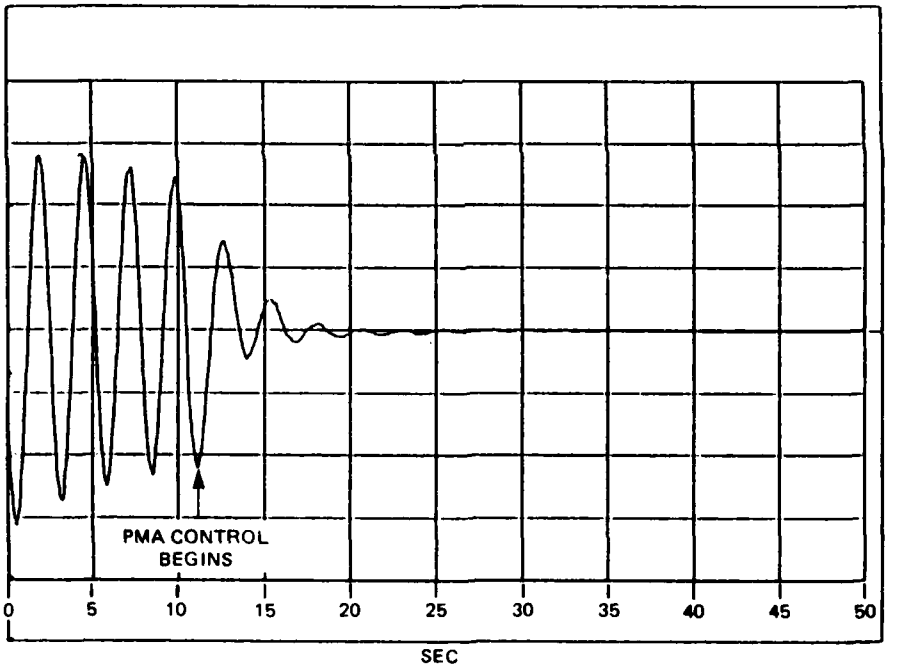

Figure 13-21. Transient damping of the single beam with PMA active.

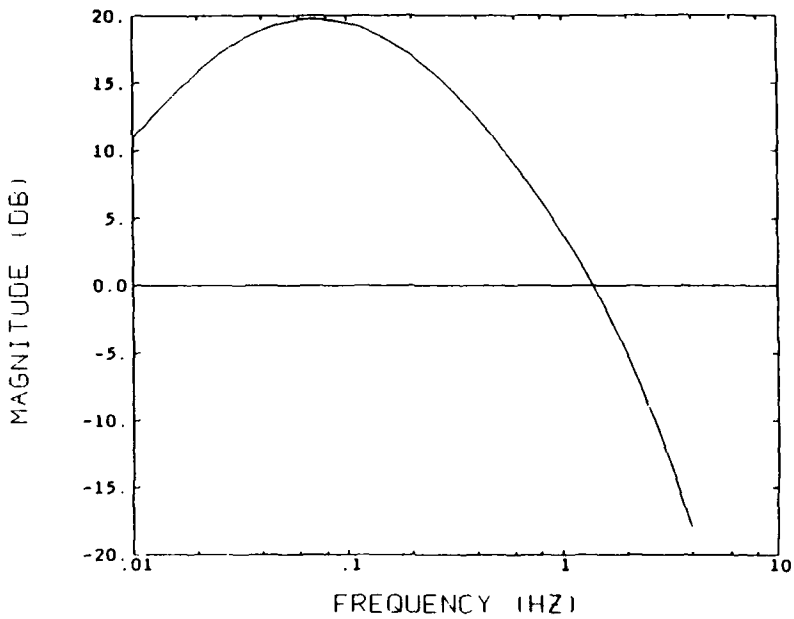

Figure 13-22. Frequency response function of the discrete-time PMA band-pass integrator.

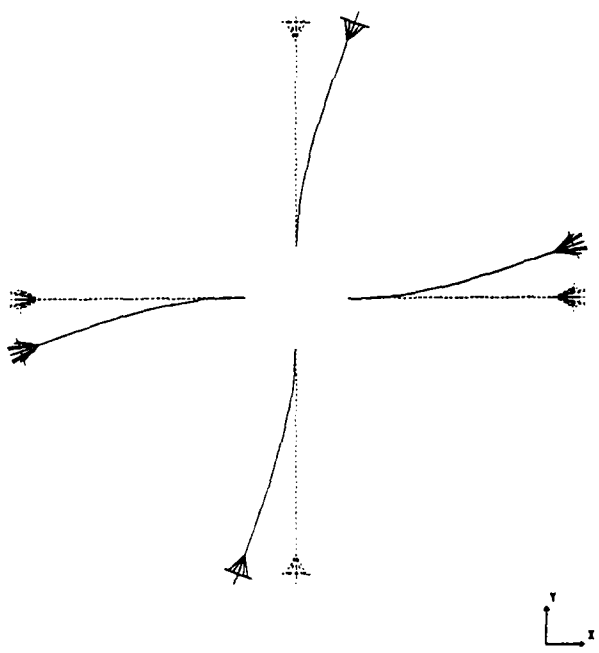

Figure 13-23. Scissors mode displacement.

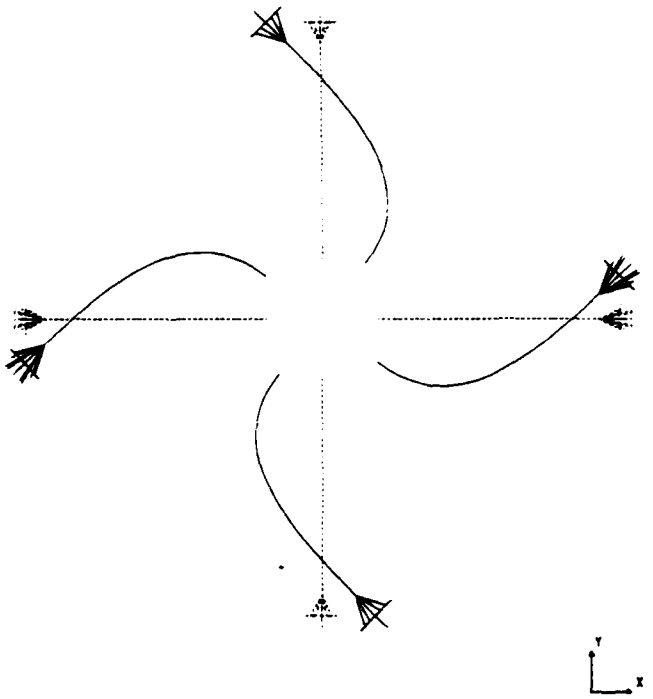

Figure 13-24. Twist mode displacement.

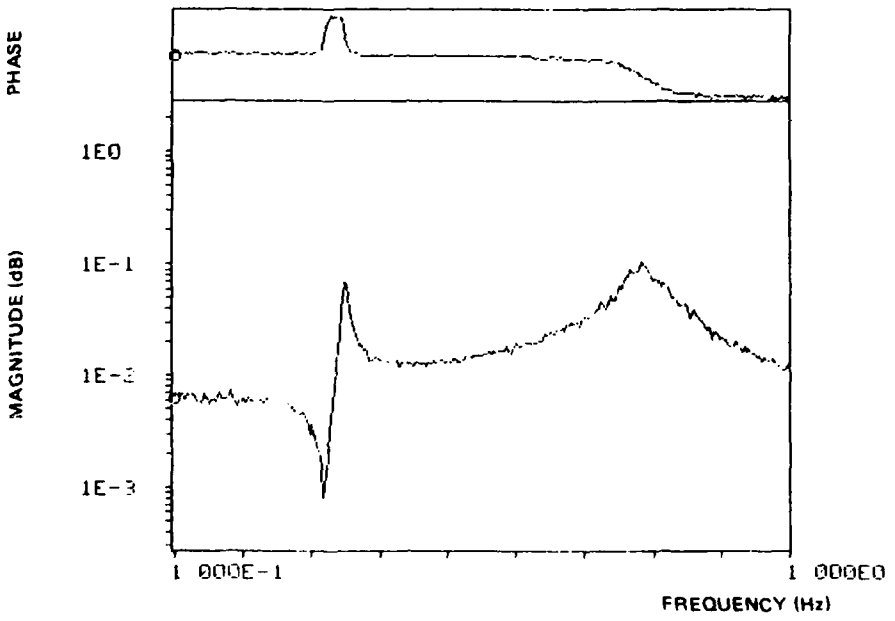

Figure 13-25. Open loop frequency response function (PMAs inactive).

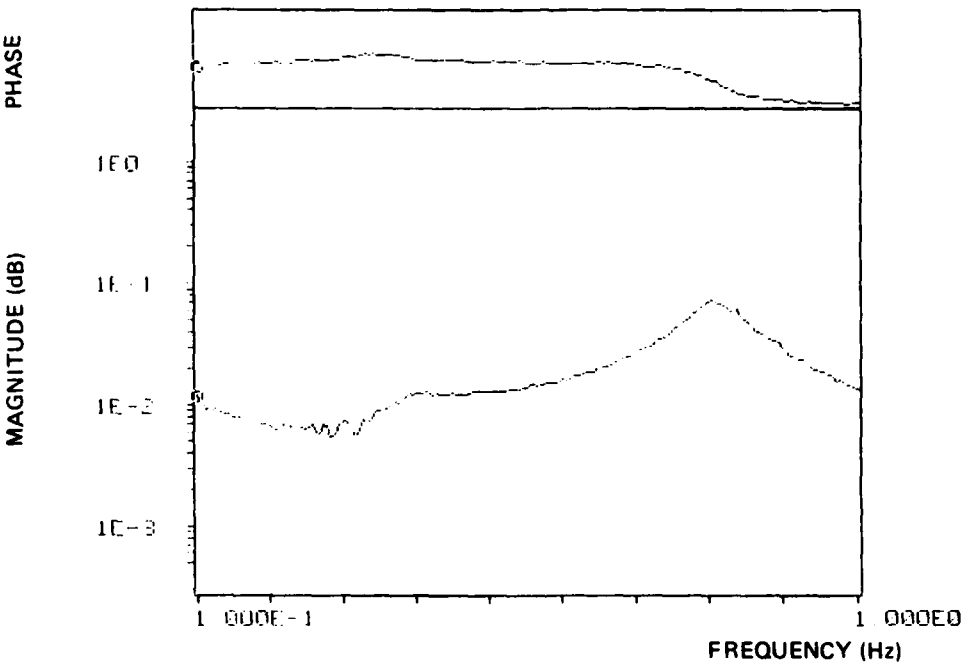

Figure 13-26. Closed loop frequency response function (PMAs active).

Section 14

Hub Torque Controller Development

14.1 Introduction

The previous section explored the use of PMAs for vibration damping using a simple dynamic model of an isolated cantilever beam. For the hub torquer control design, a structural model was developed using NASTRAN to represent the overall dynamics of the full-scale experiment. For hub-actuated fine pointing, the primary actuator applies torque to the hub and the relevant output is the hub angle. The three dominant structural modes were included in the model—the rigid body mode, the twist mode, and the scissors mode. The first two symmetric modes of the structure were also included in the NASTRAN model, but because they do not involve hub motion, they are neither controllable nor observable with the hub torquer and hub angle sensor, respectively. As in the analysis of the previous section, the group of cantilevered-beam second bending modes were excluded from the analysis because they are separated from the controller bandwidth by more than a decade in frequency. Furthermore, the hub torquer does not significantly excite these modes. The desired bandwidth of the controller is low enough that significant spillover to these modes was not expected to be a problem. Examination of the plant frequency response from the hub torquer input to the hub angle output, Figure 14-1, shows that the twist mode resonance at 0.80 Hz dominates the response. Consequently, the main goal in the synthesis of a hub torquer control law is to damp this resonance while achieving sufficient pointing control bandwidth of the structure as a whole.

14.2 Hub Torquer Control Law Development

The PMAs are only capable of AC force generation and thus are only useful as vibration control actuators. However, the hub torquer is effective for both vibration damping and fine pointing/tracking. Consequently, the hub compensator was designed to accomplish both of these control functions. As discussed in the previous section, the

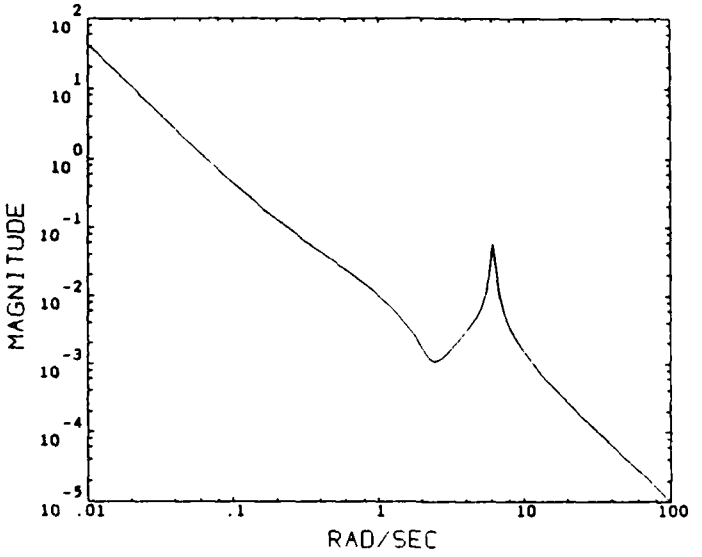

Figure 14-1. Plant frequency response (hub torquer input to hub angle output).

PMA controller is well suited to a decentralized control approach because of the superior stability robustness properties of the colocated actuator/sensor control law used in that design.

The initial control synthesis for the hub torquer took the form of a proportional, integral, and derivative (PID) feedback design. The design objective was to achieve 'adequate' performance using a simple control law which would serve as a point of comparison with more complex controller designs.

14.2.1 PID Control for the Hub Torquer

The design of the PID control initially ignored the flexible modes of the structure. A loop was closed around the rigid-body mode, and the selection of the feedback parameters depended solely upon a choice of the appropriate closed loop bandwidth ω_n, and damping ζ. The structure was modelled by its inertia J, and a double integrator. The feedback terms, namely proportional (K_p), integral (K_i), and differential (K_d) were determined using the following relationships:

$$K_p = J\,\omega_n^2 \qquad (14-1)$$

$$K_i = 0.1414\,J\,\omega_n^3 \qquad (14-2)$$

$$K_d = 1.414\,J\,\omega_n \qquad (14-3)$$

These feedback parameters result in a critically-damped closed-loop response for a system in which the structural mode frequencies are well separated from the controller

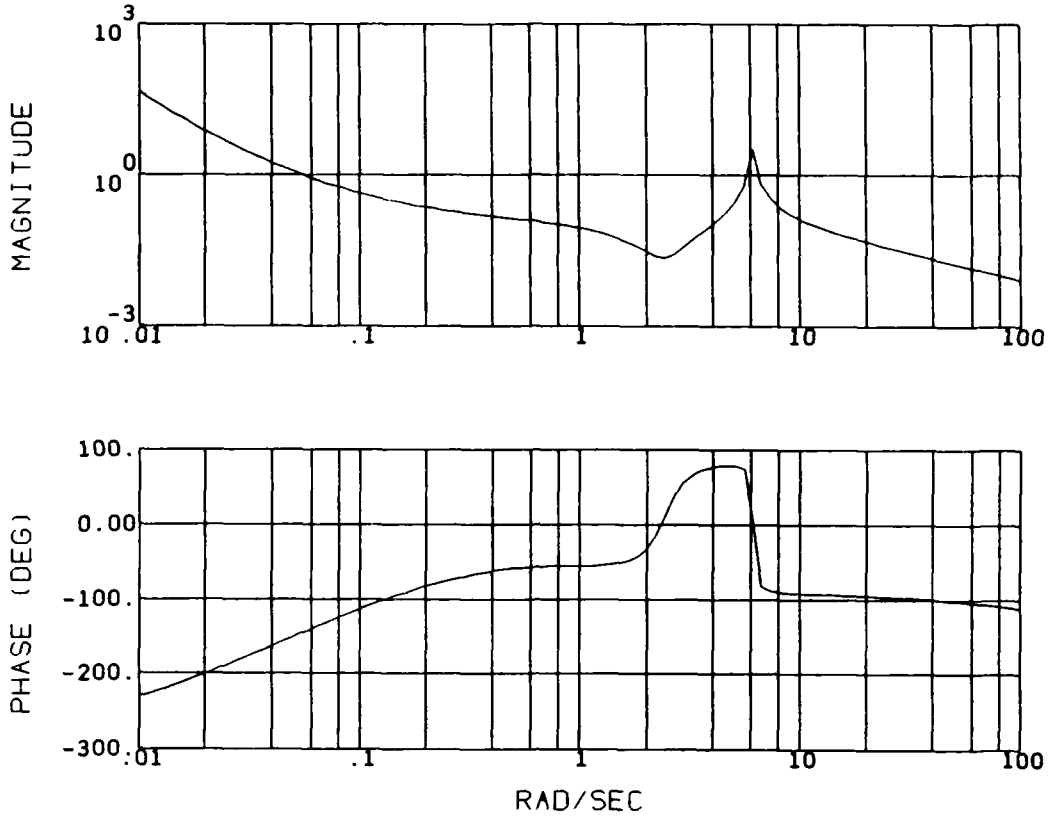

Figure 14-2. Forward-loop frequency response (PID control, $\omega_n = 0.1$ rad/sec).

bandwidth ω_n. However, the existence of flex modes closer to the controller bandwidth will impact the performance of the system.

The important parameter in this design is the choice of bandwidth. As the bandwidth is increased to achieve faster pointing response, the closed-loop system can be destabilized due to spillover from the twist mode resonance. If the bandwidth is decreased significantly, the pointing performance suffers. Consequently, the joint objectives of performance and stability must be balanced; both transient response and frequency domain information can be used to aid this task.

The initial performance objective was a controller bandwidth of $\omega_n = 0.1$ rad/sec. The forward-loop frequency response for this system is shown in Figure 14-2. While the system is stable, the step response as seen in Figure 14-3 is sluggish and is underdamped. Also evident is the twist mode resonance in the initial stage of the response.

To improve the response, a notch filter was added to the compensator at the frequency of the twist mode. This filter minimized the torque command input in the frequency range of the twist mode resonance, thus minimizing the excitation of the twist mode. The frequency response of the compensator including the notch is shown in Figure 14-4. Note that the forward-loop frequency response shown in Figure 14-5

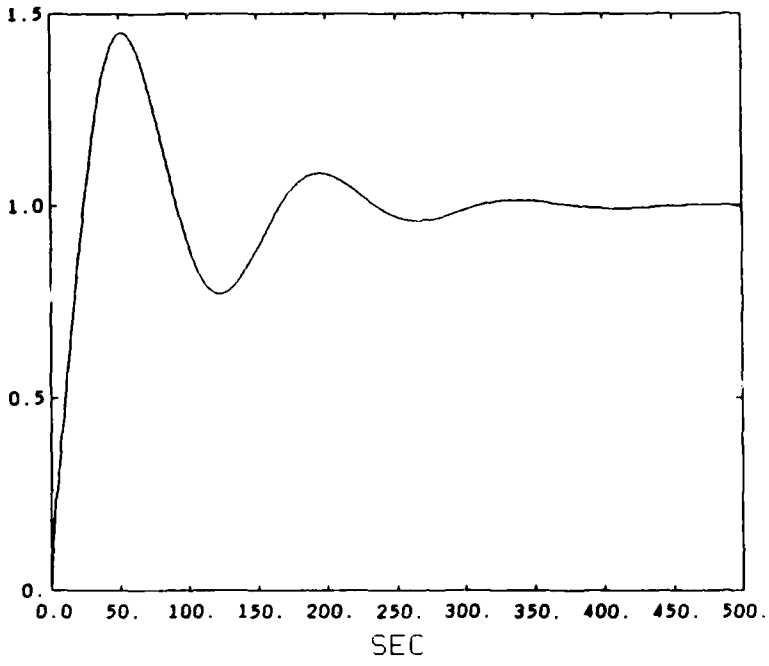

Figure 14-3. Step response (PID control, $\omega_n = 0.1$ rad/sec).

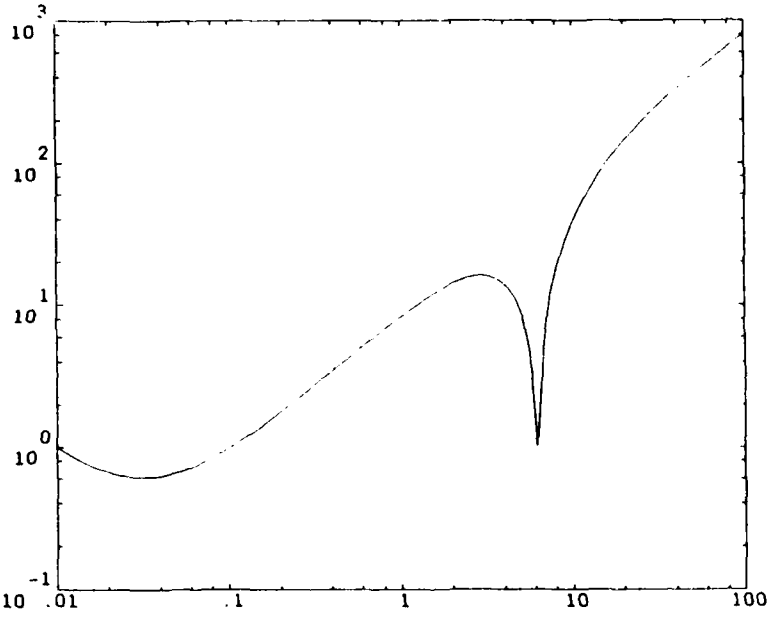

Figure 14-4. Compensator frequency response (PID controller with twist mode notch filter).

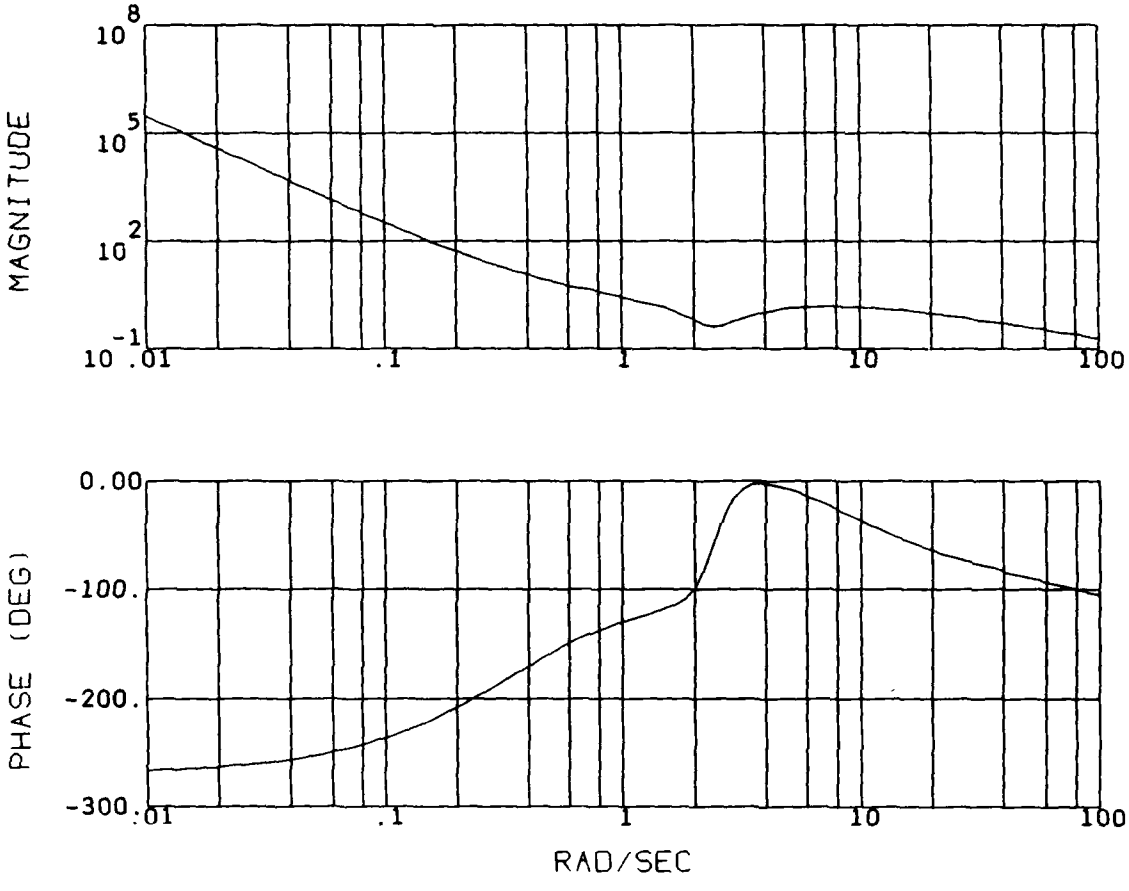

Figure 14-5. Forward-loop frequency response (PID plus notch filter compensator).

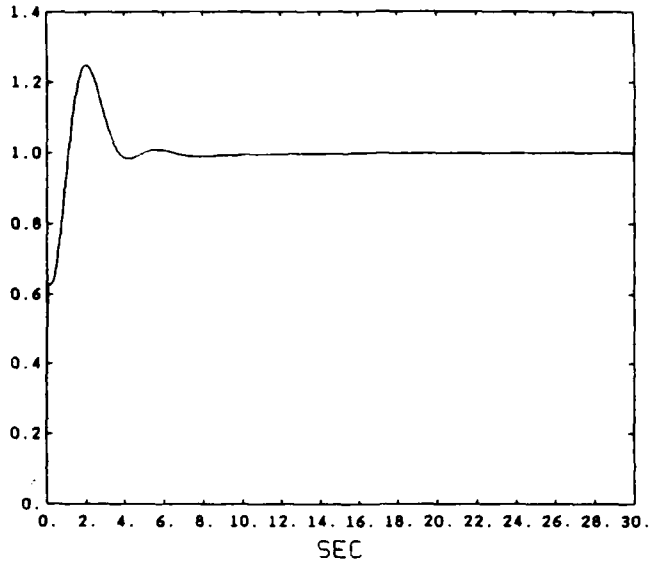

Figure 14-6. Step response (PID control with notch filter).

no longer exhibits a strong resonance of the twist mode. The controller bandwidth was raised to $\omega_n = 2.0$ rad/sec, improving performance while still maintaining stability.

This final PID design produced excellent transient response characteristics for the closed-loop system as seen in Figure 14-6.

However, the notch made the system extremely sensitive to errors in the modelling of the lightly damped twist mode. This sensitivity is characteristic of any design approach in which system dynamics are cancelled by compensator dynamics. Performance was degraded for errors as small as 3% in the frequency of the twist mode. While the addition of the notch was necessary to achieve satisfactory performance with the PID controller, the poor performance robustness associated with this compensation precluded its implementation as the baseline hub controller.

14.3 Dynamic Compensator Design with Loop Transfer Recovery

In an attempt to improve system performance in light of the difficulties encountered with the PID-plus-notch controller design, a model-based compensator design approach was undertaken. This method, incorporating the flexible modes into the design process, resulted in superior system response and stability robustness.

The first step in the Linear Quadratic Gaussian/Loop Transfer Recovery (LQG/LTR) compensator design sequence [35] is to develop a state-feedback control law that demonstrates satisfactory performance in both the time and frequency domains. In the case of the hub controller, time domain performance was represented by the traditional method

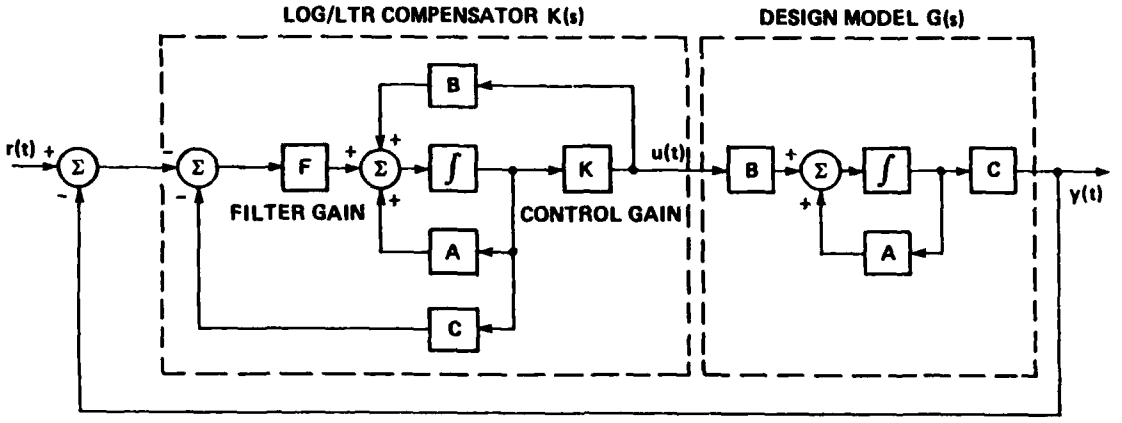

Figure 14-7. The LQG/LTR controller configuration.

of step response. Good frequency domain performance was measured by the achievement of sufficient roll-off in the singular value frequency response, thus assuring robustness with respect to unmodelled dynamics. Once the regulator problem is solved, an estimator is designed which "recovers" the frequency domain characteristics of the full-state feedback regulator design. This latter step is referred to as *loop transfer recovery* (LTR). Because the hub control loop was represented as a single-input/single-output (SISO) system, the singular value decomposition and frequency response defaults to the standard frequency response. In the version of the control design method described here, the loop matrix transfer function is constructed with the loop broken at the input to the plant.* The general configuration of a LQG/LTR control law implementation is illustrated in Figure 14-7. The LQG/LTR compensator consists of the full-state estimator cascaded with the LQR controller gain matrix.

14.3.1 Plant Model Modification and Augmentation

Before commencing the LQG/LTR design process, two changes were made to the design model in order to improve model fidelity and potential system performance. The first change was to incorporate the experimentally measured vibration damping effected by the PMAs by increasing th modal damping parameters of the plant. Ultimately, both the the hub torquer and PMAs will be simultaneously activated during the experiment slew maneuvers, and the modified plant model more accurately reflects the PMA

*Because the system is SISO this choice is not restrictive.

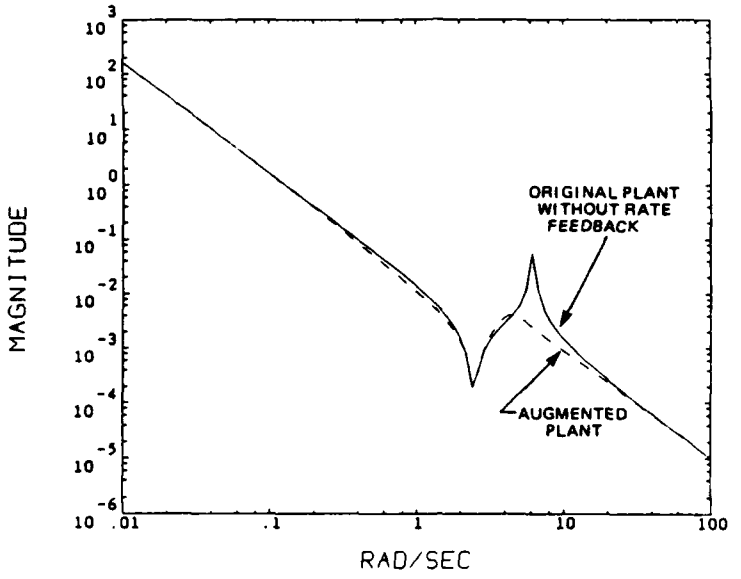

Figure 14-8. Plant frequency response with and without inner damping loop.

vibration suppression capability.

Secondly, in order to reduce the resonant peak associated with the twist mode, a frequency-shaped, attitude-rate feedback loop was added to the system. This velocity feedback loop is high-passed so that its damping effect is primarily realized on the flex modes. This approach provided additional damping of the flex modes while simultaneously permitting a faster 'rigid-body' transient response.

The plant augmentation was effective in reducing the resonance of the twist mode without overdamping the low frequency response associated with the fine pointing control function. For the model-based compensator design, the inner damping loop was included as part of the plant. The frequency response of the augmented, updated design plant is compared with the updated system without the rate feedback loop in Figure 14-8.

14.3.2 Linear Quadratic Regulator Design

The first step in generating the state-feedback gains of the LQ regulator was to choose which states and controls should be weighted in the cost function J, defined as follows:*

$$J = \int_0^\infty x^T Q\, x \; + \; u^T R\, u \; dt \qquad (14-4)$$

*For a comprehensive description of the LQR design process see Kwakernaak and Sivan (Section 3.3 of Reference [36]).

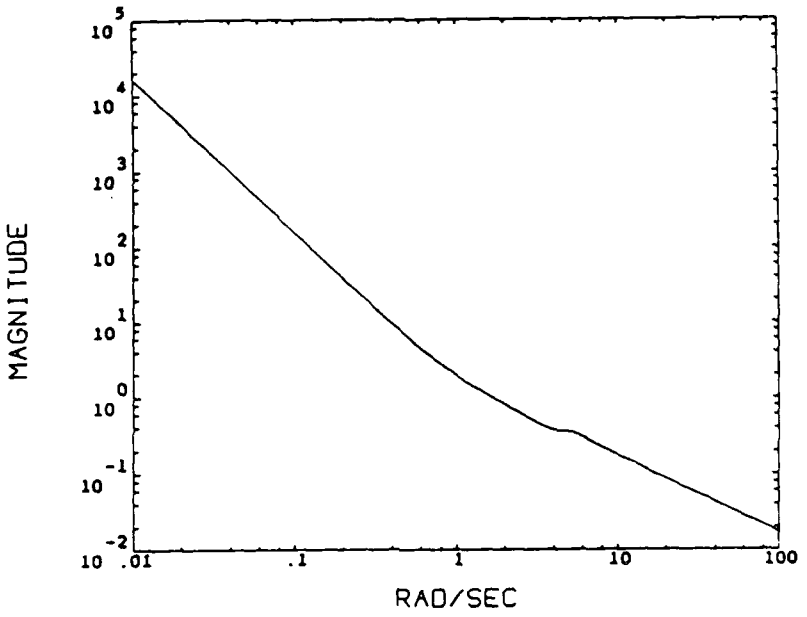

Figure 14-9. Forward-loop frequency response of the LQR design.

Linear quadratic regulator design involves the minimization of this cost function for a given Q (state weighting matrix) and R (control weighting matrix). Through selection of the appropriate elements of Q and R, both the frequency and time domain performance of the state-feedback regulated system are determined.

Because the controller configuration is SISO, there is only one control input, and therefore R is a scalar weighting term. Consequently, R was held constant and Q varied to achieve the desired performance. Alternatively Q could be fixed and R varied if a suitable form for the many elements of Q was known a priori. Because the function required of the hub torquer is to minimize the simulated satellite pointing error, there was an easily defined, structured choice for Q. As introduced in Section 8.2.1.1, the hub angle y_h is the regulated parameter, where

$$y_h = C_h\, x \qquad (14-5)$$

Thus, with C_h defined as the row of C corresponding to the hub angle measurement, the cost function becomes:

$$J = \int_0^\infty \{y_h\}^T \{y_h\} \; + \; R\, u^2 dt = \int_0^\infty x^T \underbrace{C_h^T C_h}_{Q}\, x \; + \; R\, u^2 dt \qquad (14-6)$$

The design process called for fixing Q as defined in Eq. (14-6), and varying the scalar R until the desired performance was achieved.

Using this LQR design method, a suitable state feedback design was generated. The open-loop frequency response for this system is shown in Figure 14-9. Note that the resonance associated with the twist mode is almost completely nullified and this result should translate to improved transient response.

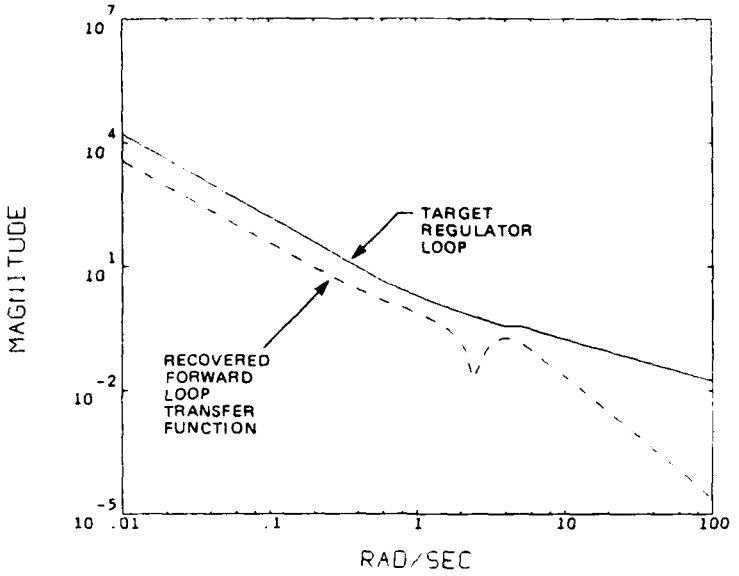

Figure 14-10. Recovery of loop transfer function.

14.3.3 LQG/LTR Compensator Design

While the LQR design displayed excellent frequency domain characteristics, it could not be directly implemented as a practical control system. To do so would require that all system states be measurable and available to be fed back to construct the control input. If only one output variable is measured, a filter must be constructed to estimate the missing states. The conventional design of a Kalman filter requires representing the process and sensor noise by quantities which are commensurate in magnitude with the noise intensities of the actual processes. The LQG/LTR estimator design is not saddled with this constraint. The process and sensor noise quantities no longer represent particular physical properties—they are treated solely as design parameters which may be varied to achieve a particular design objective. Selection of these parameters follows a specified format.

Following Reference [35], the 'fictitious' Kalman filter process noise intensity is fixed and the sensor noise intensity is varied until the frequency domain characteristics of the full-state feedback LQR design have been sufficiently recovered. Note that because the hub torque controller is SISO, the sensor noise intensity term is scalar so that the design sequence is relatively straightforward. The end result of this design process is shown in Figure 14-10 which displays the original LQR frequency response and the frequency response of the recovered fictitious Kalman filter. The recovery procedure is an inexact process: better recovery can be achieved by further increases in the filter gain. However, the objective is to find a design which comes sufficiently close to recovering the singular value frequency response characteristics of the LQR loop transfer function without requiring excessive gain.

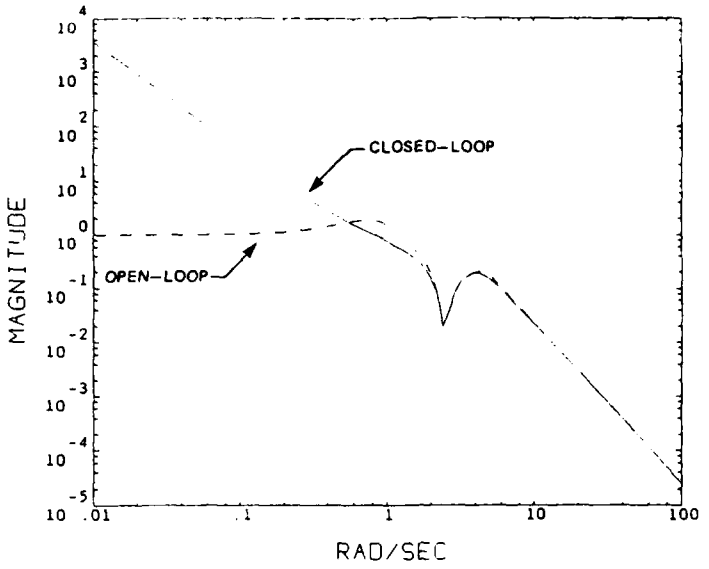

Figure 14-11. Open and closed-loop frequency response incorporating the LQG/LTR compensator.

14.3.4 Hub Torquer Control Performance

The frequency response of the open and closed-loop systems including the LQG/LTR dynamic compensator is shown in Figure 14-11. Note that the resonant peak of the twist mode has been reduced significantly, although this damping is primarily the result of the inner (high-passed) velocity feedback loop. The step response of the closed loop system, as seen in Figure 14-12, reflects a well-damped system despite the obviously high overshoot of the system. The oscillatory part of the response was damped out within one or two cycles, indicating that the overshoot was associated with the system zeroes and was not a consequence of inherent light damping of the system.

14.3.4.1 Addition of Pre-filter

Because closed-loop compensation cannot effect the open-loop zeroes of a system, some pre-compensation was desired to eliminate the overshoot in response to sharp-edged (i.e. step) commands. A pre-compensator shapes the input to the closed-loop system and thus has no effect on the internal closed-loop system dynamics.

A simple first-order filter was used as the pre-compensator, viz.,

$$G_{pf}(s) = \frac{3.25}{s + 3.25} \qquad (14-7)$$

This filter eliminated the overshoot to a step input command while retaining the overall rapid response of the controller. The original and prefiltered step responses are both

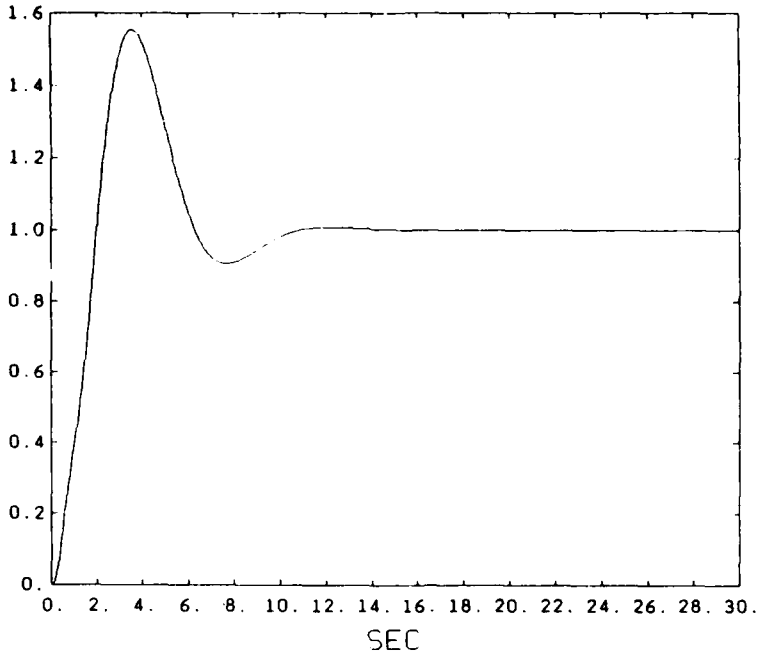

Figure 14-12. Closed-loop step response of LQG/LTR controller.

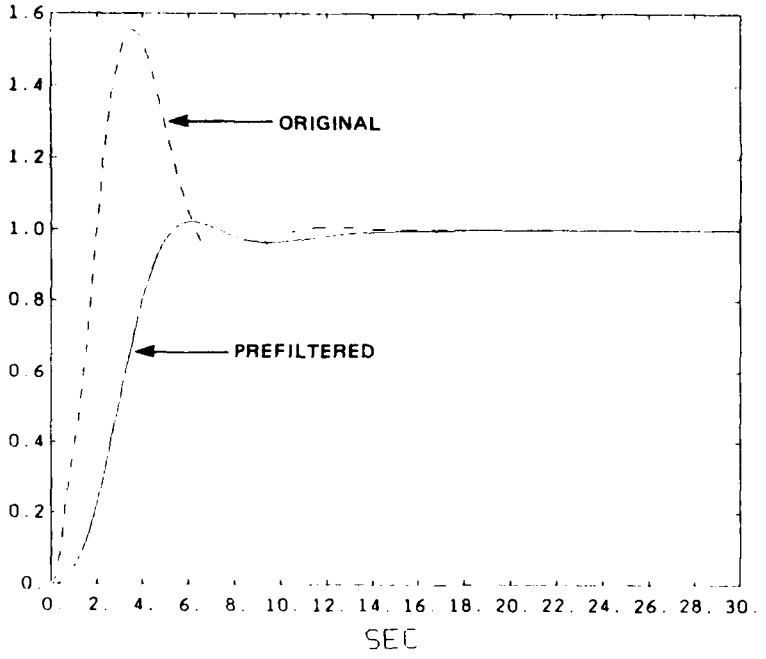

Figure 14-13. Original and prefiltered step responses.

illustrated in Figure 14-13. The performance of the prefiltered system was sufficiently fast and well-damped; consequently, it was decided to integrate this controller into the full-scale CSDL/AFAL experiment.

14.4 Implementation of Hub Torquer Control Laws

The dynamic compensator design described above is represented by the following continuous-time state-space representation:

$$\begin{aligned} \dot{q} &= A_c q + F y \\ u_h &= K q \end{aligned} \qquad (14-8)$$

where q is the internal compensator state vector (state estimates for a full-order compensator), A_c is defined as $[A - BK - FC]$, F is the Kalman filter gain matrix and K is the LQ controller gain vector. The plant model (A, B, C, D) derived using NASTRAN is given in Appendix I. The hub compensator matrices (F, K) are given in Appendix L.

To implement the digital control system, the continuous-time controller defined by Eq. (14-8) was converted to a discrete-time form using the zero-order hold transformation [34] as discussed in Section 13.4.

The format of this SISO hub torque controller is compatible with the general filter propagation routine, *GENFILTER*, introduced in Section 13.4. Additionally, the filters used for the internal velocity feedback path and the prefilter were converted to discrete-time using the zero-order hold transformation and propagated using this same general filter routine. The discrete-time representations of the dynamic compensator and the other filters are given in Appendix L. Because the filter routine was previously developed for the PMA control laws, the implementation of the hub torquer control laws was very straightforward with regard to software development. A block diagram of the complete hub torque control system is shown in Figure 14-14. Note that the 'augmented plant' consists of the original plant and the high-passed velocity feedback loop.

Because the hub torquer control design model consisted of ten states, and was supplemented with the two states of the inner velocity feedback loop, the LQG/LTR compensator was 12^{th} order. This relatively high order compensator placed a burden on the computational capacity of the control computer and the overall control algorithm. Consequently, the possibility of eliminating extraneous states from the compensator was explored. Using the staircase algorithm [37], those states of the dynamic compensator which had minimal controllability and observability were removed. The resulting 8^{th} order compensator reproduced the frequency domain characteristics of the original 12^{th} order system almost perfectly, yet required significantly fewer computations during execution. The large difference in computation time for these two compensators is displayed in Table 14-1. The 50% reduction in time required is quite significant, permitting fast sample rates to be used during the experimental testing.

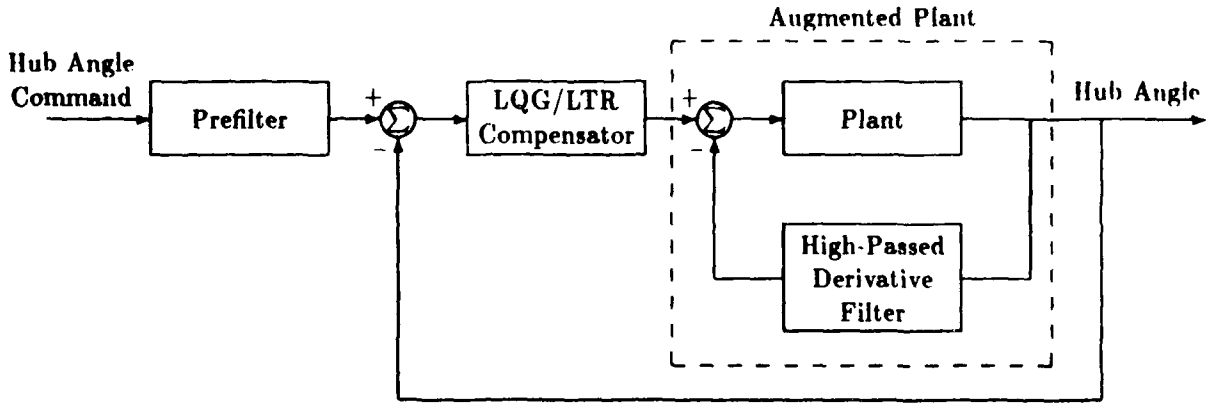

Figure 14-14. Configuration of complete hub torque controller implementation.

Table 14-1. Computation time for the dynamic compensators on Microvax II.

Computation Time (ms)	
8^{th} Order	12^{th} Order
1.06	2.17

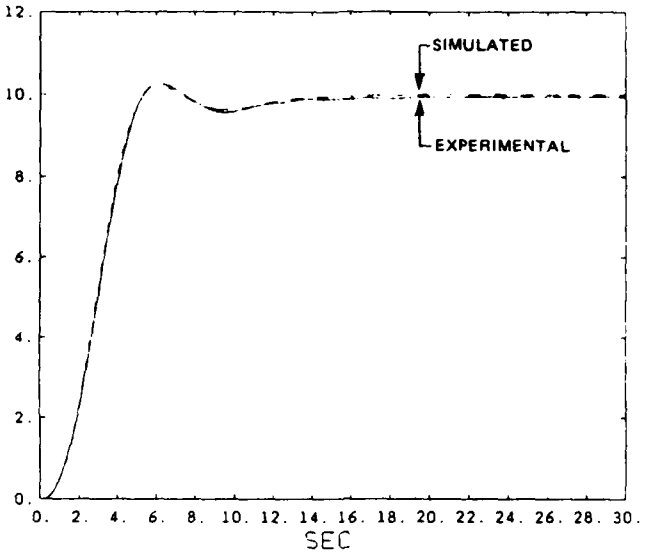

Figure 14-15. Simulated and actual slew response under hub torque control.

If the computational requirements had been such that further order-reduction was called for, a more sophisticated order-reduction technique might have been required. Optimal projection, as described in Section 5, is one such technique. However, the computational capabilities of the Microvax II allowed a satisfactory implementation of the 8^{th} order compensator in conjunction with the remaining control tasks (the PMA and thruster control law computations, and data logging) while retaining the desired 50Hz sample rate.

14.5 System Performance on the Full-Scale Experiment

Actual slew testing, similar to that simulated above, was performed on the full-scale CSDL/AFAL experiment structure. In order to verify the performance of the hub control algorithm and the accuracy of the NASTRAN system modelling, this test incorporated only the hub torquer and PMAs—the thrusters and their associated control algorithm were not used. Both the simulated and actual responses are illustrated in Figure 14-15.

The simulated step response can be seen to be remarkably close to that of the true system. This result reflects well upon the hub torquer control law design, and also justifies the effort expended in generating an accurate NASTRAN model. Because of the demonstrated performance of the system, it was integrated into the overall control strategy with confidence that the hub torquer would improve the fine-pointing and tracking capabilities of the CSDL/AFAL experiment.

Section 15

Summary of Software Development

15.1 Introduction

This section briefly describes the major software applications and routines developed during this study. The software routines could be divided into three main areas: real-time executive routines, device driver routines, and routines which implemented control algorithms. The real-time executive routines provided the main application structure by scheduling the execution of other routines (such as initialization, data acquisition, control calculation, etc.). The device driver routines provided a high-level interface between the executive routines and the operation of the input and output devices. The control algorithm routines implemented specific control laws (such as the single-step-optimal thruster control) and any associated functions (such as state estimation or parameter initialization). The device driver and real-time executive routines were, by necessity, intimately dependent on the hardware of the control computer and the timing relations between events both internal and external to the MicroVAX II control computer. Development and debugging of the real-time control applications were the most time consuming tasks performed throughout this program.

All of the routines were written using VAX ELN, Digital Equipment Corporation's real-time cross-development toolkit for VAX processors. The VAX ELN toolkit produces standalone applications (i.e., they do not need the VMS operating system to run the application) and provides extensive source-code-level debugging capabilities.

15.2 Device Driver Routines

The device driver routines provided a high-level interface between the executive routines and the operation of the input and output devices. The functions provided by the driver routines varied between particular devices, but generally included reset and initialization, device status, perform an input and/or output function, scale raw data,

Table 15-1. Device driver routines used during the study.

Library	Device(s)	Lines of code
ANALOG	Data Translation model 3366 D/A and model 3382 A/D interface boards.	5300
DRVJ	DEC DRV11-J. (4) 16-bit parallel I/O ports with control lines and interrupts.	1800
DRVW	DEC DRV11-W. 16-bit parallel I/O port with DMA.	800
MTIMER	Codar M-Timer. (15) 16-bit counter/timer channels with interrupts	4300
UTILITY	General routines commonly used in device drivers.	1100

and handle interrupts. The devices for which driver routines were developed and/or debugged are listed in Table 15-1.

The general procedure to develop driver routines for a new device was to (i) define data structures for internal and external registers of the device, (ii) define allowable low-level device operations, (iii) define desired high-level functions the device should perform, and (iv) implement the desired functions as sequences of single device operations. The low-level device operations generally provided functionality such as loading a particular register or memory location. The high-level functions would, for example, load several registers to prepare for a data transfer or read all the device registers to report its status. Common sequences of low-level operations became the basic routines of the device driver library.

Testing of the driver routines began by stepping through them with the VAX ELN debugger. The device registers were manually examined (with the debugger) frequently to determine that the routines performed the desired operation. As individual routines were debugged, they were combined to perform more complete high-level functions.

Testing of the high-level functions was performed by programming the device to repeatedly produce an output or condition that could be monitored (e.g., a saw-tooth signal from the D/A board). This testing allowed timing parameters of the device (such as channel-to-channel delays, maximum throughput, settling times, etc.) to be observed and measured. The testing also revealed timing related problems and interactions between devices. An oscilloscope became an important software debugging tool. In one case, a set of routines performed correctly for a low repetition rate, but incorrectly for a

Table 15-2. Control routines developed during the study.

Library	Control algorithm	Lines of code
THRUSTER	Single-step-optimal thruster control for slewing maneuvers.	2200
PMA	Local velocity feedback with proof-mass displacement constraints for vibration control using PMAs.	100
HUB	LQG/LTR model-based compensator for fine pointing/tracking and vibration control using hub torquer.	200
GEN FILTER	Generalized state-space filter routines used by linear actuator algorithms.	200

high rate. The problem was traced to a timeout in the device logic. For low repetition rates, the timeout occurred and reset the device appropriately. However, at the higher rates, the device needed to be reset explicitly. Another example was that Ethernet controller activity (used during debugging) caused computational delays which prevented a device from being reset properly between sample cycles.

The most difficult problems encountered while developing the driver routines were when the device did not behave as documented in its manual. If no programming errors were found, the device manufacturer was consulted (sometimes several times) to resolve the problem. In some cases the manual had been mis-interpreted, while in others the manual was incorrect or incomplete.

15.3 Control Algorithm Routines

The control algorithm routines implemented specific control laws and any associated functions, such as state estimation and parameter initialization. The control routines were generally straightforward implementations of the desired control algorithm and were debugged by providing inputs from known test cases and examining the resulting outputs. Table 15-2 lists the control algorithms developed in the study.

The thruster control routines were more extensive than the linear actuator control routines because much more computation was needed to calculate the feedback gains and initialize the controller for the single-step-optimal control strategy. The routines which calculated the thruster command every sample interval consisted of 500 lines of code.

Much of the linear actuator control algorithms involved passing signals through several stages of filters (e.g., integrators and low-pass filters), so a set of routines to implement generalized state-space filters was written. The routines allowed any discrete-time filter (or system) represented in state space format to be implemented quickly and accurately. A procedure was developed whereby a discrete-time filter (or system) designed with CTRL-C could be output to disk in a format which could later be used by the filter routines. The generalized filter library permitted the main body of the linear actuator control code to be mainly calls to propagate the states of the appropriate filters.

15.4 Real-time Executive Routines

The real-time executive routines provided the main application structure by scheduling the execution of the device driver and control calculation routines. Timing was determined by the real-time executive by waiting for the appropriate hardware interrupts (or other events) to schedule other routines. The executive also provided miscellaneous functions needed to read initialization data and to log experimental data to and from data disks. Table 15-3 lists the collections of executive routines used throughout the study.

The development of the executive routines consisted mainly of implementing the procedures or functions required to perform a particular test (e.g., read initialization data, prompt for user input, wait for an interrupt, etc.). The executive would either implement a procedure directly (such as waiting for the next sample interval interrupt), or call the appropriate device driver or control calculation procedure (such as scaling raw input data to be passed to a control calculation subroutine). The executives were debugged by repeatedly calling device driver output routines in a specified order and monitoring the outputs of the devices. Correct scheduling and timing of the executive routines were verified by observing the order of and timing between output events.

Table 15-3. Real-time executive routines used during the study.

Library	Test performed	Lines of code
THR_EXEC	Slewing maneuvers using single-step-optimal thruster control. Thrusters were the only actuator. Used to debug the thruster control algorithm and develop the thruster constraints.	3300
PMA_EXEC	Vibration damping using only the PMAs. Used to develop the PMA control algorithm and determine appropriate control gains.	600
HUB_EXEC	Slewing maneuvers and vibration damping using only the hub torquer. Used to develop the hub control algorithm and determine appropriate gains.	600
LIN_EXEC	Slewing maneuvers and vibration damping using thrusters, PMAs, and the hub torquer combined. Used to perform slewing tests with on-off thrusters in combination with linear actuators.	3500

Section 16

Experimental Results and Discussion

16.1 Introduction

This section describes the test methods used and results obtained on the full-scale CSDL/AFAL experiment. Slew maneuvers were conducted using both the on-off thrusters and linear actuators (viz., proof-mass actuators and the hub torquer) to accomplish the integrated control of large angle slew motion, fine pointing, and structural vibration suppression.

16.2 Experimental Method

In order to establish a basis for comparison between the use of different combinations of actuators to perform the slew maneuver and fine pointing control, a standard format was selected for the experimental runs. All test runs consisted of a 15 degree slew, with the test terminating after 20 seconds.

However, each run differed in the selection of thruster control parameters, and the utilization of the linear actuators. Tests were conducted with the thrusters alone, with thrusters in conjunction with the PMAs, with thrusters and the hub torquer, and finally with thrusters, PMAs and the hub torquer. As discussed in Section 12, an additional test parameter was the criterion for the start of linear actuator control. For example, PMA control could be active throughout the maneuver for vibration damping, or could be activated solely for the terminal fine-pointing phase. In all cases in which the hub torquer was used, it was activated only in the terminal fine-pointing phase of the maneuver.

In all test runs, a common set of parameters was measured and recorded at each time step. These results are presented graphically in a standard format to allow easy comparison among the different test runs. The measured and calculated variables as presented for each run are as follows:

(1) **The modal displacements and velocities for each mode.** This data is the output of the state estimator used for thruster control. Mode 1 is the rigid-body mode, Mode 2 is the scissors mode, and Mode 3 is the twist mode (3 modes, 6 plots).

(2) **The measured hub angle Y1 (individual dots for each time step), and the estimated value YHAT1 (dashed line).** The target hub angle for all slews is zero degrees, with the maneuver beginning at -15 degrees (1 plot).

(3) **The vibrational energy of the complete structure.** Each mode contributes a component of the total energy, which is represented by the uppermost dashed line in the energy plot (1 plot).

(4) **The measured accelerometer signal for each beam, Y2 through Y5 (dots for each time step), and their respective estimates YHAT2 through YHAT5 (solid lines) calculated by the state estimator** (4 plots).

(5) **The thrust command from the single-step-optimal thrust controller** (1 plot).

(6) **The phase plane representation of the rigid body mode.** This modal displacement and velocity information is taken from mode 1 of the state estimator (1 plot).

(7) **The proof-mass actuator commanded force for each of the four PMAs** (1 plot). For tests in which the PMAs were not used, this plot is omitted.

(8) **The proof-mass actuator displacements for each of the four PMAs** (1 plot). For tests in which the PMAs were not used, this plot is omitted.

(9) **The hub torquer commanded force** (1 plot). For tests wherein the hub torquer was not used, this plot is omitted.

In all, there is a maximum of 17 plots for a given test run. The data *for each test* is presented on three consecutive pages of figures.

16.3 Experimental Data, Discussion, and Analysis

The following sections discuss each of the test runs and examine the key conclusions to be drawn from each.

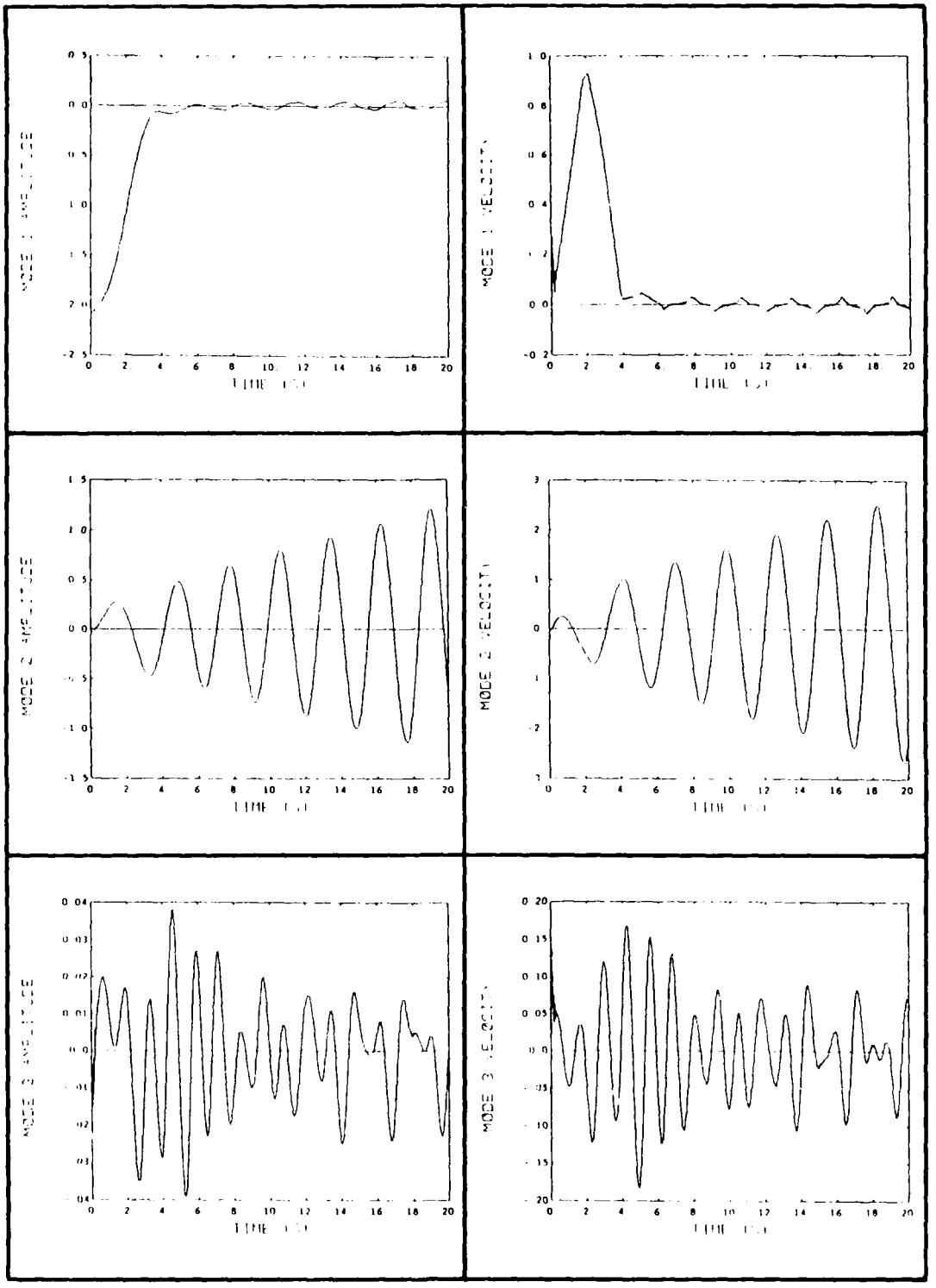

Figure 16-1. 15 degree slew, using thrusters only, without terminal phase constraints. (Modal displacements and velocities).

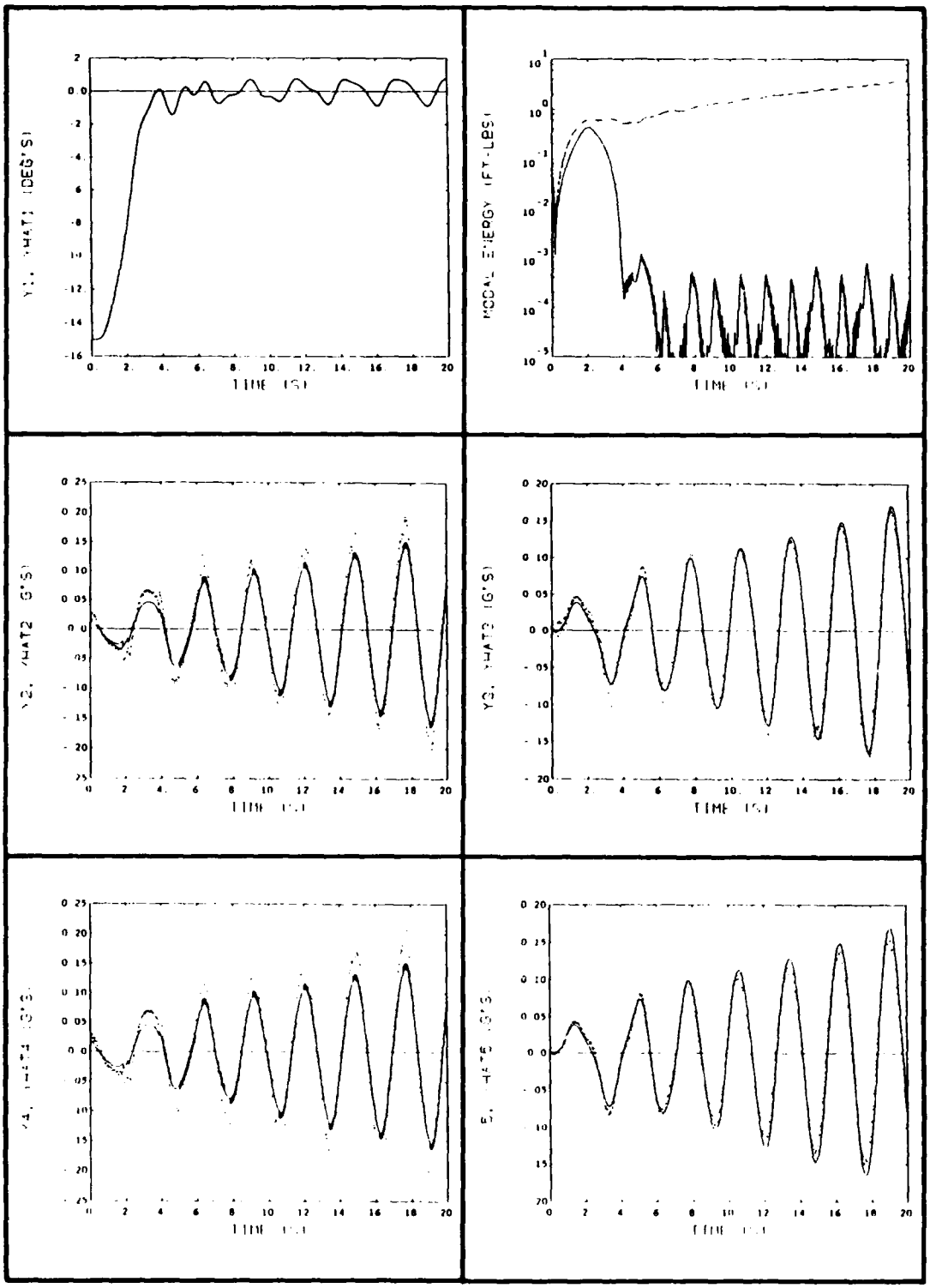

Figure 16-2. 15 degree slew, using thrusters only, without terminal phase constraints. (Hub angle, vibrational energy, and accelerometer measurements).

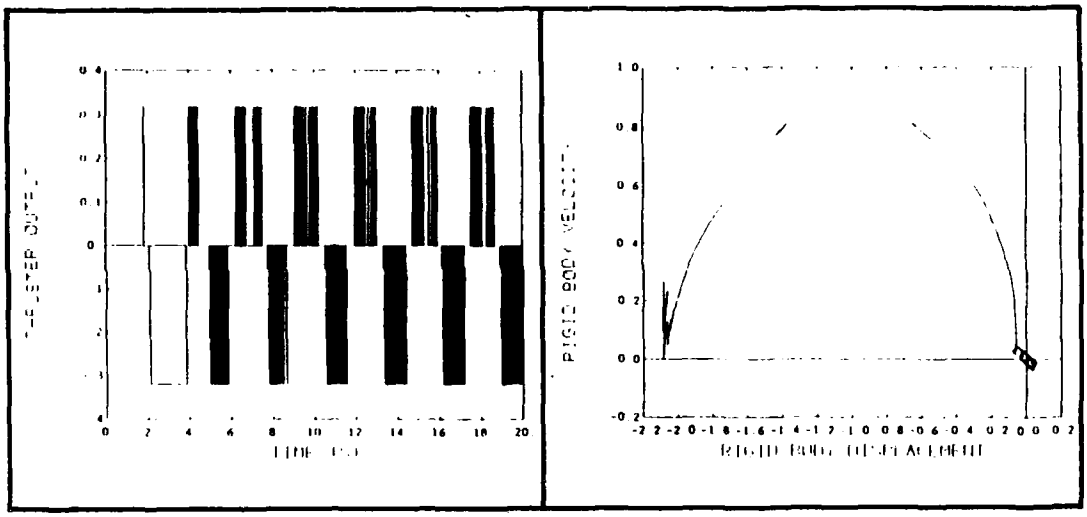

Figure 16-3. 15 degree slew, using thrusters only, without terminal phase constraints. (Rigid body phase plane and thruster force command).

16.3.1 Results of Test S15TB

Test S15TB was a 15 degree slew, using thrusters only, without terminal phase constraints.

This first test illustrates well the difficulty of applying on-off thruster control to effect fine-pointing and tracking. The experimental data is shown in Figure 16-1 through Figure 16-3. The control law used was based solely on feedback of the rigid-body displacement and velocity. While the previous experimental program [1] was hindered by high friction in the air-bearing table, the very low friction characteristic of the present table resulted in the existence of a strong limit cycle while the thruster-based controller operates in the final, fine-pointing phase. As seen in Figure 16-3, the thrusters fired to initiate the slew maneuver and then provided opposite thrust to decelerate the structure as in a classic 'bang-bang' maneuver. However, the vibrational energy imparted to the structure by these firings was not removed after the thruster control began its terminal phase firings. Mode 2 can be seen to grow in amplitude throughout the maneuver, and resulted in increasing total vibrational energy as shown in Figure 16-5. The hub angle displayed a pointing error of approximately ± 1 degree which was increasing with time.

The reason for much of the excessive vibration of the structure can be traced to a particular characteristic of this test. The 15 degree slew represents a particularly demanding task for the thruster control because the initial commanded thruster firing sequence happens to coincide with the frequency of the scissors mode. As a result, this mode grows rapidly in amplitude during the first three seconds of the maneuver.

Despite the poor performance of the controller for the fine-pointing function, the Kalman filter *does* track the system states very well as is illustrated by the tracking of the sensor measurements. The hub angle is tracked perfectly (the estimate is indiscernible from the measurement in Figure 16-2) and the accelerometer signals are also tracked very well. This excellent filter performance suggests that the system model generated using NASTRAN is a significant improvement over the model accuracy exhibited in the predecessor program [1].

16.3.2 Results of Test S15TD

Test S15TD was a 15 degree slew, using thrusters only, with terminal phase constraints.

In an attempt to reduce the limit-cycling characteristic of the previous test run, new constraints were added to the thruster control logic. When the terminal phase of the maneuver is begun (i. e. , when the structure enters a displacement and velocity deadband about the commanded hub angle), a terminal phase constraint is initiated. This constraint prevents thruster firings which do not oppose the tip velocity; it is

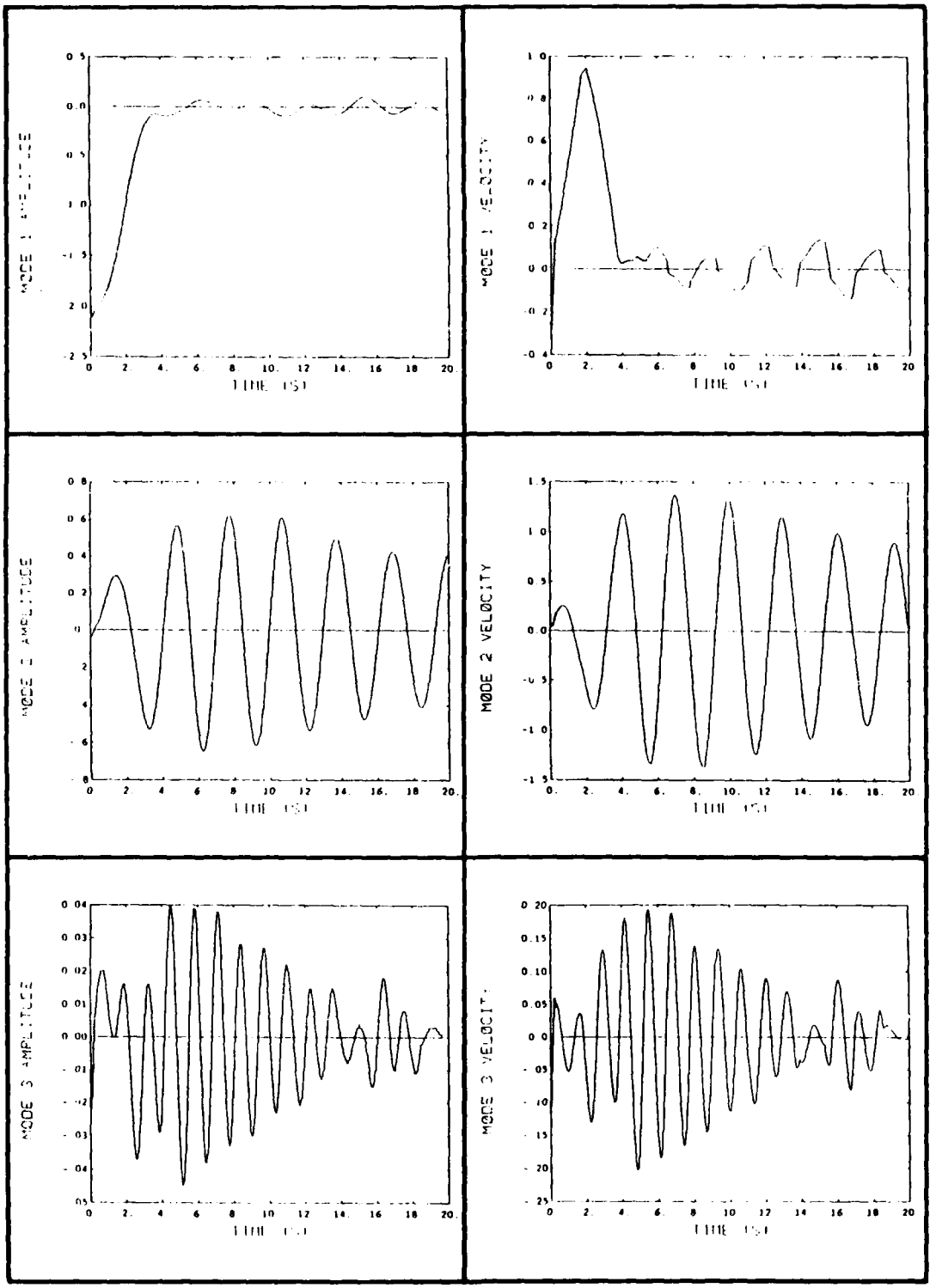

Figure 16-4. 15 degree slew, using thrusters only, with terminal phase constraints. (Modal displacements and velocities).

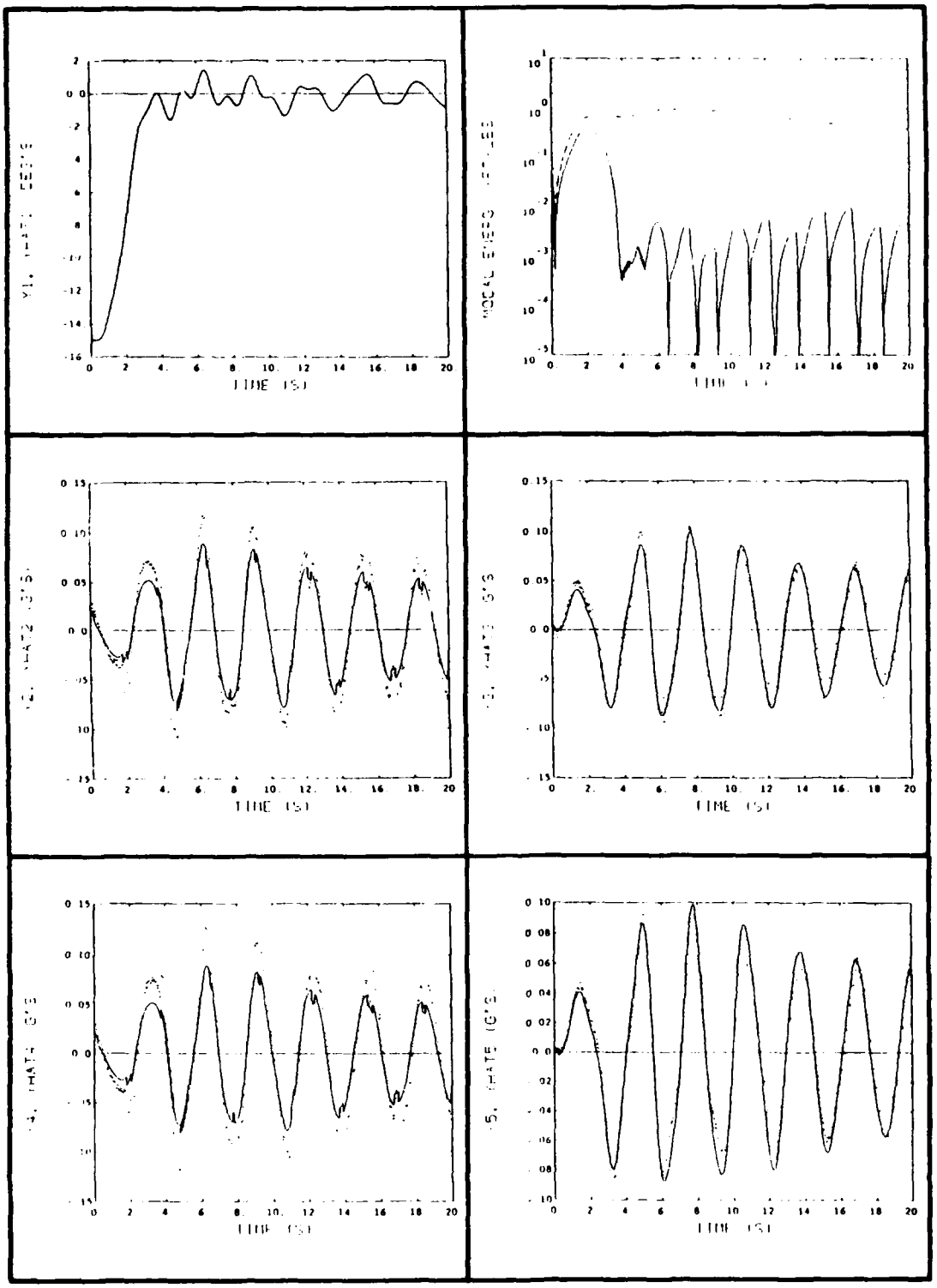

Figure 16-5. 15 degree slew, using thrusters only, with terminal phase constraints. (Hub angle, vibrational energy, and accelerometer measurements).

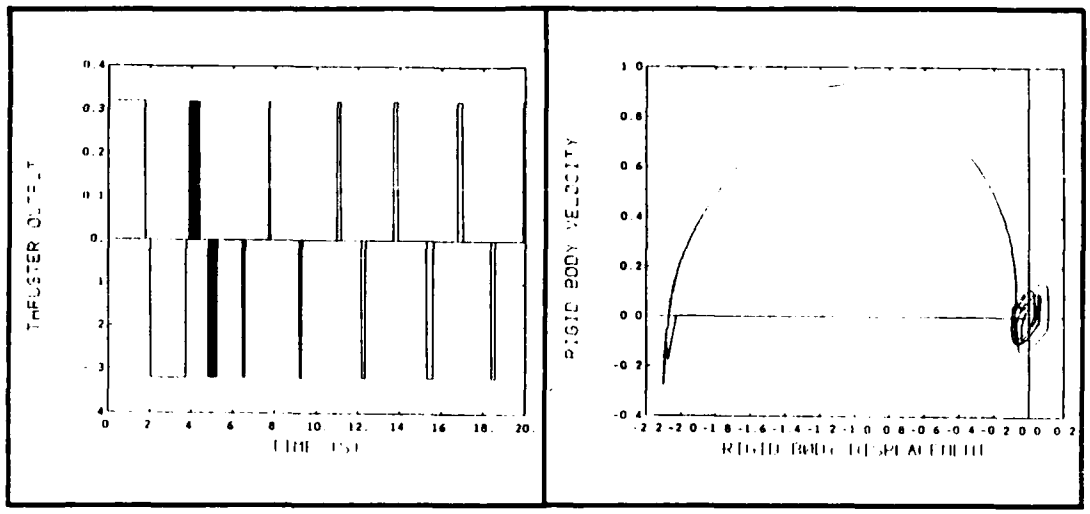

Figure 16-6. 15 degree slew, using thrusters only, with terminal phase constraints. (Rigid body phase plane and thruster force command).

discussed in further detail in Section 11. The results of this test run are displayed in Figure 16-4 through Figure 16-6.

Note that while there is still a large hub oscillation about the commanded angle, the system is no longer unstable and appears to be settling. Mode 2 is decreasing in amplitude, and the vibrational energy of the structure is actually decreasing (although very slowly). The limit cycle is still evident, as illustrated by the repetitive thruster firings. However, these firings are less intense than those commanded by the control law in the previous test which did not include the terminal phase constraint. Nevertheless, the hub angle pointing accuracy is still quite poor (± 1 degree).

16.3.3 Results of Test S15TPA

Test S15TPA was a 15 degree slew, using thrusters with terminal phase constraints, and with PMAs active in the terminal phase.

The addition of the PMAs to the control system provides a strong contrast to the previous results. As shown in Figure 16-7 through Figure 16-9, the limit-cycle has been eliminated, and the majority of the visible oscillation has been damped out before the fourteenth second of the test run. The PMAs were centered using a position loop, and active PMA vibration damping was initiated when the system entered the terminal phase approximately 6 seconds into the test run. In this test, the terminal phase constraint is applied to the thrusters to minimize the terminal phase excitation of the structure.

The vibrational energy is seen to decrease rapidly once the PMAs are activated. Until the vibration damping is activated, the system performs exactly as in previous runs—thruster firings are beginning to excite the system, as illustrated by the positive slope of the energy plot until the 6 second point. However, the thruster firings cease at the 13 second point leaving the hub within the desired deadband, while the PMAs continue to remove the vibrational energy.

The decentralized nature of the control system is evidenced by the contamination of the sensor signals with unmodelled PMA dynamics. Note that while the filter performance is still satisfactory, the estimates of the sensor measurements do not track as well as before. The PMA forces are not included in the Kalman filter state propagation, so this contamination is to be expected.

The pointing accuracy of the overall control system was improved remarkably by the addition of the PMAs. There are no visible oscillations of the hub angle at the end of the maneuver, and the final pointing error was within the thruster firing deadband of ± 0.25 degrees.

16.3.4 Results of Test S15TPD

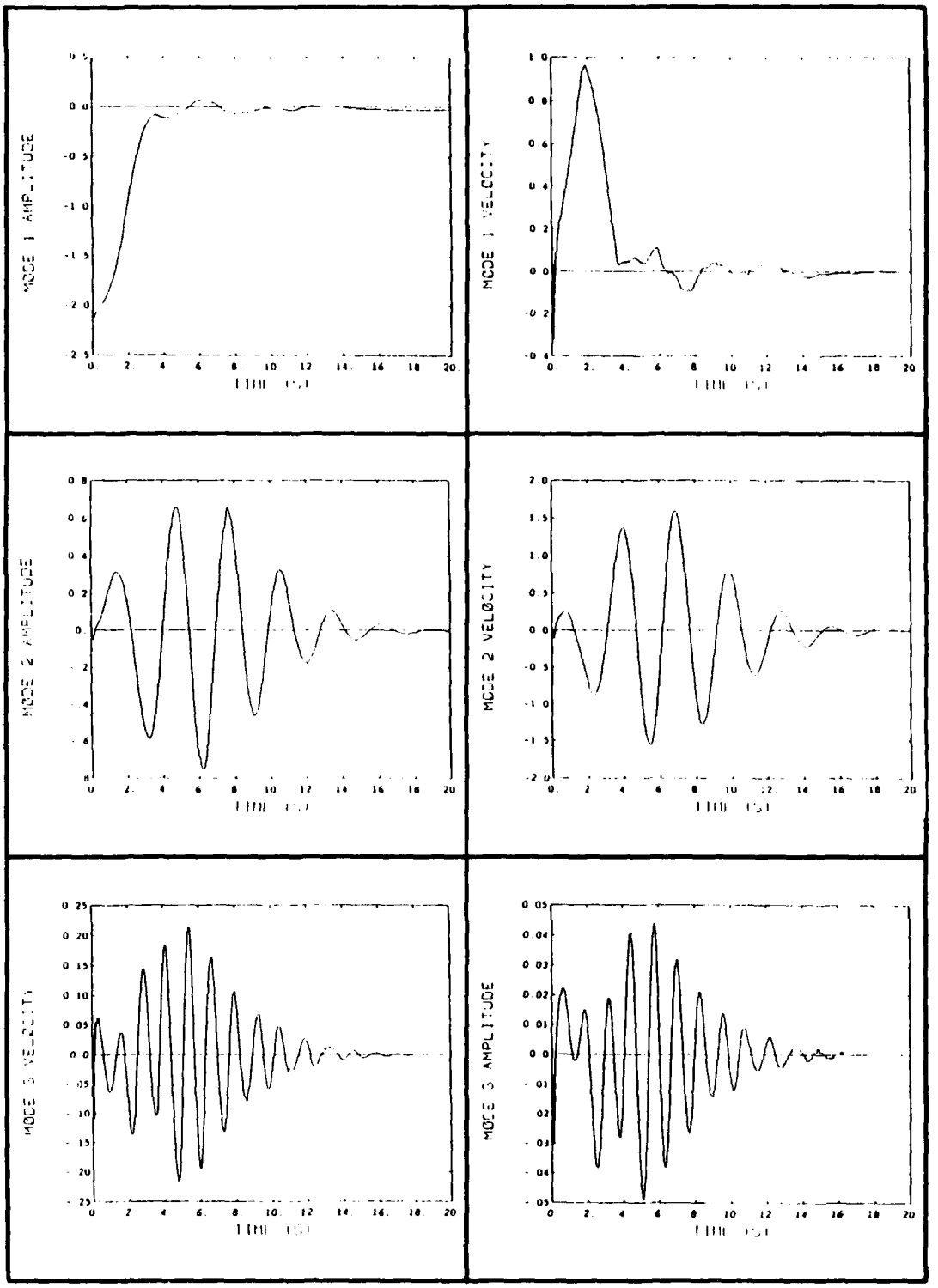

Figure 16-7. 15 degree slew, using thrusters with terminal phase constraints, and with PMAs active in the terminal phase. (Modal displacements and velocities).

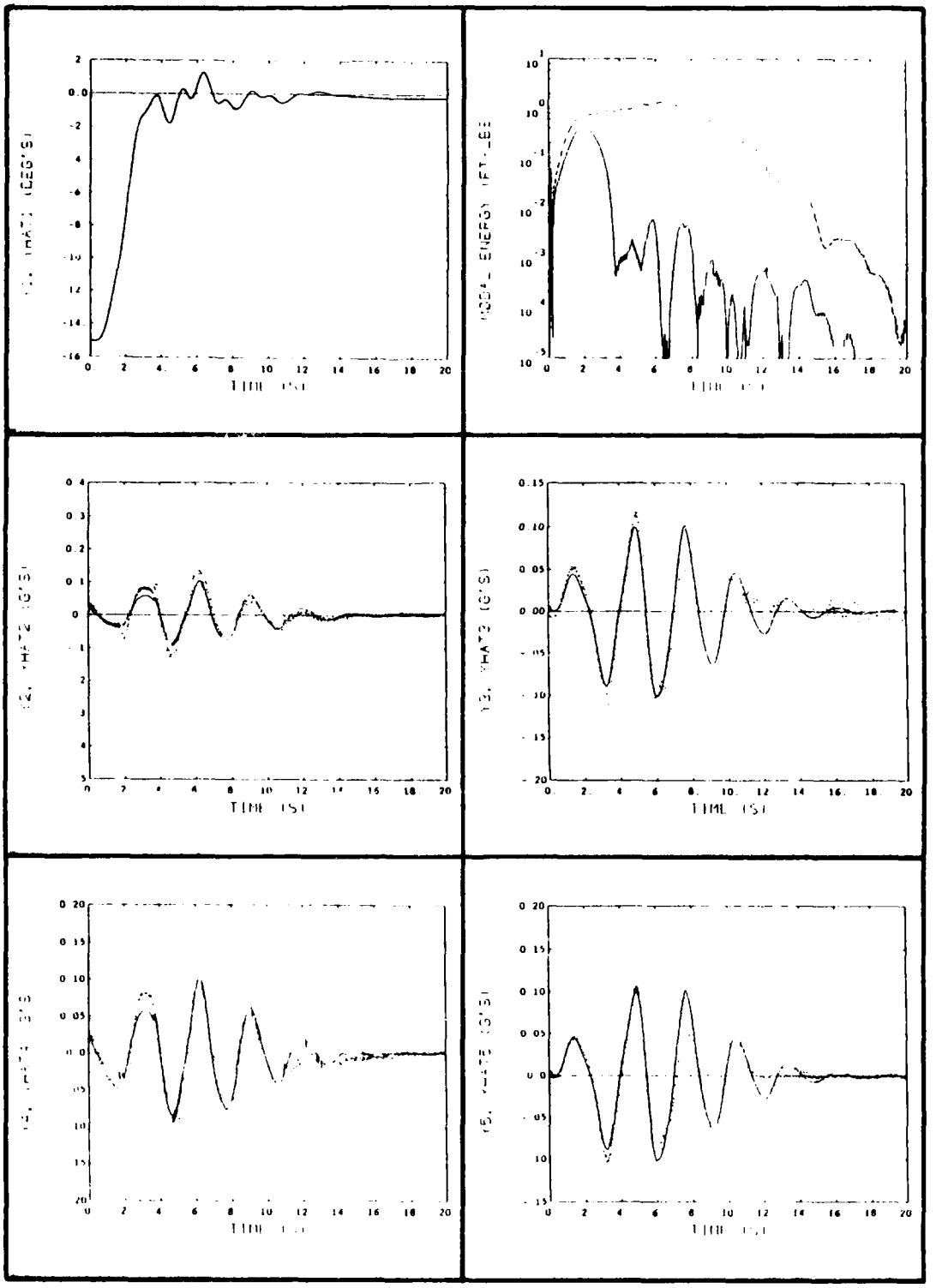

Figure 16-8. 15 degree slew, using thrusters with terminal phase constraints, and with PMAs active in the terminal phase. (Hub angle, vibrational energy, and accelerometer measurements).

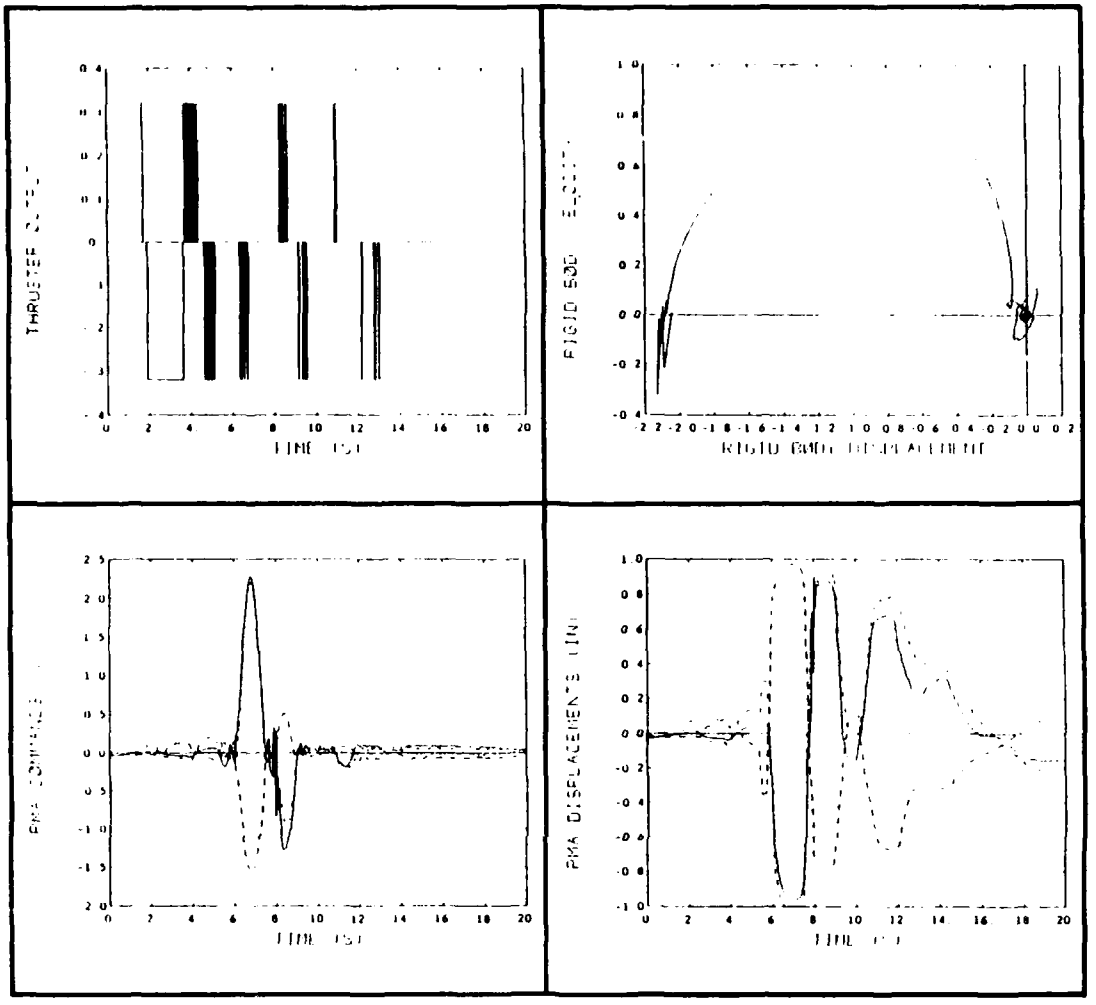

Figure 16-9. 15 degree slew, using thrusters with terminal phase constraints, and with PMAs active in the terminal phase. (Rigid body phase plane, thruster force command, PMA displacements, and PMA force commands).

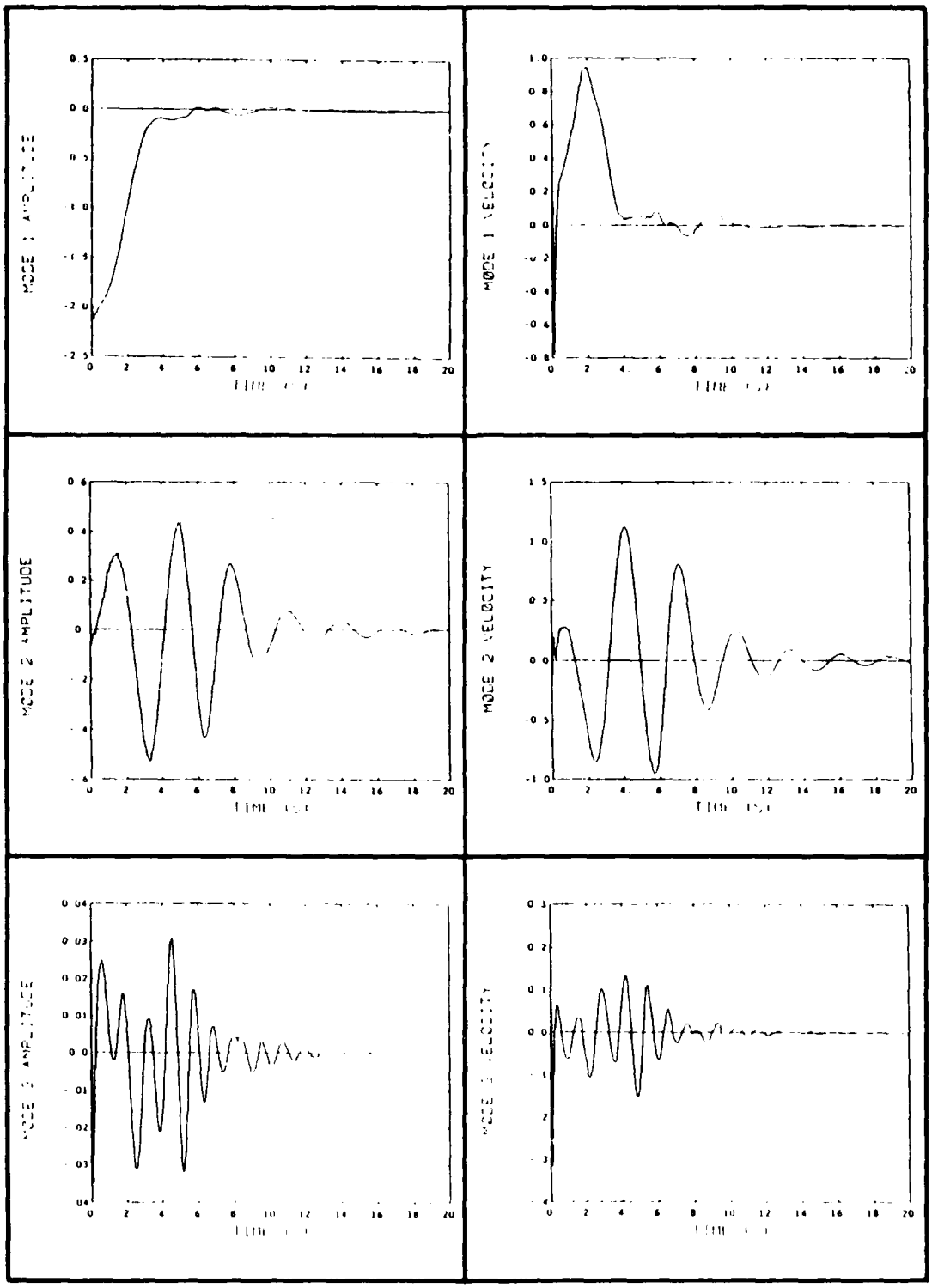

Figure 16-10. 15 degree slew, using thrusters with terminal phase constraints, and with PMAs active throughout the test. (Modal displacements and velocities).

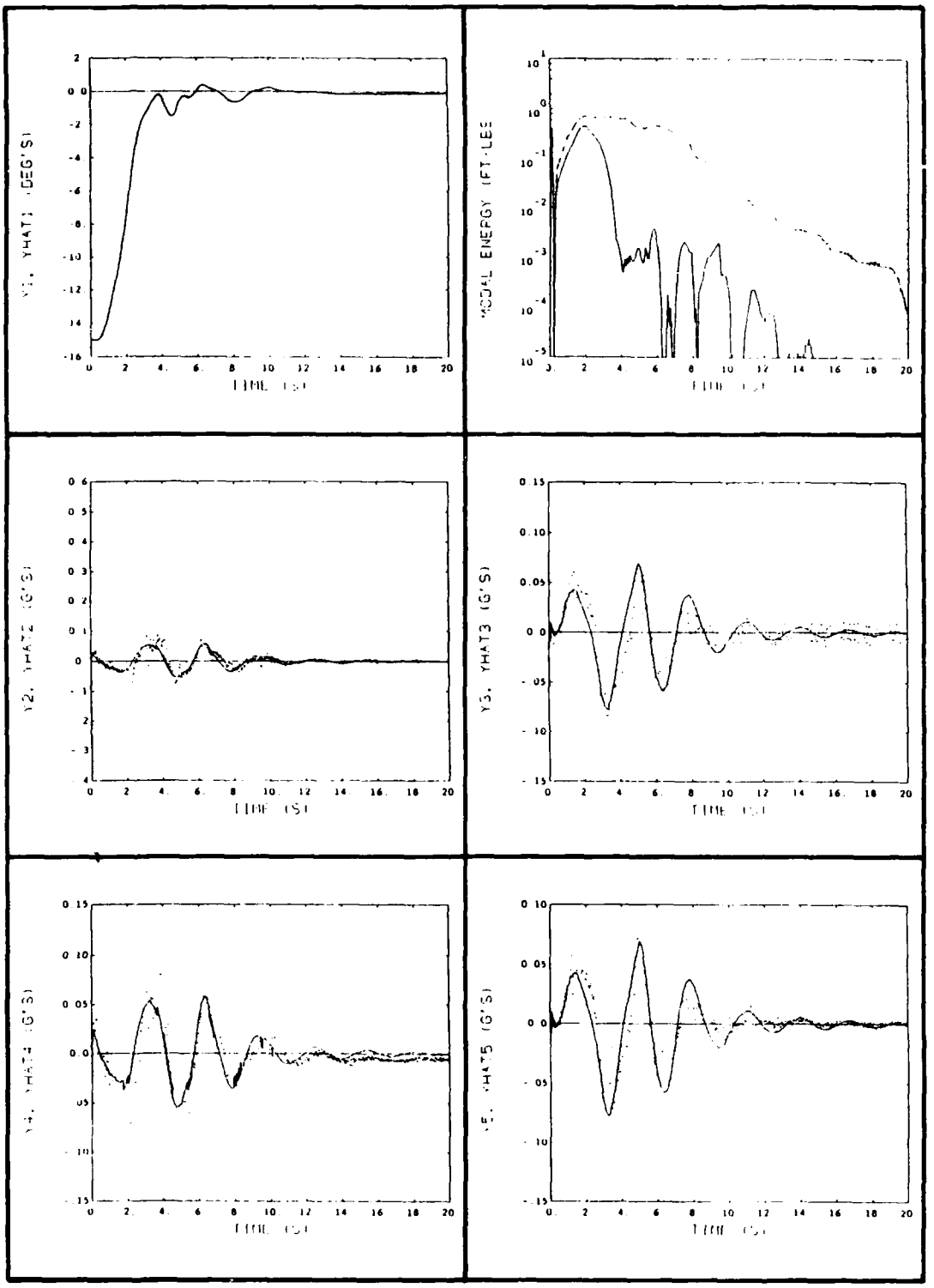

Figure 16-11. 15 degree slew, using thrusters with terminal phase constraints, and with PMAs active throughout the test. (Hub angle, vibrational energy, and accelerometer measurements).

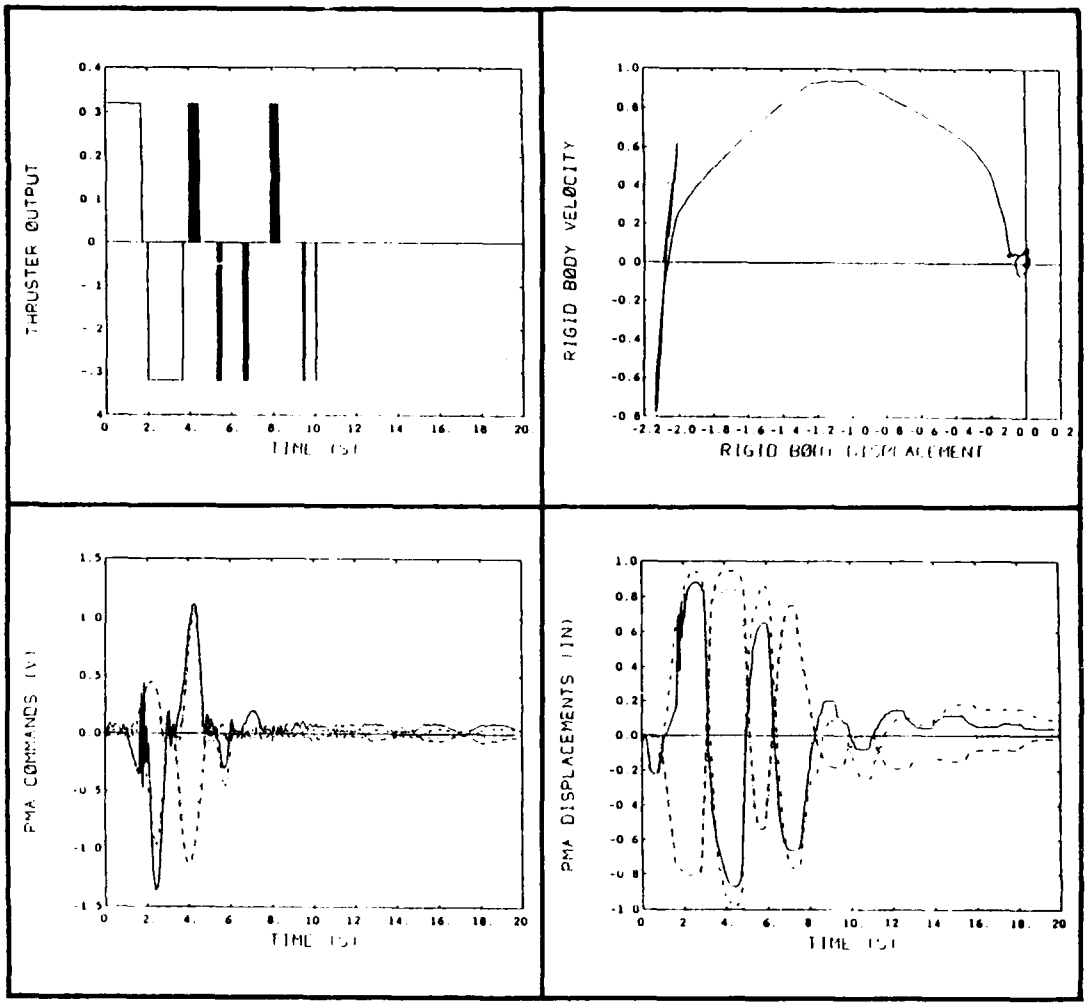

Figure 16-12. 15 degree slew, using thrusters with terminal phase constraints, and with PMAs active throughout the test. (Rigid body phase plane, thruster force command, PMA displacements, and PMA force commands).

Test S15TPF was a 15 degree slew, using thrusters with terminal phase constraints, and with PMAs active throughout the test.

The previous test verified that the PMAs were quite effective in removing the vibrational energy introduced into the system by the thruster firings. In order to reduce the amplitude of the vibration before the system enters the terminal phase, the PMAs were activated for vibration suppression throughout the slew maneuver. The results of this test are illustrated in Figure 16-10 through Figure 16-12.

One concern was whether the PMAs would saturate during the slew and, consequently, be less effective when the displacement limit was reached. The PMAs do move to the limit of their allowable motion; nevertheless, they remain quite effective. The vibrational energy, which reached a high of 1.5 ft-lbs in the previous test, never increases beyond 0.8 ft-lbs. At the 6 second point, the time at which the PMAs were activated in the previous test, the vibrational energy was reduced to below 0.6 ft-lbs.

The use of the PMAs throughout the test did tend to contaminate the filter estimates more than previously occurred, but the slewing performance did not appear to be degraded. The pointing capability displayed by this system is excellent, with structural pointing at the end of the maneuver within the deadband of the thruster control law.

16.3.5 Results of Test S15TPE

Test S15TPE was a 15 degree slew, using thrusters without terminal phase constraints, and with PMAs active throughout the test.

Because the PMAs were so effective in preventing the buildup of modal vibrations, the terminal phase thruster constraint, described in Section 16.3.2, was removed for this test run. As is seen in Figure 16-13 through Figure 16-15, there is no loss in performance when this previously essential constraint is removed. Vibrational energy is removed at approximately the same rate as was previously achieved with the PMAs, and the pointing accuracy remains within the specified deadband.

16.3.6 Results of Test S15THA

Test S15THA was a 15 degree slew, using thrusters with terminal phase constraints, and with the hub torquer active in the terminal phase.

This test provides a separate evaluation of the capabilities of the hub torquer to effect fine pointing. The results of the test run are shown in Figure 16-16 through Figure 16-18. As discussed in Section 12, the thrusters and the hub torquer do not operate simultaneously, and control is passed to the hub torque control law when the system enters the terminal phase of the maneuver. This transition occurs at the 5 second mark,

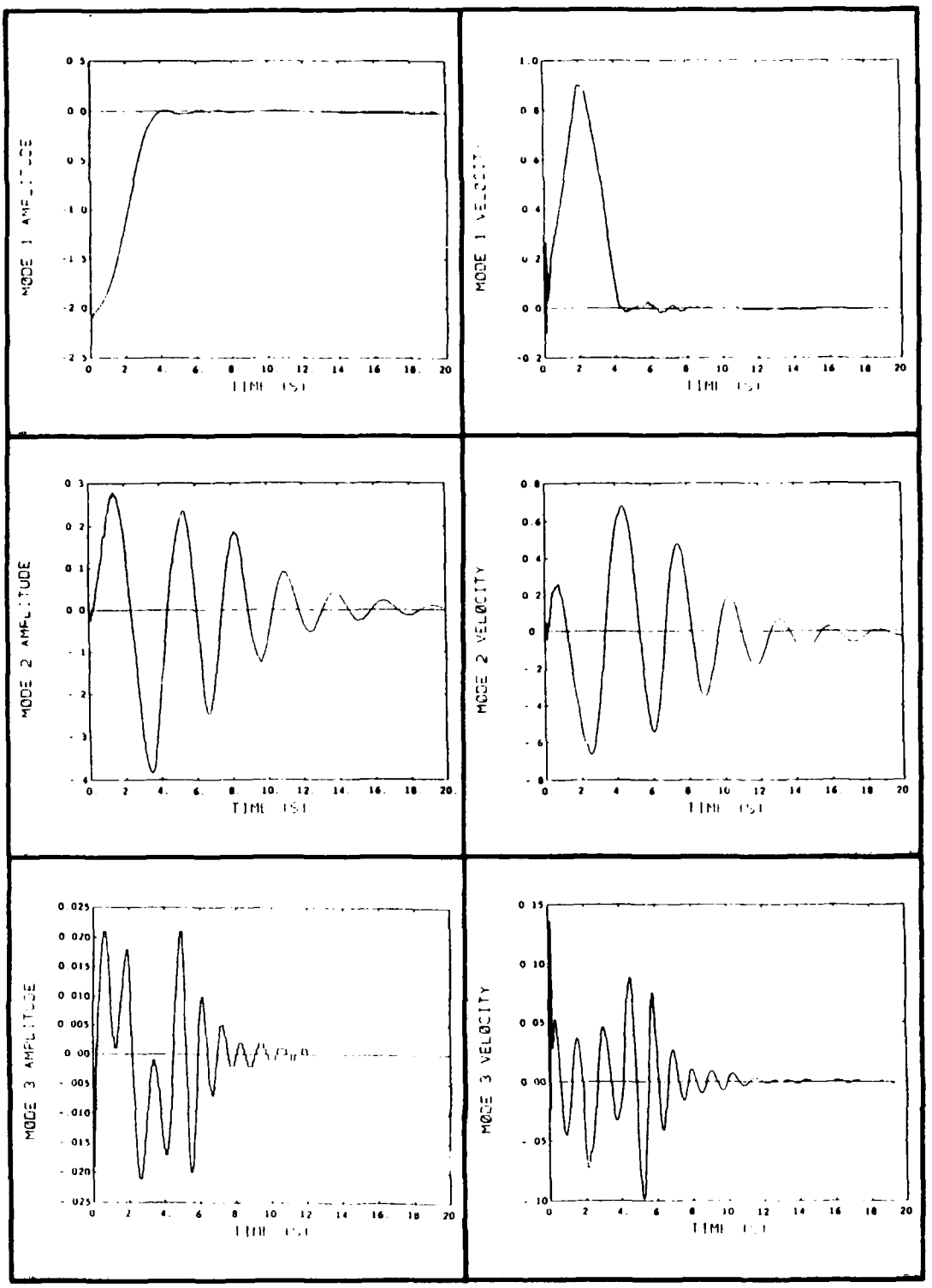

Figure 16-13. 15 degree slew, using thrusters without terminal phase constraints, and with PMAs active throughout the test. (Modal displacements and velocities).

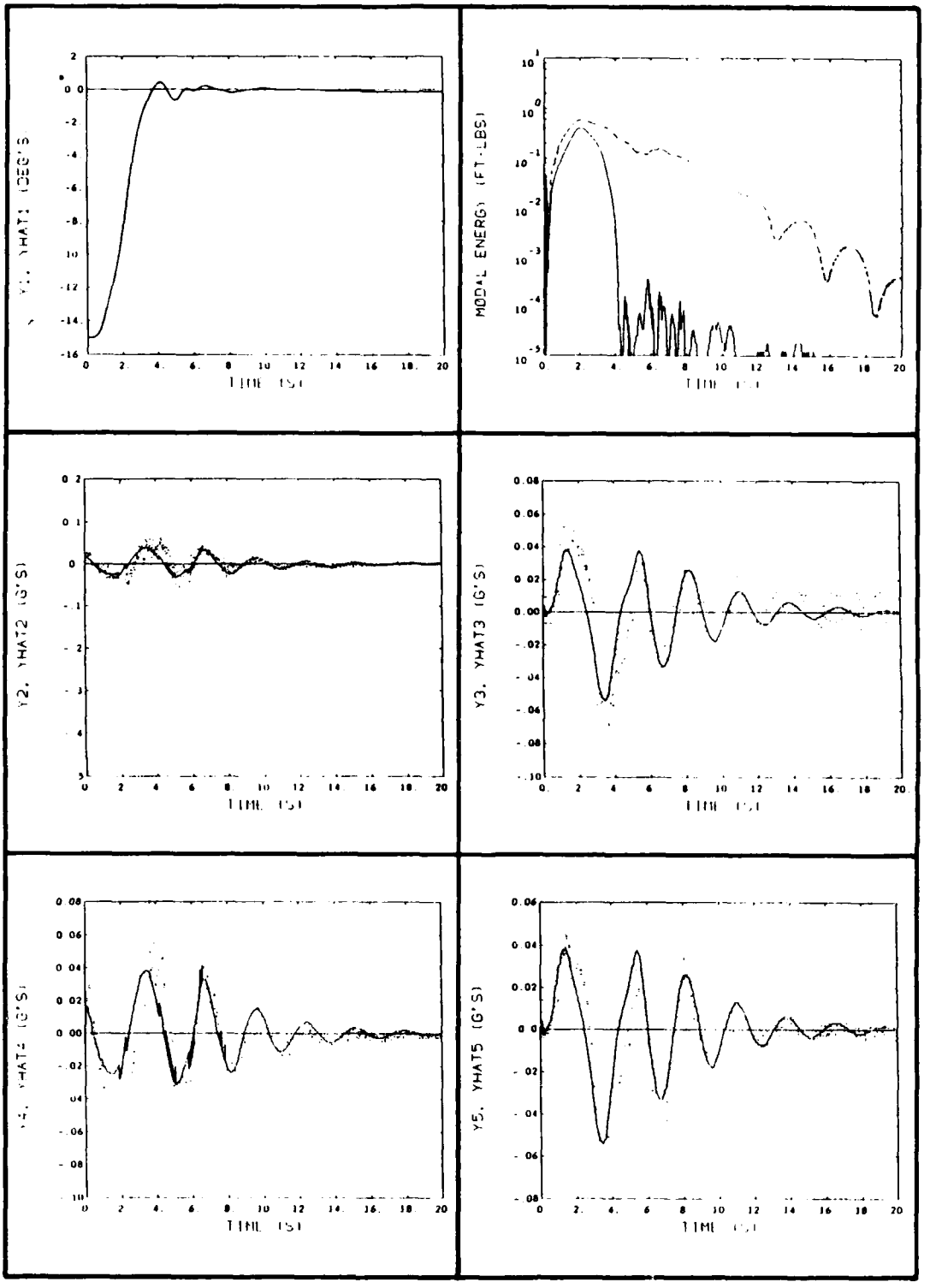

Figure 16-14. 15 degree slew, using thrusters without terminal phase constraints, and with PMAs active throughout the test. (Hub angle, vibrational energy, and accelerometer measurements).

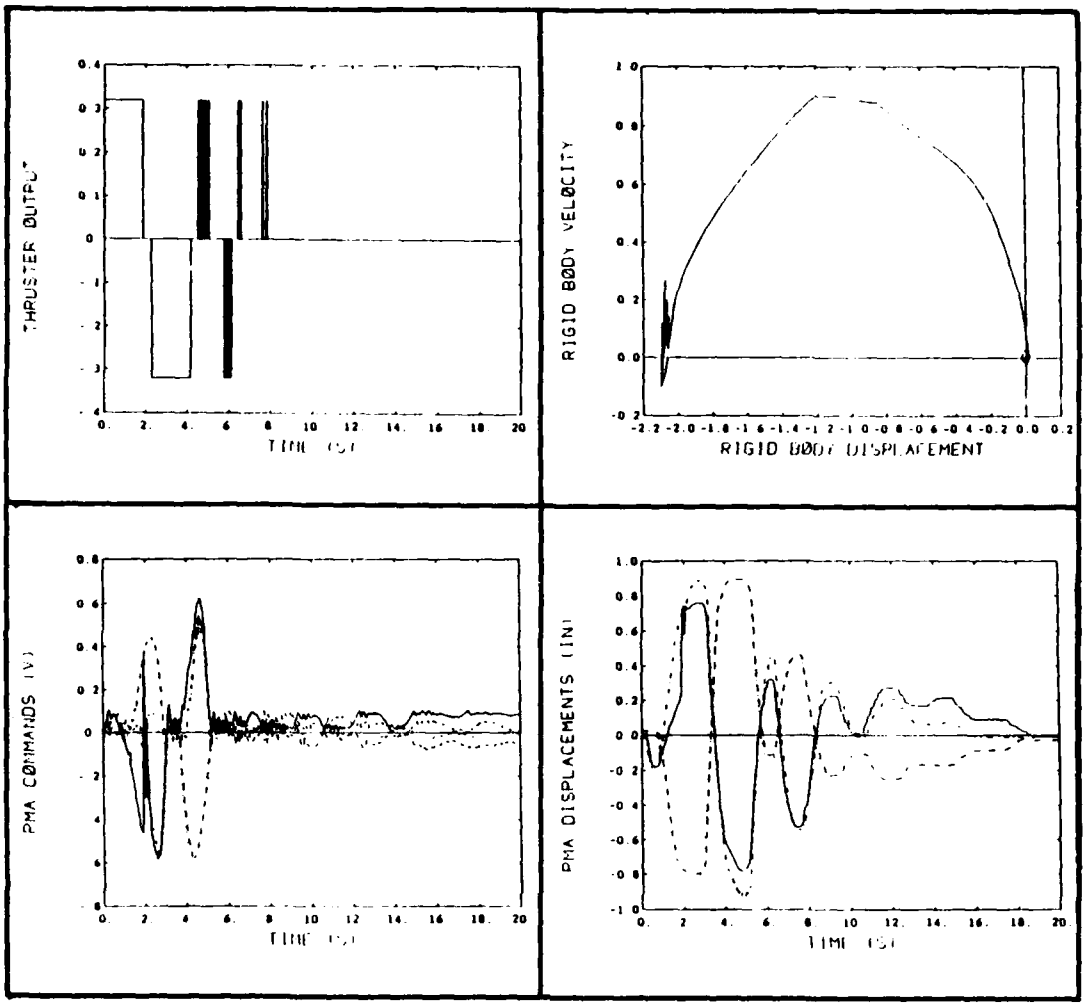

Figure 16-15. 15 degree slew, using thrusters without terminal phase constraints, and with PMAs active throughout the test. (Rigid body phase plane, thruster force command, PMA displacements, and PMA force commands).

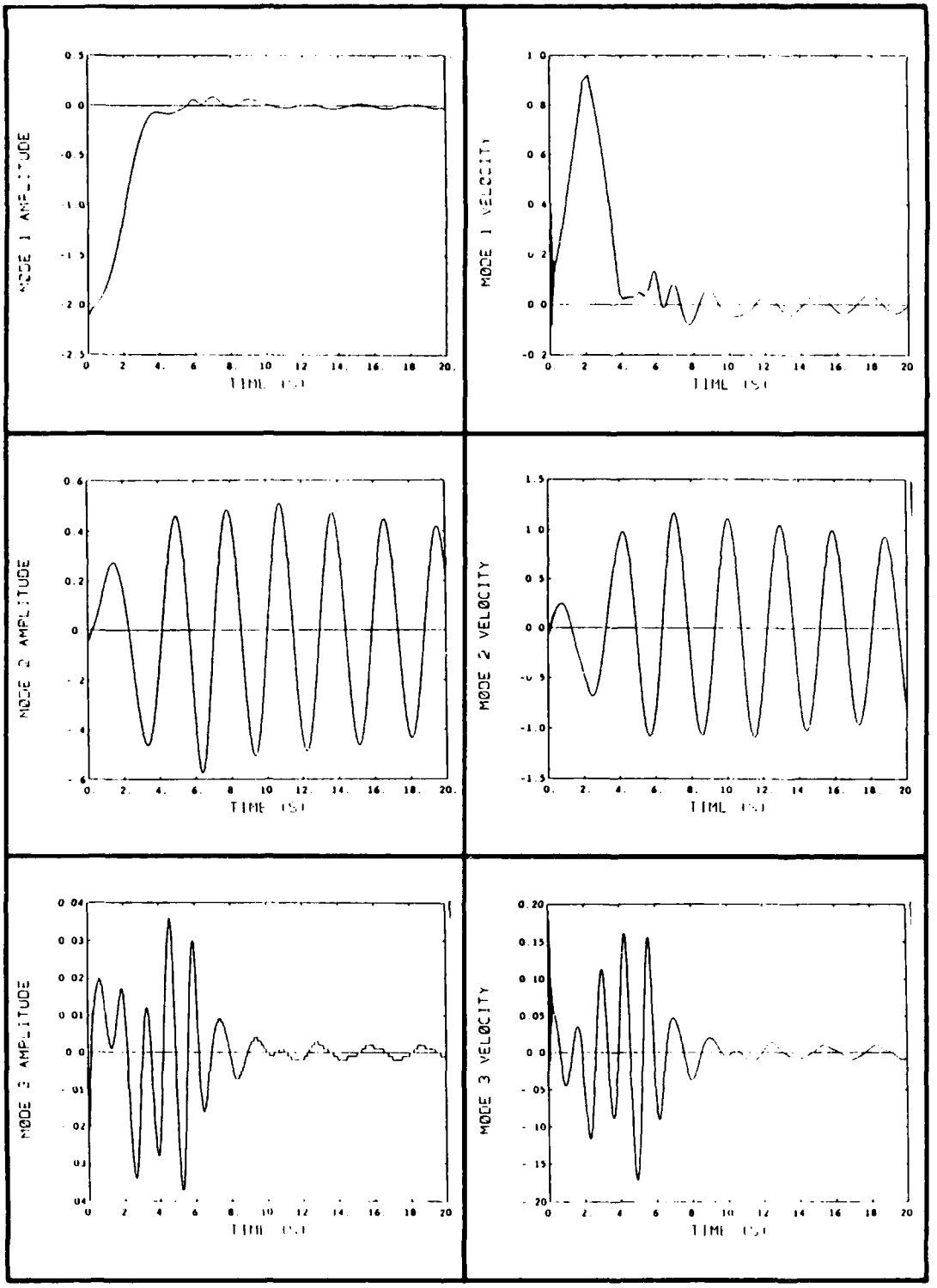

Figure 16-16. 15 degree slew, using thrusters with terminal phase constraints, and with the hub torquer active in the terminal phase. (Modal displacements and velocities).

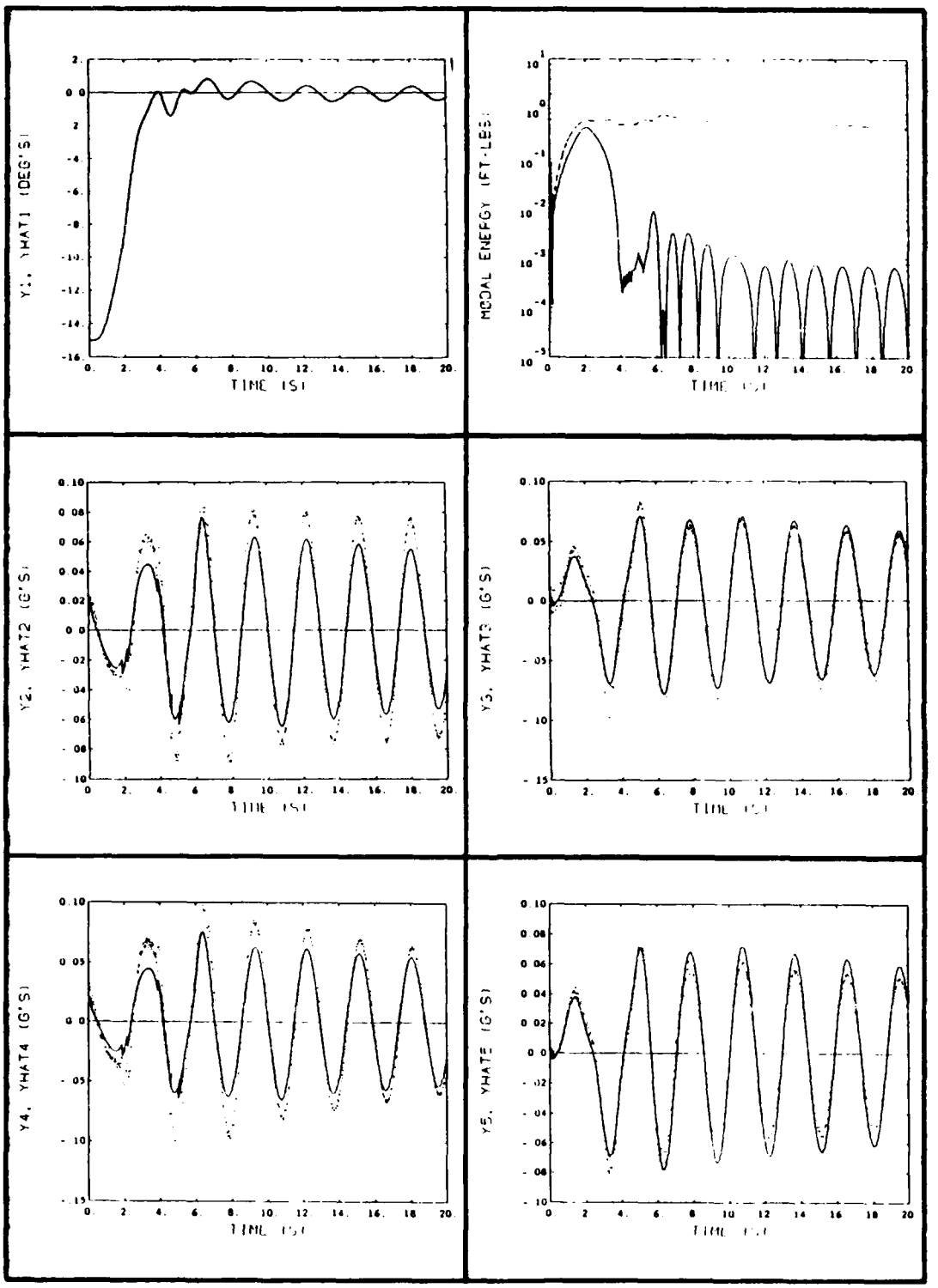

Figure 16-17. 15 degree slew, using thrusters with terminal phase constraints, and with the hub torquer active in the terminal phase. (Hub angle, vibrational energy, and accelerometer measurements).

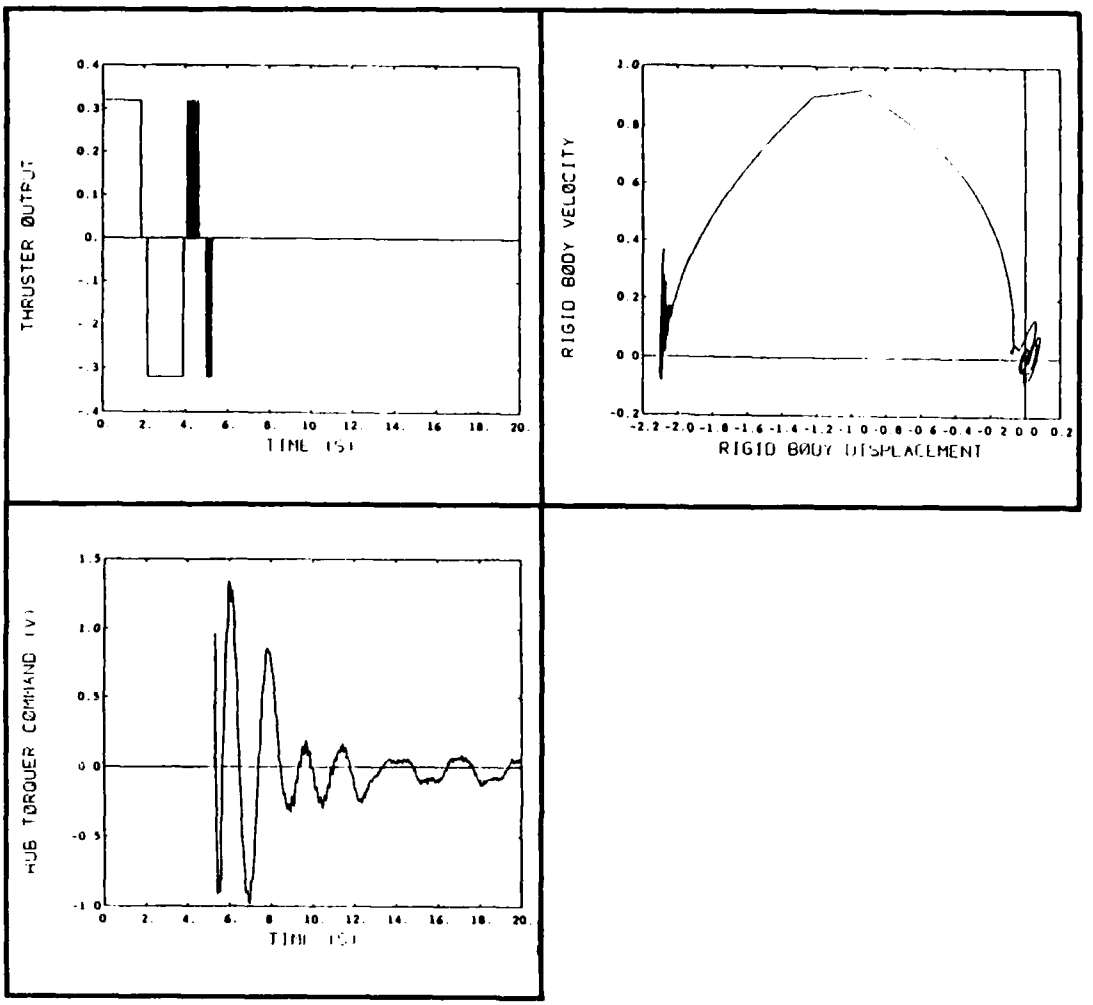

Figure 16-18. 15 degree slew, using thrusters with terminal phase constraints, and with the hub torquer active in the terminal phase. (Rigid body phase plane, thruster force command, and hub torque commands).

where the thruster commands are seen to end, and the hub torque command begins. The most dominant characteristic of this test is the inability of the hub torquer to quickly remove the vibration of Mode 2, the scissors mode. This inability translates to little decrease in the system vibrational energy once the hub torquer becomes active. The continuing second mode vibrations also result in oscillations about the commanded hub angle of approximately ± 0.5 degree magnitude. A higher gain controller might have been more effective, but the controller bandwidth was selected to be commensurate with requirements of the fine pointing/tracking function and not primarily to improve structural damping.

16.3.7 Results of Test S15TPHB

Test S15TPHB was a 15 degree slew, using thrusters with terminal phase constraints, with the hub torquer active in the terminal phase, and with PMAs active throughout the test.

This test uses all of the linear actuators implemented on the CSDL/AFAL experiment. The PMAs augmented structural damping throughout the maneuver, and the hub torque controller was activated when the system entered the terminal phase. The results of this test are displayed in Figures 16-19 through 16-21. They reflect the best fine pointing accuracy of any test reported herein. The final error in the hub angle was less than 0.05 degrees. This pointing error results in a hub torque command less than the air-bearing table friction level. Consequently, lesser errors can not be achieved with this bandwidth hub torque controller and the present air-bearing table.

The previous test highlighted the inability of the hub torquer to significantly damp the scissors mode; however, the simultaneous operation of the PMAs and the hub torquer in the terminal phase of the maneuver eliminates the need for hub-actuated vibration suppression. The PMAs remove any significant scissors mode vibration, while the hub torquer ensures accurate pointing of the structure as a whole. Thus, this test further illustrates the particular value of each of the actuators used in combination.

The thrusters are most effective as actuators for large-angle fast slewing maneuvers because of their capability to generate large torques on the structure. The PMAs are most effective at removing higher frequency vibration from modes with anti-nodes near their location on the structure. Thus, the PMAs were especially effective at damping the scissors mode which produces large linear tip motion. The PMAs were less effective in damping the twist mode, which consists primarily of angular hub and tip motion. The hub torquer was limited in its vibration suppression capability because of the controller bandwidth and its low control influence on the scissors mode. Nevertheless, the hub torquer provided effective fine pointing control of the structure—neither the on-off thrusters nor the PMAs could effectively provide this function. However, used in combination, the actuators provided an effective system for slewing, fine-pointing/tracking,

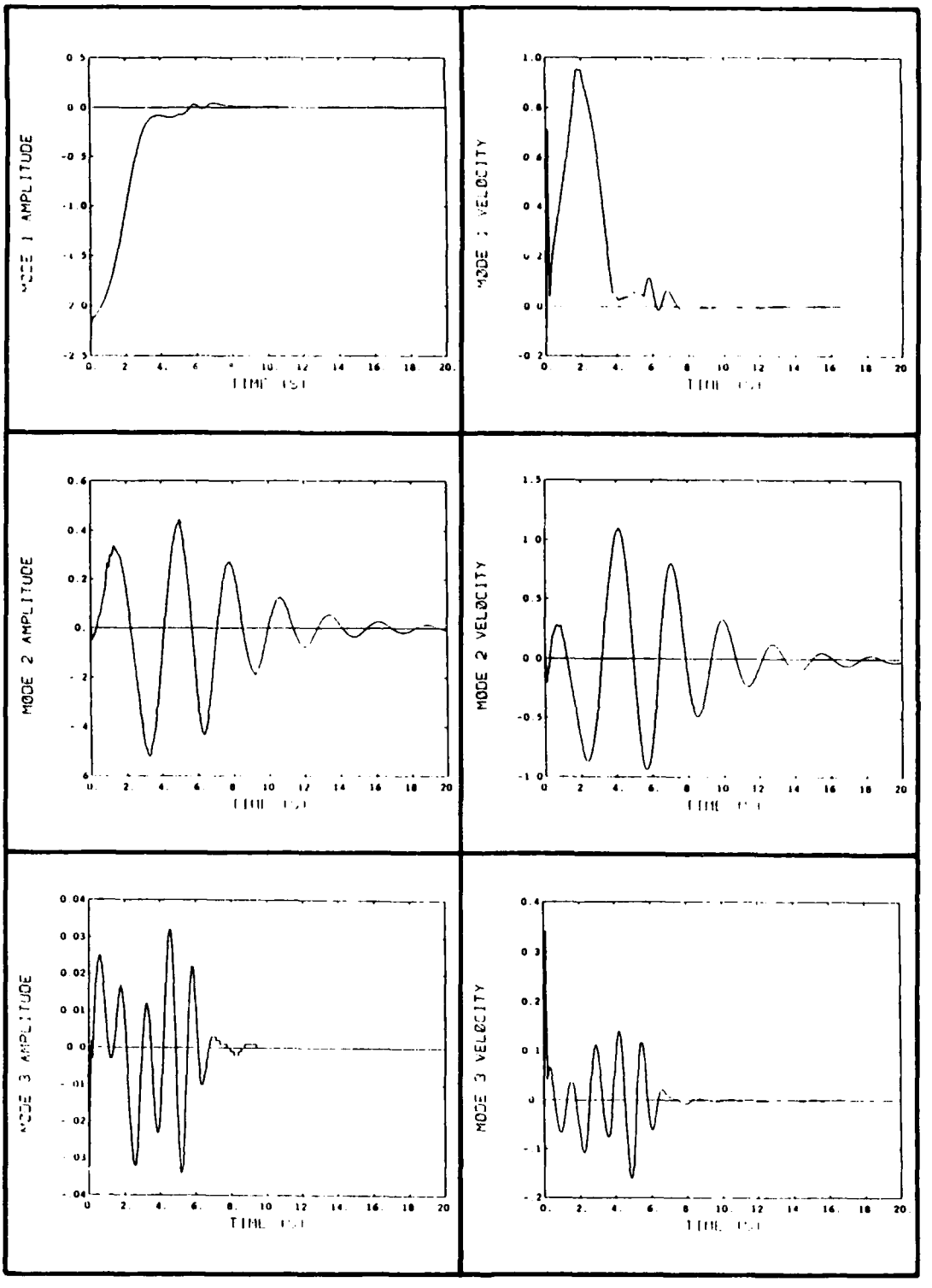

Figure 16-19. 15 degree slew, using thrusters with terminal phase constraints, with the hub torquer active in the terminal phase, and with PMAs active throughout the test. (Modal displacements and velocities).

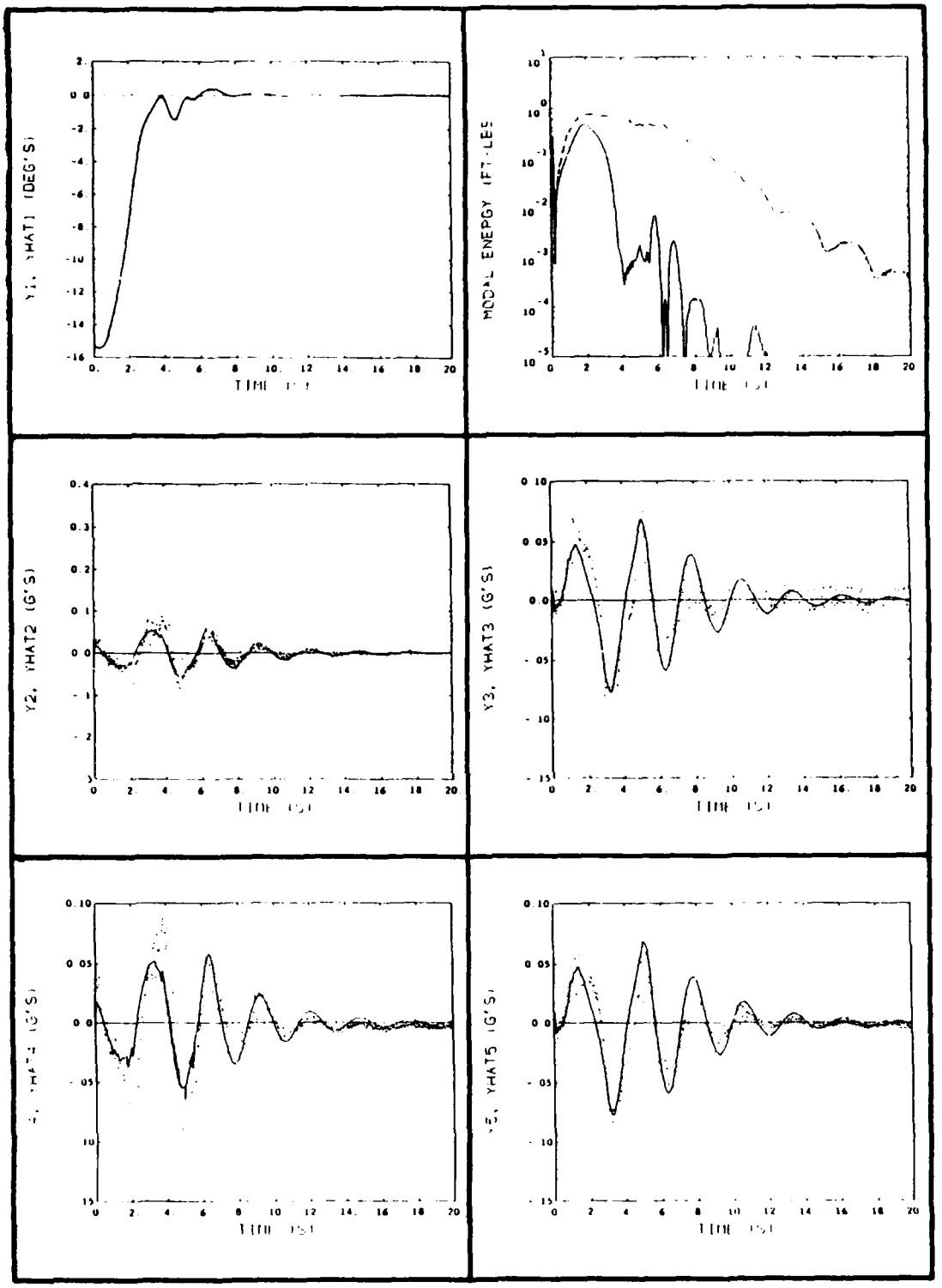

Figure 16-20. 15 degree slew, using thrusters with terminal phase constraints, with the hub torquer active in the terminal phase, and with PMAs active throughout the test. (Hub angle, vibrational energy, and accelerometer measurements).

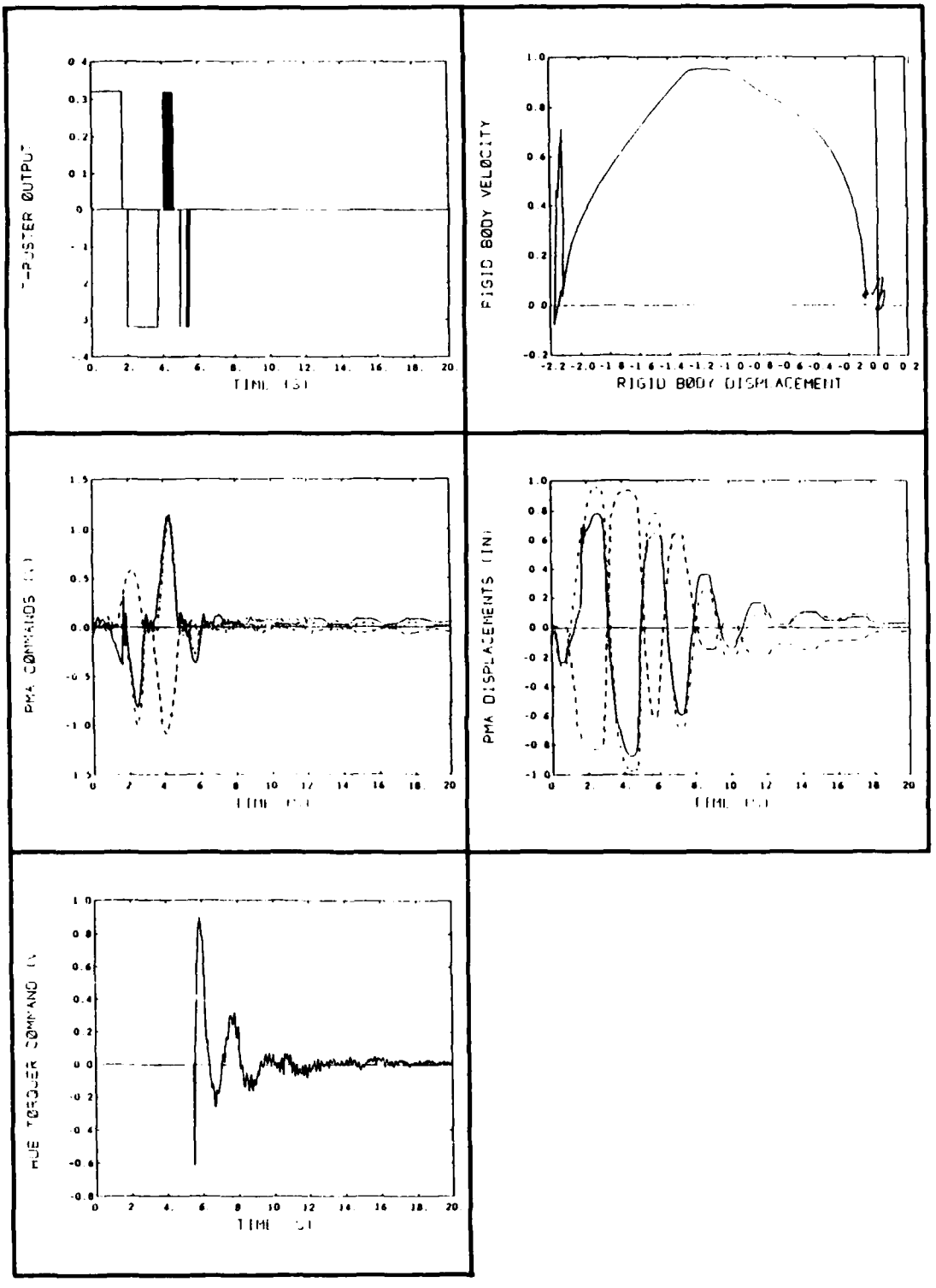

Figure 16-21. 15 degree slew, using thrusters with terminal phase constraints, with the hub torquer active in the terminal phase, and with PMAs active throughout the test. (Rigid body phase plane, thruster force command, PMA displacements, PMA force commands, and hub torque command).

and structural vibration control.

16.3.8 Miscellaneous Test Runs

Certain other tests were conducted to provide additional insight into the characteristics of the AFAL experiment. Discussion of these runs is included here to illustrate some interesting properties of the system. The actual test data plots are given in Appendix M.

Each of the supplementary sets of tests were conducted with the following controls active: thrusters alone (LVF constrained); thrusters (LVF constrained) and PMAs active throughout the test; and, finally, with thrusters (LVF constrained), PMAs active throughout the test, and hub torque control active in the terminal phase.

The first two sets of tests were (i) 45 degree and (ii) 2 degree slew maneuvers. Previously, it was claimed that the 15 degree slew maneuver was a particularly demanding task for the RCS controller because it results in excessive excitation of the twist mode. The 45 degree and 2 degree slew tests were conducted to investigate the maneuver dependent performance characteristics.

The 45 degree test results clearly show a marked improvement in system performance. This effect is most clearly demonstrated by the vibrational energy traces of the 'thruster only' test. While the peak energy reaches values comparable to those of the 15 degree slew maneuvers, by the time the structure has reached 45 degrees, the energy has dropped by an order of magnitude. The increased thruster firing time allows the vibrational modes to cycle multiple times during firing, and the thruster switching is no longer phased so as to excite the scissors mode. Consequently, the limit-cycle is not induced during the test, this despite the use of thrusters alone. The subsequent tests incorporating the linear actuators predictably improve performance even further.

By contrast, the 2 degree maneuver did not prevent the excitation of a limit-cycle. While the overall vibrational energy of the system is gradually decreasing, the thruster firings continue through the end of the 20 second test. However, the addition of the PMAs again removed enough scissors-mode energy to prevent the limit-cycle. The structure quickly settles down and comes to rest at the boundary of the ± 0.25 degree deadband, preventing further thruster firings. However, it is this group of 2 degree slew tests which clearly demonstrate the utility of the hub torque controller. The thrusters plus PMA combination produced a terminal error of exactly the size of the deadband, while the hub torque control produced a zero-error final condition, subject only to the friction level of the air-bearing table.

The final set of supplementary tests explored the effects of higher thruster force levels. All previous tests were conducted with a 300 lb. line pressure. Before the addition of linear actuators, the use of a 500 lb. line pressure (which produces a higher thrust level) resulted in an extremely violent limit-cycle as seen in the 'thruster only'

test. The vibrational motion was so great that the thrusters were disabled 14 seconds into the test to prevent damage to the structure. Activation of the PMAs improved the performance, yet did not provide sufficient vibrational damping to eliminate the limit-cycle. Activation of the hub torquer in the terminal phase resulted in a satisfactory slew response, although this was primarily because the thruster control is simultaneously deactivated. While the initial intent of increasing the thrust level was to speed up the maneuver, the increase in vibrational energy imparted by the thrusters reduced the benefit of the faster slew—significantly more time was required to damp out the added vibrational energy and to satisfy the pointing goals.

Section 17

Conclusions

17.1 Primary Objectives

The experimental program verified the ability to perform fast, large angle slews on a simulated flexible space structure, and to successfully integrate additional discrete, nominally linear actuators with the reaction control system. The linear actuators improved significantly the fine pointing/tracking and vibration suppression capability of the controller.

The predecessor program was never able to fully demonstrate the suitability of the RCS single-step optimal control law for slewing and fine-pointing of the AFAL experiment structure [1]. Because of the high friction present in the first air-bearing table, the previous experiment was quite benign and did not accurately represent a lightly damped flexible space structure. The flexible appendage vibrations were lightly damped, but the rigid body motion was significantly damped. While good slewing performance was demonstrated, the experiment limitations precluded an accurate indication of the performance capabilities or shortfalls of this type of thruster control.

The present program, utilizing a new low-friction air-bearing table, demonstrated more convincingly the limited capability of an RCS to remove vibrational energy imparted to a structure during a high rate slew maneuver. More accurate system modelling and RCS thruster firing constraints improved performance significantly; however, the basic limitations of the unthrottleable nonlinear actuators remained and were readily demonstrated. The limitations included excitation of higher frequency modes, a pronounced tendency to limit cycle, and that nonlinear constraints were needed to reduce the tendency to limit cycle.

The addition of nominally linear actuators to the system improved remarkably the performance of the slew maneuver and terminal phase fine pointing/tracking. The proofmass actuators mounted at each beam tip increased the system damping by a factor of 20 over the uncontrolled damping. While the PMAs had essentially no capability to effect rigid-body hub pointing, the high structural damping they provide prevented the large

overshoot and limit cycling previously evidenced by the RCS thrusters only. Because the PMAs were only effective for vibration damping, the system pointing performance was still limited by the deadband required for thruster control. The addition of the PMAs permitted reduction of the deadband from ± 0.5 degrees to ± 0.25 degrees, yet this limitation on absolute pointing remained.

The hub torque actuator complemented the other controls by eliminating the deadband during the terminal phase of the maneuver. By assuming the fine pointing control task, this actuator demonstrated a terminal pointing capability of ± 0.05 degrees, an accuracy that would have required an extremely narrow deadband, and guaranteed limit cycling if using the thruster controller alone.

The results show very emphatically how effective the linear actuators were in improving the fine-pointing and vibration suppression performance of the AFAL experiment. However, significant additional information gained in this investigation had less to do with slewing performance or pointing accuracies and more with the actual physical development of suitable actuator devices and the process of designing, constructing and running a ground-based experiment of this type. Some of the more important conclusions concerning these aspects of the experimental program are delineated below.

Finally, the implications of ground-based testing need to be better understood. While the AFAL experiment structure was probably well-suited to its early objectives as purely an RCS slewing maneuver testbed, the objectives of the present program might have been better addressed on a modified experimental facility. For example, the addition of the proof-mass actuators to the beam tips resulted in excessive torsional vibration and droop of the beams. This motion limited the frequency range over which the PMAs could be effectively utilized, thus limiting the scope of the vibration control experiment. The potential for higher bandwidth vibration suppression was consequently never realized.

17.2 Specific Comments

Noted below are some specific comments and conclusions concerning the experimental program. They relate to particular experiment hardware and to the implementation of the control system.

As always, attention to good experimental practices (i.e., shielding and grounding, designing reliable and repeatable tests, etc.) greatly reduced the potential for experimental problems when the actual tests were performed and significantly increased the quality of the data.

17.2.1 Air-Bearing Table

The specifications for the new air-bearing table appeared to be adequate to perform convincing ground-based tests on flexible satellite type space structures. The air-bearing friction level (approximately 7 in·oz of running friction torque) proved to be comparable to if not less than that of the Rapid Retargeting and Precision Pointing (R2P2) facility operated by Martin-Marietta in Denver for the SDIO.

17.2.2 Hub Torque Actuator Simulation

The air-bearing table torque motor was used to emulate a spacecraft-bus momentum exchange actuator such as a reaction wheel or single-axis control moment gyro. Because the primary use of the table motor was to provide this emulation capability, the characteristics of the torque motor and its controller could be chosen to be emulate the actual device. While this was not a primary objective in the experiment reported herein, the combination low-noise, low-torque capability of the specified motor and the inherent low table friction resulted in a useful simulation of an actual device.

17.2.3 Proof-Mass Actuators

Much time was spent overcoming the nonlinearities inherent in the voice-coil design of the PMAs. Additionally, while most non-experimental studies blindly propose the use of PMAs to provide inertial forces on a flexible structure, the proof-mass displacement constraint complicated the dynamics of the actuator significantly. In fact, the need to develop an effective control law for the PMA which explicitly recognized the physical stroke limitation led to a feedback law quite different from that which had been originally proposed. It was only as a result of requirements realized through experimentation using real hardware that these significant problems were addressed. It should be noted that the force and bandwidth capabilities of the PMAs developed and tested in this experiment are representative of the requirements for actual hardware on some contemplated flight tests.

The actuators specified for this experiment would be better suited to a higher mode frequency, lower amplitude damping application requiring reduced proof-mass travel. Most of the difficulties introduced by the actuator nonlinearities would then diminish.

17.2.4 Gravity Effects

Gravity was the most significant ground-based limitation for the AFAL experiment facility. Other factors (such air drag) were negligible for the experiments performed

during the study. The gravity effects resulted in contamination of the tip accelerometer signals and caused PMA motion to excite torsional modes of the arms. As the arms underwent horizontal bending motion, the weight of the tip mass caused the arms to droop to the side, exposing the accelerometers to a gravity component and thereby contaminating the accelerometer signals. The gravity contamination of the accelerometer signals was a possible cause of the terminal-phase limit cycle experienced by the RCS controller.

When a PMA was not at the center of its stroke, the gravity force on the center of gravity of the PMA assembly caused a torque about the longitudinal axis of the arm. Consequently, PMA motion would excite the (uncontrolled) torsional modes of the structure. The augmented torsional motion of the arms exposed the accelerometers to a larger gravity component and caused additional contamination of the accelerometer signals.

17.2.5 Control System Digital Implementation

Important factors concerning the digital implementation of the control system were the choice of the processor and the I/O subsystem, and the quality of the software development tools. The complete system, including the development tools, must be considered when choosing, or designing, a digital controller.

The processor and I/O subsystem (including the operating system software) require 'real-time' capabilities, judged in the time frame of the intended application (namely, interrupts handled quickly, little overhead needed to initiate I/O, etc.). Also, the computational capability of the processor and the throughput of the I/O system must minimally meet the requirements of the control tasks, and should preferably provide reasonable performance margins. The performance margins allow effort to be directed to exploring variations of control algorithms rather than developing the most computationally efficient implementation. This is particularly important in an experimental program where the control algorithms are subject to frequent change.

The software development tools should provide the means to build and debug applications which use a real-time kernel or operating system. The supported language(s) should include extensions to easily implement device driver routines, if necessary, and to interact with the operating system routines (to provide scheduling, handle interrupts, etc.). It is nearly essential that the debugger provide source-code level debugging while the application is running on the target processor. Early in the program, programmers were restricted to assembly-code level debugging only, which greatly increased the time needed to debug routines. The addresses of variable locations were difficult to resolve and tedious to examine. In contrast, when the source-code level debugger became available, variables could be referenced by name and entire data structures (records, arrays, etc.) could be examined easily.

The MicroVAX II-based controller readily met the computational and I/O performance needs of the AFAL experiments. The VAX ELN toolkit provided the development tools to easily design and implement real-time routines, including device drivers and interrupt handlers. Most importantly, VAX ELN included an excellent source-code level symbolic debugger. The symbolic debugger greatly increased the productivity of the programmers and allowed complex algorithms and data structures to be debugged in a straightforward manner.

References

[1] Floyd, M.A., "Single-Step Optimal Control of Large Space Structures", M.I.T. Dept. of Aeronautics & Astronautics, Sc.D. thesis, April 1984. Also CSDL report # CSDL-T-840.

[2] Bailey, T., Gruzen, A. and Madden, P., "RCS/Linear Discrete Actuator Study Interim Technical Report", CSDL report # CSDL-T-840.

[3] Moore, B.C., "Principal Component Analysis in Linear Systems: Controllability, Observability, and Model Reduction", IEEE Trans. Automat. Contr., vol. AC-26, pp. 17-32, Feb 1981.

[4] Enns, D.F., "Model Reduction with Balanced Realizations: An Error Bound and a Frequency Weighted Generalization", Conf. on Decision and Control, Las Vegas, 1984.

[5] Skelton, R.E. and Yousuff, A., "Component Cost Analysis of Large Scale Systems", Int. J. Contr., vol. 37, pp. 285-304, 1983.

[6] Hyland, D.C., "Application of the Maximum Entropy/Optimal Projection Control Design Approach for Large space Structures", Large Space Antenna Systems Technology – 1984 Conference, December 4-6, 1984.

[7] Bernstein, D.S. and Hyland, D.C., "Optimal Projection/Maximum Entropy Stochastic Modelling and Reduced-Order Design Synthesis", IFAC Workshop on Model Error Concepts and Compensation, Boston, MA, June 1985.

[8] Bernstein, D.S. and Greeley, S.W., "Robust Controller Synthesis Using the Maximum Entropy Design Equations", submitted for publication.

[9] Hyland, D.C., "Comparison of Various Controller-Reduction Methods: Suboptimal Versus Optimal Projection", Proc. AIAA Dynamics Specialists Conference, Palm Springs, CA, May 1984.

[10] Hyland, D.C. and Bernstein, D.S., "The Optimal Projection Equations for Model Reduction and the Relationships Among the Methods of Wilson, Skelton, and Moore", IEEE Trans. Automat. Contr., vol. AC-30, pp. 1201-1211, Dec 1985.

[11] Hyland, D.C., "The Optimal Projection Approach to Fixed-Order Compensation: Numerical Methods and Illustrative Results", AIAA 21^{st} Aerospace Sciences Meeting, Reno, NV, January 1983.

[12] Bernstein, D.S. and Hyland, D.C., "The Optimal Projection Approach to Designing Optimal Finite-Dimensional Controllers for Distributed-Parameter Systems", 23^{rd} IEEE Conference on Decision and Control, Las Vegas, NV, December 1984.

[13] Hyland, D.C. and Bernstein, D.S., "The Optimal Projection Equations for Fixed-Order Dynamic Compensation", IEEE Trans. Automat. Contr., vol. AC-29, pp. 1034-1037, Nov 1984.

[14] Hyland, D.C., "Optimality Conditions for Fixed-Order Dynamic Compensation of Flexible Spacecraft with Uncertain Parameters", Proc. AIAA 20^{th} Aerospace Sciences Meeting, paper 82-1403, January 1982.

[15] Hyland, D.C. and Madiwale, A.N., "A Stochastic Design Approach for Full-Order Compensation of Structural Systems with Uncertain Parameters", AIAA Guidance and Control Conference, Albuquerque, NM, August 1981.

[16] Bernstein, D.S. and Hyland, D.C., "The Optimal Projection Equations for Reduced-Order State Estimation", IEEE Trans. Automat. Contr., vol. AC-30, pp. 583-585, Jun 1985.

[17] Bernstein, D.S. and Hyland, D.C., "The Optimal Projection Equations for Fixed-Order Dynamic Compensation of Distributed Parameter Systems", Proc. AIAA Dynamics Specialists Conference, Palm Springs, CA, May 1984.

[18] Hyland, D.C., Mean-Square Optimal, Fixed Order Compensation— Beyond Spillover Suppression", AIAA Astrodynamics Conference, San Diego, CA, August 1982.

[19] Hyland, D.C., "Mean-Square Optimal, Full-Order Compensation of Structural Systems with Uncertain Parameters", M.I.T., Lincoln Laboratory, TR-626, June 1983.

[20] Ly, U.-L., Bryson, A.E. and Cannon, R.H., "Design of Low-order Compensators using Parameter Optimization, Automatica, vol. 21, no. 3, pp. 315-318, 1985.

[21] Ashkenazi, A. and Bryson, A.E., "Control Logic for Parameter Insensitivity and Disturbance Attenuation", AIAA J. Guidance & Control, vol. 5, no. 4, pp. 383-388, 1982.

[22] Doyle, J.C., "Guaranteed Margins for LQG Regulators" IEEE Trans. Automat. Contr., vol. AC-23, pp.756-757, Aug 1978.

[23] Jaynes, E.T., "Where Do We Stand on Maximum Entropy?" in The Maximum Entropy Formalism, Levine, D. and Tribus, M., eds., MIT Press, pp.15-118, Cambridge, MA, 1979.

[24] Athans, M., Ku, R.T. and Gershwin, S.B., "The Uncertainty Threshold Principle: Some Fundamental Limitations of Optimal Decision Making Under Dynamic Uncertainty", IEEE Trans. Automat. Contr., vol. AC-22, pp.491-495, 1977.

[25] Levine, W.S., Johnson, T.L., and Athans, M., "Optimal Limited State Variable Feedback Controllers for Linear Systems", IEEE Trans. Automat. Contr., vol. AC-16, pp. 785-793, 1971.

[26] Strang, G., Linear Algebra and its Applications, MIT Press, Cambridge, MA, 1980.

[27] Private communication with Dennis Bernstein and Larry Davis of the Harris Corp., Controls Analysis and Synthesis Group, GASD, Melbourne, FL.

[28] Pearson, R., "Optimal Velocity Feedback Control of Flexible Structures", M.I.T. Dept. of Electrical Engineering & Computer Science, Ph.D. thesis, January, 1982. Also CSDL report # CSDL-T-771.

[29] Safonov, M.G. and Athans, M., "Gain and Phase Margins for Multiloop LQG Regulators", IEEE Trans. Automat. Contr., vol. AC-22, April 1977.

[30] Private communication with "SANDY" users presently at the C.S. Draper Labs, NASA Programs Dept., Control & Dynamics Div.

[31] CTRL-C Users Guide, version 3.0, August 1985, Systems Control Technology, Palo Alto, CA.

[32] Martin, G.D. and Bryson, A.E., "Attitude Control of a Flexible Spacecraft", AIAA J. Guidance & Control, vol. 3, no. 1, pp. 37-41, 1980.

[33] Balas, M. "Feedback Control of Flexible Systems", IEEE Trans. Auto. control, 23, pp 673-679, 1978.

[34] Franklin, G.F. and Powell, J.D., Digital Control of Dynamic Systems, Addison-Wesley, 1981.

[35] Athans, M. "A Tutorial on the LQG/LTR Method", Proc. Am. Control Conf., Seattle, WA, June 1986.

[36] Kwakernaak, H. and Sivan, R., Linear Optimal Control Systems, John Wiley & Sons, 1972.

[37] Kailath, T., Linear Systems, Prentice-Hall, 1980.

Appendix A

Sensor and Actuator Specifications

This appendix contains specifications for the new sensors and actuators which have been added to the AFAL structure.

BEI KIMCO LA16-19A linear actuators

LINEAR ACTUATOR LA16-19

-MOVING MAGNET-
-SmCo Magnet-

MECHANICAL DATA

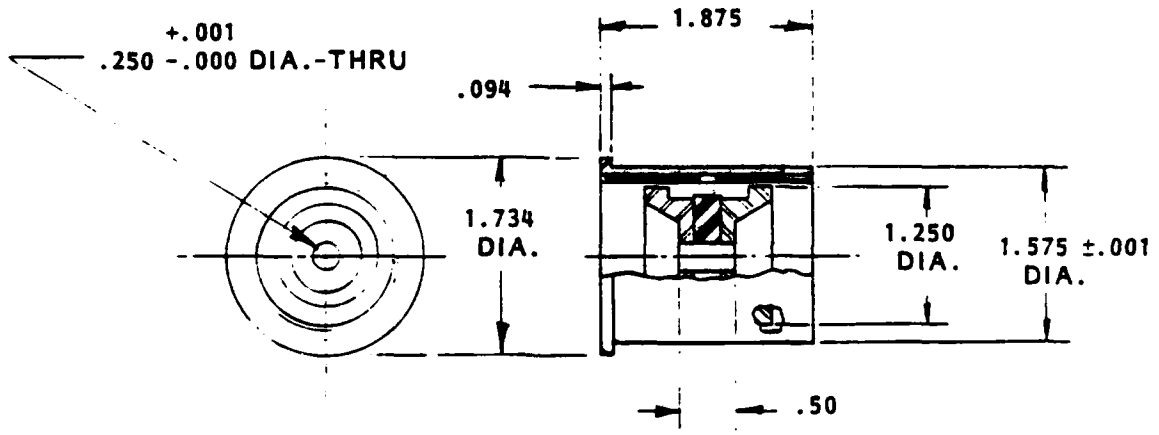

PERFORMANCE DATA

		WINDING			
		A	B	C	D
● PEAK FORCE (F_P)	LBS	2.5	2.5		
● FORCE CONSTANT (K_F)	LBS/AMP	1.0	2.0		
● BACK EMF CONSTANT (K_B)	VOLTS/FT/SEC	1.36	2.7		
● MOTOR CONSTANT (K_M)(25°C)	LBS/$\sqrt{\text{WATTS}}$	.37	.35		
● CURRENT @ PEAK FORCE (I_P)	AMP	2.5	1.3		
● POWER AT PEAK FORCE (P_P)(25°C)	WATTS	46	51		
● RESISTANCE (25°C)	OHMS	7.3	30		
● ELECT. TIME CONSTANT	MICRO. SEC	380	380		
● THERMAL RESISTANCE OF COIL	°C/WATT	3.6	3.6		
● STROKE	INCH±	.25	.25		
● CLEARANCE EACH SIDE OF COIL	INCH	.015	.015		
● MAX. ALLOWABLE COIL TEMP.	°C	155	155		
● WEIGHT MOVING MAGNET ASSEMBLY	LBS	.22	.22		
● TOTAL WEIGHT	LBS	.6	.6		

BEI KIMCO LA23-43-001 linear actuators

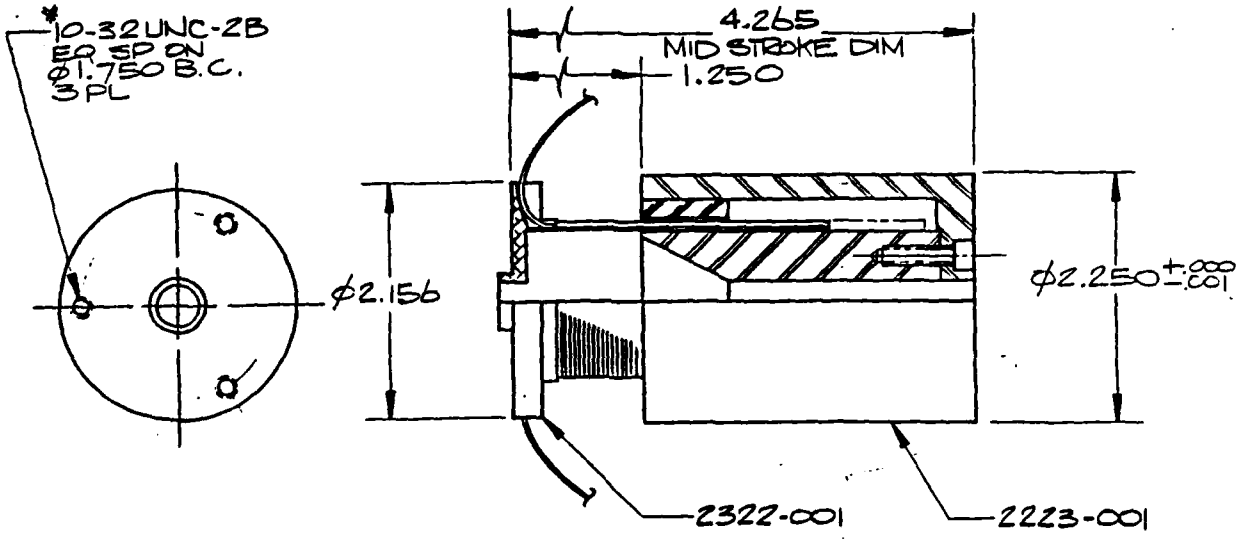

PERFORMANCE DATA

BACK EMF CONSTANT (KB) (VOLTS/FT/SEC)	2.71
MOTOR CONSTANT (KM) 25°C (LBS/√WATTS)	.94
CURRENT @ PEAK FORCE (AMP)	2.75
POWER @ PEAK FORCE (WATTS)	54.0
PEAK FORCE (FP) (INTERMITTENT) (LBS)	5.5
FORCE CONSTANT KF (IN.) (LBS/AMP)	2.0
STROKE	±.875"
RESISTANCE (OHMS @ 25°C)	4.5 Ω
MAX. ALLOWABLE COIL TEMP (°C)	155°C
NOMINAL CLEARANCE GAP EACH SIDE OF COIL (IN.)	.025"
THERMAL RESISTANCE OF COIL (°C/WATT)	TBD
WEIGHT OF MOVING COIL (LBS)	.50
TOTAL WEIGHT (LBS)	2.4

NOTES: (UNLESS OTHERWISE SPECIFIED)

1. COIL ASSY SHOWN IN MID TRAVEL

Endevco 7302B angular accelerometers

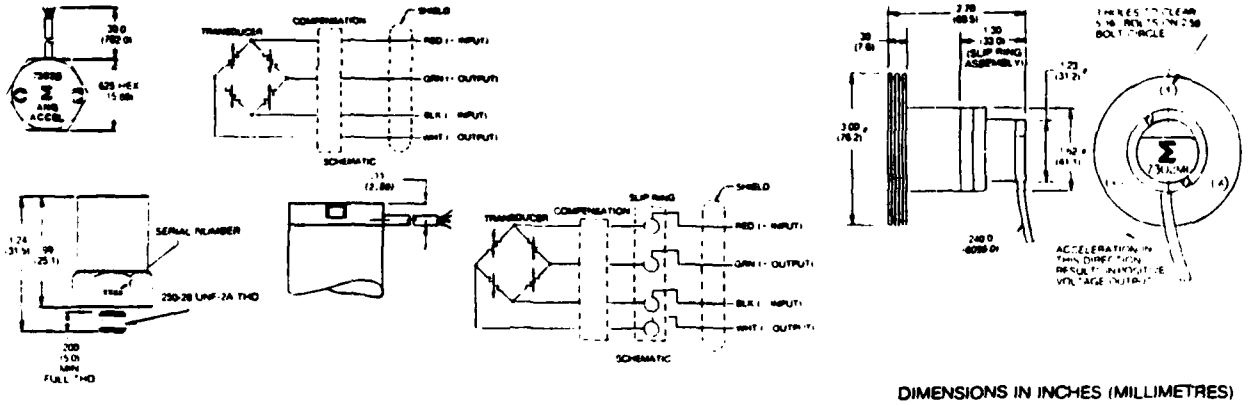

DIMENSIONS IN INCHES (MILLIMETRES)

SPECIFICATIONS FOR MODELS 7302B AND 7302M1 ACCELEROMETERS

DYNAMIC

Sensitivity (at 10 Vdc)	4.0 μV per rad/s^2 typical, 3.0 to 5.5 μV per rad/s^2	
Full Scale	50 000 rad/s^2	
Amplitude Linearity	Data suggest that sensitivity at full scale is ±1% relative to sensitivity at 1000 rad/s^2. Measurement uncertainties prevent stating this as a specification limit.	
Mounted Resonant Frequency	2700 to 3300 Hz, 3000 Hz typical	
Frequency Response	±4%, 1 Hz to 600 Hz, typical, reference 100 Hz	
Phase Response	Typical of 0.05 critically damped single-degree-of-freedom system	
Transverse Angular Sensitivity	2% maximum	
Linear Acceleration Sensitivity	Data suggests direct proportionality with frequency below 600 Hz, and a value of less than 1.0 equivalent rad/s^2 per g in any direction at 100 Hz. Measurement uncertainities prevent stating this as a specification limit.	
Sensitivity Deviation Due to Temperature	**Temp**	**Typical** / **Maximum**
	50°F	±3% / ±5%
	125°F	from / from
	200°F	average / average

ELECTRICAL

Excitation	10.0 Vdc, 14 Vdc maximum
Electrical Confguration	Four-active-arm piezoresistive bridge
Polarity	Positive output for counterclockwise acceleration of mounting surface, as viewed from the top.
Input/Output Resistance	2400Ω/1600Ω typical
Insulation Resistance	100 MΩ between pins and pins to case. Case is grounded.
Zero Measurand Output	±25 mV maximum
Background Noise	10 μV rms

PHYSICAL

Weight	1.23 oz (35 g)/10.58 oz (300 g)
Case Material	Stainless Steel
Mounting	1/4-28 Integral stud Recommended mounting torque 10 lbf-in (1.1 N-m)
Moment of Intertia	Approximately 0.00015 oz f-in-s^2 (10 g-cm^2)/approx 1700 g-cm^2

ENVIRONMENTAL

Temperature		0°F to +250°F (−18°C to +120°C) continuous operation
Shock	Angular Acceleration:	500 000 rad/s^2
	Linear Acceleration:	2500 g
Humidity		Hermetically sealed with all-welded case

Schaevitz 1000 DC-D LVDTs

DC-D SERIES—HYBRID THICK-FILM CIRCUITRY

- COMPUTER-DESIGNED FOR EXCEPTIONAL LINEARITY
- RESISTS SHOCK AND VIBRATION

The *DC-D Series combines a hybrid microcircuit signal* conditioner with a computer-designed AC-LVDT. This results in an extremely reliable DC-operated position transducer. The DC-D is normally powered by a regulated ±15V DC supply and converts core displacements into proportional outputs up to ±10V DC. Microminiature components used in the construction of DC-D's are selected for maximum stability. All electrical connections are hand-soldered with the aid of special tools. Vacuum encapsulation of all elements produces an assembly that is virtually indestructible when exposed to shock, vibration, and other forms of physical abuse. Double magnetic shielding provides protection against stray electrical fields.

GENERAL SPECIFICATIONS

Input . . . . . ±15 V DC (nominal), ±20 ma
Operating Temperature Range . . . . . 0°F to +160°F (-18°C to +70°C)
Survival Temperature Range . . . . . -65°F to +200°F (-55°C to +95°C)
Null Voltage . . . . . 0 V DC
Ripple . . . . . Less than 25 mV rms
Linearity . . . . . 0.25% full range
Stability . . . . . 0.125% full scale
Temperature Coefficient of Scale Factor . . . . . 0.04%/°F (0.08%/°C)
Shock Survival . . . . . 250 *g* for 11 milliseconds
Vibration Tolerance . . 10 *g* up to 2 kHz
Coil Form Material . . High density, glass-filled polymer
Housing Material . . . AISI 400 series stainless steel
Lead Wires . . . . . 28 AWG, stranded copper, Teflon-insulated, 12 inches (300 mm) long (nominal)
Output Impedance . . Less than 1 Ohm

PERFORMANCE SPECIFICATIONS AND DIMENSIONS

LVDT MODEL NUMBER	NOMINAL LINEAR RANGE	SCALE FACTOR	RESPONSE -3dB	WEIGHT Grams		DIMENSIONS A (Body)	B (Core)	P
	Inches	V/Inch	Hz	Body	Core	Inches	Inches	Inches
050 DC-D	±0.050	200	500	62	2	2.10	0.58	0.50
100 DC-D	±0.100	100	500	69	3	2.83	1.10	0.93
200 DC-D	±0.200	50	500	73	5	3.80	1.80	1.35
500 DC-D	±0.500	20	200	82	8	5.49	3.00	2.20
1000 DC-D	±1.000	10	200	120	10	7.75	3.80	3.28
2000 DC-D	±2.000	5.0	200	155	13	11.12	5.00	5.01
3000 DC-D	±3.000	3.3	200	268	14	16.32	6.20	7.55
5000 DC-D	±5.000	2.0	200	325	17	20.15	6.20	9.53
10000 DC-D	±10.00	1.0	200	445	24	35.38	12.00	16.58

ORDERING INFORMATION

(Fold out page 32 for instructions on how to use this chart.)

OPTION NO.	000	010	020	040	000
MODEL NO.	METRIC THREAD CORE (NOTE 1)	TEFLON BORELINER	SMALL DIAMETER CORE (NOTE 2)	10 FOOT (3m) LEADS	MILDLY RADIATION RESISTANT
050 DC-D	N	B	B	F	X
100 DC-D	N	B	B	F	X
200 DC-D	N	B	B	F	X
500 DC-D	N	B	B	F	X
1000 DC-D	N	C	X	F	X
2000 DC-D	N	C	X	F	X
3000 DC-D	N	C	X	F	X
5000 DC-D	N	C	X	F	X
10000 DC-D	N	C	X	F	X

Note 1: See outline drawing for metric thread size
Note 2: Consult factory for mass, dimensions, and thread size

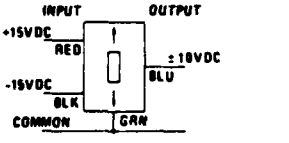

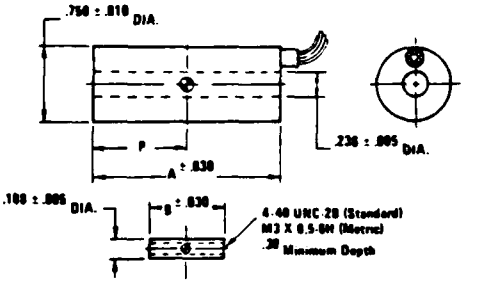

Appendix B

Reduced Order Compensators for Ly, Bryson, and Cannon's Problem

Full Order LQG Compensator

AC7 =

-0.5898	0.0465	0.0023	-0.1128	-0.0281	0.4181	-0.0039
0.0445	-1.9395	1.7254	-2.4239	0.0650	-0.0119	2.0397
2.8060	-0.8192	-4.3289	-10.6396	-2.5503	-1.5378	4.7276
0.0308	0.0000	1.0000	-0.6888	0.0187	-0.0308	0.0000
-0.0855	-1.0000	0.0000	2.2263	-0.4305	0.0855	0.0000
2.8630	0.0000	0.0000	0.1844	0.0077	-3.3450	0.0000
0.1671	0.0000	0.0000	-1.8559	0.1035	-0.1671	-1.0570

F7 =

0.2538	-0.2152	-0.0043
-0.3428	2.1574	-0.1300
0.1796	0.2420	0.0168
-0.0308	0.6888	-0.0187
0.0855	-0.4663	0.4305
-2.8630	-0.1844	-0.0077
-0.1671	1.8559	-0.1035

K7 =

0.2541	0.2855	-0.1226	-0.9452	-0.2303	-0.1388	0.0698
0.2910	-0.0105	-0.0023	0.0060	0.0324	-0.1193	-0.0321

4^{th} Order Optimal Projection Compensator

AC4 =

-0.1261	-0.5046	1.4662	2.1907
0.6468	0.0161	-0.9776	0.2823
-0.4383	0.4245	-1.7091	0.0714
-0.6446	-0.1808	1.5061	-4.0980

F4 =

0.3181	0.1725	0.0462
-0.1184	0.4303	-0.0081
-0.4227	0.3846	-0.1762
0.9704	-0.0251	-0.1304

K4 =

-0.0301	-0.1190	0.3677	0.5152
-0.0257	-0.0382	-0.3295	0.3001

3^{rd} Order Optimal Projection Compensator

AC3 =

-1.7764	-0.0934	-0.4453
-1.5303	-4.1113	0.6738
1.4203	-2.2543	-0.0702

F3 =

-0.4551	0.3838	-0.1769
-0.9461	0.0470	0.1357
0.3207	0.1774	0.0460

K3 =

0.3548	-0.5236	-0.0162
-0.3338	-0.2939	-0.0261

2nd Order Optimal Projection Compensator

```
AC2          =

  -0.0639   -1.6751
   0.7081   -2.4724

F2           =

  -0.4242   -0.3181   -0.0409
  -0.6416    0.4077   -0.2434

K2           =

   0.0010    0.3443
   0.0873   -0.2971
```

1st Order Optimal Projection Compensator

```
AC1          =

  -2.7513

F1           =

   0.4875    1.3274    0.3660

K1           =

  -0.5929
   0.4399
```

Appendix C

Vibrational Modes of the AFAL Experimental Structure

In addition to the rigid body mode, the following anti-symmetrical structural modes were included in the dynamic model, as described in Section 7.1.1. This model was used only for the initial OP/ME compensator development and does not reflect the updated NASTRAN model used in the latter stages of the experimental program, although the modeshapes were visually quite similar.

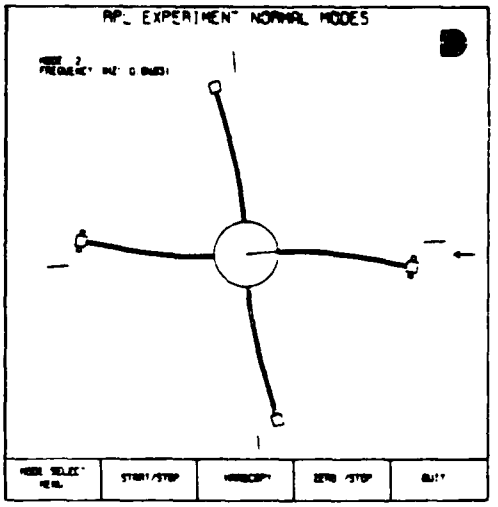

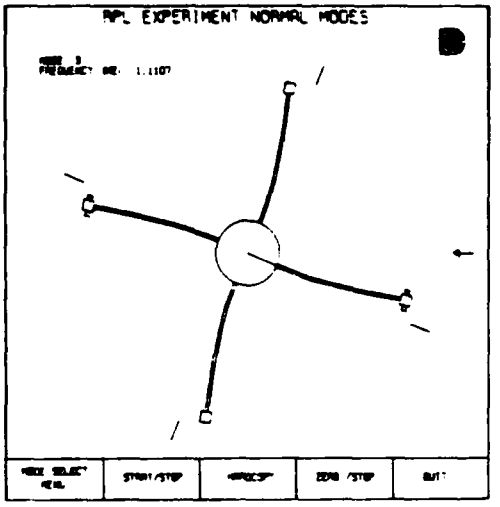

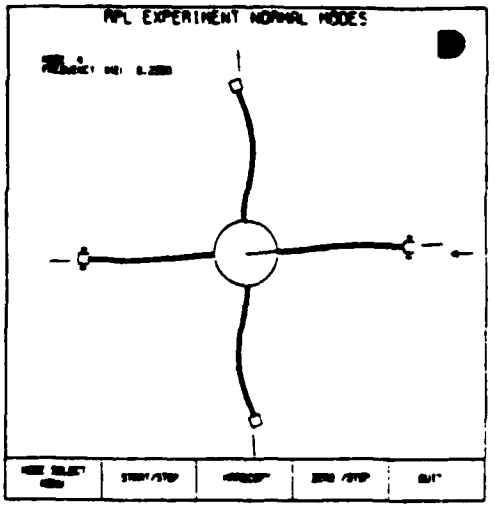
RPL EXPERIMENT NORMAL MODES

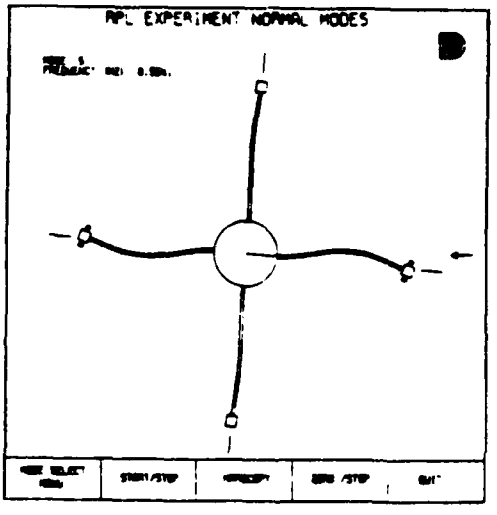
RPL EXPERIMENT NORMAL MODES

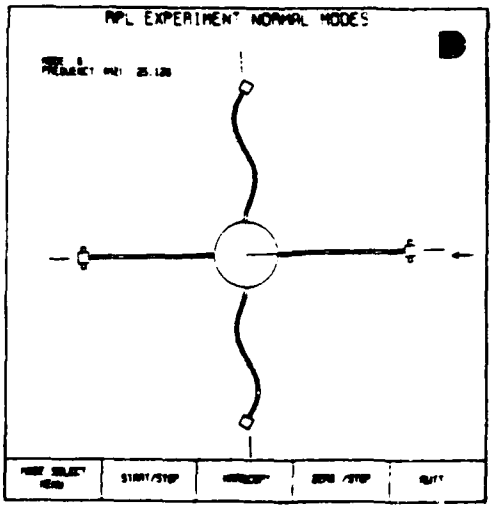
RPL EXPERIMENT NORMAL MODES

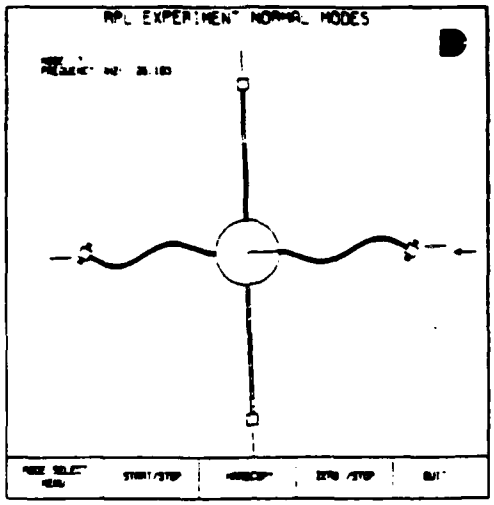
APL EXPERIMENT NORMAL MODES
START/STOP
QUIT

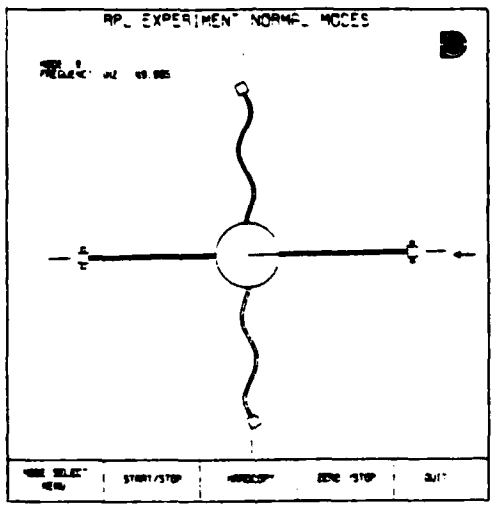
APL EXPERIMENT NORMAL MODES
START/STOP
QUIT

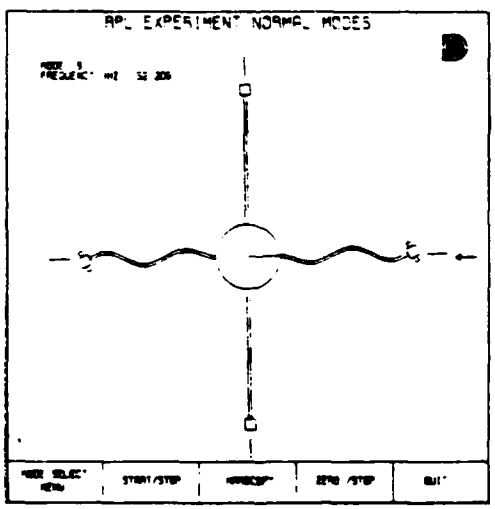
APL EXPERIMENT NORMAL MODES
START/STOP
QUIT

Appendix D

Preliminary System Dynamics Matrices for the AFAL Experimental Structure

This model was developed in the predecessor program and has been used only for the initial OP/ME compensator development. The model does not reflect the updated NASTRAN model used in the latter stages of the experimental program. The updated model is presented in Appendix I.

A matrix

A =

Starting at row 1 columns 1 thru 8

0.0000	0.0000	0.0000	0.0000	0.0000	0.0000	0.0000	0.0000
0.0000	0.0000	0.0000	0.0000	0.0000	0.0000	0.0000	0.0000
0.0000	0.0000	0.0000	0.0000	0.0000	0.0000	0.0000	0.0000
0.0000	0.0000	0.0000	0.0000	0.0000	0.0000	0.0000	0.0000
0.0000	0.0000	0.0000	0.0000	0.0000	0.0000	0.0000	0.0000
0.0000	0.0000	0.0000	0.0000	0.0000	0.0000	0.0000	0.0000
0.0000	0.0000	0.0000	0.0000	0.0000	0.0000	0.0000	0.0000
0.0000	0.0000	0.0000	0.0000	0.0000	0.0000	0.0000	0.0000
0.0000	0.0000	0.0000	0.0000	0.0000	0.0000	0.0000	0.0000
0.0000	0.0000	0.0000	0.0000	0.0000	0.0000	0.0000	0.0000
0.0000	-4.0735	0.0000	0.0000	0.0000	0.0000	0.0000	0.0000
0.0000	0.0000	-6.9790	0.0000	0.0000	0.0000	0.0000	0.0000
0.0000	0.0000	0.0000	-51.8675	0.0000	0.0000	0.0000	0.0000
0.0000	0.0000	0.0000	0.0000	-53.7469	0.0000	0.0000	0.0000
0.0000	0.0000	0.0000	0.0000	0.0000	-157.8845	0.0000	0.0000
0.0000	0.0000	0.0000	0.0000	0.0000	0.0000	-164.5096	0.0000
0.0000	0.0000	0.0000	0.0000	0.0000	0.0000	0.0000	-313.9392
0.0000	0.0000	0.0000	0.0000	0.0000	0.0000	0.0000	0.0000
0.0000	0.0000	0.0000	0.0000	0.0000	0.0000	0.0000	0.0000
0.0000	-3.7906	3.3806	-4.0919	-14.7802	1.0167	-23.0243	-0.2883
0.0000	0.0000	0.0000	0.0000	0.0000	0.0000	0.0000	0.0000
0.0000	4.8430	6.0405	23.2128	-6.4394	-36.4551	-1.5629	25.6167

Starting at row 1 columns 9 thru 16

0.0000	1.0000	0.0000	0.0000	0.0000	0.0000	0.0000	0.0000
0.0000	0.0000	4.0735	0.0000	0.0000	0.0000	0.0000	0.0000
0.0000	0.0000	0.0000	6.9790	0.0000	0.0000	0.0000	0.0000
0.0000	0.0000	0.0000	0.0000	51.8675	0.0000	0.0000	0.0000
0.0000	0.0000	0.0000	0.0000	0.0000	53.7469	0.0000	0.0000
0.0000	0.0000	0.0000	0.0000	0.0000	0.0000	157.8845	0.0000
0.0000	0.0000	0.0000	0.0000	0.0000	0.0000	0.0000	164.5096
0.0000	0.0000	0.0000	0.0000	0.0000	0.0000	0.0000	0.0000
0.0000	0.0000	0.0000	0.0000	0.0000	0.0000	0.0000	0.0000
0.0000	0.0000	0.0000	0.0000	0.0000	0.0000	0.0000	0.0000
0.0000	0.0000	-0.0815	0.0000	0.0000	0.0000	0.0000	0.0000
0.0000	0.0000	0.0000	-0.1396	0.0000	0.0000	0.0000	0.0000
0.0000	0.0000	0.0000	0.0000	-1.0374	0.0000	0.0000	0.0000
0.0000	0.0000	0.0000	0.0000	0.0000	-1.0749	0.0000	0.0000
0.0000	0.0000	0.0000	0.0000	0.0000	0.0000	-3.1577	0.0000
0.0000	0.0000	0.0000	0.0000	0.0000	0.0000	0.0000	-3.2902
0.0000	0.0000	0.0000	0.0000	0.0000	0.0000	0.0000	0.0000
-328.0362	0.0000	0.0000	0.0000	0.0000	0.0000	0.0000	0.0000
0.0000	0.0000	0.0000	0.0000	0.0000	0.0000	0.0000	0.0000
16.1724	0.0000	-0.0758	0.0676	-0.0018	-0.2956	0.0203	-0.4605
0.0000	0.0000	0.0000	0.0000	0.0000	0.0000	0.0000	0.0000
0.3719	0.0000	0.0969	0.1208	0.4643	-0.1288	-0.7291	-0.0313

A matrix, continued:

Starting at row 1 columns 17 thru 22

0.0000	0.0000	0.0000	0.0000	0.0000	0.0000
0.0000	0.0000	0.0000	0.0000	0.0000	0.0000
0.0000	0.0000	0.0000	0.0000	0.0000	0.0000
0.0000	0.0000	0.0000	0.0000	0.0000	0.0000
0.0000	0.0000	0.0000	0.0000	0.0000	0.0000
0.0000	0.0000	0.0000	0.0000	0.0000	0.0000
0.0000	0.0000	0.0000	0.0000	0.0000	0.0000
313.9392	0.0000	0.0000	0.0000	0.0000	0.0000
0.0000	328.0362	0.0000	0.0000	0.0000	0.0000
0.0000	0.0000	-0.0038	-0.0093	-0.0038	-0.0093
0.0000	0.0000	0.0043	0.0105	-0.0054	-0.0134
0.0000	0.0000	-0.0022	-0.0054	-0.0040	-0.0097
0.0000	0.0000	0.0004	0.0009	-0.0020	-0.0050
0.0000	0.0000	0.0013	0.0031	0.0005	0.0013
0.0000	0.0000	0.0000	-0.0001	0.0011	0.0026
0.0000	0.0000	0.0006	0.0016	0.0000	0.0001
-6.2788	0.0000	0.0000	0.0000	-0.0004	-0.0009
0.0000	-6.5607	-0.0002	-0.0006	0.0000	0.0000
0.0000	0.0000	0.0000	1.0000	0.0000	0.0000
-0.0056	0.3234	-0.1659	-0.4070	0.0000	0.0000
0.0000	0.0000	0.0000	0.0000	0.0000	1.0000
0.5123	0.0074	0.0000	0.0000	-0.1659	-0.4070

B matrix

0.0000	0.0000
0.0000	0.0000
0.0000	0.0000
0.0000	0.0000
0.0000	0.0000
0.0000	0.0000
0.0000	0.0000
0.0000	0.0000
0.0000	0.0000
1.6609	1.6609
-1.8611	2.3778
0.9688	1.7310
-0.1578	0.8951
-0.5500	-0.2396
0.0129	-0.4618
-0.2799	-0.0190
-0.0018	0.1632
0.0986	0.0023
0.0000	0.0000
68.6861	0.0000
0.0000	0.0000
0.0000	66.2203

C matrix

```
C          =

    Starting at row    1 columns    1 thru    8
    9.5162    0.5442   -1.8844    0.0299   -0.0517    0.0060    0.0063    0.0020
    0.0000    3.7906   -3.3806    4.0919   14.7802   -1.0167   23.0243    0.2803
    0.0000   -4.8430   -6.0405  -23.2128    6.4394   36.4551    1.5629  -25.6167
    0.0000    3.7906   -3.3806    4.0919   14.7802   -1.0167   23.0243    0.2803
    0.0000   -4.8430   -6.0405  -23.2128    6.4394   36.4551    1.5629  -25.6167
    0.0000    0.0000    0.0000    0.0000    0.0000    0.0000    0.0000    0.0000
    0.0000    0.0000    0.0000    0.0000    0.0000    0.0000    0.0000    0.0000

    Starting at row    1 columns    9 thru   16
    0.0019    0.0000    0.0000    0.0000    0.0000    0.0000    0.0000    0.0000
  -16.1724    0.0000    0.0758   -0.0676    0.0818    0.2956   -0.0203    0.4605
   -0.3719    0.0000   -0.0969   -0.1208   -0.4643    0.1288    0.7291    0.0313
  -16.1724    0.0000    0.0758   -0.0676    0.0818    0.2956   -0.0203    0.4605
   -0.3719    0.0000   -0.0969   -0.1208   -0.4643    0.1288    0.7291    0.0313
    0.0000    0.0000    0.0000    0.0000    0.0000    0.0000    0.0000    0.0000
    0.0000    0.0000    0.0000    0.0000    0.0000    0.0000    0.0000    0.0000

    Starting at row    1 columns   17 thru   22
    0.0000    0.0000    0.0000    0.0000    0.0000    0.0000
    0.0056   -0.3234    0.0000    0.0000    0.0000    0.0000
   -0.5123   -0.0074    0.0000    0.0000    0.0000    0.0000
    0.0056   -0.3234    0.0000    0.0000    0.0000    0.0000
   -0.5123   -0.0074    0.0000    0.0000    0.0000    0.0000
    0.0000    0.0000    1.0000    0.0000    0.0000    0.0000
    0.0000    0.0000    0.0000    0.0000    1.0000    0.0000
```

D matrix

```
D          =

    0.0000    0.0000
    3.7882    0.0000
    0.0000    6.2540
    3.7882    0.0000
    0.0000    6.2540
    0.0000    0.0000
    0.0000    0.0000
```

Appendix E

On-Off Thruster Slew Simulation

The following plots represent simulation number #LNEMNF095 taken from Ref [1]. The state vector at 2.98 seconds was chosen as an initial condition state vector for transient response simulations.

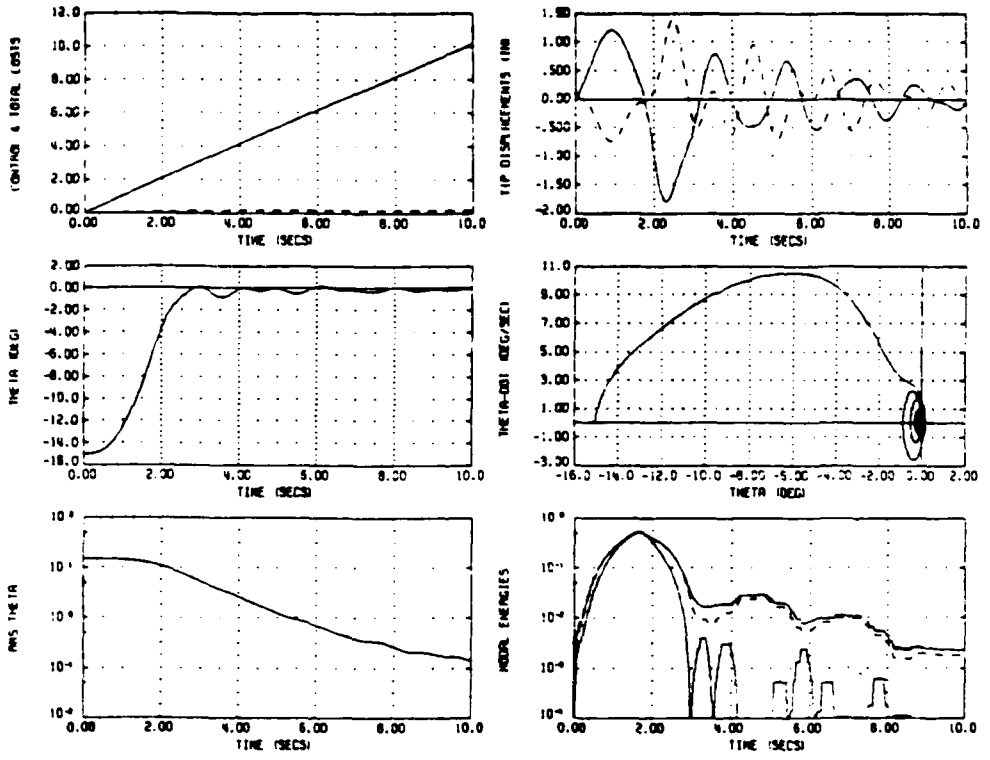

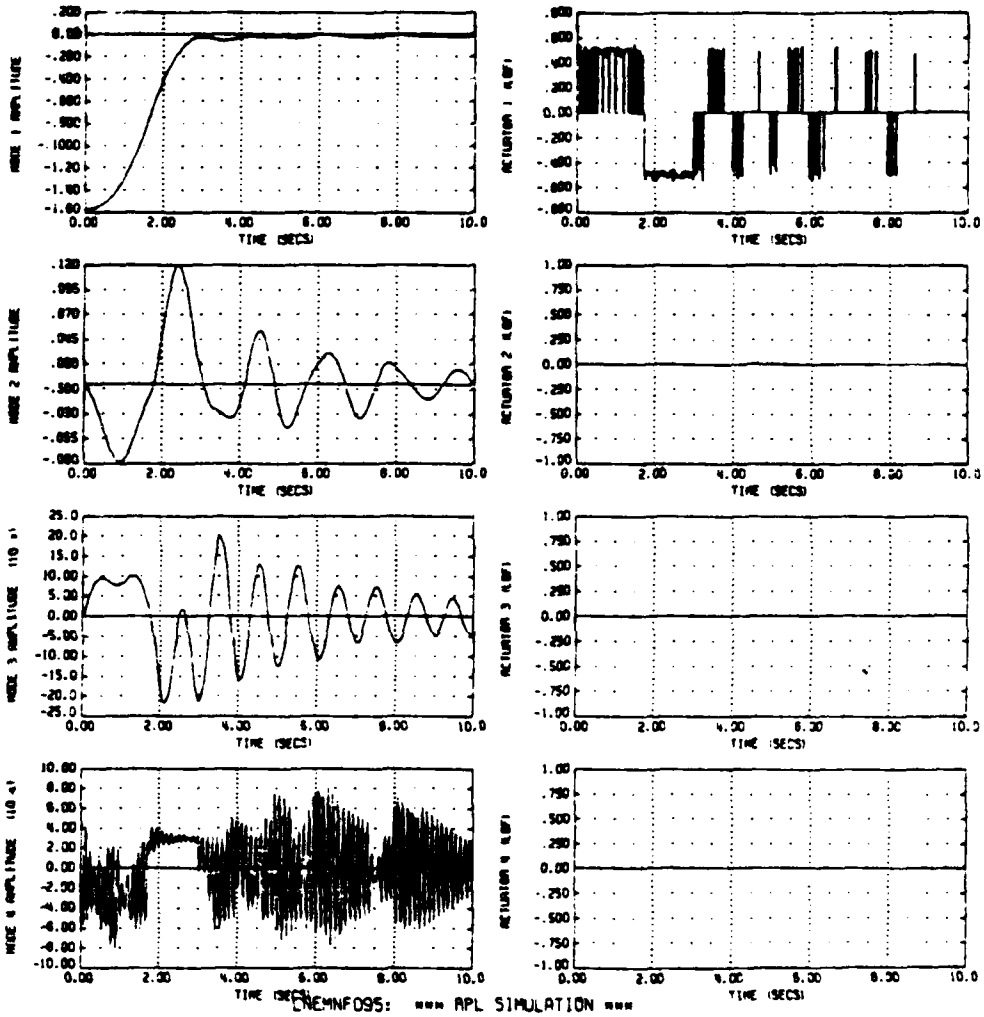

CNEMNF095: *** RPL SIMULATION ***

Appendix F

Parameter Variations Used in Perturbed Plants

The following multiplicative perturbations were applied to the modal frequencies (RDFREQ), to the modeshape as seen by the accelerometers and effected upon by the actuators (RDMSHAP), and as observed by the hub angle encoder (RDHUBSHAP). The elements of the 8×10 matrices correspond to multiplicative errors in the 8 flexible modes of the 10 perturbed plants.

RDFREQ =

0.7276	1.2381	1.2455	1.3053	0.9632	1.4039	0.8235	0.9788	0.8690	0.8152
0.9749	0.9732	0.8539	0.9574	0.9324	0.9107	1.2181	0.7929	1.0590	0.8953
1.1948	1.0992	0.8510	0.7536	0.9843	1.0580	1.1049	0.8837	0.7194	1.1019
0.9092	0.9500	0.8129	0.8065	0.7823	0.9029	0.9258	0.8551	1.2407	1.1515
0.8827	1.0787	1.1897	1.1010	1.0907	0.9086	0.8521	1.0186	1.0159	1.1218
1.2956	0.7154	0.8949	1.1266	1.1845	0.8280	1.0395	1.1583	0.8714	1.2555
1.0077	0.7941	1.1873	0.9471	1.2807	0.9813	1.2449	0.9691	1.2193	0.8816
1.0075	1.1513	0.9648	1.0025	0.7818	1.0065	0.7912	1.3435	1.0054	0.7772

RDMSHAP =

0.7307	1.2757	0.9279	0.9439	0.9314	0.6711	1.1398	1.1376	1.1428	0.9966
1.2429	1.0983	0.9063	1.1162	1.1319	0.8895	0.7526	0.9352	1.0295	0.7305
1.1006	1.0545	1.0422	0.9415	1.3266	0.9921	0.7724	0.7494	0.9926	1.1860
1.0707	1.0133	0.9613	0.9944	0.8167	1.1137	1.2379	0.8584	1.1227	1.1274
1.0514	1.1145	1.2023	1.2240	0.8248	1.0446	0.8764	0.8622	0.9288	1.2377
0.9635	0.9214	1.3139	0.9874	1.0724	1.2334	1.0419	1.2856	0.6011	1.0015
0.7486	0.7607	0.7848	1.1515	0.8519	0.9036	1.0851	1.0640	1.0410	0.8997
1.0918	0.7616	0.8614	0.6411	1.0442	1.1520	1.0939	1.1077	1.1415	0.8205

RDHUBSHAP =

1.0229	1.0300	1.0156	0.7238	0.9913	0.9264	1.0297	1.0036	1.0705	1.1544
0.9079	0.8244	0.7405	1.0292	0.9249	0.6886	1.1958	1.2583	0.9708	0.9849
0.9227	1.1053	1.0484	1.1986	0.9069	1.2903	1.1279	1.0825	0.9655	1.3076
1.4202	0.9589	1.1271	1.1150	0.9849	0.9083	0.9622	0.9941	0.7179	1.0240
0.8157	1.3961	1.3450	1.0574	1.3627	1.1721	1.1741	0.7753	0.8673	0.7667
1.0581	0.9471	1.0676	0.7170	1.1646	0.9048	0.7678	1.2302	0.9564	0.9988
0.8609	0.9193	0.9039	1.1903	0.8292	1.1251	0.8470	0.8046	1.1329	0.7452
1.0250	1.0166	0.8630	0.9771	0.7873	1.0073	1.1476	0.8168	1.3536	1.0042
0.9666	0.8024	0.8890	0.9916	1.0481	0.9770	0.7479	1.0344	0.9650	0.9342

Appendix G

LQG Compensator Design Parameters Used in OP/ME Design

These parameters define the cost-functional used in the initial LQG design. This design is used as a baseline for subsequent reduced-order and robustified compensator designs. The matrices are defined as follows: R_1 is the state weighting matrix, R_2 is the control weighting matrix, V_1 is the process noise intensity matrix, and V_2 is the sensor noise intensity matrix.

The Matrices R_1, R_2, V_1, and V_2

R1 =

Starting at row 1 columns 1 thru 8

0.0000	0.0000	0.0000	0.0000	0.0000	0.0000	0.0000	0.0000
0.0000	0.2962	-1.0255	0.0163	-0.0281	0.0033	0.0035	0.0011
0.0000	-1.0255	3.5508	-0.0563	0.0974	-0.0114	-0.0120	-0.0037
0.0000	0.0163	-0.0563	0.0009	-0.0015	0.0002	0.0002	0.0001
0.0000	-0.0281	0.0974	-0.0015	0.0027	-0.0003	-0.0003	-0.0001
0.0000	0.0033	-0.0114	0.0002	-0.0003	0.0000	0.0000	0.0000
0.0000	0.0035	-0.0120	0.0002	-0.0003	0.0000	0.0000	0.0000
0.0000	0.0011	-0.0037	0.0001	-0.0001	0.0000	0.0000	0.0000
0.0000	0.0011	-0.0037	0.0001	-0.0001	0.0000	0.0000	0.0000
0.0000	0.0000	0.0000	0.0000	0.0000	0.0000	0.0000	0.0000
0.0000	0.0000	0.0000	0.0000	0.0000	0.0000	0.0000	0.0000
0.0000	0.0000	0.0000	0.0000	0.0000	0.0000	0.0000	0.0000
0.0000	0.0000	0.0000	0.0000	0.0000	0.0000	0.0000	0.0000
0.0000	0.0000	0.0000	0.0000	0.0000	0.0000	0.0000	0.0000
0.0000	0.0000	0.0000	0.0000	0.0000	0.0000	0.0000	0.0000
0.0000	0.0000	0.0000	0.0000	0.0000	0.0000	0.0000	0.0000
0.0000	0.0000	0.0000	0.0000	0.0000	0.0000	0.0000	0.0000
0.0000	0.0000	0.0000	0.0000	0.0000	0.0000	0.0000	0.0000
0.0000	0.0000	0.0000	0.0000	0.0000	0.0000	0.0000	0.0000
0.0000	0.0000	0.0000	0.0000	0.0000	0.0000	0.0000	0.0000
0.0000	0.0000	0.0000	0.0000	0.0000	0.0000	0.0000	0.0000
0.0000	0.0000	0.0000	0.0000	0.0000	0.0000	0.0000	0.0000

The matrix R_1 continued:

Starting at row 1 columns 9 thru 16

0.0000	0.0000	0.0000	0.0000	0.0000	0.0000	0.0000	0.0000
0.0011	0.0000	0.0000	0.0000	0.0000	0.0000	0.0000	0.0000
-0.0037	0.0000	0.0000	0.0000	0.0000	0.0000	0.0000	0.0000
0.0001	0.0000	0.0000	0.0000	0.0000	0.0000	0.0000	0.0000
-0.0001	0.0000	0.0000	0.0000	0.0000	0.0000	0.0000	0.0000
0.0000	0.0000	0.0000	0.0000	0.0000	0.0000	0.0000	0.0000
0.0000	0.0000	0.0000	0.0000	0.0000	0.0000	0.0000	0.0000
0.0000	0.0000	0.0000	0.0000	0.0000	0.0000	0.0000	0.0000
0.0000	0.0000	0.0000	0.0000	0.0000	0.0000	0.0000	0.0000
0.0000	0.0000	0.0000	0.0000	0.0000	0.0000	0.0000	0.0000
0.0000	0.0000	0.2962	-1.0255	0.0163	-0.0281	0.0033	0.0035
0.0000	0.0000	-1.0255	3.5508	-0.0563	0.0974	-0.0114	-0.0120
0.0000	0.0000	0.0163	-0.0563	0.0009	-0.0015	0.0002	0.0002
0.0000	0.0000	-0.0281	0.0974	-0.0015	0.0027	-0.0003	-0.0003
0.0000	0.0000	0.0033	-0.0114	0.0002	-0.0003	0.0000	0.0000
0.0000	0.0000	0.0035	-0.0120	0.0002	-0.0003	0.0000	0.0000
0.0000	0.0000	0.0011	-0.0037	0.0001	-0.0001	0.0000	0.0000
0.0000	0.0000	0.0011	-0.0037	0.0001	-0.0001	0.0000	0.0000
0.0000	0.0000	0.0000	0.0000	0.0000	0.0000	0.0000	0.0000
0.0000	0.0000	0.0000	0.0000	0.0000	0.0000	0.0000	0.0000
0.0000	0.0000	0.0000	0.0000	0.0000	0.0000	0.0000	0.0000
0.0000	0.0000	0.0000	0.0000	0.0000	0.0000	0.0000	0.0000

Starting at row 1 columns 17 thru 22

0.0000	0.0000	0.0000	0.0000	0.0000	0.0000
0.0000	0.0000	0.0000	0.0000	0.0000	0.0000
0.0000	0.0000	0.0000	0.0000	0.0000	0.0000
0.0000	0.0000	0.0000	0.0000	0.0000	0.0000
0.0000	0.0000	0.0000	0.0000	0.0000	0.0000
0.0000	0.0000	0.0000	0.0000	0.0000	0.0000
0.0000	0.0000	0.0000	0.0000	0.0000	0.0000
0.0000	0.0000	0.0000	0.0000	0.0000	0.0000
0.0000	0.0000	0.0000	0.0000	0.0000	0.0000
0.0000	0.0000	0.0000	0.0000	0.0000	0.0000
0.0011	0.0011	0.0000	0.0000	0.0000	0.0000
-0.0037	-0.0037	0.0000	0.0000	0.0000	0.0000
0.0001	0.0001	0.0000	0.0000	0.0000	0.0000
-0.0001	-0.0001	0.0000	0.0000	0.0000	0.0000
0.0000	0.0000	0.0000	0.0000	0.0000	0.0000
0.0000	0.0000	0.0000	0.0000	0.0000	0.0000
0.0000	0.0000	0.0000	0.0000	0.0000	0.0000
0.0000	0.0000	0.0000	0.0000	0.0000	0.0000
0.0000	0.0000	0.6000	0.0000	0.0000	0.0000
0.0000	0.0000	0.0000	0.0000	0.0000	0.0000
0.0000	0.0000	0.0000	0.0000	0.1200	0.0000
0.0000	0.0000	0.0000	0.0000	0.0000	0.0000

R2 =

0.0100	0.0000
0.0000	0.0100

The matrix V_1

```
V1         =

   1.0D-04 *

  Starting at row   1 columns   1 thru   8
```

0.0000	0.0000	0.0000	0.0000	0.0000	0.0000	0.0000	0.0000
0.0000	0.0000	0.0000	0.0000	0.0000	0.0000	0.0000	0.0000
0.0000	0.0000	0.0000	0.0000	0.0000	0.0000	0.0000	0.0000
0.0000	0.0000	0.0000	0.0000	0.0000	0.0000	0.0000	0.0000
0.0000	0.0000	0.0000	0.0000	0.0000	0.0000	0.0000	0.0000
0.0000	0.0000	0.0000	0.0000	0.0000	0.0000	0.0000	0.0000
0.0000	0.0000	0.0000	0.0000	0.0000	0.0000	0.0000	0.0000
0.0000	0.0000	0.0000	0.0000	0.0000	0.0000	0.0000	0.0000
0.0000	0.0000	0.0000	0.0000	0.0000	0.0000	0.0000	0.0000
0.0000	0.0000	0.0000	0.0000	0.0000	0.0000	0.0000	0.0000
0.0000	0.0000	0.0000	0.0000	0.0000	0.0000	0.0000	0.0000
0.0000	0.0000	0.0000	0.0000	0.0000	0.0000	0.0000	0.0000
0.0000	0.0000	0.0000	0.0000	0.0000	0.0000	0.0000	0.0000
0.0000	0.0000	0.0000	0.0000	0.0000	0.0000	0.0000	0.0000
0.0000	0.0000	0.0000	0.0000	0.0000	0.0000	0.0000	0.0000
0.0000	0.0000	0.0000	0.0000	0.0000	0.0000	0.0000	0.0000
0.0000	0.0000	0.0000	0.0000	0.0000	0.0000	0.0000	0.0000
0.0000	0.0000	0.0000	0.0000	0.0000	0.0000	0.0000	0.0000
0.0000	0.0000	0.0000	0.0000	0.0000	0.0000	0.0000	0.0000
0.0000	0.0000	0.0000	0.0000	0.0000	0.0000	0.0000	0.0000
0.0000	0.0000	0.0000	0.0000	0.0000	0.0000	0.0000	0.0000
0.0000	0.0000	0.0000	0.0000	0.0000	0.0000	0.0000	0.0000

```
  Starting at row   1 columns   9 thru  16
```

0.0000	0.0000	0.0000	0.0000	0.0000	0.0000	0.0000	0.0000
0.0000	0.0000	0.0000	0.0000	0.0000	0.0000	0.0000	0.0000
0.0000	0.0000	0.0000	0.0000	0.0000	0.0000	0.0000	0.0000
0.0000	0.0000	0.0000	0.0000	0.0000	0.0000	0.0000	0.0000
0.0000	0.0000	0.0000	0.0000	0.0000	0.0000	0.0000	0.0000
0.0000	0.0000	0.0000	0.0000	0.0000	0.0000	0.0000	0.0000
0.0000	0.0000	0.0000	0.0000	0.0000	0.0000	0.0000	0.0000
0.0000	0.0000	0.0000	0.0000	0.0000	0.0000	0.0000	0.0000
0.0000	0.0000	0.0000	0.0000	0.0000	0.0000	0.0000	0.0000
0.0000	0.0001	-0.0001	0.0000	0.0000	0.0000	0.0000	0.0000
0.0000	-0.0001	0.0001	0.0000	0.0000	0.0000	0.0000	0.0000
0.0000	0.0000	0.0000	0.0000	0.0000	0.0000	0.0000	0.0000
0.0000	0.0000	0.0000	0.0000	0.0000	0.0000	0.0000	0.0000
0.0000	0.0000	0.0000	0.0000	0.0000	0.0000	0.0000	0.0000
0.0000	0.0000	0.0000	0.0000	0.0000	0.0000	0.0000	0.0000
0.0000	0.0000	0.0000	0.0000	0.0000	0.0000	0.0000	0.0000
0.0000	0.0000	0.0000	0.0000	0.0000	0.0000	0.0000	0.0000
0.0000	0.0000	0.0000	0.0000	0.0000	0.0000	0.0000	0.0000
0.0000	0.0000	0.0000	0.0000	0.0000	0.0000	0.0000	0.0000
0.0000	0.0028	-0.0032	0.0017	-0.0003	-0.0009	0.0000	-0.0005
0.0000	0.0000	0.0000	0.0000	0.0000	0.0000	0.0000	0.0000
0.0000	0.0002	0.0003	0.0002	0.0001	0.0000	-0.0001	0.0000

The matrix V_1 continued:

```
  Starting at row   1 columns  17 thru  22
  0.0000    0.0000    0.0000    0.0000    0.0000    0.0000
  0.0000    0.0000    0.0000    0.0000    0.0000    0.0000
  0.0000    0.0000    0.0000    0.0000    0.0000    0.0000
  0.0000    0.0000    0.0000    0.0000    0.0000    0.0000
  0.0000    0.0000    0.0000    0.0000    0.0000    0.0000
  0.0000    0.0000    0.0000    0.0000    0.0000    0.0000
  0.0000    0.0000    0.0000    0.0000    0.0000    0.0000
  0.0000    0.0000    0.0000    0.0000    0.0000    0.0000
  0.0000    0.0000    0.0000    0.0000    0.0000    0.0000
  0.0000    0.0000    0.0000    0.0028    0.0000    0.0002
  0.0000    0.0000    0.0000   -0.0032    0.0000    0.0003
  0.0000    0.0000    0.0000    0.0017    0.0000    0.0002
  0.0000    0.0000    0.0000   -0.0003    0.0000    0.0001
  0.0000    0.0000    0.0000   -0.0009    0.0000    0.0000
  0.0000    0.0000    0.0000    0.0000    0.0000   -0.0001
  0.0000    0.0000    0.0000   -0.0005    0.0000    0.0000
  0.0000    0.0000    0.0000    0.0000    0.0000    0.0000
  0.0000    0.0000    0.0000    0.0002    0.0000    0.0000
  0.0000    0.0000    0.0000    0.0000    0.0000    0.0000
  0.0000    0.0002    0.0000    0.1172    0.0000    0.0000
  0.0000    0.0000    0.0000    0.0000    0.0000    0.0000
  0.0000    0.0000    0.0000    0.0000    0.0000    0.0073

V2          =

   1.0D-05 *

   0.0169    0.0000    0.0000    0.0000    0.0000    0.0000    0.0000
   0.0000    0.0055    0.0000    0.0000    0.0000    0.0000    0.0000
   0.0000    0.0000    0.0271    0.0000    0.0000    0.0000    0.0000
   0.0000    0.0000    0.0000    0.0185    0.0000    0.0000    0.0000
   0.0000    0.0000    0.0000    0.0000    0.4142    0.0000    0.0000
   0.0000    0.0000    0.0000    0.0000    0.0000    0.0002    0.0000
   0.0000    0.0000    0.0000    0.0000    0.0000    0.0000    0.0002
```

Appendix H

Compensator Gains for OP/ME Designs

LQG Compensator

AC =

1.0D+03 *

Starting at row	1 columns	1 thru	8				
0.0000	0.0000	-0.0004	0.0000	0.0001	0.0000	0.0001	0.0000
0.0000	-0.0022	0.0047	-0.0011	-0.0019	0.0010	-0.0030	-0.0006
0.0001	-0.0001	-0.0096	-0.0003	0.0021	0.0010	0.0027	-0.0007
0.0000	-0.0004	0.0001	-0.0002	-0.0002	0.0003	-0.0003	-0.0002
0.0000	-0.0006	0.0048	-0.0002	-0.0013	0.0000	-0.0019	0.0001
0.0000	0.0000	0.0001	0.0000	0.0000	0.0000	0.0000	0.0000
0.0000	-0.0001	0.0008	-0.0001	-0.0002	0.0000	-0.0004	0.0000
0.0000	0.0000	0.0000	0.0000	0.0000	0.0000	0.0000	0.0000
0.0000	0.0000	0.0000	0.0000	0.0000	0.0000	0.0000	0.0000
0.0000	-0.0068	-0.0541	-0.0002	0.0020	0.0001	0.0018	-0.0001
0.0000	-0.0216	-0.0091	-0.0006	-0.0015	0.0003	-0.0020	-0.0001
0.0000	-0.0084	-0.0503	-0.0002	0.0011	0.0000	0.0009	0.0000
0.0000	-0.0055	-0.0118	-0.0520	-0.0001	0.0000	-0.0002	0.0000
0.0000	0.0007	0.0117	0.0001	-0.0540	-0.0001	-0.0001	0.0001
0.0000	0.0027	0.0073	0.0001	-0.0001	-0.1579	0.0000	0.0000
0.0000	-0.0003	0.0041	0.0000	-0.0001	0.0000	-0.1645	0.0000
0.0000	-0.0010	-0.0026	0.0000	0.0000	0.0000	0.0000	-0.3139
0.0000	0.0001	-0.0016	0.0000	0.0000	0.0000	0.0000	0.0000
-0.0001	0.0031	-0.0154	0.0013	0.0047	-0.0006	0.0069	0.0003
0.0003	0.1275	-1.1146	0.0023	0.0594	-0.0027	0.0572	0.0000
-0.0001	-0.0013	0.0010	-0.0007	-0.0008	0.0008	-0.0013	-0.0005
-0.0002	-0.3915	-1.0756	0.0080	0.0010	-0.0287	-0.0072	0.0200

Starting at row	1 columns	9 thru	16				
-0.0001	0.0010	-0.0001	0.0001	0.0000	0.0000	0.0000	0.0000
0.0021	0.0000	0.0062	0.0016	-0.0002	0.0000	0.0000	-0.0001
-0.0019	0.0000	-0.0022	0.0103	0.0000	0.0001	0.0001	0.0001
0.0002	0.0000	0.0002	0.0006	0.0518	0.0000	0.0000	0.0000
0.0013	0.0000	0.0014	-0.0007	-0.0001	0.0537	0.0000	-0.0001
0.0000	0.0000	0.0000	-0.0001	0.0000	0.0000	0.1579	0.0000
0.0002	0.0000	0.0003	-0.0001	0.0000	0.0000	0.0000	0.1645
0.0000	0.0000	0.0000	0.0000	0.0000	0.0000	0.0000	0.0000
0.0000	0.0000	0.0000	0.0000	0.0000	0.0000	0.0000	0.0000
-0.0013	0.0000	-0.0107	0.0276	-0.0001	0.0004	0.0004	0.0004
0.0014	0.0000	0.0077	0.0330	-0.0012	0.0001	0.0005	-0.0001
-0.0006	0.0000	-0.0069	0.0271	-0.0003	0.0003	0.0004	0.0003
0.0001	0.0000	0.0000	0.0130	-0.0014	0.0001	0.0002	0.0000
0.0000	0.0000	0.0028	-0.0044	0.0000	-0.0011	-0.0001	-0.0001
0.0000	0.0000	0.0004	-0.0068	0.0001	-0.0001	-0.0033	0.0000
0.0000	0.0000	0.0013	-0.0006	0.0000	0.0000	0.0000	-0.0033
0.0000	0.0000	-0.0002	0.0024	-0.0001	0.0000	0.0000	0.0000
-0.3280	0.0000	-0.0005	0.0002	0.0000	0.0000	0.0000	0.0000
-0.0048	0.0000	-0.0052	0.0007	0.0003	0.0002	0.0000	0.0003
-0.0406	0.0000	-0.3782	0.1022	0.0160	0.0061	0.0003	0.0104
0.0009	0.0000	0.0009	0.0016	-0.0001	0.0000	0.0000	0.0000
0.0041	0.0000	-0.0626	1.0010	-0.0210	0.0087	0.0131	0.0041

LQG Compensator, A_C continued:

```
  Starting at row    1 columns  17 thru  22
  0.0000    0.0000   -0.0005    0.0000   -0.0002    0.0000
  0.0000    0.0001    0.0049    0.0003   -0.0012   -0.0001
  0.0000   -0.0001   -0.0044   -0.0004   -0.0006   -0.0002
  0.0000    0.0000    0.0004    0.0000   -0.0002    0.0000
  0.0000    0.0000    0.0024    0.0002    0.0000    0.0000
  0.0000    0.0000    0.0000    0.0000    0.0000    0.0000
  0.0000    0.0000    0.0004    0.0000    0.0000    0.0000
  0.3139    0.0000    0.0000    0.0000    0.0000    0.0000
  0.0000    0.3280    0.0000    0.0000    0.0000    0.0000
 -0.0001   -0.0001   -0.0184   -0.0022   -0.0055   -0.0015
 -0.0002    0.0001    0.0162    0.0008   -0.0091   -0.0021
 -0.0001   -0.0001   -0.0105   -0.0015   -0.0053   -0.0016
 -0.0001    0.0000    0.0007   -0.0002   -0.0031   -0.0008
  0.0000    0.0000    0.0045    0.0005    0.0006    0.0002
  0.0000    0.0000    0.0003    0.0002    0.0016    0.0004
  0.0000    0.0000    0.0022    0.0002    0.0000    0.0000
 -0.0063    0.0000   -0.0001   -0.0001   -0.0006   -0.0001
  0.0000   -0.0066   -0.0008   -0.0001    0.0000    0.0000
  0.0000   -0.0001   -0.0209    0.0001    0.0006    0.0000
 -0.0001   -0.0039   -0.7063   -0.0644    0.0332   -0.0018
  0.0000    0.0000    0.0015    0.0001   -0.0067    0.0009
 -0.0044   -0.0012   -0.0556   -0.0251   -0.2516   -0.0594
```

```
F          =

   0.0015   -0.0047   -0.0004   -0.0014    0.0000    0.2951    0.1498
   0.0038    0.1024   -0.0224    0.0305   -0.0015   -1.1909    0.4676
  -0.0121   -0.0903   -0.0282   -0.0269   -0.0018    0.7872    0.1186
   0.0000    0.0117   -0.0065    0.0035   -0.0004    0.0015   -0.0024
  -0.0001    0.0619    0.0034    0.0184    0.0002    0.0014    0.0006
   0.0000   -0.0002    0.0008   -0.0001    0.0000    0.0000    0.0004
   0.0000    0.0118    0.0001    0.0035    0.0000    0.0007    0.0000
   0.0000    0.0000    0.0000    0.0000    0.0000    0.0000   -0.0001
   0.0000   -0.0005    0.0000   -0.0002    0.0000   -0.0001    0.0000
  -0.0001   -0.0604   -0.0053   -0.0180   -0.0003    1.8218    0.4597
   0.0006    0.0674   -0.0041    0.0200   -0.0003   -1.5263   -0.0397
  -0.0016   -0.0293   -0.0016   -0.0087   -0.0001    0.3165   -0.1822
   0.0000    0.0071    0.0003    0.0021    0.0000    0.0034   -0.0013
   0.0001    0.0021    0.0021    0.0006    0.0001    0.0072    0.0025
   0.0000   -0.0002    0.0000   -0.0001    0.0000    0.0000    0.0001
   0.0000    0.0002    0.0001    0.0001    0.0000    0.0003    0.0001
   0.0000    0.0000    0.0000    0.0000    0.0000    0.0000    0.0000
   0.0000    0.0001    0.0000    0.0000    0.0000   -0.0001    0.0000
   0.0065   -0.2302    0.0070   -0.0685    0.0005   12.2435    0.0451
  -0.0294   -2.6966   -0.0199   -0.8020   -0.0013   76.0433    0.2668
   0.0141    0.0437   -0.0185    0.0130   -0.0012    0.0451    6.1615
   0.0251    0.1846   -0.1970    0.0549   -0.0129    0.1382   19.0610
```

```
K          =

  Starting at row    1 columns   1 thru   8
  0.0000   -1.4509   13.4707    0.0903   -0.2727    0.0111    0.0039    0.0016
  0.0000    5.8203   16.1906    0.1393   -0.1459    0.0023    0.0065    0.0020

  Starting at row    1 columns   9 thru  16
  0.0028    0.0000    4.6159   -1.2254   -0.1938   -0.0655   -0.0033   -0.1132
  0.0013    0.0000    0.9897  -14.8369    0.3131   -0.1322   -0.2023   -0.0643

  Starting at row    1 columns  17 thru  22
  0.0007    0.0383    7.6879    0.7808   -0.4137    0.0211
  0.0708    0.0197    0.9239    0.3826    3.4354    0.8743
```

Optimal Projection Reduced Order Compensators

18^{th} Order Compensator

AC =

Starting at row 1 columns 1 thru 8

-81.5672	-0.2204	10.2190	7.4521	-8.5795	-6.5028	14.8185	-22.3428
-27.2789	-0.6925	-22.8884	3.9565	0.9927	0.5621	4.5186	-4.4353
12.6761	6.3291	-41.7960	-1.1233	6.3091	-10.6089	-3.6634	5.9872
-35.9462	-5.3592	2.8674	0.1962	-1.0565	-0.7673	1.1410	-8.3403
23.8840	-0.0811	-7.8309	-0.4782	0.7648	-3.4499	-0.4554	5.3689
8.7843	-2.3366	33.7289	0.3692	2.4352	0.5443	0.7194	-0.4384
-57.0881	-8.0420	50.7170	1.0203	-2.3042	-1.7290	0.0627	-16.6379
-16.2856	-0.9457	2.0238	0.2541	-0.5588	-0.5876	1.5612	-6.1529
1.1231	0.7359	-5.3869	-0.0362	0.7383	-1.2503	-0.2669	0.4205
0.0731	0.0700	-1.1048	-0.4048	-0.1146	-0.2728	-0.3502	54.9591
-0.4415	-0.0317	0.2009	0.0056	0.0047	0.0051	0.0273	-0.2157
-0.1424	-0.1283	4.3473	0.0674	-0.2959	0.4175	-0.0117	-0.1783
35.1612	2.7012	13.8443	2.1603	0.1779	1.3662	-8.7875	7.1149
0.5982	0.1426	-1.0297	-0.0228	0.1205	-0.2055	-0.0849	0.1677
-1.4057	-0.0942	0.1869	0.0100	0.0403	-0.0251	0.0900	-0.6958
0.3858	0.0654	-2.3762	-0.0707	0.1197	-0.0858	-0.0206	0.0025
3.9422	0.2576	-0.7586	-0.0074	-0.0430	0.0527	-0.2503	1.9931
-2.3535	-0.1428	0.0082	-0.0246	0.0321	-0.0755	0.1395	-1.3286

Starting at row 1 columns 9 thru 16

-0.8543	6.1555	-0.7957	1.8840	-5.2850	0.0907	-0.0830	4.0512
-2.5180	1.3431	-0.1478	2.9641	-1.8617	-0.3926	-0.0045	0.6309
-2.9373	-0.6022	0.2342	4.5233	-0.1729	-0.6313	0.0451	-1.0616
-0.4030	1.6994	-0.2869	0.7822	-1.6992	0.0262	-0.0295	1.4543
-0.3911	-0.9544	0.1854	0.0038	1.7045	-0.1197	0.0211	-0.9646
3.1996	-0.4156	-0.0218	-3.4040	0.1041	0.5700	-0.0167	0.2687
3.4150	2.5858	-0.5802	-3.2718	9.5512	0.8048	-0.0799	3.1585
-0.0221	-53.3338	-0.3124	0.7741	0.0208	0.0822	-0.0322	1.5958
-0.4252	0.0498	0.0175	0.5353	-0.1189	-0.1188	0.0042	-0.0908
-0.1285	-0.4101	0.0913	-0.2604	0.5387	-0.0209	0.0096	-0.4558
0.0113	0.0218	-1.6835	-0.0778	-0.0103	0.0049	-384.4268	0.0715
0.3794	0.2794	0.0715	-1.4071	-0.0514	0.0785	-0.0014	52.2055
1.8515	-1.7401	0.2412	-2.4244	-0.8784	0.2463	0.0174	-1.1421
-0.0332	-0.0216	0.0072	0.0918	0.0020	-0.0159	0.0012	-0.0357
-0.0036	0.0302	276.3188	0.0063	-0.0198	0.0074	-7.2888	0.1018
-0.2008	-0.0761	0.1801	-51.6529	0.0229	-0.0439	0.0186	-0.4589
-0.0095	0.0666	0.9577	0.2284	0.0168	-0.0239	0.0986	-0.0451
-0.0341	-0.1331	0.5344	0.3394	0.0331	0.0057	0.0546	0.2162

Starting at row 1 columns 17 thru 18

4.9571	2.9301
0.9989	0.6489
-1.2814	-0.6445
1.7835	1.0443
-1.1354	-0.6531
0.0289	-0.0681
3.4570	1.9041
1.9096	1.2170
-0.0887	-0.0383
-0.5821	-0.3277
0.7230	-0.3331
-0.6063	-0.4377
-1.5549	-0.9539
-0.0407	-0.0217
2.2049	-1.1157
-1.1628	-0.7231
-3.1189	164.3879
-164.4799	-0.9969

18th Order Compensator continued:

```
F           =

    0.6794   24.9507    1.9246    7.4202    0.1260 -825.4599  -29.8313
   -0.3433    2.2639    0.4076    0.6733    0.0267 -256.2337   12.5474
   -0.4315   -2.5166   -6.9819   -0.7484   -0.4572   92.7018  451.3082
    0.3423   10.7487   -1.5202    3.1966   -0.0995 -127.0271   -2.4718
    0.9859    3.3215    0.2947    0.9878    0.0193  149.6942   84.5802
    1.7871    6.1671    6.1022    1.8340    0.3996    2.5417  -55.6369
    0.7301    4.7687    2.4285    1.4182    0.1590   10.3193    4.5914
    0.1225    5.3233    0.4738    1.5831    0.0310 -101.8185   -5.6156
   -0.1887   -0.0851   -0.7641   -0.0253   -0.0500    3.5329   52.1907
   -0.0454    0.6067   -0.2107    0.1804   -0.0138   32.7145   10.1773
    0.0028    0.0883    0.0195    0.0263    0.0013   -2.8333   -0.8475
    0.0358   -0.3924    0.5708   -0.1167    0.0374   -2.2763  -28.4171
   -2.5748  -19.0241   -5.5722   -5.6577   -0.3649   84.5738   24.0605
    0.0401   -0.1124   -0.1491   -0.0334   -0.0098    3.8024    9.3964
    0.0076    0.3670    0.0159    0.1094    0.0010   -8.5051    0.1560
   -0.0112    0.1907   -0.3738    0.0567   -0.0245    4.7533   11.1922
   -0.0200   -1.3216   -0.0825   -0.3930   -0.0054   21.0476    1.6198
    0.0091    1.0562    0.0020    0.3141    0.0001   -9.8240    1.7703

K           =

    Starting at row   1 columns   1 thru   8
   -0.1832   -0.0144   -0.0129    0.0009   -0.0064   -0.0035    0.0128   -0.0428
   -0.0332   -0.0085    0.0967    0.0007   -0.0016    0.0006   -0.0047   -0.0144

    Starting at row   1 columns   9 thru  16
   -0.0046    0.0091   -0.0015    0.0069    0.0079   -0.0003   -0.0001    0.0073
    0.0079    0.0013   -0.0005   -0.0085    0.0063    0.0016   -0.0001    0.0030

    Starting at row   1 columns  17 thru  18
    0.0092    0.0055
    0.0029    0.0014
```

14^{th} Order Compensator

AC =

Starting at row 1 columns 1 thru 8

-81.5658	-10.2138	-0.2194	7.4521	-8.5797	-6.5033	14.8180	-5.2855
-12.6709	-41.7422	-6.3249	1.1234	-6.3120	10.6080	3.6625	0.1704
-27.2824	22.8481	-0.6954	3.9565	0.9948	0.5627	4.5190	-1.8599
-35.9459	-2.8681	-5.3589	0.1962	-1.0564	-0.7676	1.1408	-1.6993
23.8831	7.8235	-0.0818	-0.4782	0.7652	-3.4497	-0.4552	1.7049
8.7893	-33.6753	-2.3326	0.3693	2.4325	0.5434	0.7187	0.1017
-57.0804	-50.6434	-8.0358	1.0203	-2.3079	-1.7307	0.0612	9.5477
35.1635	-13.8162	2.7030	2.1603	0.1765	1.3659	-8.7877	-0.8795
16.2855	2.0244	0.9456	-0.2541	0.5588	0.5876	-1.5611	-0.0208
1.1204	5.3743	0.7345	-0.0360	0.7378	-1.2488	-0.2662	-0.1186
3.9457	0.7626	0.2579	-0.0075	-0.0429	0.0524	-0.2505	0.0169
-0.0729	-1.1037	-0.0699	0.4048	0.1145	0.2728	0.3501	-0.5387
-2.3494	0.0005	-0.1424	-0.0248	0.0325	-0.0762	0.1394	0.0333
0.6009	1.0369	0.1437	-0.0230	0.1218	-0.2076	-0.0856	0.0020

Starting at row 1 columns 9 thru 14

22.3449	-0.8566	4.9623	-6.1519	2.9257	0.0934
6.0058	2.9271	1.2854	-0.5893	0.6372	0.6390
4.4217	-2.5117	0.9988	-1.3514	0.6501	-0.3967
8.3402	-0.4035	1.7854	-1.6984	1.0427	0.0272
-5.3715	-0.3894	-1.1368	0.9520	-0.6517	-0.1215
0.4566	3.1907	0.0305	0.4276	-0.0709	0.5764
16.6631	3.4018	3.4628	-2.5670	1.8971	0.8151
-7.1055	1.8475	-1.5558	1.7453	-0.9540	0.2485
-6.1528	0.0225	-1.9115	-53.3341	-1.2152	-0.0828
-0.4222	-0.4235	-0.0889	-0.0516	-0.0376	-0.1197
-1.9946	-0.0097	-3.1281	-0.0665	164.3957	-0.0242
54.9595	0.1283	0.5827	-0.4096	0.3273	0.0212
1.3263	-0.0349	-164.4896	0.1335	-0.9958	0.0056
-0.1694	-0.0335	-0.0410	0.0214	-0.0216	-0.0162

F =

0.6794	24.9507	1.9246	7.4202	0.1260	-825.4599	-29.8314
0.4316	2.5166	6.9819	0.7484	0.4572	-92.7016	-451.3135
-0.3433	2.2639	0.4076	0.6733	0.0267	-256.2334	12.5474
0.3423	10.7487	-1.5922	3.1966	-0.0995	-127.0271	-2.4719
0.9859	3.3215	0.2947	0.9878	0.0193	149.6946	84.5800
1.7871	6.1671	2.1022	1.8340	0.3996	2.5416	-55.6369
0.7301	4.7687	2.4285	1.4182	0.1590	18.3193	4.5914
-2.5748	-19.0241	-5.5722	-5.6577	-0.3649	84.5738	24.0605
-0.1225	-5.3233	-0.4738	-1.5831	-0.0310	101.8185	5.6156
-0.1886	-0.0846	-0.7632	-0.0252	-0.0500	3.5156	52.1302
-0.0200	-1.3224	-0.0831	-0.3933	-0.0054	21.0688	1.6417
0.0454	-0.6067	0.2107	-0.1804	0.0138	-32.7145	-10.1773
0.0091	1.0561	0.0008	0.3141	0.0001	-9.7953	1.8228
0.0400	-0.1130	-0.1505	-0.0336	-0.0099	3.8227	9.4846

K =

Starting at row 1 columns 1 thru 8

-0.1832	0.0128	-0.0144	0.0009	-0.0064	-0.0035	0.0128	0.0079
-0.0332	-0.0965	-0.0085	0.0007	-0.0016	0.0006	-0.0047	0.0063

Starting at row 1 columns 9 thru 14

0.0427	-0.0046	0.0092	-0.0091	0.0055	-0.0003
0.0144	0.0078	0.0029	-0.0013	0.0014	0.0016

10^{th} Order Compensator

AC =

```
   Starting at row   1 columns   1 thru   8
-81.5862   -5.2806   -0.2250   10.1434    7.4473   -8.5690   -6.5166   14.8189
 35.1573   -0.8759    2.6983   13.8802    2.1584    0.1792    1.3633   -8.7862
-27.2581   -1.8700   -0.6835  -22.9564    3.9598    0.9854    0.5722    4.5143
 12.5695   -0.1930    6.3367  -41.7718   -1.1090    6.2698  -10.5653   -3.6365
-35.9420   -1.6962   -5.3614    2.8407    0.1950   -1.0497   -0.7782    1.1398
 23.8941    1.7019   -0.0762   -7.8115   -0.4780    0.7592   -3.4410   -0.4549
  8.7335    0.1154   -2.3492   33.7706    0.3679    2.4465    0.5224    0.7241
-57.1224    9.5724   -8.0600   50.6975    1.0115   -2.2753   -1.7759    0.0670
 16.2596   -0.0301    0.9578   -2.0757   -0.2558    0.5604    0.5847   -1.5613
  1.1215   -0.1219    0.7434   -5.4259   -0.0353    0.7395   -1.2558   -0.2670

   Starting at row   1 columns   9 thru  10
 22.5847   -0.8614
 -7.1218    1.8682
  4.3604   -2.5433
 -6.1944   -2.9696
  8.4476   -0.4065
 -5.4657   -0.3931
  0.6190    3.2285
 17.0884    3.4448
 -6.2049    0.0190
 -0.4536   -0.4324
```

F =

```
  0.6792   24.9515    1.9270    7.4204    0.1262 -825.5406  -30.0642
 -2.5751  -19.0261   -5.5735   -5.6583   -0.3649   84.5909   24.0771
 -0.3448    2.2581    0.4037    0.6715    0.0264 -256.2449   12.5447
 -0.4288   -2.4701   -6.9642   -0.7346   -0.4560   91.3163  450.5205
  0.3426   10.7490   -1.5190    3.1967   -0.0995 -127.0206   -2.4873
  0.9865    3.3228    0.2964    0.9882    0.0194  149.7210   84.5892
  1.7859    6.1610    6.1015    1.8323    0.3995    2.3592  -55.6782
  0.7295    4.7640    2.4270    1.4168    0.1589   18.3456    4.5973
 -0.1223   -5.3321   -0.4782   -1.5857   -0.0313  101.4761    5.9784
 -0.1888   -0.0815   -0.7690   -0.0242   -0.0504    3.4365   52.5464
```

K =

```
   Starting at row   1 columns   1 thru   8
-0.1832    0.0079   -0.0144   -0.0131    0.0009   -0.0063   -0.0035    0.0128
-0.0333    0.0064   -0.0085    0.0967    0.0007   -0.0016    0.0006   -0.0047

   Starting at row   1 columns   9 thru  10
 0.0432   -0.0046
 0.0150    0.0079
```

8^{th} Order Compensator

AC =

-80.7504	-5.3237	-0.2174	-10.1454	7.4234	-6.4754	-6.4243	14.6732
34.6643	-0.8466	2.5492	-13.9383	2.1654	-0.3424	1.3298	-8.7418
-26.3552	-1.7099	-0.6268	21.9585	3.8745	0.9905	0.5013	4.4002
-12.7711	0.1908	-6.3760	-42.2523	1.1022	-4.0203	10.6935	3.6547
-35.4953	-1.7171	-5.2627	-2.8588	0.1785	-0.1228	-0.7236	1.0865
21.2177	1.8139	-0.1816	1.2110	-0.8892	0.2799	-2.7894	-0.8565
8.6013	0.1304	-2.3378	-33.8695	0.3534	2.1157	0.5511	0.7249
-56.2329	9.5352	-7.9851	-50.8537	0.9515	-0.8527	-1.6284	-0.0847

F =

0.6784	24.9882	1.9180	7.4313	0.1256	-826.2740	-29.0532
-2.5746	-19.0217	-5.5712	-5.6569	-0.3648	84.5399	24.0474
-0.2887	2.3717	0.4534	0.7053	0.0297	-247.3862	12.3086
0.4470	2.5788	7.0264	0.7669	0.4601	-94.3425	-454.0853
0.3428	10.7541	-1.5192	3.1982	-0.0995	-127.0878	-2.4641
0.9099	2.5785	0.3246	0.7668	0.0213	152.4598	58.7827
1.7886	6.1824	6.1059	1.8386	0.3998	2.2554	-55.6483
0.7285	4.7556	2.4238	1.4143	0.1587	18.6541	4.6248

K =

-0.1806	0.0078	-0.0140	0.0131	0.0008	-0.0027	-0.0033	0.0125
-0.0328	0.0064	-0.0086	-0.0970	0.0006	-0.0004	0.0007	-0.0048

6^{th} Order Compensator

AC =

-54.7997	32.2398	6.4133	-7.5936	-3.5704	8.4075
44.2432	-31.2623	-3.0519	-31.9894	6.9198	-1.8697
-36.7211	21.5053	-1.0927	-9.2598	-0.0398	1.0443
10.5661	-6.2792	-0.3454	-41.6801	4.4389	10.7864
15.1738	-11.9204	-2.4058	-2.9299	0.4272	2.7451
-18.2667	5.1465	0.7087	-37.1519	-1.5980	1.1451

F =

-0.1198	-20.3931	-0.4163	-6.0648	-0.0273	677.6299	-74.0903
0.7283	14.2409	2.5223	4.2352	0.1652	-487.7367	-140.0557
-2.7136	-20.3171	-5.9021	-6.0422	-0.3865	96.5596	21.7689
0.6460	1.7026	6.9839	0.5064	0.4573	-101.5996	-425.5664
-1.1325	-5.1618	-0.2779	-1.5351	-0.0182	-155.3594	-65.9880
1.8914	4.5799	6.2273	1.3620	0.4078	61.3017	-54.1430

K =

0.1585	-0.0971	0.0071	0.0060	0.0045	-0.0021
0.0199	-0.0272	0.0071	-0.1017	0.0018	0.0025

4th Order Compensator

```
Ac          =

 -54.7997   32.2398    6.4133   -7.5936
  44.2432  -31.2623   -3.0519  -31.9894
 -36.7211   21.5053   -1.0927   -9.2598
  10.5661   -6.2792   -0.3454  -41.6801

B           =

  -0.1198  -20.3931   -0.4163   -6.0648   -0.0273  677.6299  -74.0903
   0.7283   14.2409    2.5223    4.2352    0.1652 -487.7367 -140.0557
  -2.7136  -20.3171   -5.9021   -6.0422   -0.3865   96.5596   21.7689
   0.6460    1.7026    6.9839    0.5064    0.4573 -101.5996 -425.5664

C           =

   0.1585   -0.0971    0.0071    0.0060
   0.0199   -0.0272    0.0071   -0.1017
```

Maximum Entropy Robustified Compensators

Initial Robustified Compensator

```
Ac          =

   1.0e+03 *

    Starting at row    1 columns    1 thru    8
  0.0000    0.0001   -0.0005    0.0000    0.0001    0.0000    0.0002    0.0000
  0.0000   -0.0035    0.0052   -0.0011   -0.0020    0.0010   -0.0031   -0.0006
  0.0001    0.0000   -0.0100   -0.0003    0.0021    0.0010    0.0028   -0.0007
  0.0000   -0.0006    0.0001   -0.0002   -0.0002    0.0003   -0.0003   -0.0002
  0.0000   -0.0010    0.0049   -0.0002   -0.0013    0.0000   -0.0018    0.0001
  0.0000    0.0001    0.0001    0.0000    0.0000    0.0000    0.0000    0.0000
  0.0000   -0.0002    0.0009   -0.0001   -0.0002    0.0000   -0.0004    0.0000
  0.0000    0.0000    0.0000    0.0000    0.0000    0.0000    0.0000    0.0000
  0.0000    0.0000    0.0000    0.0000    0.0000    0.0000    0.0000    0.0000
  0.0000   -0.0085   -0.0553   -0.0002    0.0021    0.0001    0.0020   -0.0002
  0.0000   -0.0319   -0.0060   -0.0006   -0.0016    0.0002   -0.0022   -0.0001
  0.0000   -0.0116   -0.0503   -0.0002    0.0011    0.0000    0.0009    0.0000
  0.0000   -0.0083   -0.0113   -0.0520   -0.0001    0.0000   -0.0002    0.0000
  0.0000    0.0005    0.0119    0.0001   -0.0540   -0.0001   -0.0001    0.0001
  0.0000    0.0040    0.0071    0.0001   -0.0001   -0.1579    0.0000    0.0000
  0.0000   -0.0007    0.0043    0.0000   -0.0001    0.0000   -0.1645    0.0000
  0.0000   -0.0014   -0.0025    0.0000    0.0000    0.0000    0.0000   -0.3139
  0.0000    0.0003   -0.0014    0.0000    0.0000    0.0000    0.0000    0.0000
  0.0000    0.0052   -0.0195    0.0013    0.0054   -0.0004    0.0079    0.0001
  0.0003    0.2357   -1.1890    0.0024    0.0635   -0.0014    0.0638   -0.0010
 -0.0001   -0.0019   -0.0005   -0.0007   -0.0004    0.0009   -0.0007   -0.0006
 -0.0001   -0.5839   -1.0507    0.0000    0.0024   -0.0283   -0.0054    0.0197

    Starting at row    1 columns    9 thru   16
 -0.0001    0.0010   -0.0002    0.0001    0.0000    0.0000    0.0000    0.0000
  0.0022    0.0000    0.0077    0.0008   -0.0002   -0.0001    0.0001   -0.0001
 -0.0020    0.0000   -0.0031    0.0108    0.0000    0.0001    0.0001    0.0001
  0.0002    0.0000    0.0004    0.0005    0.0518    0.0005    0.0000    0.0000
  0.0013    0.0000    0.0021   -0.0011   -0.0001    0.0537    0.0000   -0.0001
  0.0000    0.0000    0.0000   -0.0001    0.0000    0.0000    0.1579    0.3000
  0.0002    0.0000    0.0004   -0.0002    0.0000    0.0000    0.0000    0.1645
  0.0000    0.0000    0.0000    0.0000    0.0000    0.0000    0.0000    0.0000
  0.0000    0.0000    0.0000    0.0000    0.0000    0.0000    0.0000    0.0000
 -0.0014    0.0000   -0.0129    0.0295   -0.0001    0.0004    0.0003    0.0004
  0.0015    0.0000    0.0170    0.0290   -0.0014    0.0001    0.0006   -0.0002
 -0.0006    0.0000   -0.0068    0.0277   -0.0003    0.0003    0.0004    0.0003
  0.0001    0.0000    0.0019    0.0124   -0.0018    0.0001    0.0002    0.0000
  0.0000    0.0000    0.0038   -0.0050    0.0000   -0.0012    0.0000   -0.0001
  0.0000    0.0000   -0.0004   -0.0066    0.0002   -0.0001   -0.0033    0.0000
  0.0000    0.0000    0.0020   -0.0010   -0.0001    0.0000    0.0000   -0.0033
  0.0000    0.0000    0.0001    0.0023   -0.0001    0.0000    0.0000    0.0000
 -0.3280    0.0000   -0.0007    0.0003    0.0000    0.0000    0.0000    0.0000
 -0.0055    0.0000   -0.0088    0.0032    0.0003    0.0002    0.0000    0.0003
 -0.0447    0.0000   -0.5817    0.2117    0.0195    0.0878   -0.0012    0.0119
  0.0005    0.0000    0.0011    0.0018   -0.0001    0.0000    0.0001    0.0000
  0.0029    0.0000    0.0471    0.9728   -0.0235    0.0001    0.0144    0.0036
```

Initial Robustified Compensator, A_C continued:

```
 Starting at row    1 columns  17 thru  22
 0.0000    0.0000   -0.0005    0.0000   -0.0001    0.0000
 0.0000    0.0001    0.0049    0.0004   -0.0013   -0.0002
 0.0000   -0.0001   -0.0044   -0.0005   -0.0005   -0.0002
 0.0000    0.0000    0.0004    0.0000   -0.0002    0.0000
 0.0000    0.0000    0.0024    0.0003   -0.0001    0.0000
 0.0000    0.0000    0.0000    0.0000    0.0000    0.0000
 0.0000    0.0000    0.0004    0.0001    0.0000    0.0000
 0.3139    0.0000    0.0000    0.0000    0.0000    0.0000
 0.0000    0.3280    0.0000    0.0000    0.0000    0.0000
-0.0001   -0.0001   -0.0187   -0.0023   -0.0051   -0.0015
-0.0002    0.0001    0.0158    0.0012   -0.0095   -0.0024
-0.0001   -0.0001   -0.0107   -0.0015   -0.0052   -0.0016
-0.0001    0.0000    0.0005   -0.0001   -0.0032   -0.0009
 0.0000    0.0000    0.0046    0.0006    0.0006    0.0002
 0.0000    0.0000    0.0004    0.0001    0.0016    0.0004
 0.0000    0.0000    0.0022    0.0003   -0.0001    0.0000
-0.0063    0.0000   -0.0002    0.0000   -0.0006   -0.0002
 0.0000   -0.0066   -0.0008   -0.0001    0.0000    0.0000
 0.0000   -0.0002   -0.0211   -0.0001    0.0017    0.0001
 0.0004   -0.0045   -0.7060   -0.0736    0.0448    0.0042
 0.0000    0.0000    0.0013    0.0001   -0.0062    0.0009
-0.0048   -0.0010   -0.0671   -0.0205   -0.2493   -0.0648


F          =

   0.0029   -0.0060   -0.0007   -0.0018    0.0000    0.2557    0.1101
   0.0042    0.1036   -0.0220    0.0308   -0.0014   -1.1417    0.5169
  -0.0128   -0.0923   -0.0286   -0.0275   -0.0019    0.7224    0.0538
   0.0000    0.0117   -0.0065    0.0035   -0.0004    0.0005   -0.0033
  -0.0002    0.0616    0.0033    0.0183    0.0002   -0.0070   -0.0079
   0.0000   -0.0002    0.0008   -0.0001    0.0000   -0.0001    0.0003
   0.0000    0.0117    0.0001    0.0035    0.0000   -0.0009   -0.0016
   0.0000    0.0000    0.0000    0.0000    0.0000    0.0000   -0.0001
   0.0000   -0.0005    0.0000   -0.0002    0.0000    0.0000    0.0001
  -0.0019   -0.0663   -0.0065   -0.0197   -0.0004    1.6342    0.2723
   0.0025    0.0737   -0.0028    0.0219   -0.0002   -1.3261    0.1601
  -0.0016   -0.0294   -0.0016   -0.0087   -0.0001    0.3140   -0.1847
   0.0000    0.0071    0.0003    0.0021    0.0000    0.0023   -0.0024
   0.0001    0.0020    0.0021    0.0006    0.0001    0.0058    0.0011
   0.0000   -0.0002    0.0000   -0.0001    0.0000    0.0000    0.0001
   0.0000    0.0002    0.0001    0.0001    0.0000    0.0003    0.0001
   0.0000    0.0000    0.0000    0.0000    0.0000    0.0000    0.0000
   0.0000    0.0001    0.0000    0.0000    0.0000   -0.0001    0.0000
  -0.0037   -0.2637    0.0002   -0.0784    0.0000   11.1808   -1.0152
  -0.0876   -2.8877   -0.0586   -0.8588   -0.0038   69.9838   -5.7809
   0.0085    0.0257   -0.0222    0.0077   -0.0015   -0.5268    5.5914
   0.0077    0.1271   -0.2085    0.0378   -0.0137   -1.6697   17.2563

K          =

 Starting at row    1 columns   1 thru   8
 0.0000   -3.0031   14.1531    0.0885   -0.2708    0.0112    0.0039    0.0016
 0.0000    8.6550   15.7489    0.1401   -0.1484    0.0024    0.0063    0.0020

 Starting at row    1 columns   9 thru  16
 0.0028    0.0000    7.0460   -2.4889   -0.2346   -0.0832    0.0148   -0.1266
 0.0013    0.0000   -0.6231  -14.4092    0.3512   -0.1225   -0.2207   -0.0551

 Starting at row    1 columns  17 thru  22
-0.0055    0.0432    7.6665    0.8817   -0.4866   -0.0547
 0.0772    0.0163    1.0873    0.3116    3.4255    0.9519
```

Final Robustified Compensator

AC =

1.0D+03 *

Starting at row 1 columns 1 thru 8

0.0000	0.0002	-0.0007	0.0000	0.0002	0.0000	0.0002	0.0000
0.0000	-0.0061	0.0056	-0.0011	-0.0020	0.0010	-0.0031	-0.0006
0.0001	0.0007	-0.0105	-0.0003	0.0022	0.0010	0.0029	-0.0008
0.0000	-0.0011	0.0002	-0.0002	-0.0002	0.0003	-0.0003	-0.0002
0.0000	-0.0020	0.0050	-0.0002	-0.0013	0.0000	-0.0018	0.0001
0.0000	0.0001	0.0001	0.0000	0.0000	0.0000	0.0000	0.0000
0.0000	-0.0004	0.0009	-0.0001	-0.0002	0.0000	-0.0003	0.0000
0.0000	0.0000	0.0000	0.0000	0.0000	0.0000	0.0000	0.0000
0.0000	0.0000	0.0000	0.0000	0.0000	0.0000	0.0000	0.0000
0.0000	-0.0101	-0.0574	-0.0002	0.0023	0.0002	0.0022	-0.0002
0.0000	-0.0521	-0.0050	-0.0006	-0.0018	0.0002	-0.0024	-0.0001
0.0000	-0.0166	-0.0513	-0.0002	0.0011	0.0000	0.0009	0.0000
0.0000	-0.0136	-0.0115	-0.0520	0.0000	0.0000	-0.0002	0.0000
0.0000	-0.0002	0.0123	0.0001	-0.0540	-0.0001	-0.0001	0.0001
0.0000	0.0065	0.0072	0.0001	-0.0001	-0.1579	0.0000	0.0000
0.0000	-0.0016	0.0044	0.0000	-0.0001	0.0000	-0.1645	0.0000
0.0000	-0.0023	-0.0026	0.0000	0.0000	0.0000	0.0000	-0.3139
0.0000	0.0006	-0.0015	0.0000	0.0000	0.0000	0.0000	0.0000
0.0002	0.0105	-0.0241	0.0013	0.0063	-0.0001	0.0091	-0.0001
0.0015	0.5501	-1.2483	0.0025	0.0679	0.0000	0.0697	-0.0021
0.0000	-0.0027	-0.0027	-0.0007	0.0001	0.0010	-0.0001	-0.0007
0.0001	-0.9311	-1.0777	0.0078	0.0045	-0.0279	-0.0033	0.0194

Starting at row 1 columns 9 thru 16

-0.0002	0.0010	-0.0003	0.0003	0.0000	0.0000	0.0000	0.0000
0.0022	0.0000	0.0092	-0.0007	-0.0002	-0.0001	0.0001	-0.0001
-0.0020	0.0000	-0.0039	0.0117	0.0001	0.0001	0.0000	0.0001
0.0002	0.0000	0.0006	0.0003	0.0518	0.0000	0.0000	0.0000
0.0013	0.0000	0.0028	-0.0018	-0.0001	0.0537	0.0000	-0.0001
0.0000	0.0000	0.0000	-0.0001	0.0000	0.0000	0.1579	0.0000
0.0002	0.0000	0.0005	-0.0003	0.0000	0.0000	0.0000	0.1645
0.0000	0.0000	0.0000	0.0000	0.0000	0.0000	0.0000	0.0000
0.0000	0.0000	0.0000	0.0000	0.0000	0.0000	0.0000	0.0000
-0.0015	0.0000	-0.0152	0.0319	-0.0001	0.0004	0.0004	0.0004
0.0017	0.0000	0.0263	0.0196	-0.0017	-0.0001	0.0007	-0.0003
-0.0006	0.0000	-0.0067	0.0277	-0.0004	0.0003	0.0004	0.0002
0.0001	0.0000	0.0038	0.0105	-0.0015	0.0001	0.0002	0.0000
0.0000	0.0000	0.0047	-0.0060	-0.0001	-0.0012	0.0000	-0.0001
0.0000	0.0000	-0.0011	-0.0059	0.0002	0.0000	-0.0033	0.0000
0.0000	0.0000	0.0026	-0.0016	-0.0001	0.0000	0.0000	-0.0033
0.0000	0.0000	0.0004	0.0021	-0.0001	0.0000	0.0000	0.0000
-0.3280	0.0000	-0.0009	0.0005	0.0000	0.0000	0.0000	0.0000
-0.0064	0.0000	-0.0131	0.0080	0.0004	0.0003	-0.0001	0.0004
-0.0493	0.0000	-0.7882	0.4209	0.0245	0.0106	-0.0033	0.0139
0.0001	0.0000	0.0010	0.0022	-0.0001	0.0000	0.0001	0.0000
0.0014	0.0000	0.1521	0.8677	-0.0279	0.0065	0.0166	0.0023

Final Robustified Compensator, A_C continued:

```
   Starting at row    1 columns  17 thru  22
    0.0000   0.0000   -0.0005    0.0000   -0.0001    0.0000
    0.0000   0.0001    0.0049    0.0005   -0.0013   -0.0002
    0.0000  -0.0001   -0.0044   -0.0005   -0.0004   -0.0001
    0.0000   0.0000    0.0004    0.0001   -0.0002   -0.0001
    0.0000   0.0000    0.0023    0.0003   -0.0001    0.0000
    0.0000   0.0000    0.0000    0.0000    0.0000    0.0000
    0.0000   0.0000    0.0004    0.0001    0.0000    0.0000
    0.3139   0.0000    0.0000    0.0000    0.0000    0.0000
    0.0000   0.3280    0.0000    0.0000    0.0000    0.0000
   -0.0001  -0.0001   -0.0189   -0.0024   -0.0049   -0.0015
   -0.0002   0.0001    0.0156    0.0020   -0.0097   -0.0030
   -0.0001  -0.0001   -0.0109   -0.0015   -0.0052   -0.0017
   -0.0001   0.0000    0.0004    0.0001   -0.0032   -0.0010
    0.0000   0.0000    0.0046    0.0006    0.0006    0.0002
    0.0000   0.0000    0.0004    0.0001    0.0016    0.0005
    0.0000   0.0000    0.0022    0.0003   -0.0001    0.0000
   -0.0063   0.0000   -0.0002    0.0000   -0.0006   -0.0002
    0.0000  -0.0066   -0.0008   -0.0001    0.0000    0.0000
    0.0000  -0.0002   -0.0214   -0.0006    0.0029    0.0002
    0.0011  -0.0053   -0.7068   -0.0884    0.0540    0.0132
    0.0000   0.0000    0.0012    0.0000   -0.0055    0.0008
   -0.0056  -0.0006   -0.0726   -0.0107   -0.2469   -0.0741


P           =

    0.0024   -0.0075   -0.0010   -0.0022   -0.0001    0.2083    0.0628
    0.0047    0.1053   -0.0216    0.0313   -0.0014   -1.0892    0.5694
   -0.0135   -0.0948   -0.0291   -0.0282   -0.0019    0.6460   -0.0226
    0.0000    0.0116   -0.0065    0.0035   -0.0004   -0.0008   -0.0046
   -0.0003    0.0613    0.0033    0.0182    0.0002   -0.0177   -0.0185
    0.0000   -0.0002    0.0008   -0.0001    0.0000   -0.0002    0.0002
    0.0000    0.0117    0.0001    0.0035    0.0000   -0.0028   -0.0036
    0.0000    0.0000    0.0000    0.0000    0.0000    0.0000   -0.0001
    0.0000   -0.0005    0.0000   -0.0002    0.0000    0.0001    0.0002
   -0.0040   -0.0733   -0.0079   -0.0218   -0.0005    1.4149    0.0529
    0.0046    0.0806   -0.0014    0.0240   -0.0001   -1.1059    0.3803
   -0.0016   -0.0293   -0.0016   -0.0087   -0.0001    0.3150   -0.1836
    0.0000    0.0070    0.0003    0.0021    0.0000    0.0010   -0.0037
    0.0000    0.0020    0.0020    0.0006    0.0001    0.0040   -0.0007
    0.0000   -0.0002    0.0000   -0.0001    0.0000    0.0000    0.0001
    0.0000    0.0002    0.0001    0.0001    0.0000    0.0002    0.0000
    0.0000    0.0000    0.0000    0.0000    0.0000    0.0000    0.0000
    0.0000    0.0001    0.0000    0.0000    0.0000   -0.0001    0.0000
   -0.0159   -0.3038   -0.0079   -0.0903   -0.0005    9.9156   -2.2804
   -0.1548   -3.1079   -0.1031   -0.9243   -0.0068   63.0358  -12.7288
    0.0018    0.0037   -0.0266    0.0011   -0.0017   -1.2208    4.8975
   -0.0139    0.0564   -0.2229    0.0168   -0.0146   -3.9018   15.0241

K           =

   Starting at row    1 columns   1 thru   8
    0.0000  -6.5331   14.6034    0.0865   -0.2653    0.0112    0.0039    0.0016
    0.0000  13.7758   16.0487    0.1422   -0.1554    0.0024    0.0063    0.0020

   Starting at row    1 columns   9 thru  16
    0.0028   0.0000    9.4739   -4.9107   -0.2925   -0.1142    0.0417   -0.1487
    0.0013   0.0000   -2.1871  -12.8340    0.4158   -0.0982   -0.2530   -0.0354

   Starting at row    1 columns  17 thru  22
   -0.0148   0.0512    7.6555    1.0472   -0.5192   -0.1667
    0.0884   0.0090    1.1613    0.1617    3.4201    1.0879
```

OP/ME Reduced Order Robustified Compensator

AC =

Starting at row 1 columns 1 thru 8

-85.2148	4.8731	-13.3450	-9.1857	-1.7628	-6.5114	7.3892	-32.8112
33.7817	-3.7991	3.8718	4.8301	-1.8956	0.0855	1.0902	11.1593
-4.3494	6.1436	-43.7770	-1.0522	3.7310	9.9430	3.7759	-10.7231
53.1232	-9.6161	13.8721	0.2917	-0.4447	-0.1301	-0.7713	18.9072
27.4549	1.6306	-28.7718	-1.9970	-0.7216	-0.3501	-1.6635	5.9879
7.1080	5.8421	-40.9570	2.3596	1.1977	-0.7555	-3.1583	-2.2414
-20.6526	-0.6121	-3.4930	-1.8416	0.2912	2.9045	0.5576	-6.1576
-25.7714	3.0283	-2.5670	-0.8360	0.6405	-0.6863	0.7498	-11.9565
-51.9106	13.0846	-44.2577	0.3688	7.9163	-3.8764	0.6074	-21.9358
3.7072	-0.0734	-6.8625	-0.8505	0.7013	4.0226	0.2492	0.1889

Starting at row 1 columns 9 thru 10

13.2944	13.8708
-5.1753	-4.8026
1.4104	-26.8960
-2.2844	-3.3050
-7.8809	-23.1056
3.5071	-25.0993
-0.9197	2.6113
2.4794	4.7722
0.1228	-14.9665
-1.1187	-10.6833

F =

0.5346	36.0148	1.6900	10.7106	0.1107	-737.2143	187.2943
-0.1552	-3.4646	-7.0957	-1.0303	-0.4646	273.9925	-27.4348
-0.0563	0.1810	11.4562	0.0538	0.7501	-23.7076	-375.1629
-0.1223	-20.9716	1.6640	-6.2368	0.1090	138.2030	-3.4658
-0.4530	-19.9423	-3.8585	-5.9307	-0.2527	58.6976	-5.7945
0.4829	3.8707	10.0127	1.1511	0.6556	24.0909	-62.3177
-0.2556	-5.8370	1.5864	-1.7359	0.1039	-106.9263	-36.8861
0.1188	10.1325	1.1072	3.0134	0.0725	-154.1999	15.7426
-0.0072	6.4996	2.6385	1.9329	0.1728	-5.1506	-21.6191
-0.2218	-2.9730	3.4271	-0.8842	0.2244	12.6699	-104.2132

K =

Starting at row 1 columns 1 thru 8

-0.1839	0.0216	-0.0148	-0.0013	0.0114	-0.0037	0.0060	-0.0641
-0.0164	0.0140	-0.0797	0.0005	0.0033	-0.0020	-0.0021	-0.0139

Starting at row 1 columns 9 thru 10

0.0070	0.0327
-0.0029	-0.0441

Appendix I

NASTRAN-Derived System Dynamics Matrices for Linear Actuator Control Design

The model includes the first five vibrational modes of the system, both symmetric and anti-symmetric. The dynamic model uses the standard notation:

$$\begin{aligned} \dot{x} &= A\,x + B\,u \\ y &= C\,x + D\,u \end{aligned}$$

and has 5 inputs and 5 outputs as follows:

$$u = \begin{bmatrix} \text{hub torque command (ft-lb)} \\ \text{PMA force, arm 1 (lbs)} \\ \text{PMA force, arm 2 (lbs)} \\ \text{PMA force, arm 3 (lbs)} \\ \text{PMA force, arm 4 (lbs)} \end{bmatrix}$$

$$y = \begin{bmatrix} \text{hub angle measurement (deg)} \\ \text{tip acceleration, arm 1 (ft/sec}^2\text{)} \\ \text{tip acceleration, arm 2 (ft/sec}^2\text{)} \\ \text{tip acceleration, arm 3 (ft/sec}^2\text{)} \\ \text{tip acceleration, arm 4 (ft/sec}^2\text{)} \end{bmatrix}$$

A matrix

0.0000	0.0000	0.0000	0.0000	0.0000	1.0000	0.0000	0.0000	0.0000	0.0000
0.0000	0.0000	0.0000	0.0000	0.0000	0.0000	1.0000	0.0000	0.0000	0.0000
0.0000	0.0000	0.0000	0.0000	0.0000	0.0000	0.0000	1.0000	0.0000	0.0000
0.0000	0.0000	0.0000	0.0000	0.0000	0.0000	0.0000	0.0000	1.0000	0.0000
0.0000	0.0000	0.0000	0.0000	0.0000	0.0000	0.0000	0.0000	0.0000	1.0000
0.0000	0.0000	0.0000	0.0000	0.0000	0.0000	0.0000	0.0000	0.0000	0.0000
0.0000	-5.7605	0.0000	0.0000	0.0000	0.0000	-0.0408	0.0000	0.0000	0.0000
0.0000	0.0000	-6.2005	0.0000	0.0000	0.0000	0.0000	-0.0423	0.0000	0.0000
0.0000	0.0000	0.0000	-6.6579	0.0000	0.0000	0.0000	0.0000	-0.0439	0.0000
0.0000	0.0000	0.0000	0.0000	-37.9982	0.0000	0.0000	0.0000	0.0000	-0.1048

B matrix

0.0000	0.0000	0.0000	0.0000	0.0000
0.0000	0.0000	0.0000	0.0000	0.0000
0.0000	0.0000	0.0000	0.0000	0.0000
0.0000	0.0000	0.0000	0.0000	0.0000
0.0000	0.0000	0.0000	0.0000	0.0000
-0.1275	-0.6838	0.6838	0.6838	-0.6838
0.0000	1.0341	0.0000	1.0341	0.0000
0.0101	-0.7171	-0.7998	0.7171	0.7998
0.0000	0.0000	1.1116	0.0000	1.1116
-0.2887	0.2967	-0.3601	-0.2967	0.3601

C matrix

-7.3038	0.0000	0.5783	0.0000	-16.5400	0.0000	0.0000	0.0000	0.0000	0.0000
0.0000	-5.4706	4.0710	0.0000	-8.0866	0.0000	-0.0387	0.0278	0.0000	-0.0223
0.0000	0.0000	4.5680	-6.7987	10.3186	0.0000	0.0000	0.0312	-0.0448	0.0285
0.0000	-5.4706	-4.0710	0.0000	8.0866	0.0000	-0.0387	-0.0278	0.0000	0.0223
0.0000	0.0000	-4.5680	-6.7987	-10.3186	0.0000	0.0000	-0.0312	-0.0448	-0.0285

D matrix

0.0000	0.0000	0.0000	0.0000	0.0000
0.0152	1.9627	0.0018	0.0013	-0.0018
-0.0123	0.0010	2.2689	-0.0010	0.0014
-0.0152	0.0013	-0.0018	1.9627	0.0018
0.0123	-0.0010	0.0014	0.0010	2.2689

Appendix J

NASTRAN-Derived System Dynamics Matrices for Thruster Control Design

The model includes the rigid body mode and the first two anti-symmetric vibrational modes of the system. The dynamic model uses the standard notation:

$$\begin{aligned} \dot{x} &= A\,x + B\,u \\ y &= C\,x + D\,u \end{aligned}$$

and has 1 input and 5 outputs as follows:

$$u = \left[\text{ thruster force command (lbs) } \right]$$

$$y = \begin{bmatrix} \text{hub angle measurement (rad)} \\ \text{tip acceleration, arm 1 (ft/sec}^2\text{)} \\ \text{tip acceleration, arm 2 (ft/sec}^2\text{)} \\ \text{tip acceleration, arm 3 (ft/sec}^2\text{)} \\ \text{tip acceleration, arm 4 (ft/sec}^2\text{)} \end{bmatrix}$$

A matrix

0.0000	0.0000	0.0000	1.0000	0.0000	0.0000
0.0000	0.0000	0.0000	0.0000	1.0000	0.0000
0.0000	0.0000	0.0000	0.0000	0.0000	1.0000
0.0000	0.0000	0.0000	0.0000	0.0000	0.0000
0.0000	-6.2005	0.0000	0.0000	-0.0423	0.0000
0.0000	0.0000	-37.9982	0.0000	0.0000	-0.1048

B matrix

C matrix

-0.1275	0.0101	-0.2887	0.0000	0.0000	0.0000
0.0000	4.0710	-8.0866	0.0000	0.0278	-0.0223
0.0000	-4.5680	-10.3186	0.0000	-0.0312	-0.0285
0.0000	4.0710	-8.0866	0.0000	0.0278	-0.0223
0.0000	-4.5680	-10.3186	0.0000	-0.0312	-0.0285

D matrix

0.0000
1.0481
-0.0027
1.0481
-0.0027

Appendix K

Discrete-Time Bandpass Integrating Filter Used for PMA Control

The PMA controller consisted of a discrete-time bandpass filter implemented as follows:

$$x[n+1] = \Phi x[n] + \Gamma u[n]$$

$$y[n] = Cx[n] + Du[n]$$

These filter matrices were derived for the 50 Hz sample rate using a zero-order hold.

$$\Phi = \begin{bmatrix} 0.5186 & -3.3337 & 0 & 0 \\ 0.0148 & 0.9631 & 0 & 0 \\ 0 & 3.4652 & 0.9802 & 0 \\ 0 & 0 & 0.2994 & 0.9960 \end{bmatrix}$$

$$\Gamma = \begin{bmatrix} 0.0148 \\ 0.0002 \\ 0 \\ 0 \end{bmatrix}$$

$$C = \begin{bmatrix} 0 & 0 & 15.0 & -0.20 \end{bmatrix}$$

$$D = [0]$$

Appendix L

Compensator Gains for the Hub Torque Controller

The dynamic compensator design for hub torque control is represented by the following continuous-time state-space system:

$$\begin{aligned} \dot{q} &= A_c\, q + F\, y \\ u_h &= K\, q \end{aligned}$$

where q is the internal compensator state vector (state estimates for a full-order compensator), A_c is defined as $[A - BK - FC]$, F is the Kalman filter gain matrix and K is the LQ controller gain vector. The plant model (A, B, C, D) derived using NASTRAN is given in Appendix I.

The hub torque compensator matrices are as follows:

Regulator Gain Matrix K

```
  Starting at row   1 columns   1 thru   8
-12.7466    0.0000    0.2071    0.0000   -7.4495  -11.8366    0.0000    0.0152

  Starting at row   1 columns   9 thru  12
 0.0000   -0.6703   96.2591   36.2666
```

Kalman Filter Gain Matrix F

-10.2714
0.0000
0.0094
0.0000
-0.3553
-7.2110
0.0000
-0.0207
0.0000
-0.2695
0.2020
0.2576

Appendix M

Supplementary Test Data

The figures presented in this appendix show the results of the supplementary tests described in Section 16.3.8. For a summary of the test method, see Section 16.2. The test parameters of these slew maneuvers were as follows:

Test S45T was a 45 degree slew, using thrusters only, with terminal phase constraints. The test results are presented in Figure M-1 through Figure M-3.

Test S45TP was a 45 degree slew, using thrusters with terminal phase constraints, and with PMAs active throughout the test. The test results are presented in Figure M-4 through Figure M-6.

Test S45TPH was a 45 degree slew, using thrusters with terminal phase constraints, with the hub torquer active in the terminal phase, and with PMAs active throughout the test. The test results are presented in Figure M-7 through Figure M-9.

Test S2T was a 2 degree slew, using thrusters only, with terminal phase constraints. The test results are presented in Figure M-10 through Figure M-12.

Test S2TP was a 2 degree slew, using thrusters with terminal phase constraints, and with PMAs active throughout the test. The test results are presented in Figure M-13 through Figure M-15.

Test S2TPH was a 2 degree slew, using thrusters with terminal phase constraints, with the hub torquer active in the terminal phase, and with PMAs active throughout the test. The test results are presented in Figure M-16 through Figure M-18.

Test S15T5 was a 15 degree slew, using high-authority thrusters (500 lb. line pressure) only, with terminal phase constraints. The test results are presented in Figure M-19 through Figure M-21.

Test S15T5P was a 15 degree slew, using high-authority thrusters (500 lb. line pressure) with terminal phase constraints, and with PMAs active throughout the test. The test results are presented in Figure M-22 through Figure M-24.

Test S15T5PH was a 15 degree slew, using high-authority thrusters (500 lb. line pressure) with terminal phase constraints, with the hub torquer active in the terminal

phase, and with PMAs active throughout the test. The test results are presented in Figure M-25 through Figure M-27.

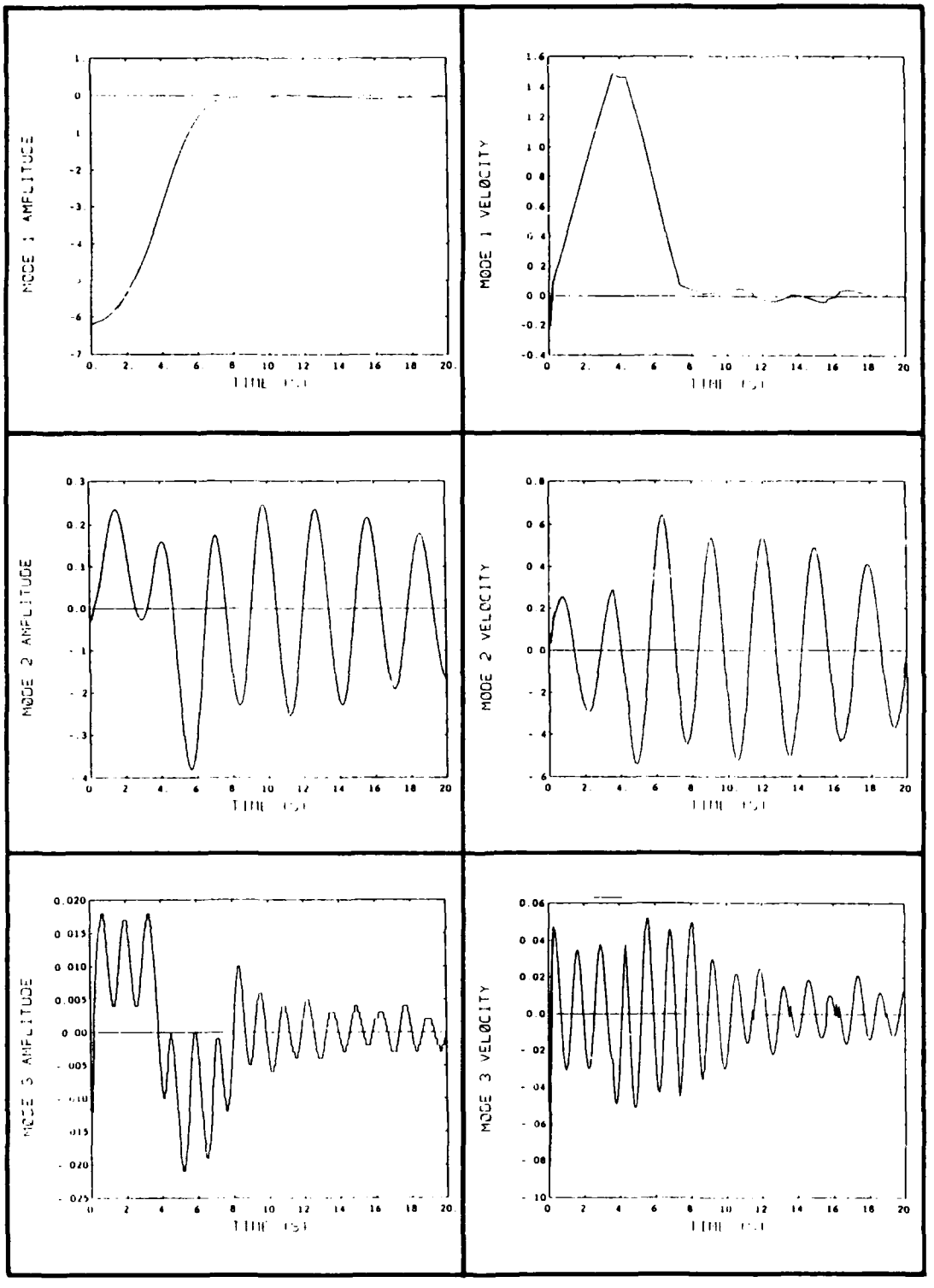

Figure M-1. 45 degree slew, using thrusters only, with terminal phase constraints. (Modal displacements and velocities).

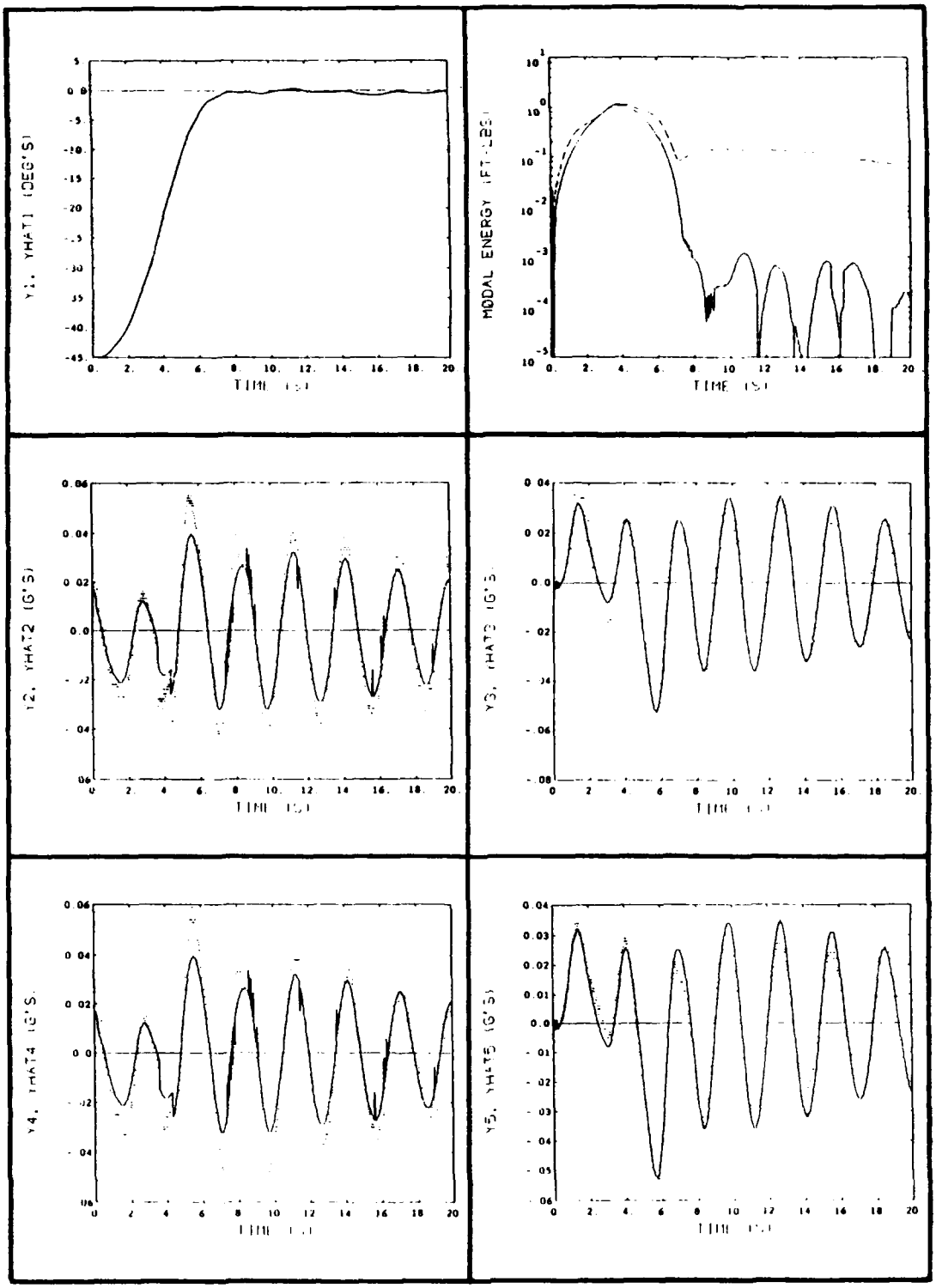

Figure M-2. 45 degree slew, using thrusters only, with terminal phase constraints. (Hub angle, vibrational energy, and accelerometer measurements).

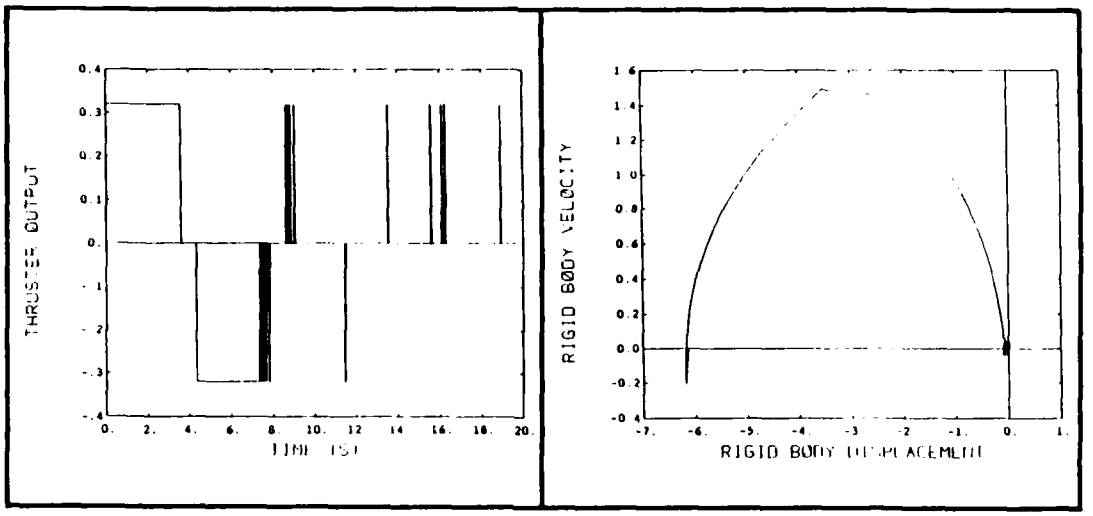

Figure M-3. 45 degree slew, using thrusters only, with terminal phase constraints. (Rigid body phase plane and thruster force command).

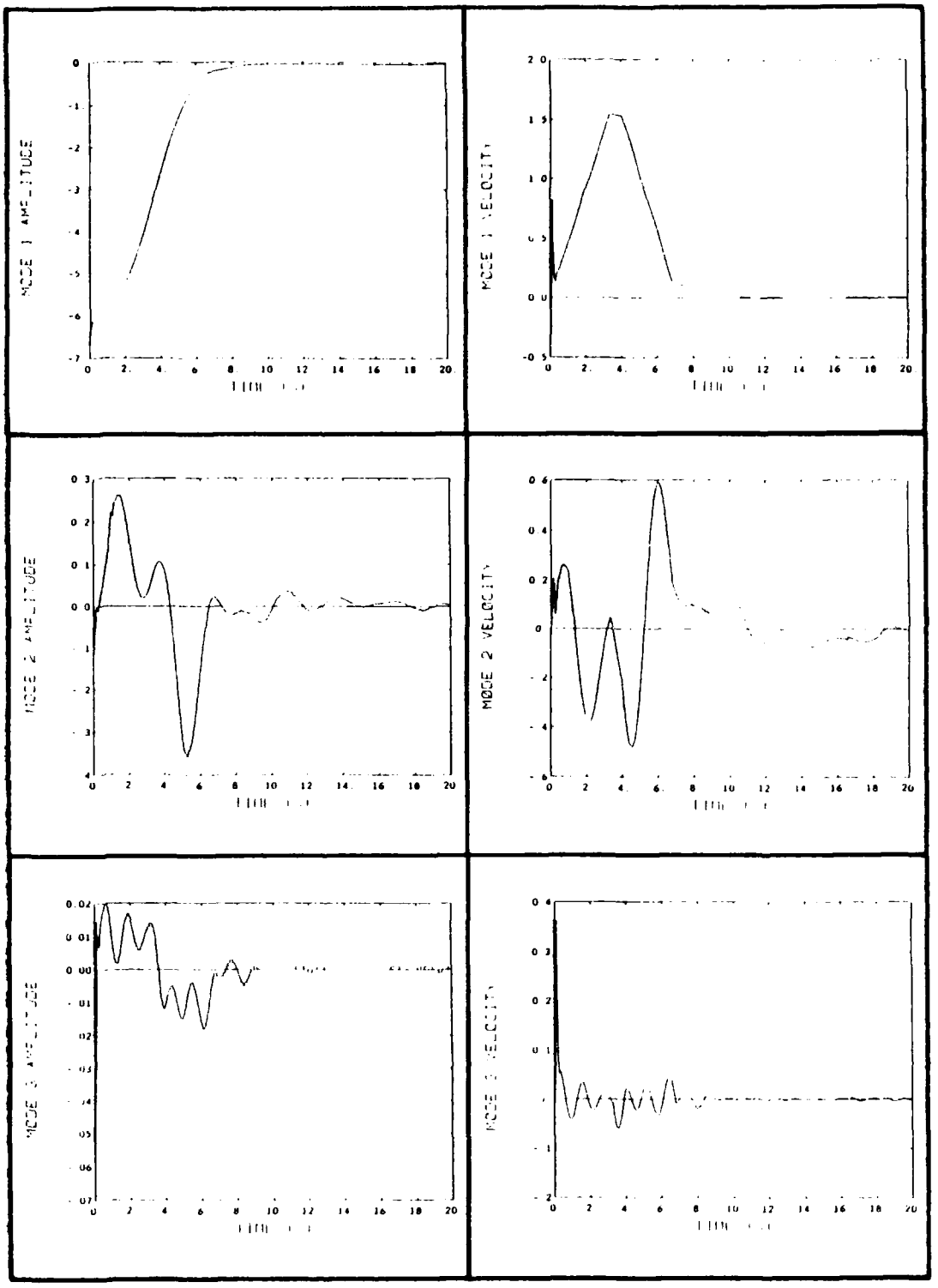

Figure M-4. 45 degree slew, using thrusters with terminal phase constraints, and with PMAs active throughout the test. (Modal displacements and velocities).

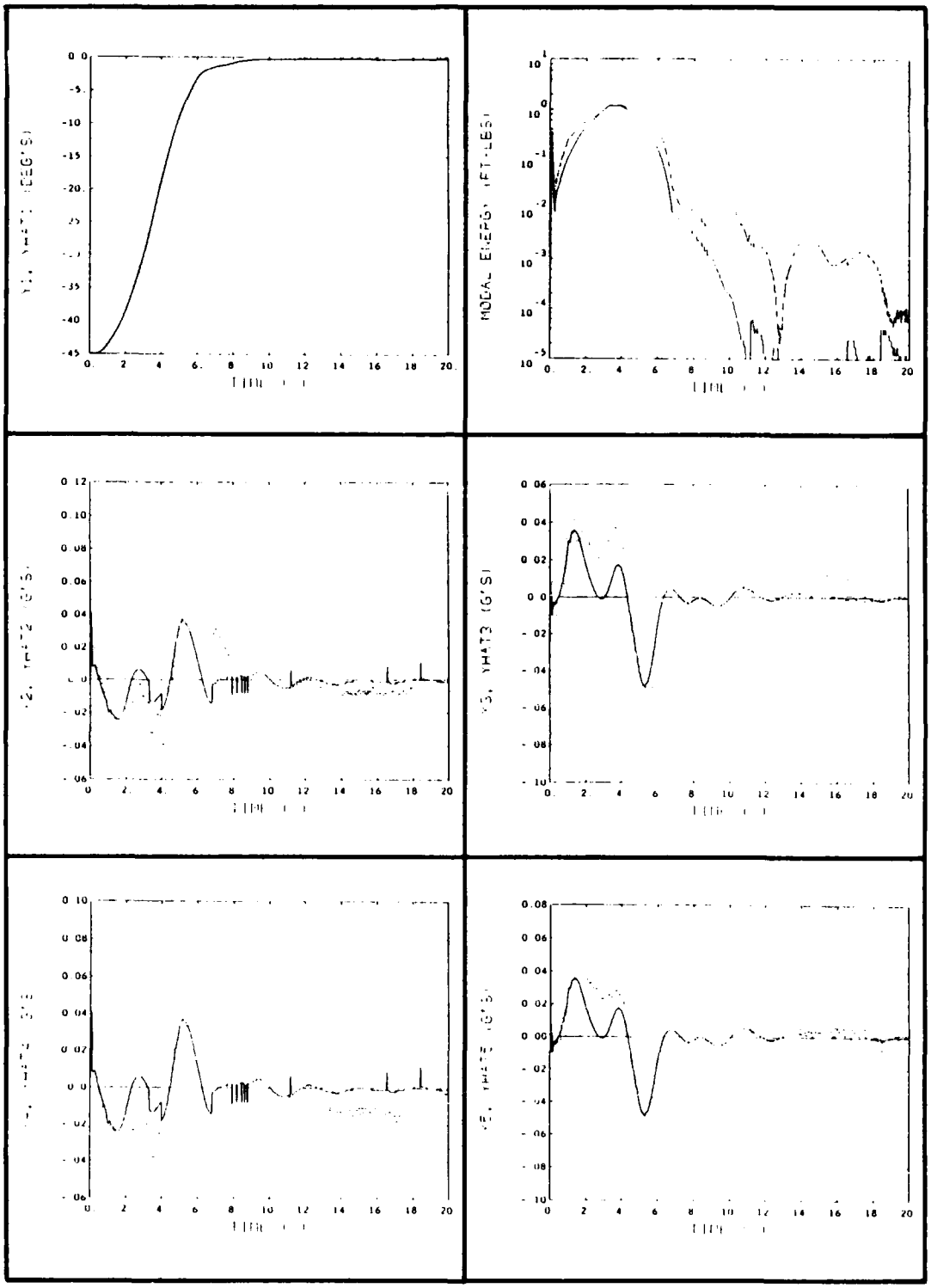

Figure M-5. 45 degree slew, using thrusters with terminal phase constraints, and with PMAs active throughout the test. (Hub angle, vibrational energy, and accelerometer measurements).

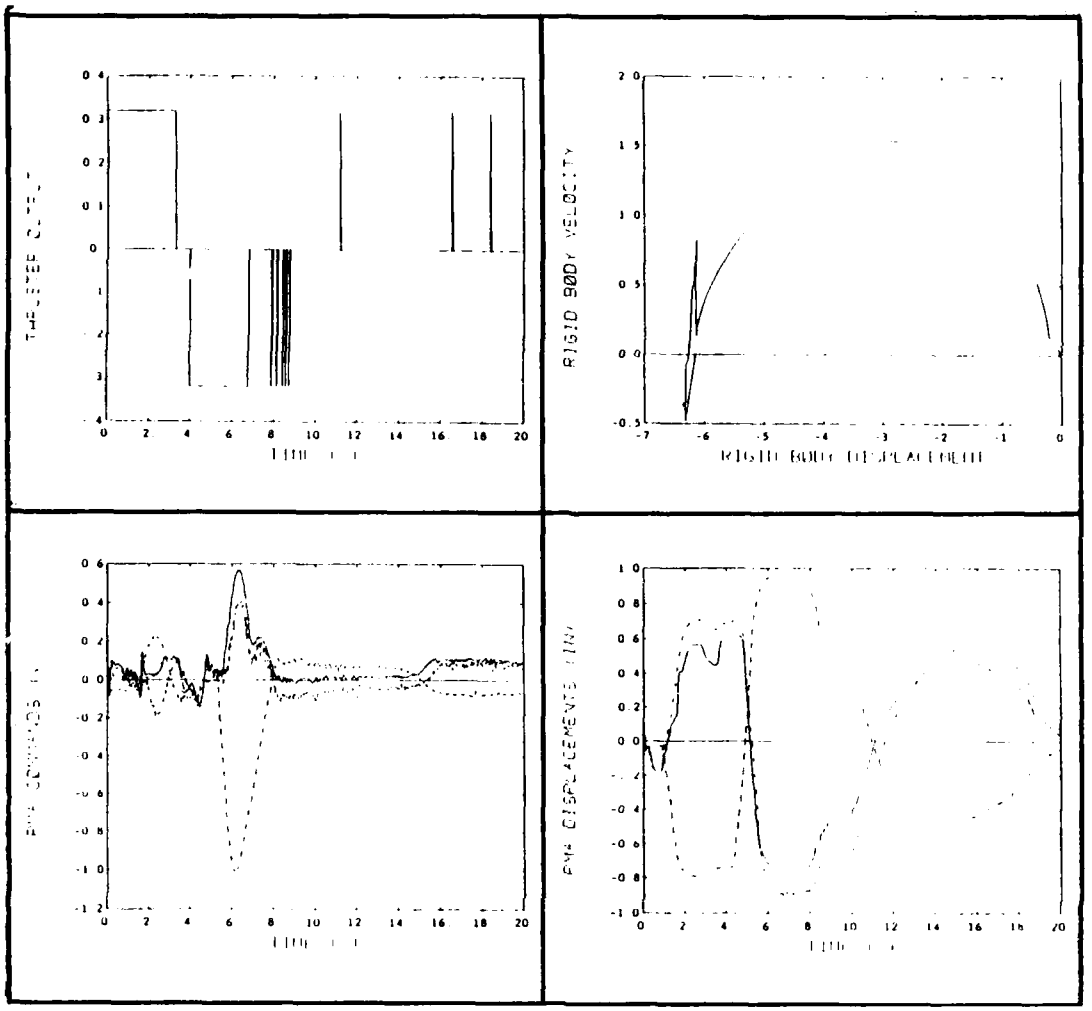

Figure M-6. 45 degree slew, using thrusters with terminal phase constraints, and with PMAs active throughout the test. (Rigid body phase plane, thruster force command, PMA displacements, and PMA force commands).

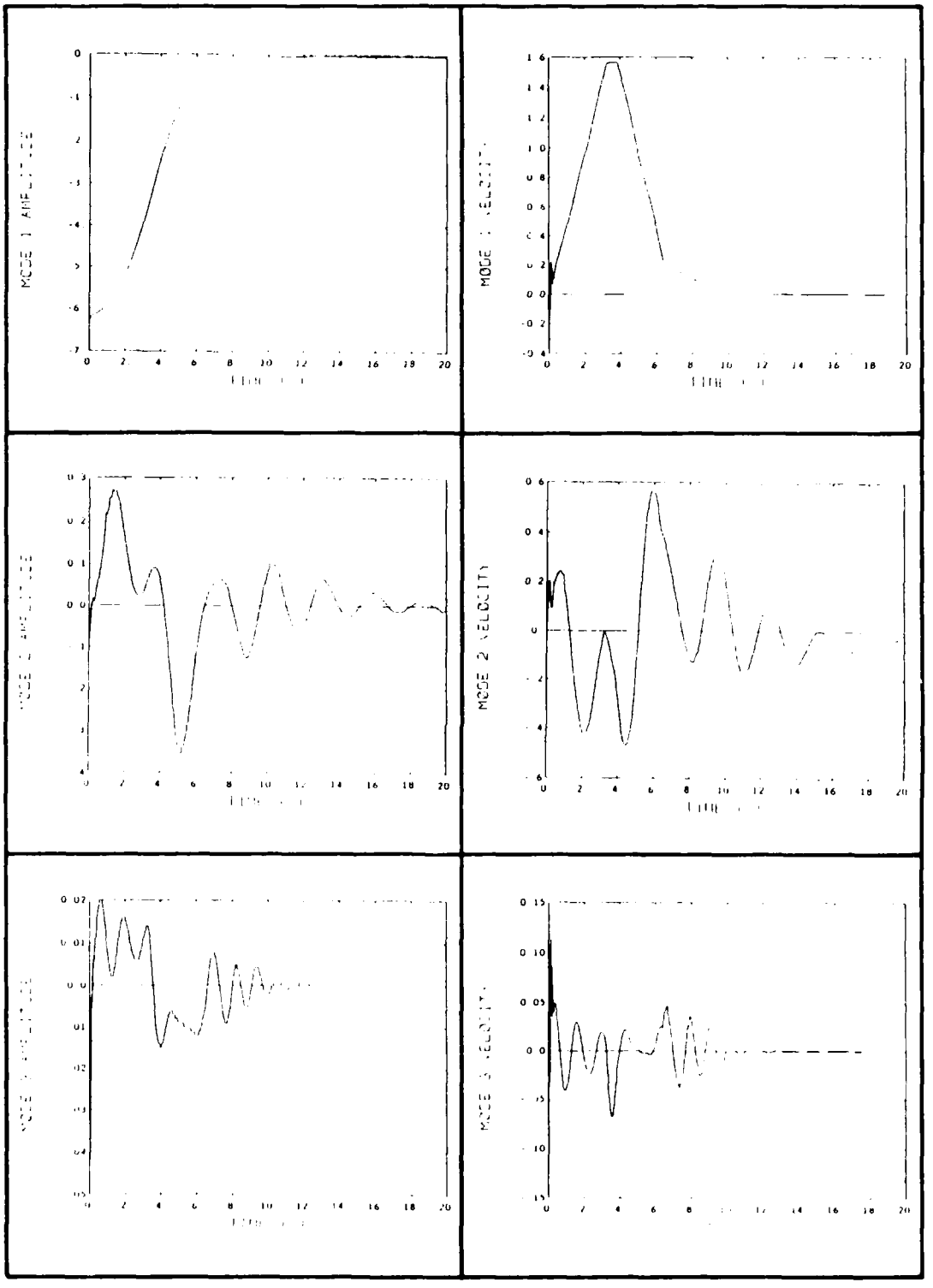

Figure M-7. 45 degree slew, using thrusters with terminal phase constraints, with the hub torquer active in the terminal phase, and with PMAs active throughout the test. (Modal displacements and velocities).

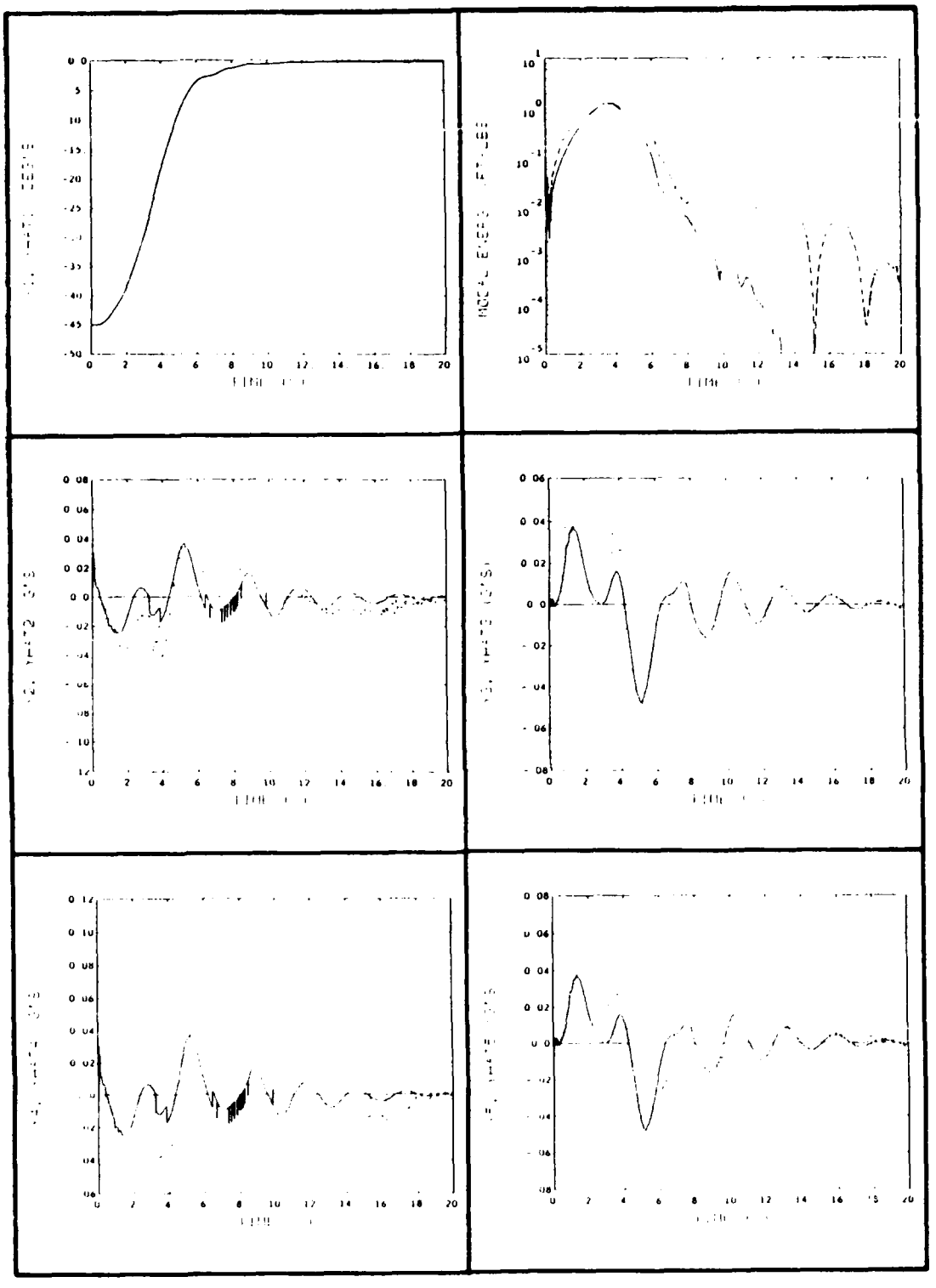

Figure M-8. 45 degree slew, using thrusters with terminal phase constraints, with the hub torquer active in the terminal phase, and with PMAs active throughout the test. (Hub angle, vibrational energy, and accelerometer measurements).

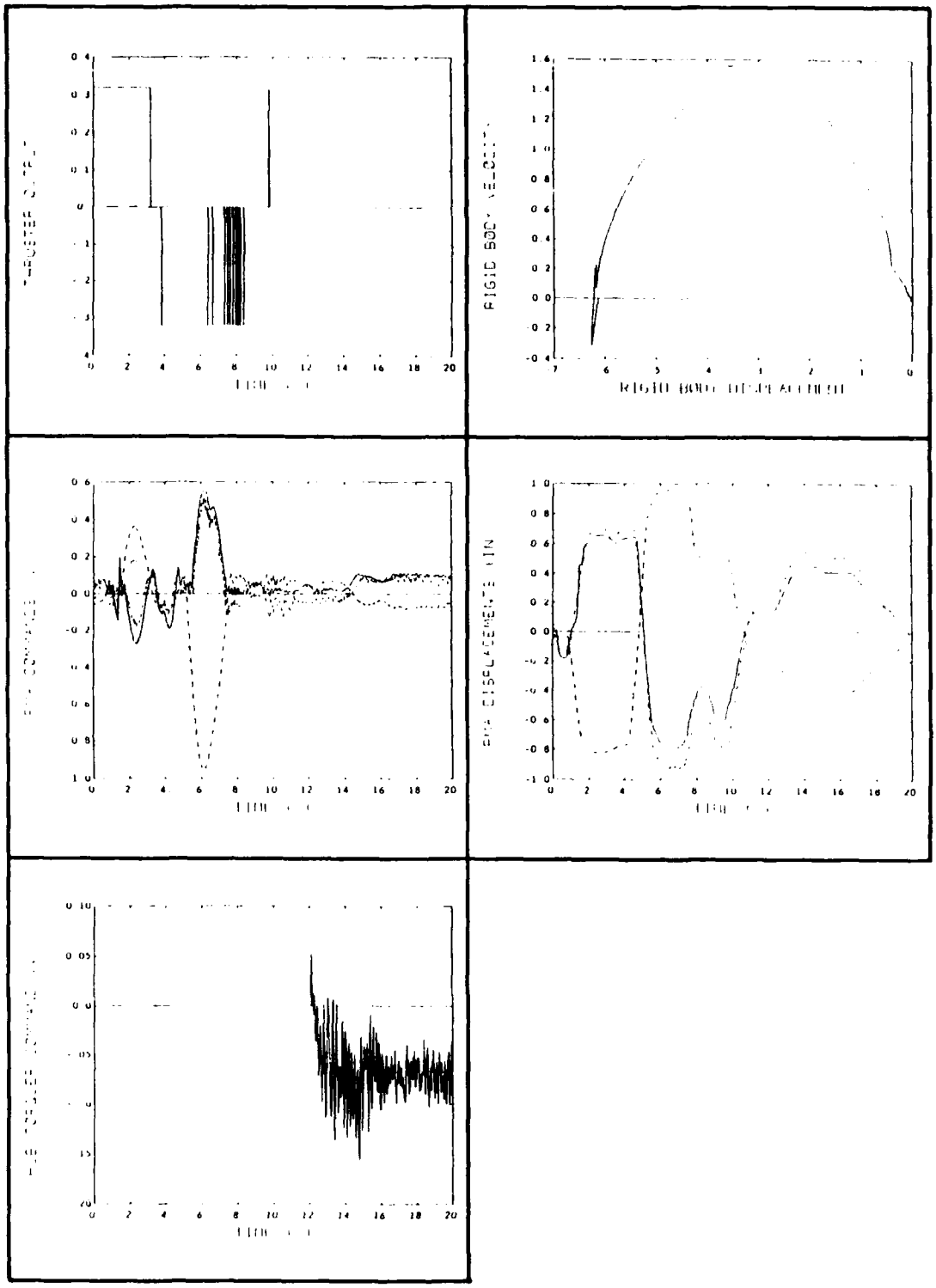

Figure M-9. 45 degree slew, using thrusters with terminal phase constraints, with the hub torquer active in the terminal phase, and with PMAs active throughout the test. (Rigid body phase plane, thruster force command, PMA displacements, PMA force commands, and hub torque command).

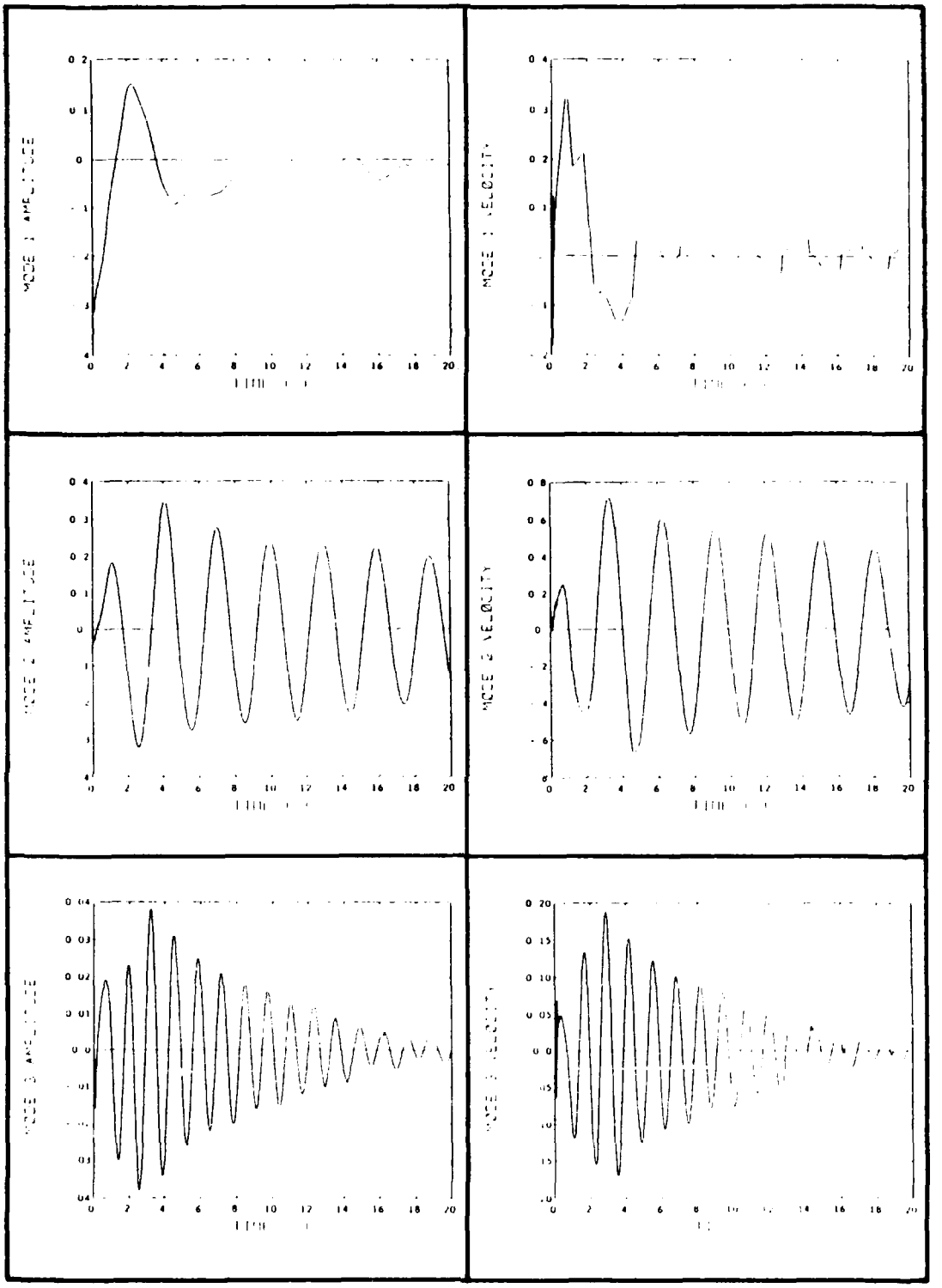

Figure M-10. 2 degree slew, using thrusters only, with terminal phase constraints. (Modal displacements and velocities).

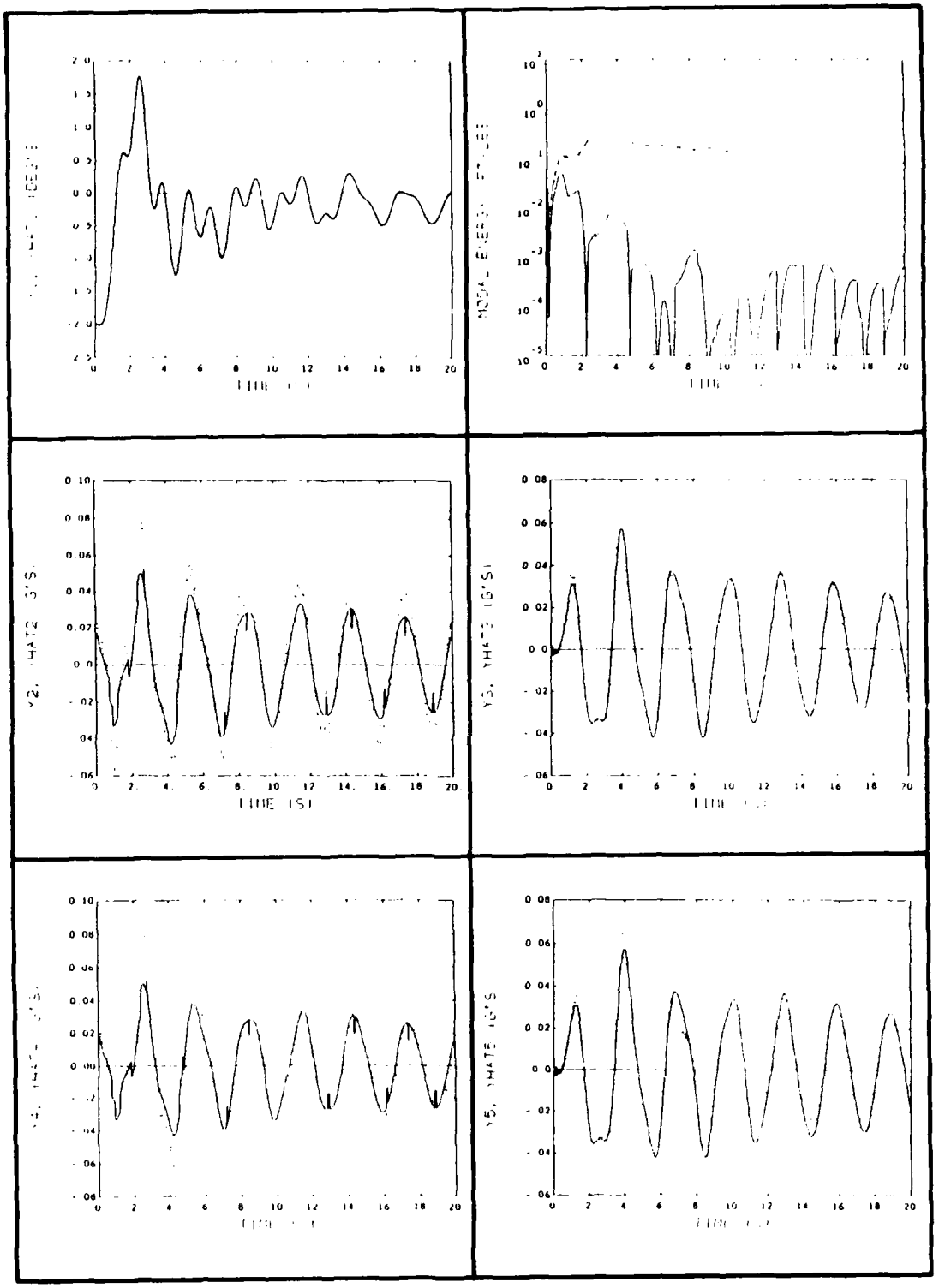

Figure M-11. 2 degree slew, using thrusters only, with terminal phase constraints. (Hub angle, vibrational energy, and accelerometer measurements).

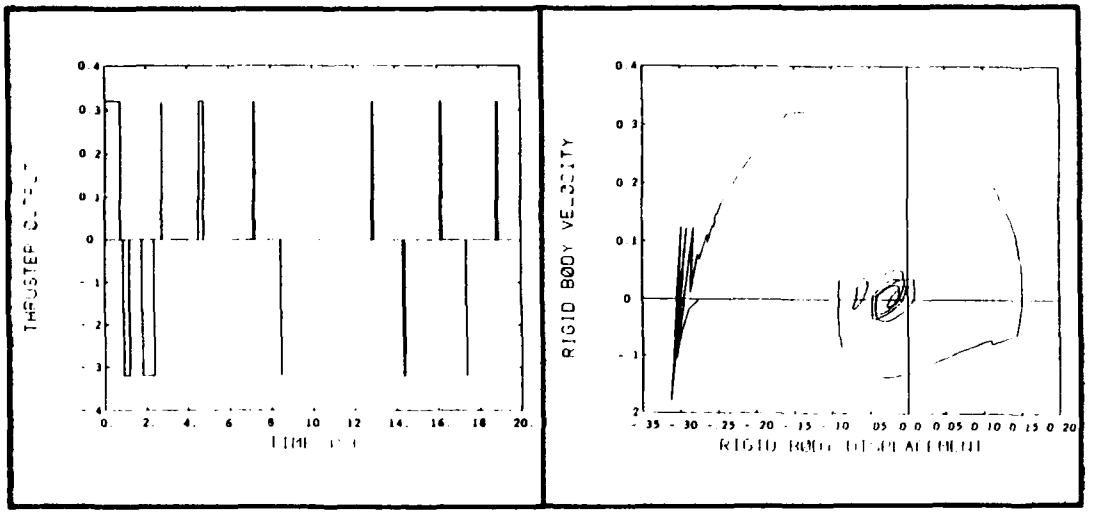

Figure M-12. 2 degree slew, using thrusters only, with terminal phase constraints. (Rigid body phase plane and thruster force command).

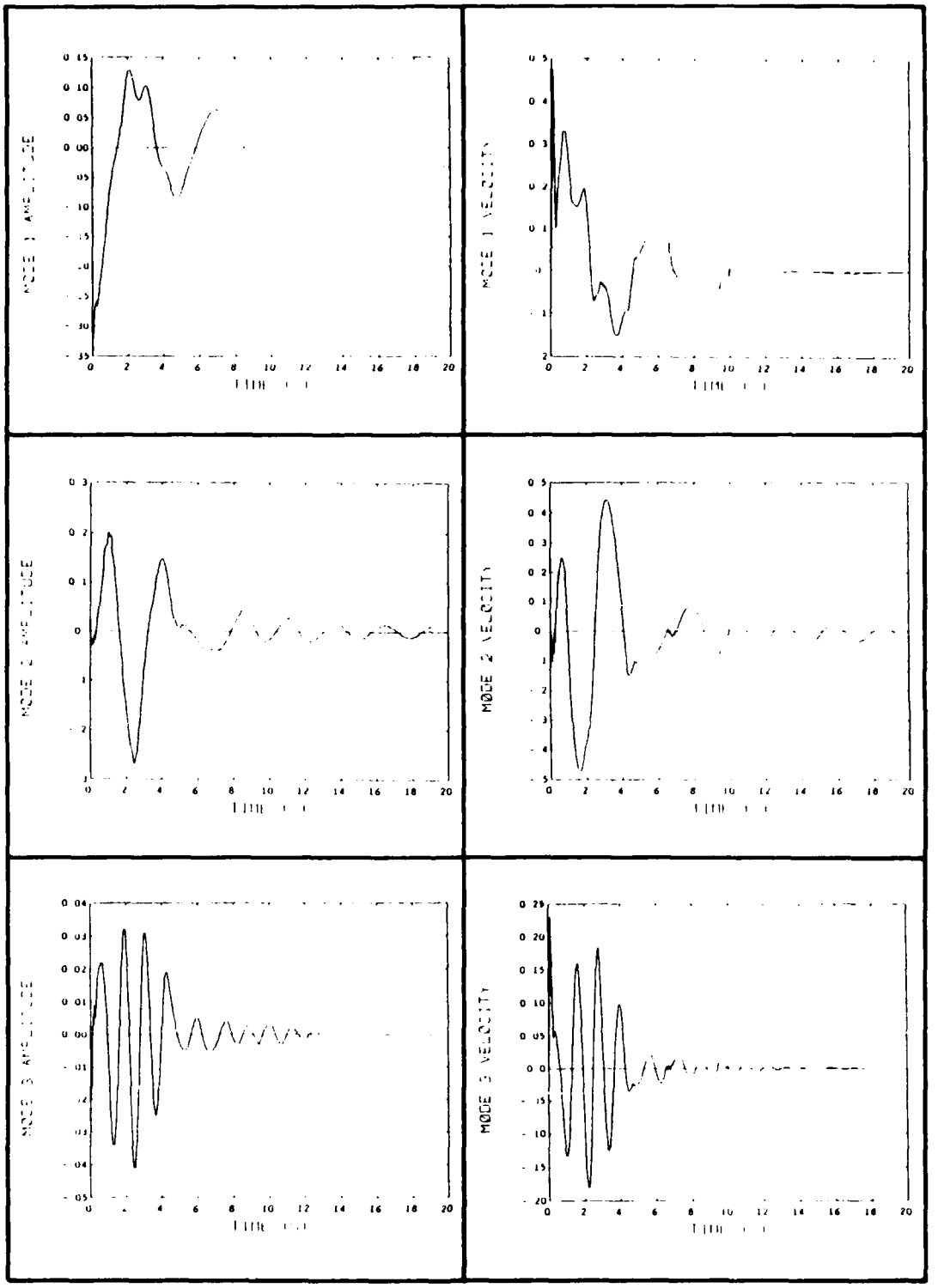

Figure M-13. 2 degree slew, using thrusters with terminal phase constraints, and with PMAs active throughout the test. (Modal displacements and velocities).

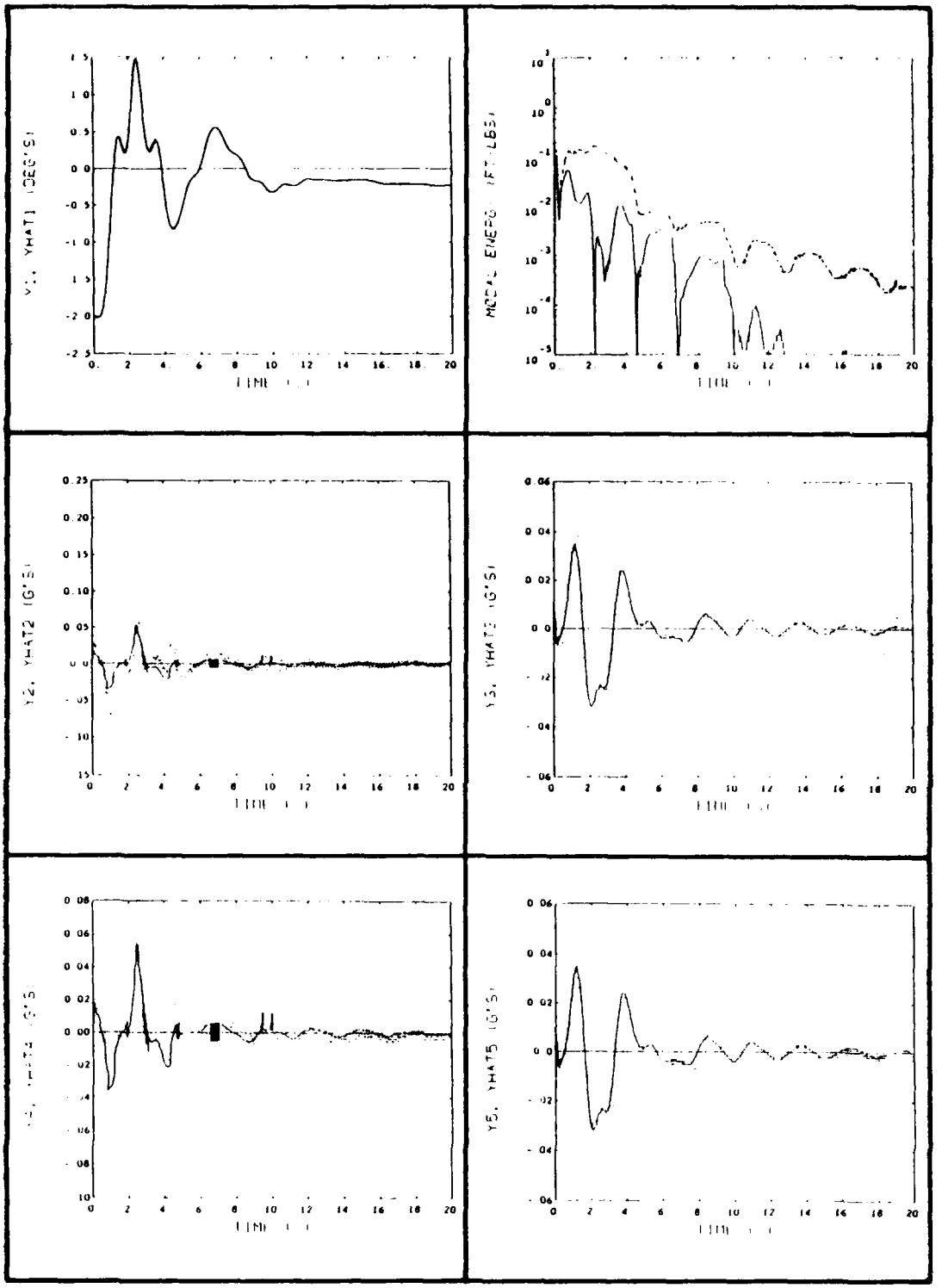

Figure M-14. 2 degree slew, using thrusters with terminal phase constraints, and with PMAs active throughout the test. (Hub angle, vibrational energy, and accelerometer measurements).

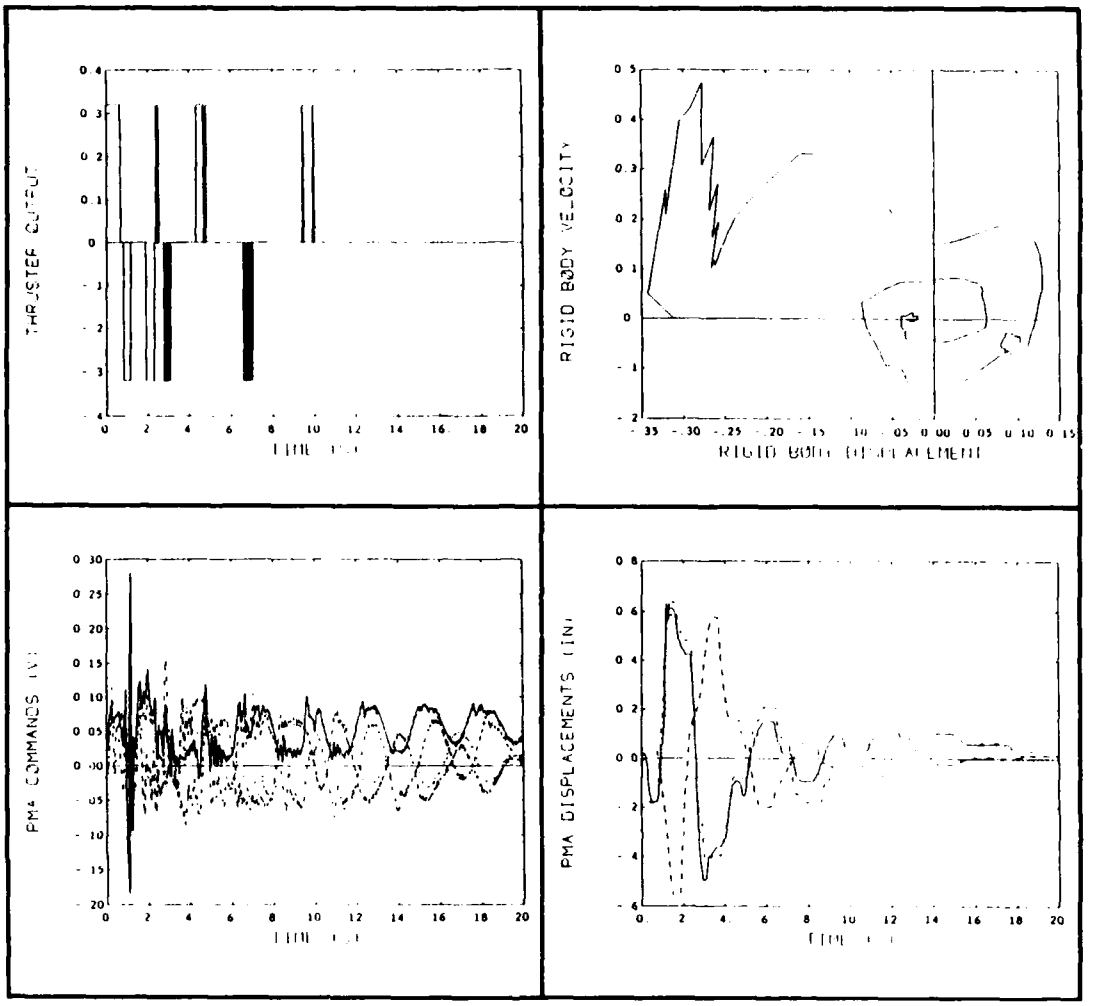

Figure M-15. 2 degree slew, using thrusters with terminal phase constraints, and with PMAs active throughout the test. (Rigid body phase plane, thruster force command, PMA displacements, and PMA force commands).

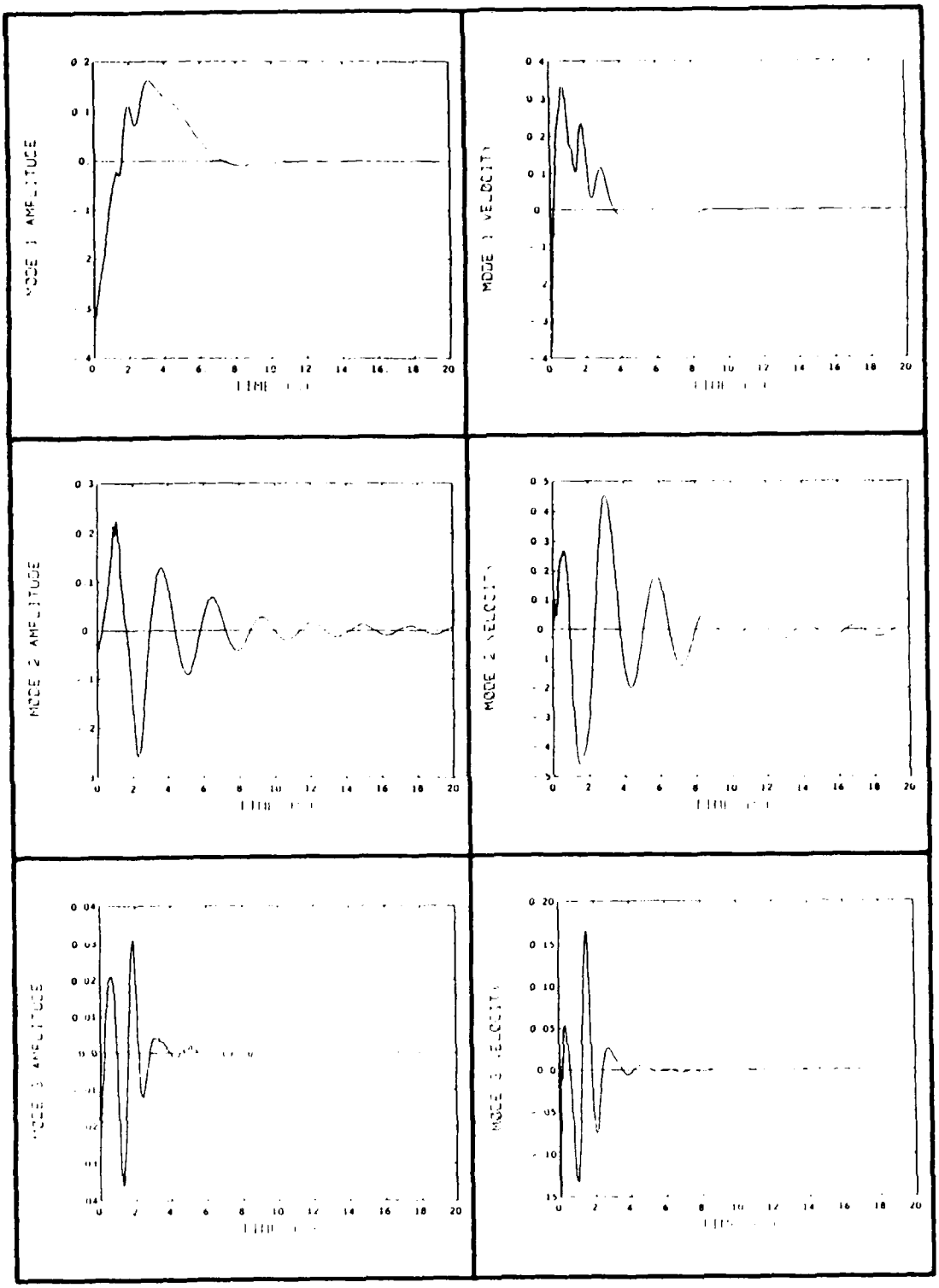

Figure M-16. 2 degree slew, using thrusters with terminal phase constraints, with the hub torquer active in the terminal phase, and with PMAs active throughout the test. (Modal displacements and velocities).

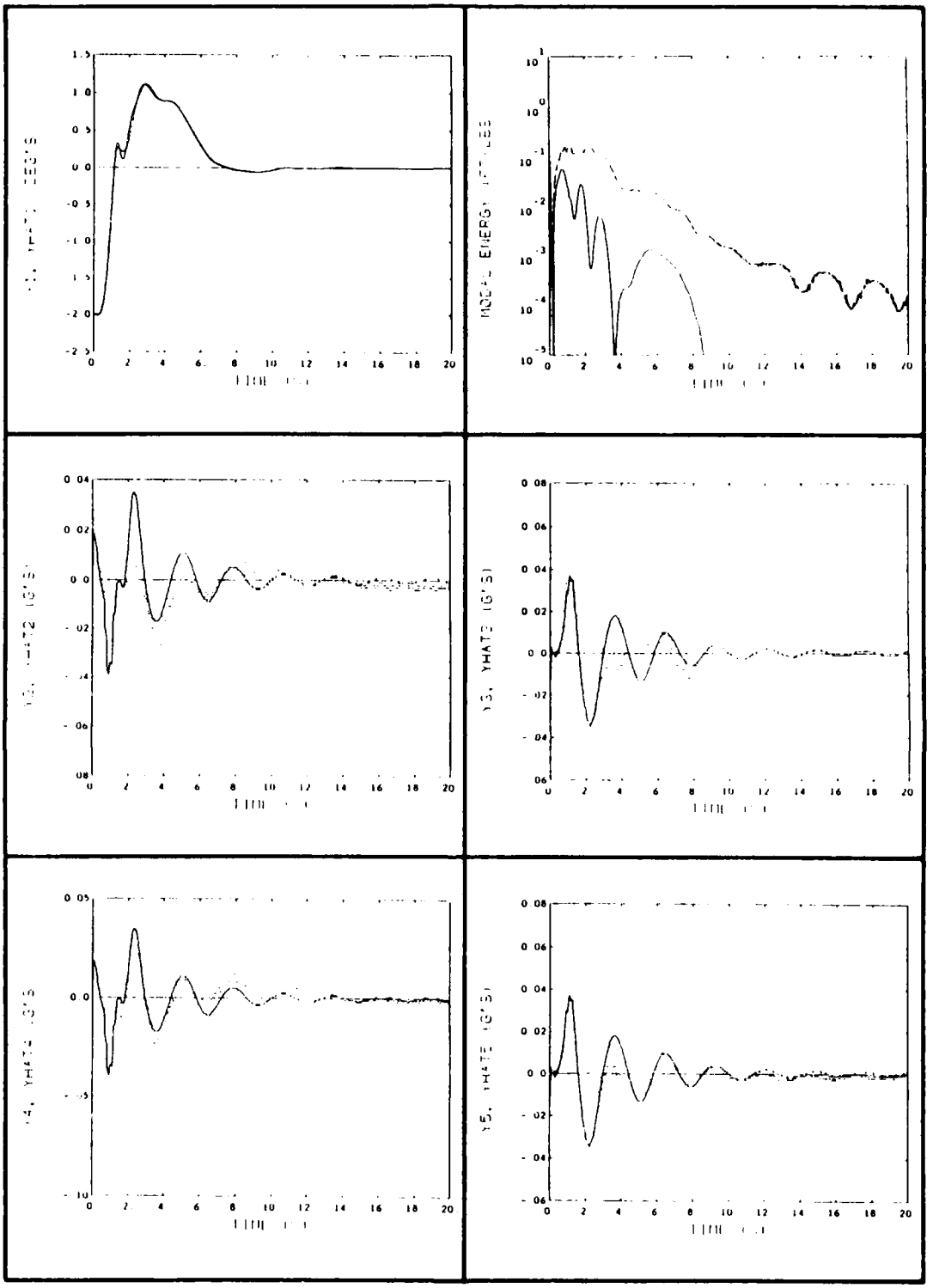

Figure M-17. 2 degree slew, using thrusters with terminal phase constraints, with the hub torquer active in the terminal phase, and with PMAs active throughout the test. (Hub angle, vibrational energy, and accelerometer measurements).

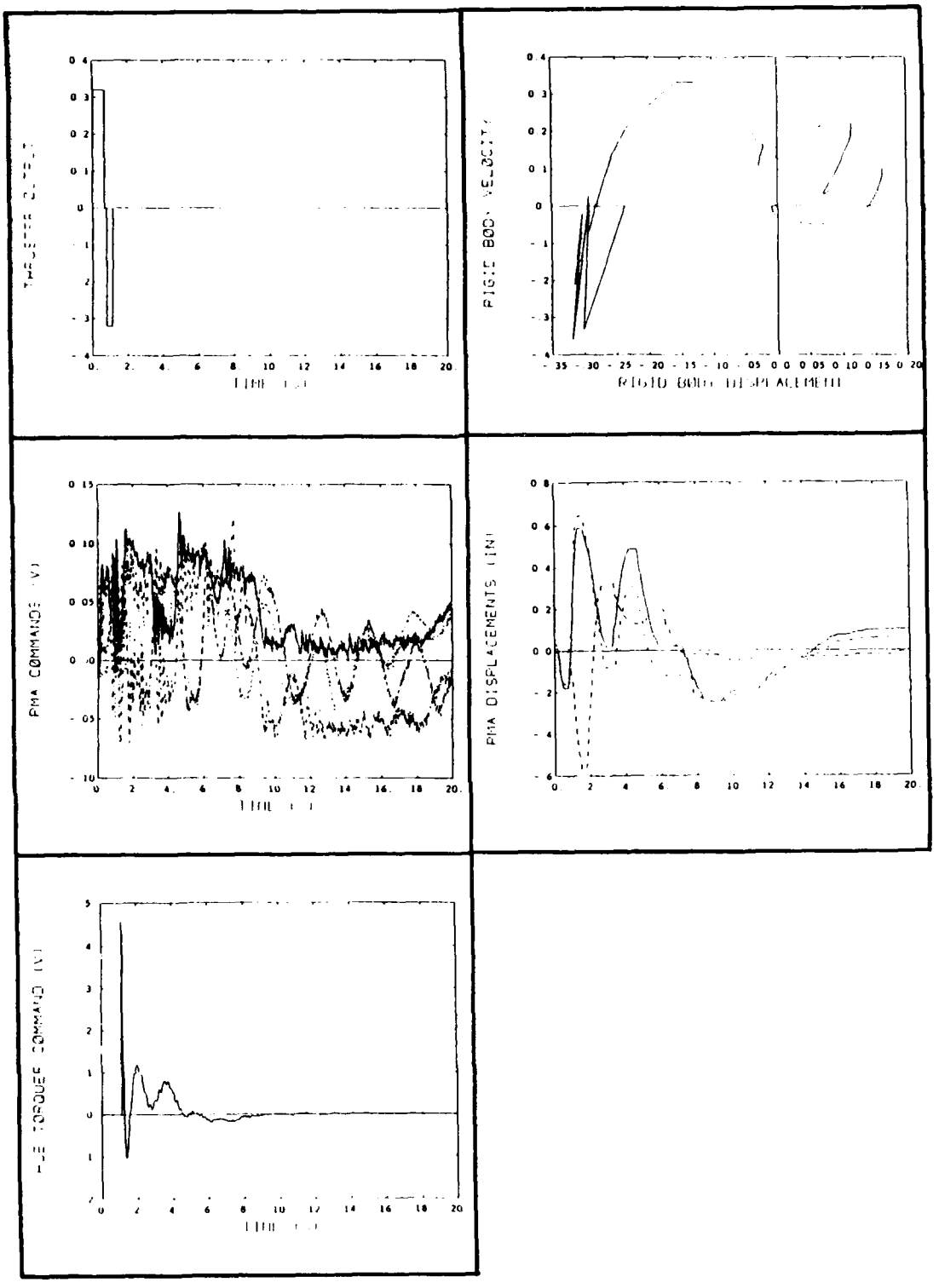

Figure M-18. 2 degree slew, using thrusters with terminal phase constraints, with the hub torquer active in the terminal phase, and with PMAs active throughout the test. (Rigid body phase plane, thruster force command, PMA displacements, PMA force commands, and hub torque command).

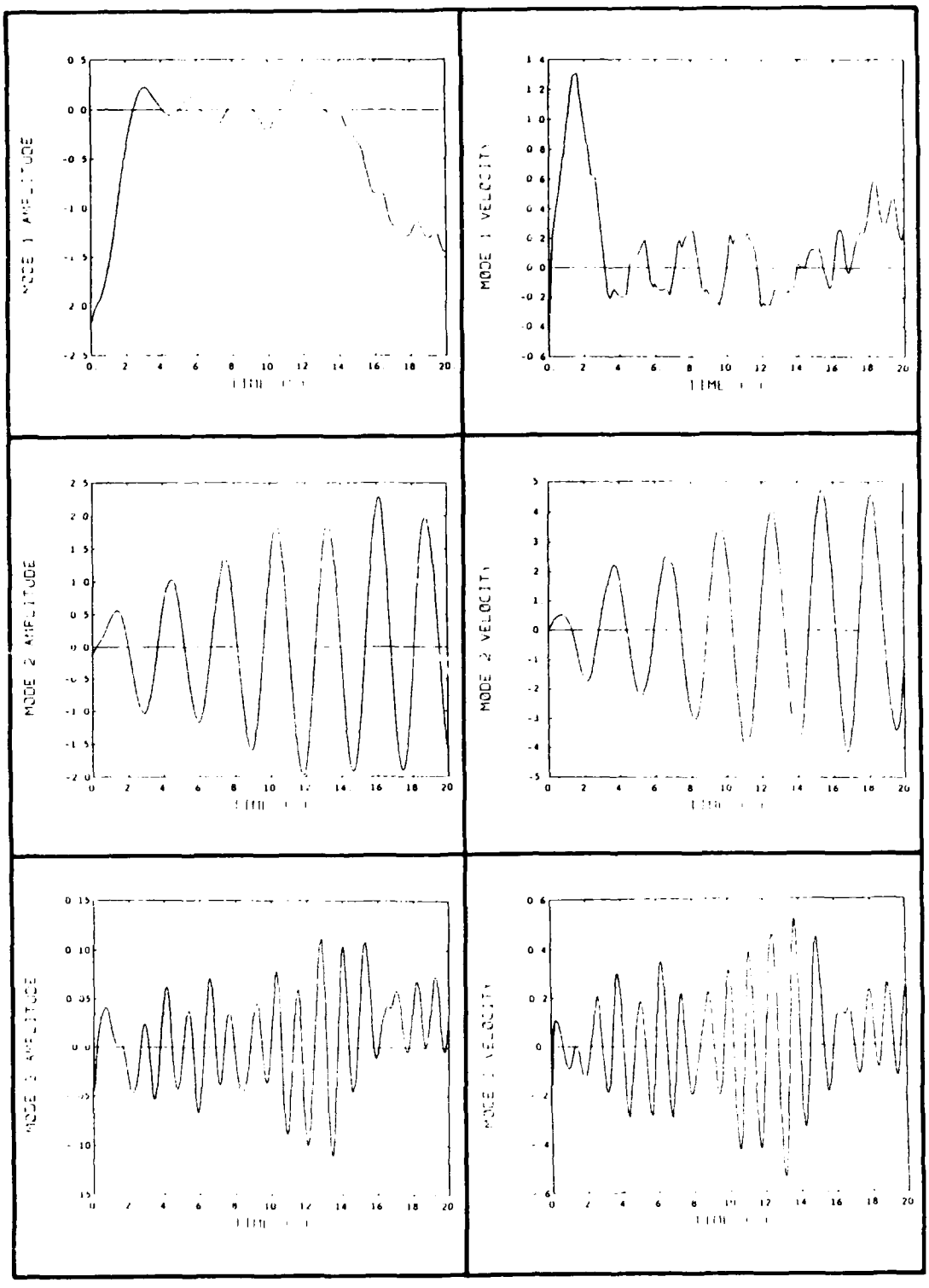

Figure M-19. 15 degree slew, using high-authority thrusters only, with terminal phase constraints. (Modal displacements and velocities).

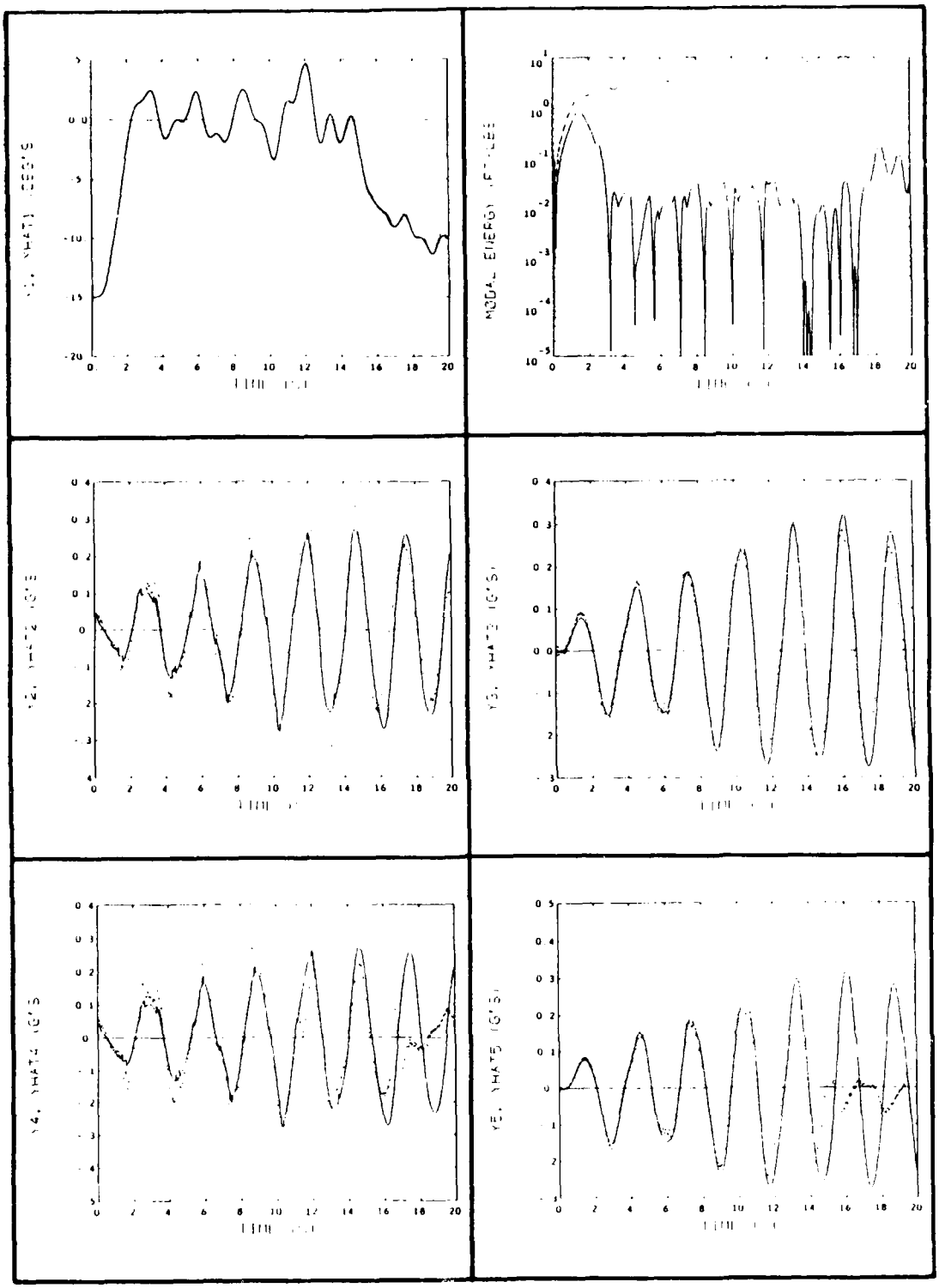

Figure M-20. 15 degree slew, using high-authority thrusters only, with terminal phase constraints. (Hub angle, vibrational energy, and accelerometer measurements).

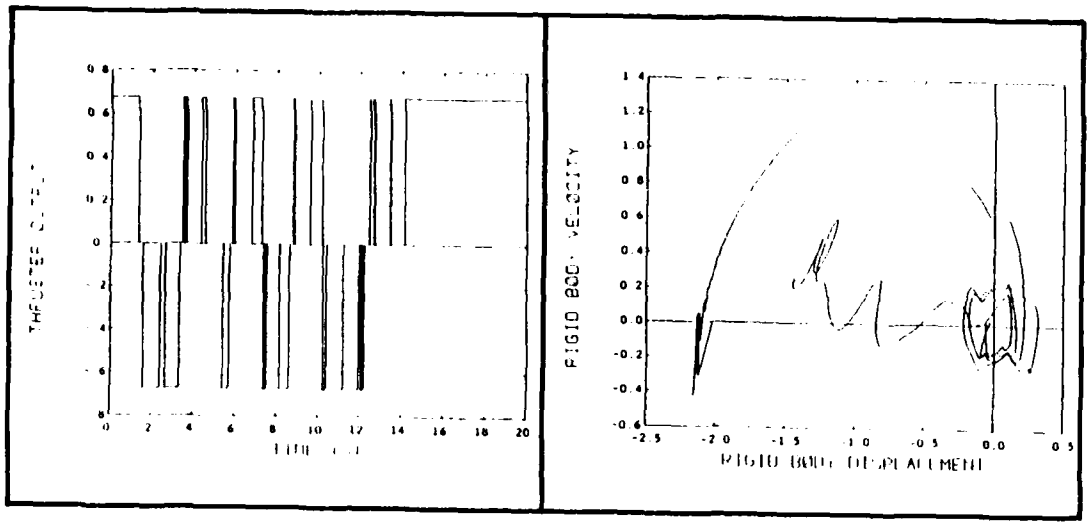

Figure M-21. 15 degree slew, using high-authority thrusters only, with terminal phase constraints. (Rigid body phase plane and thruster force command).

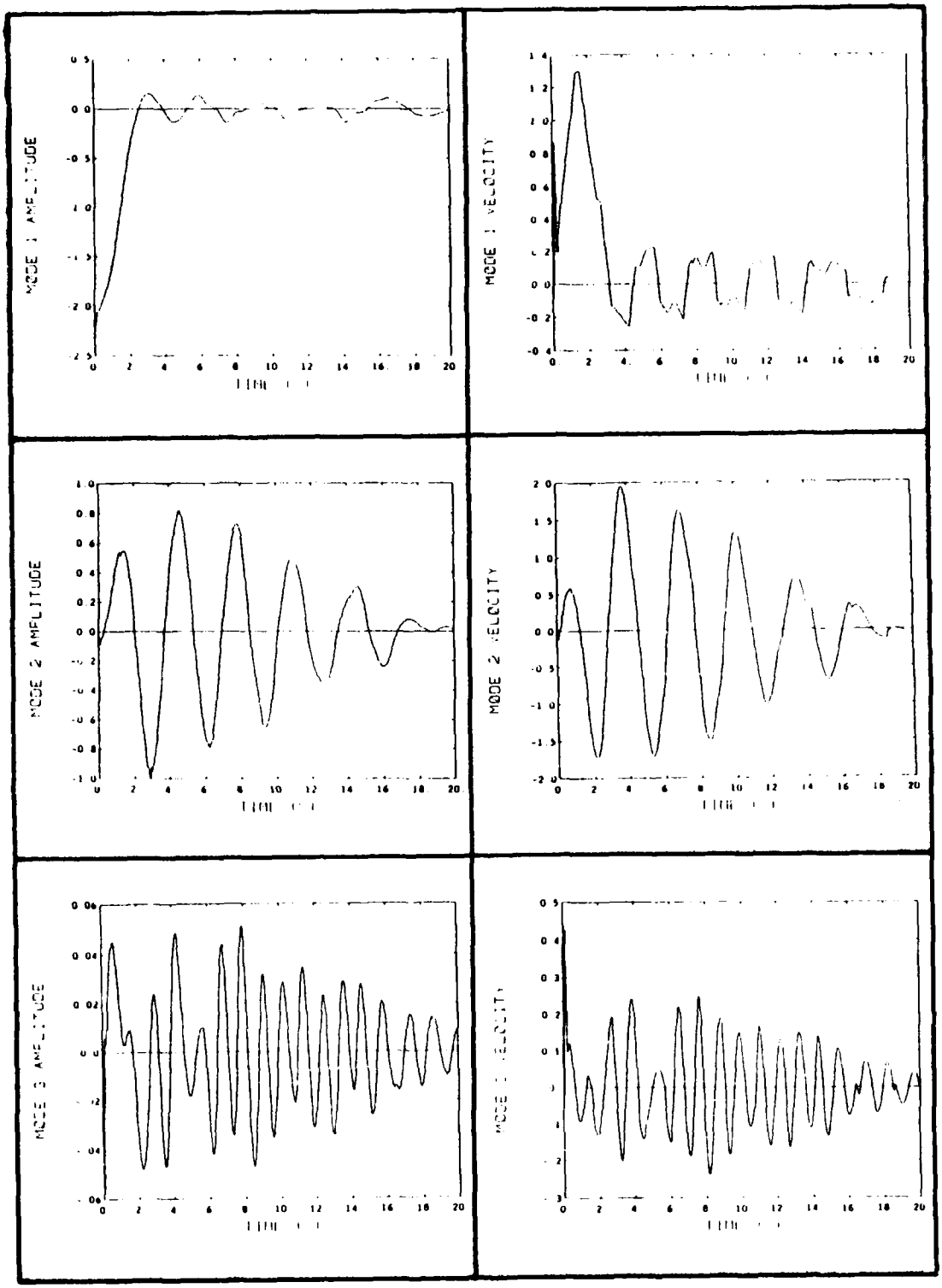

Figure M-22. 15 degree slew, using high-authority thrusters with terminal phase constraints, and with PMAs active throughout the test. (Modal displacements and velocities).

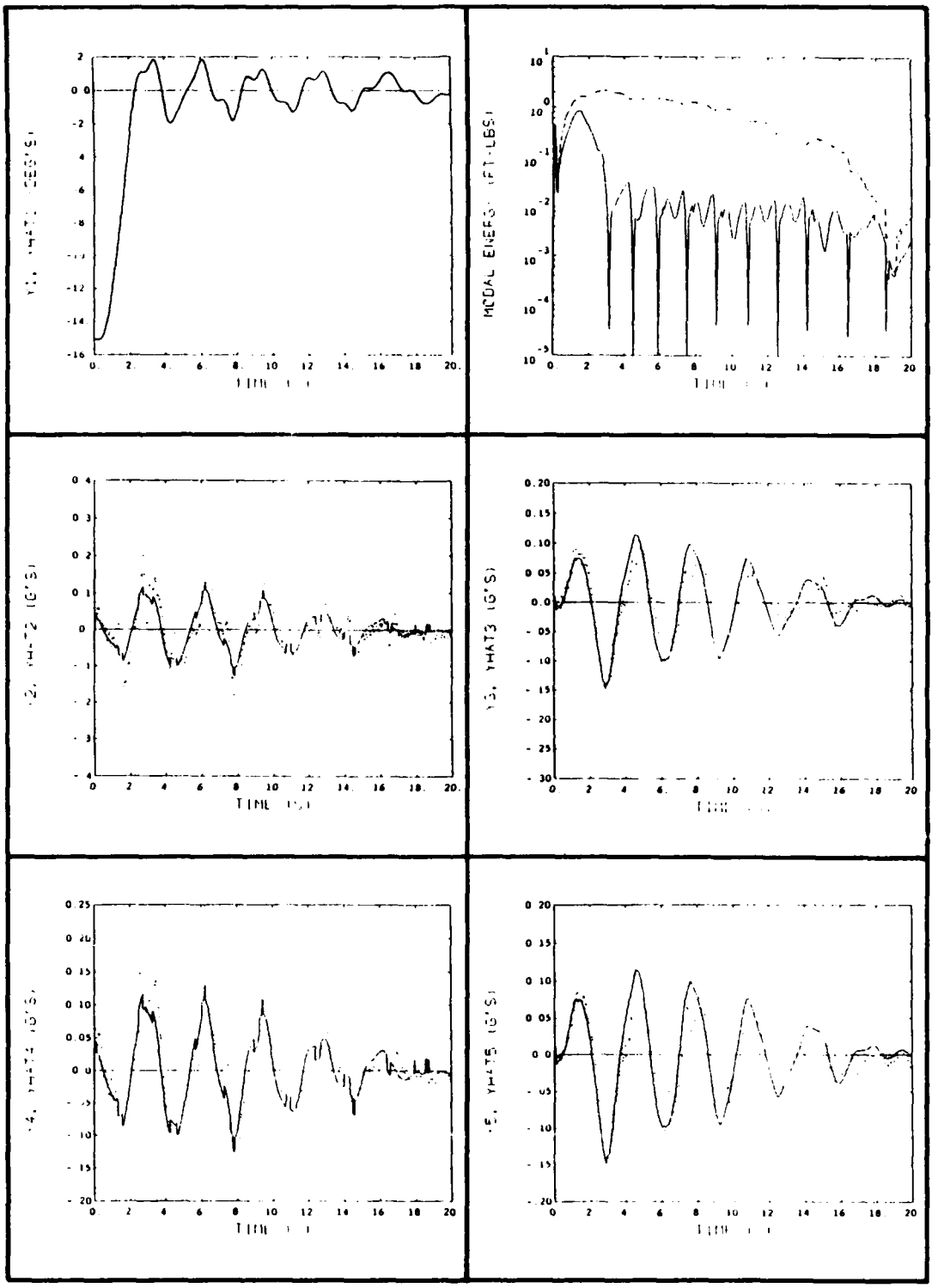

Figure M-23. 15 degree slew, using high-authority thrusters with terminal phase constraints, and with PMAs active throughout the test. (Hub angle, vibrational energy, and accelerometer measurements).

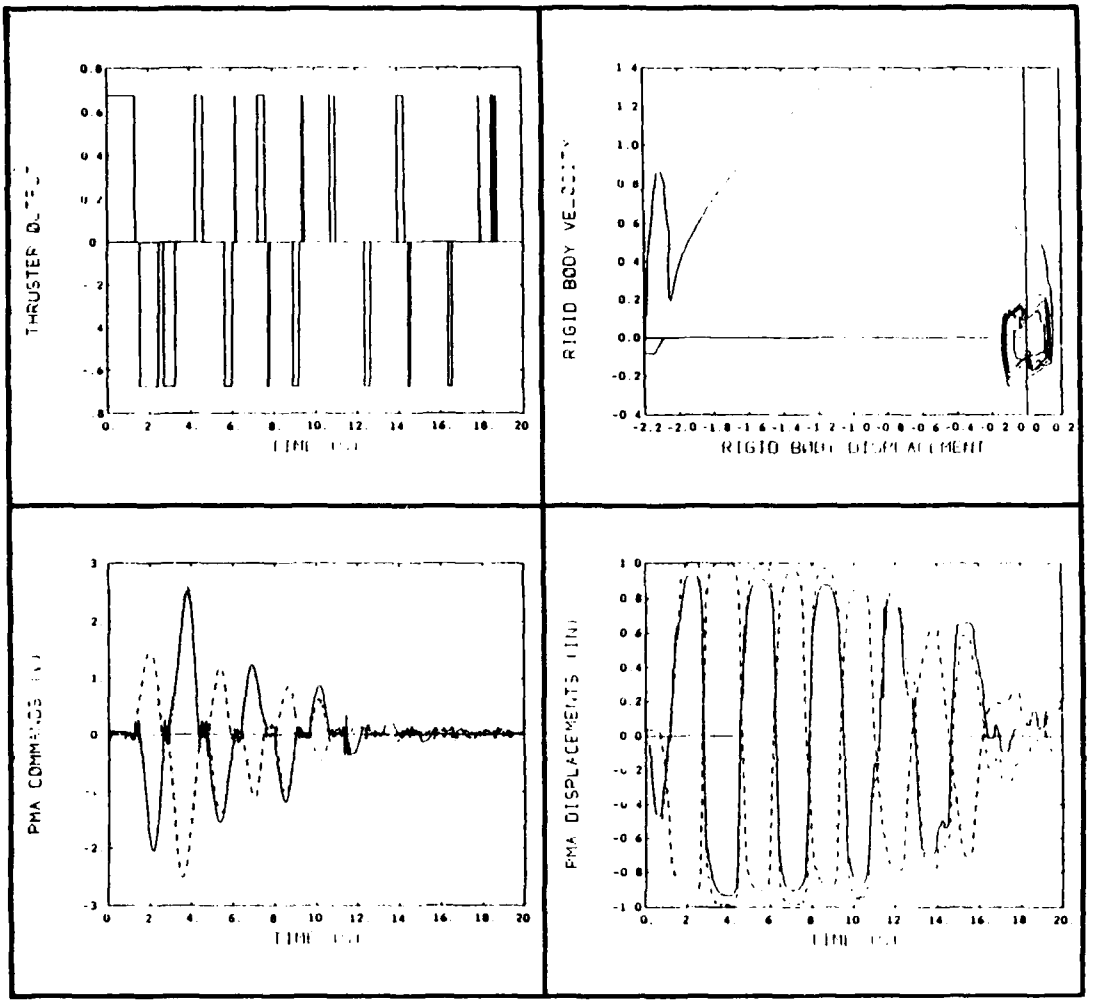

Figure M-24. 15 degree slew, using high-authority thrusters with terminal phase constraints, and with PMAs active throughout the test. (Rigid body phase plane, thruster force command, PMA displacements, and PMA force commands).

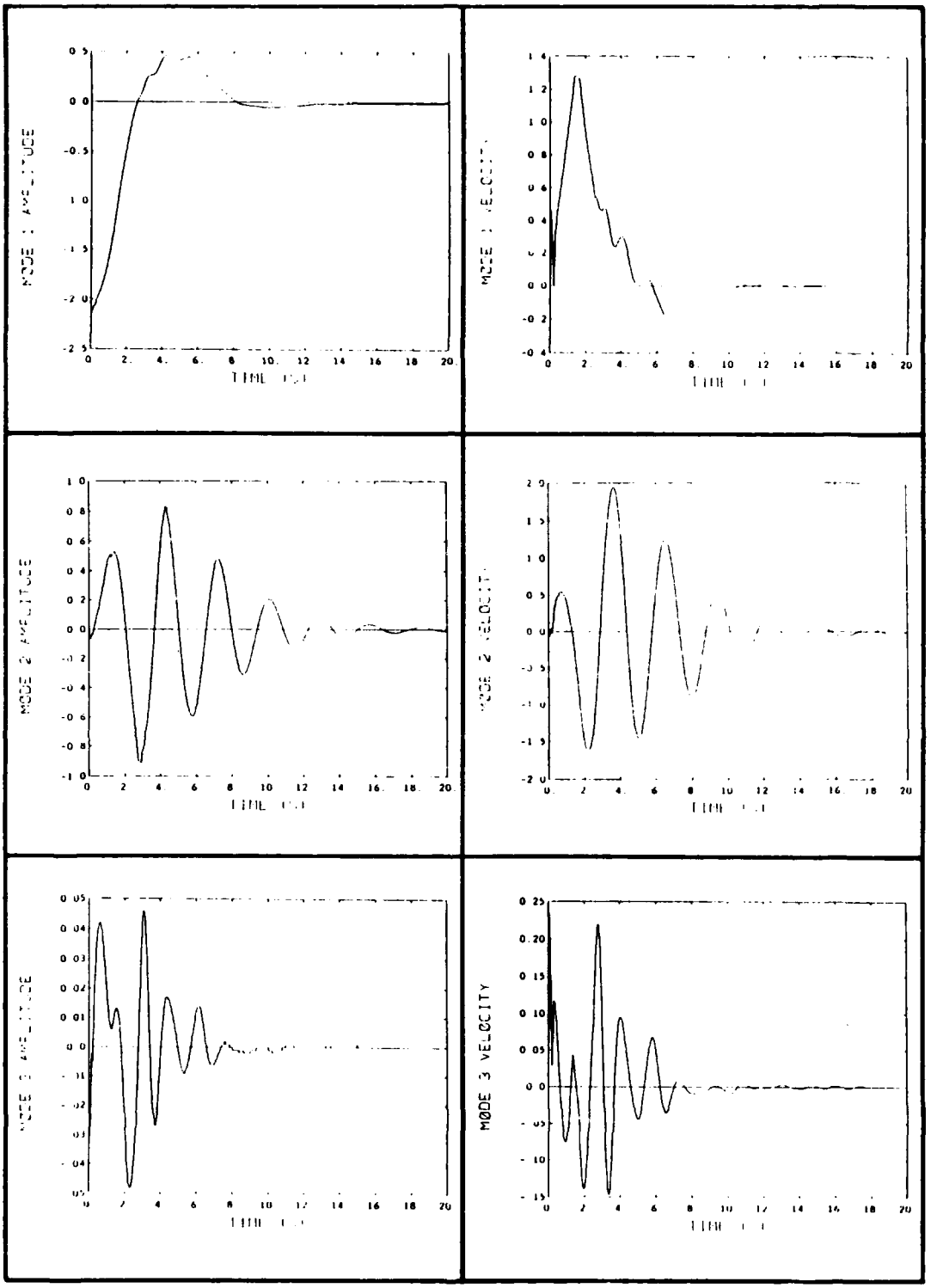

Figure M-25. 15 degree slew, using high-authority thrusters with terminal phase constraints, with the hub torquer active in the terminal phase, and with PMAs active throughout the test. (Modal displacements and velocities).

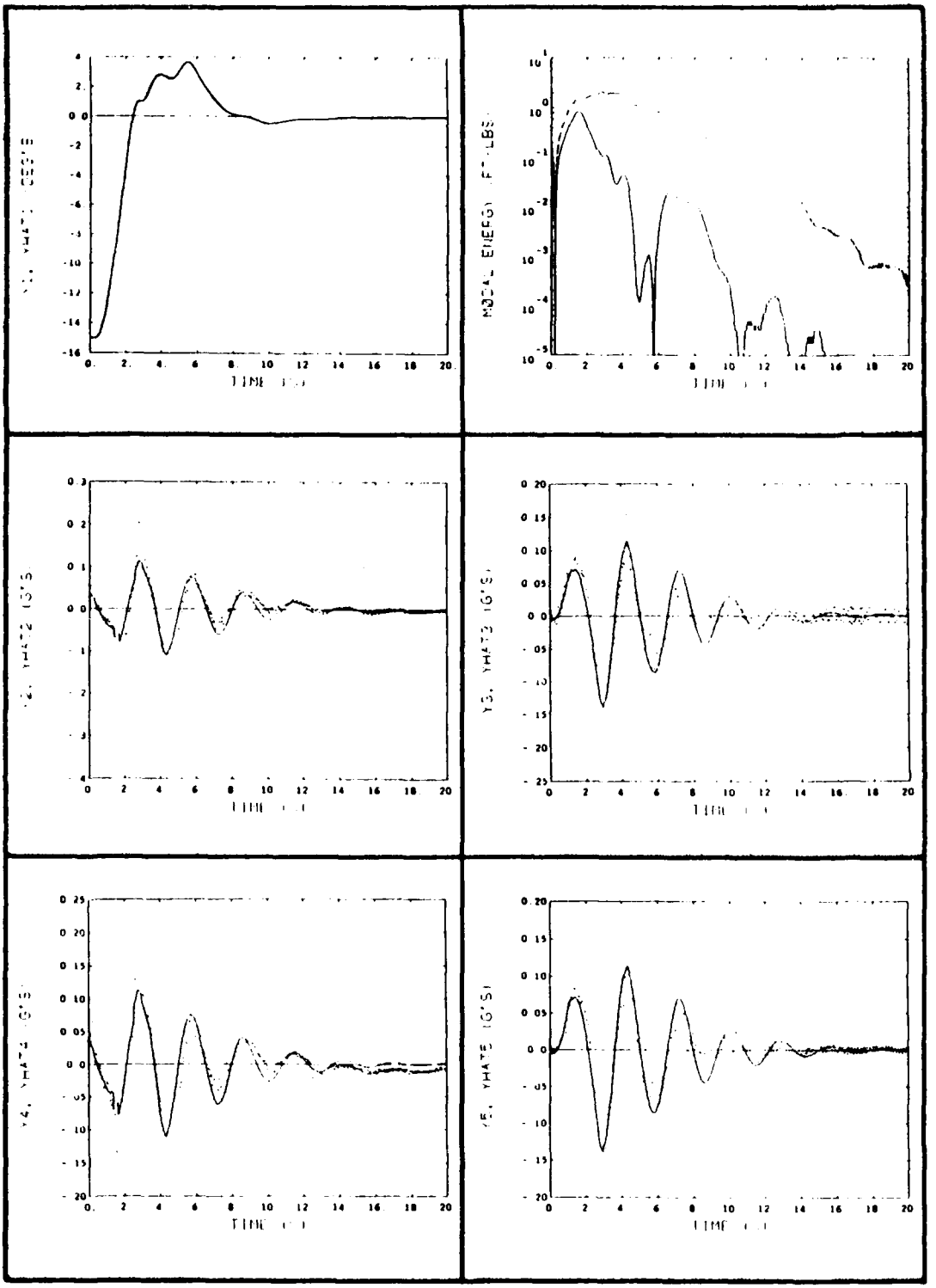

Figure M-26. 15 degree slew, using high-authority thrusters with terminal phase constraints, with the hub torquer active in the terminal phase, and with PMAs active throughout the test. (Hub angle, vibrational energy, and accelerometer measurements).

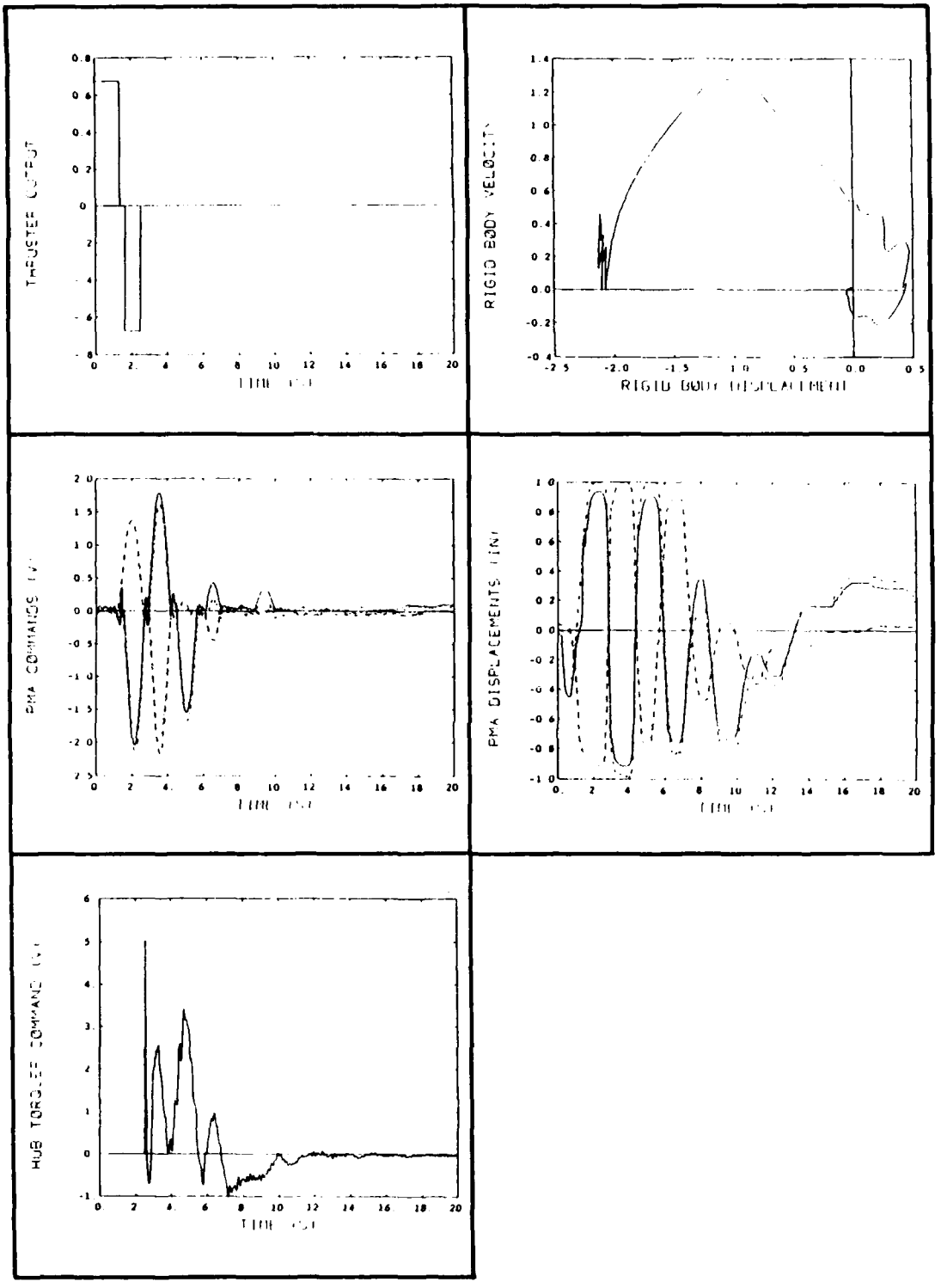

Figure M-27. 15 degree slew, using high-authority thrusters with terminal phase constraints, with the hub torquer active in the terminal phase, and with PMAs active throughout the test. (Rigid body phase plane, thruster force command, PMA displacements, PMA force commands, and hub torque command).